The Dissertation Committee for Nicolas J. Huerta certifies that this is the approved version of the following dissertation:

Time dependent leakage of CO_2 saturated water along a cement fracture

Committee:

Marc. A. Hesse Supervisor

Steven L. Bryant Co-Supervisor

Brian R. Strazisar

Peter B. Flemings

Richard A. Ketcham

Time dependent leakage of CO_2 saturated water along a cement fracture

by

Nicolas J. Huerta, B.S.; M.S.; M.S.E.

Dissertation

Presented to the Faculty of the Graduate School of

The University of Texas at Austin

in Partial Fulfillment

of the Requirements

for the Degree of

Doctor of Philosophy

The University of Texas at Austin

December 2013

Dedication

To my family and friends who have had to put up with me chasing this dream for far too long. I could not have done it without your support.

Acknowledgements

A significant portion of the hydrochloric acid experiments were performed with the assistance of undergraduate researchers Lauren Conrad, Matt Li, and Quinn Wenning. The composite core CO_2-saturated brine experiments were performed in collaboration with Jim Fazio (NETL/URS). I would like to thank Barbara Kutchko (NETL) for enlightening discussions about cement chemistry. I would also like to thank Christina Lopano (NETL) for helping with the μXRD and SEM analysis and excellent geochemistry discussions. I would also like to thank the UT Grad Rugby Team, colleagues in PGE, JSG, and GPMG for providing both distractions and fruitful scientific discussions that made my time at UT very enjoyable.

I would like to thank my thesis committee for their guidance, gentle prodding, and patience though out my time at UT. I would specifically like to thank Dr. Bryant for helping me to learn (at least in part) to think like an engineer and improve as a researcher. I would like to thank Dr. Hesse for welcoming me back to geology and showing me that there is a whole class of exciting problems in the geosciences that are begging for quantitative analysis by those brave enough to tackle the mathematics. Finally I would like to thank Dr. Strazisar who was always there to provide feedback, allow me to vent, and encourage me to keep moving forward.

Partial support for this work comes from the Geological CO_2 Storage Industrial Affiliates Program at the Center for Petroleum and Geosystems Engineering at the University of Texas at Austin. This work was also supported by the Carbon Sequestration program of the U.S. DOE National Energy Technology Laboratory.

Time dependent leakage of CO_2 saturated water along a cement fracture

Nicolas J. Huerta, Ph.D.

The University of Texas at Austin, 2013

Supervisors: Marc A. Hesse and Steven L. Bryant

Leakage of CO_2 saturated fluid along wellbores has critical implications for the feasibility of geologic CO_2 storage. Wells, which are ubiquitous in locations ideal for CO_2 storage, develop leaks (e.g. fractures) for many reasons and at different points in their age. Small leaks pose the most significant risk to geological CO_2 sequestration because they are difficult to detect and provide a direct pathway through which fluid can escape the storage formation. This dissertation shows that due to complex coupling between reaction and flow, leaking wells will tend to self-seal via secondary precipitation of calcium carbonate in the open pathway. Residence time, fluid reactivity, and initial fracture aperture all play a key role in determining the time required to seal the leakage pathway.

To test the self-sealing hypothesis, laboratory experiments were conducted to inject reactive fluids into naturally fractured cement. Restriction of the leakage pathway, i.e., the fracture, was inferred from the relationship between flow rate and pressure differential. Precipitation was observed in both constant flow rate and constant pressure differential experiments. In the former precipitation resulted in an increasing pressure differential, while precipitation caused a decrease in flow rate in the latter. Analysis by

electron microprobe and x-ray diffraction, and corroborated with effluent chemical analysis, showed that the reacted channel was depleted in calcium and enriched in silicon relative to the original material. The remaining silicon rich material prevents widening of the reacted channel and development a self-enhancing (e.g. wormhole) behavior. Self-limiting behavior is caused by calcium mixing with carbonate ions in high pH slow flow regions where local residence time is large and calcium carbonate is insoluble. Secondary precipitation initially develops next to the reacted channel and then across the fracture surface and is the source of pathway restriction and the self-sealing behavior.

Results from the experiments are used to develop a simple analytical model to forecast well scale leakage. Future work is needed to test a broader range of experimental conditions (e.g. brine salinity, cement formulations, cement-earth interface, effect of CO_2 saturation, pressure, and temperature), to improve our understanding of both the fundamental behavior and the leakage model.

Table of Contents

List of Tables

List of Figures

1. Wellbore leakage during CO_2 sequestration

1.1. SUMMARY

This chapter introduces geologic CO_2 sequestration (GCS), explains why GCS is necessary, and discusses technical issues hindering implementation. Next, an overview of wellbore leakage is presented and discussed in the context of GCS. Subsequently, the topics of well construction, cement chemistry, reactive transport, and fracture flow are introduced to set the background for material presented in the dissertation. Finally a problem statement is presented along with a hypothesis and an overview of the methods used to test the hypothesis.

1.2. REVIEW OF GEOLOGICAL CO_2 SEQUESTRATION

Over the past few decades a significant volume of research has shown that the rise in atmospheric CO_2 concentration is caused by human activity and that it is affecting global climate (IPCC, 2013; Metz et al., 2005). Climate models have shown that natural and anthropogenic forcing is accounting for the relatively rapid increase in mean surface temperature (Stott et al., 2000). While the earth naturally sequesters atmospheric CO_2 as part of the global carbon cycle the system is unable to account for the rapid anthropogenic increase in atmospheric CO_2. Additionally the capability of the oceanic and terrestrial sinks to absorb CO_2 is expected to diminish as we drive the system further out of equilibrium (Falkowski et al., 2000). Global climate change is expected to have significant and often negative impact on the earth and human society. Some examples are sea level rise which will result in the flooding of coastal cities and altered precipitation patterns that affect agricultural regions (Jevrejeva et al., 2010; Rosenzweig and Parry, 1994). The rise in global energy demand is expected to continue as developing countries

grow and prosper. Thus the use of all energy sources, including CO_2-emitting fossil fuels, is likely to increase.

To mitigate the continued release of anthropogenic CO_2 researchers have studied many methods to sequester CO_2. One of the most promising is to capture the CO_2 at point sources (such as coal fired power plants) and to inject the fluid into a subsurface formation. This method is called geologic carbon sequestration (GCS). Sedimentary basins have the capacity to store many years of CO_2 (Bruant et al., 2002; Goodman et al., 2011) but implementation of GCS has proven difficult. This is despite the fact that the oil industry has been injecting CO_2 for enhanced oil recovery for many decades and the technology is not new. However, the amount of CO_2 that needs to be sequestered to have a significant effect is much larger than what the oil companies typically use. Global CO_2 emissions from fossil fuels and cement plants in 2011 was 9,500 Mt (IPCC, 2013). To put this in perspective, Sleipner Vest Field in the North Sea has had 1 Mt of CO_2 injected into it annually (Bruant et al., 2002) and the enhanced oil recovery operations in the U.S. typically inject (half of which is not new CO_2 but recycled) 40 Mt per year (Hanisch, 1999). GCS is not a perfect solution as the power requirements are a significant fraction of a power plant's total energy production (Burton and Bryant, 2009). Additionally, because free phase CO_2 in the subsurface is buoyant the risk of CO_2 escaping the storage formation may not be trivial. Characterizing leakage risk is necessary for regulators, industry, and society as a whole to set regulations and choose to utilize the technology (Oldenburg et al., 2009). Faults and wells provide the most likely pathway for CO_2 to migrate from the storage formation up to an underground source of drinking water or back into the atmosphere. Wells in particular provide a direct pathway through the earth and the process of drilling a well and ensuring that no fluids move along a completed well is not trivial.

Depending on the specific GCS site, fluid may be injected into the storage formation for several decades and reservoir pressure will rise above a baseline value pressure (typically hydrostatic pressure). Monitoring reservoir pressure and the buoyant CO_2 plume will be required to ensure containment of the injected fluid (EPA, 2010). The elevated reservoir pressure has the capability to fracture sealing formations, reactivate faults, or open pre-existing pathways in abandoned wells (Bruant et al., 2002). Thus there is a critical need to understand how wells will behave when exposed to CO_2-rich fluids.

The research in this dissertation focuses on single-phase exposure of CO_2-saturated water to wellbore cement. Exposure of cement to free-phase CO_2 creates a carbonation zone that acts to armor the cement to further reaction (Kutchko et al., 2007). However in the presence of significant water the reaction processes are more aggressive. The environment around well cement is expected to be water saturated and studying the more reactive system is most important for risk assessment purposes. There is a possibility for multiphase fluid flow along a leaky well but data on the relative permeability properties of cement is extremely limited (Monlouis-Bonnaire et al., 2004) and the geochemical reactions studied in this dissertation will still be present. Thus it is necessary to characterize the complex coupled reactive transport processes in single-phase flow before a more complex multiphase flow study is attempted.

Depending on the subsurface conditions (e.g. pressure, temperature, and brine salinity) free phase CO_2 will dissolve into the formation brine and form carbonic acid. Once the CO_2 is dissolved the carbonate system will speciate into protons, bicarbonate, and carbonate ions according to the following reactions (Li and Duan, 2007):

$$CO_{2(aq)} + H_2O \rightleftarrows HCO_3^- + H^+ \qquad (1.1)$$

$$HCO_3^- \rightleftarrows CO_3^{2-} + H^+ \qquad (1.2)$$

At subsurface conditions of elevated pressure, temperature, and in the presence of brine the CO_2-saturated fluid is a weak acid. Increased temperature leads to less dissolved CO_2 in the brine and a relatively higher (though still acidic) pH. Increased CO_2 pressure has the opposite effect, where increased pressure causes more CO_2 to dissolve and yields a more acidic fluid. Under subsurface conditions this is one of the most important effects (Duan and Sun, 2003). Increased dissolved solids will result in a fluid with lower CO_2 solubility (Duan and Sun, 2003). At subsurface conditions pore fluid will equilibrate to have much more carbonate ion than bicarbonate ion (Li and Duan, 2007).

1.3. WELLBORE INTEGRITY ISSUES

The petroleum industry has been drilling wells for hydrocarbon exploration since the 1900's and while those early wells were only a few thousand feet, modern wells can penetrate tens of thousands of feet into the earth. It is also true that wells are most densely distributed around the sedimentary basins that are also the best candidates for GCS (Nicot, 2009).While modern wells are planned, drilled, and completed using the latest technology and according to specific guidelines they can develop leaks early on or later in life for numerous reasons (Sabins and Wiggins, 1997). Most importantly, older wells were not necessarily constructed using best the practices or materials and have had longer time to develop leaks (Watson and Bachu, 2009, 2008, 2007). Thus it is a safe assumption that wells in and around a GCS operation are likely leakage pathways and understanding the nature of the leak path is necessary.

1.3.1. Well construction

To understand the nature of leaks it is useful to review the general process of well drilling and completion (Bourgoyne et al., 1986). The construction of a well consists of drilling a hole into the sub surface to a target depth. Drilling is performed using a complex drill bit, drill collars (for weight), and drill pipe. Drilling mud is circulated through the pipe, out the bit, up the annular space outside the pipe, and back to the surface. Drilling mud prevents subsurface fluids from invading the well by providing balancing pressure the pore pressure and removes cuttings from the bottom of the hole. Once target depth is reached steel casing, often hundreds of feet long, is placed in the well. Cement is then pumped through the inside of the casing, pushed through the bottom of the hole, and back up the annular space to cure along a specific interval. Cement is used to support the casing string, prevent the steel from contacting subsurface fluids, and prevent flow of fluids along the annular space from one formation to another. Once the cement is set, the next interval is then drilled and a smaller diameter casing is inserted and cemented in place. The specific geologic conditions and well design will dictate how many times this process is repeated to reach the target depth. For example it is often required to drill below an underground source of drinking water (USDW) to seal off any potable aquifer with casing and cement the annular space back to the surface (TRRC, 2013).

The entire process of planning, drilling, and completing a well is very complex. This complexity combined with subsurface geologic heterogeneity means that each well is unique. With such variability there is a significant chance that a well could develop a leak.

Wells develop leaks for many reasons and at different stages in the life of a well (Mueller et al., 2004). Wells that develop leaks early on, for example, from poor mud

removal or insufficient wait on cement time typically have leaks that are easily detected and remediated (Milanovic and Smith, 2005). Wells that develop leaks later in life from the stress of cycling pressure and temperature associated with stimulation, water flooding, and EOR might be more difficult to detect. Indeed even a well that exhibited an early leak but was remediated can develop another leak. New wells are expected to contain mechanically durable and chemically resistant cement formulations (Moroni et al., 2008). If the wells and field are actively monitored a leak can be detected and fixed, but it is the abandoned and unmonitored wells that pose the greatest risk to be a conduit for CO_2 leakage.

The geometry of the leak path is related to the root cause. Poor mud removal or gas entrainment lead to cylindrical channels (Soter, 2003). Debonding between the casing-cement or the earth-cement interface creates a rough planar pathway (Boukhelifa et al., 2005). Tensile failure within the cemented annulus itself creates fractures (Ravi et al., 2002). The channel type behavior is more indicative of an early large leak that can be identified and remediated. The rough plane and fracture geometry is more likely to be the type present in an abandoned well and will be studied in this dissertation.

1.3.2. Wellbore cement

A well's cemented annulus plays a vital role in preventing the leakage of subsurface fluids along the wellbore and will be discussed in detail. Most cement used in the oil industry is called Ordinary Portland Cement (OPC). OPC is created by heating a blend of limestone and clay in a kiln at very high temperature. The resulting material is called clinker. The clinker is then is cooled, aged, and ground with gypsum to improve its properties (Bourgoyne et al., 1986). There are 4 key crystalline components in the clinker that hydrate to hardened cement and are shown on Table 1.1.

Table 1.1 – Cement clinker components (Bourgoyne et al., 1986).

Compound name	Shorthand	Chemical formula
Tricalcium silicate	C_3S	$3CaO \bullet SiO_2$
Dicalcium silicate	C_2S	$2CaO \bullet SiO_2$
Tricalcium aluminate	C_3A	$2CaO \bullet Al_2O_3$
Tetracalcium aluminoferrite	C_4AF	$4CaO \bullet Al_2O_3 \bullet Fe_2O_3$

C_3S is thought to contribute to initial strength development (within the first 28 days). C_2S hydrates more slowly but also contributes to the strength of the set cement. C_3A hydrates very quickly, and produces most of the early heat of hydration. C_3A hydration is controlled by gypsum addition to clinker. C_4AF does not contribute significantly to physical properties of cement (Bourgoyne et al., 1986).

To form a cement paste, the ground cement and water are mixed at a specific water-to-cement ratio. Cement hydration is an exothermic process with the following reactions (Bourgoyne et al., 1986):

$$2\left(3CaO \bullet SiO_2\right)+6H_2O \rightarrow 3CaO \bullet 2SiO_2 \bullet 3H_2O+3Ca\left(OH\right)_2 \quad (1.3)$$

$$2\left(2CaO \bullet SiO_2\right)+4H_2O \rightarrow (\text{slow})3CaO \bullet 2SiO_2 \bullet 3H_2O+Ca\left(OH\right)_2 \quad (1.4)$$

$$4CaO \bullet Al_2O_3 \bullet Fe_2O_3+10H_2O+2Ca\left(OH\right)_2 \rightarrow 6CaO \bullet Al_2O_3 \bullet Fe_2O_3 \bullet 12H_2O \quad (1.5)$$

$$3CaO \bullet Al_2O_3+12H_2O+Ca\left(OH\right)_2 \rightarrow (\text{fast})3CaO \bullet Al_2O_3 \bullet Ca\left(OH\right)_2 \bullet 12H_2O \quad (1.6)$$

$$3CaO \bullet Al_2O_3+10H_2O+CaSO_4 \bullet 2H_2O \rightarrow 3CaO \bullet Al_2O_3 \bullet CaSO_4 \bullet 12H_2O \quad (1.7)$$

These reactions form two main hydration products. The first product is Calcium Silicate Hydrate (C-S-H) which is sometimes approximated as tobermorite gel or as

jennite when numerical modeling is conducted (Huet et al., 2010). The material is a polymeric solid that can have different ratios of calcium to silicon depending on the mixing and curing conditions. The generic chemical formula is $3CaO{\bullet}2SiO_2{\bullet}3H_2O$. The second product is portlandite which is also called calcium hydroxide. The chemical formula is $Ca(OH)_2$.

C-S-H is about 70 wt.% of the hydrated cement and is the primary binding phase while portlandite is between 15 wt.% to 20 wt.% of the cement and tends to form rapidly in the available open spaces (such as pores and cracks) (Kutchko et al., 2007).

Other phases that are minor constituents of the hydrated cements are a family of hydrated calcium aluminates (AFm) (Matschei et al., 2007). One example is calcium-aluminum-monosulfate, which is relevant to the mechanisms of acid attack discussed later. The chemical formula is $3CaO{\bullet}Al_2O_3{\bullet}CaSO_4{\bullet}12H_2O$. The other AFm phase from the reactions above is $6CaO{\bullet}Al_2O_3{\bullet}Fe_2O_3{\bullet}12H_2O$.

The American Petroleum Institute (API) sets standards for the types of cement used in oil wells. There are 7 classes denoted A through H (API, 2011). Class G and H are the most common cement formulations used in the petroleum industry. The difference between G and H is the particle size of the ground cement (Nelson and Guillot, 2006). The work in this dissertation uses class H cement which is mixed, poured, and cured according to the API Recommended Practice 10B-2 (API, 1997). Table 1.2 shows the chemical requirements set forth by the API for Class H cement:

Table 1.2 – API class H maximum chemical requirements (API, 2011).

Component	%
Magnesium oxide (MgO)	6.0
Sulfur trioxide (SO_3)	3.0
Loss on ignition	3.0
Insoluble residue	0.75
Tricalcium silicate (C_3S)	58
Dicalcium silicate (C_2S)	48
Tricalcium aluminate (C_3A)	8
Total alkali content expressed as sodium oxide (Na_2O) equivalent	0.77

Many cement additives are used in the oil industry to affect the properties of the cement. In this work we use the base case of cement with no additives, referred to as *neat* cement.

1.4. CHEMICAL ALTERATION OF CEMENT

Fluid in equilibrium with cement is very basic and typically has a pH around 13 (Beddoe and Dorner, 2005). However, most subsurface pore fluids and especially acidic fluids (as we would expect with CO_2-saturated brine) have a much lower pH (Gunter et al., 2000). Thus a pH gradient exists and chemical reactions between fluid and solid phases will occur to drive the system toward equilibrium. Not only is acid concentration important but the type of acid is important, e.g. strong versus weak, which controls the degree of dissociation (Zivica and Bajza, 2001). Thus pH can be misleading when used to compare acids. This is especially true where incomplete dissociation, pH buffering, and precipitation reactions can occur.

Alteration of the cement phases occurs as acid enters the cement pore fluid and lowers the pH. Cement phases become soluble and either totally dissolve or form another stable phase. Cations are released, create concentration gradients, and diffuse toward the

cement surface. Calcium, iron, and aluminum are the main cations that are released but at different pH and from different phases. Portlandite is the most soluble and begins to dissolve at a pH of 12.6 while C-S-H becomes soluble at lower pH (around 10.5). Finally the aluminum and iron hydrates do not become insoluble until much lower pH (around 2) (Beddoe and Dorner, 2005).

Calcium that is released from the portlandite and C-S-H is by far the most abundant cation in solution. The reacted layer consists of an insoluble silica-rich phase that is higher in porosity and permeability (Zivica and Bajza, 2001). If the calcium salt becomes insoluble a secondary precipitate may form. This zone can form a barrier to further acid attack (Zivica and Bajza, 2001). The thickness of the reacted layer is controlled by diffusion (which in turn depends on transport properties) to the unreacted cement surface, primary cement dissolution, and any secondary mineral precipitation (Beddoe and Dorner, 2005). The dissolution/precipitation reactions are dependent upon the cement formulation and acidic fluid composition. The acid neutralization capacity is driven by the calcium content of cement and the CaO content of cement can provide an estimate of capacity (Beddoe and Dorner, 2005). Hydrochloric acid (HCl) and carbonic acid are used in this dissertation to study the reactive transport system and are discussed in the following sections.

1.4.1. Hydrochloric acid reaction with cement

Cement degradation by HCl does not often occur in nature but the reaction mechanisms are similar to carbonic acid and HCl is considered to be a simple acid and thus appropriate for use when studying fundamental acid reaction with cement (Chandra, 1988). HCl reacts aggressively with cement and all hydration phases are subject to decomposition. The salt produced in most reactions, calcium chloride, is very soluble in

water (Zivica and Bajza, 2001). One study (Chandra, 1988) looked at the diffusion-limited case of reaction in cement submerged in an HCl solution. The cement was cast in cubes, cured for 5 days under water and an additional 21 days in atmosphere. The cement formulation was similar to Class C cement with a high water-to-cement ratio (0.50). The study used a high concentration of HCl (15%, 5.48 M, or pH -0.739) and submerged the cubes in the HCl solution for 5 days. Unfortunately there was no report of the solution volume used or if multiple samples were placed in the glass container. However the samples were significantly damaged after 5 days, so much so that the cement cubes nearly fell apart and had to be epoxied to keep the samples intact. The samples were significantly more porous and had distinct color alteration that indicated development of reaction fronts. Figure 1.1 shows a schematic of the reaction fronts and relative element concentration for key cations in the cement. The concentrations were measured by scanning electron microscope (SEM) and energy dispersive X-ray spectroscopy (EDAX) and cation values were normalized to the element's theoretical value for unaltered cement. For chlorine, the value was normalized for the concentration in the acidic solution. In contact with the acid was a light grey high porosity zone depleted in calcium. A brown iron rich layer formed next to the unaltered cement and might have formed a low porosity protective coating (Chandra, 1988). The lack of chlorine penetration past this zone is evidence that diffusion of the acid was halted by this zone.

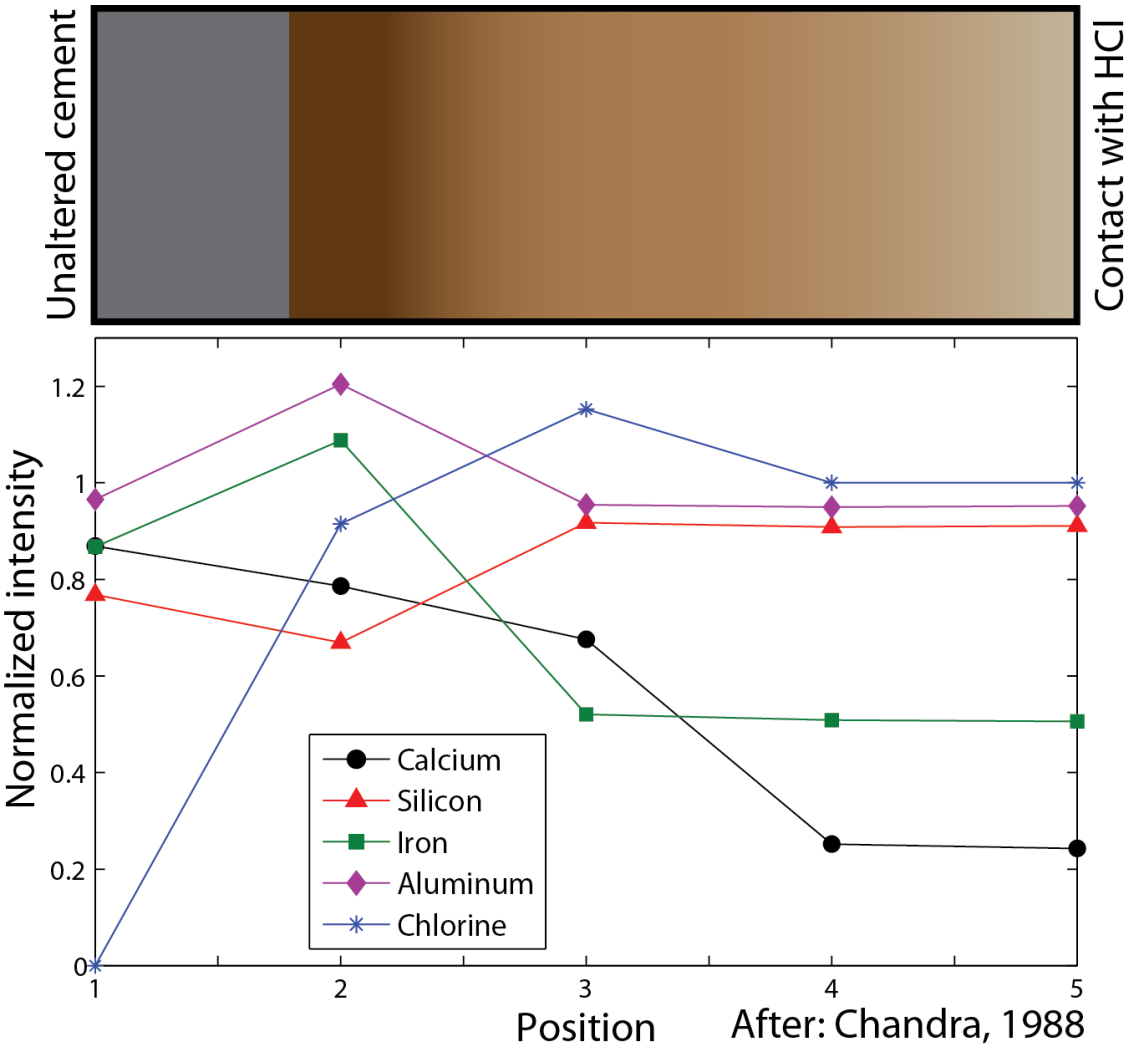

Figure 1.1 – Schematic showing diffusion dominated degradation of cement in contact with HCl. Distinct reaction fronts are identified by visible color alteration. EDAX also showed element concentrations for each zone. Cations were normalized to their theoretical value for unreacted cement. Chlorine was normalized to the concentration in the acid solution.

Another immersion type study performed over 2 years looked at various formulations of cement exposed to more dilute HCl solution (1%, 0.556 M , pH 0.255) that was refreshed several times (De Ceukelaire, 1992). The cement samples had a 0.5 water-to-cement ratio and were mixed with aggregate to form concrete. The results

showed similar acid attack behavior but identified the low porosity zone adjacent to the unreacted cement as a calcium carbonate zone. The presence of calcium carbonate mineral was unexpected as the reaction vessels were reported to be sealed to isolate the fluid from equilibrating with atmospheric CO_2. The source of carbonate was not addressed in the publication but it could be that only a minor concentration in the fluid was needed to promote precipitation.

These studies show that acidic fluids, here HCl, progressively penetrate into cement, leaching calcium and leaving behind a silicon rich material that is more porous and mechanically weaker. A significant observation is that a carbonation layer may form that acts as a retarding front for further acid penetration into the cement.

1.4.2. Carbonic acid reaction with cement

Cement degradation by carbonic acid (H_2CO_3) is a much more complicated process than reaction with HCl because speciation of the carbonate system will buffer pH to remain low but the salt that forms from the acid's anion (carbonate) is relatively insoluble and secondary calcium carbonate precipitation will occur (Zivica and Bajza, 2001). The buffering nature of the carbonate system is greatly enhanced under the high pressure conditions of the subsurface, where significantly more CO_2 can be dissolved in the liquid phase. Several experimental studies have looked at the degradation of cement due to diffusion of CO_2-saturated brine. One study exposed class H neat cement samples with water-to-cement ratio of 0.38 at reservoir conditions (50 °C and 30.3 MPa) to a free phase CO_2 headspace and a CO_2-saturated brine (1% NaCl) for up to a year (Kutchko et al., 2008, 2007). During this time reaction in the CO_2-saturated brine portion showed progressive leaching of portlandite and C-S-H and the formation of calcite in an intermediate zone before leaching all calcium phases and leaving behind a silicon-rich

phase. Later experiments (Mason et al., 2013) showed that the final product of reaction was likely an amorphous zeolite.

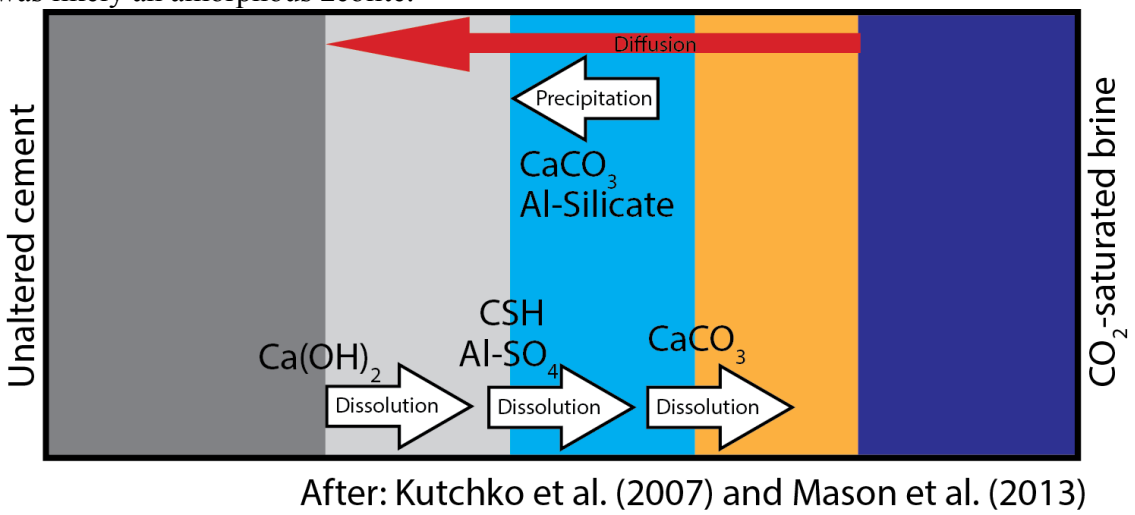

Figure 1.2 – Carbonic acid attack on cement. Progression of the front is from right to left.

Figure 1.2 shows the reaction progress into the cement. As protons diffuse into the cement mineral solubility is affected and distinct zones develop according to the following reactions. First portlandite dissolves neutralizing protons and release calcium ions.

$$Ca(OH)_2 + 2H^+ \rightarrow Ca^{2+} + 2H_2O \qquad (1.8)$$

Next, acid attacks C-S-H to release calcium and silica:

$$2(3CaO{\bullet}2SiO_2{\bullet}3H_2O) + 12H^+ \rightarrow 6Ca^{2+} + 4SiO_2 + 12H_2O \qquad (1.9)$$

Calcium-aluminum-monosulfate reacts with acid to release calcium, aluminum, and sulfate:

$$3CaO{\bullet}Al_2O_3{\bullet}CaSO_4{\bullet}12H_2O + 12H^+ \rightarrow 4Ca^{2+} + 2Al^{3+} + SO_4^{2-} + 18H_2O \qquad (1.10)$$

The principle phase that precipitates in the carbonation zone is calcite and the reaction is:

$$CO_2 + H_2O + Ca^{2+} \rightarrow CaCO_3 + 2H^+ \qquad (1.11)$$

Portlandite dissolution that leads to calcite precipitation is called carbonation in some publication (Regnault et al., 2009). However, with so many calcium-rich species present in cement and with the acids used in this dissertation at a pH that is well below the threshold for solubility of many hydrated cement phases, the overall process of calcium carbonate precipitation (from any primary cement phase) will be referred to as carbonation. The remaining material undergoes alteration and was originally described as an amorphous silicate (Kutchko et al., 2007) but later analysis by nuclear magnetic resonance showed the remnant solid is actually an amorphous zeolite (Mason et al., 2013). The specific mineralogy of the remaining zeolite might be dependent on the specific chemical formulation and brine composition used. The development of the carbonation zone has a significant effect of the penetration rate into cement. The calcite phase precipitates in the cement's pore structure and reduces porosity and diffusion rate into cement. This has an effect of retarding diffusion into cement to a rate slower than the expected rate, which is proportional to the square root of time for normal Fickian diffusion (Kutchko et al., 2008). Very few studies exist on field scale cement exposure to CO_2 but one study showed excellent agreement between laboratory experiments and samples retrieved from a well subject to 30 years of CO_2 exposure (Carey et al., 2007). Another study based on geothermal wells showed similar behavior described above (Shen and Pye, 1989).

Several numerical models have studied the diffusion-limited case of reaction between cement and CO_2-saturated brine (Carey et al., 2007; Huet et al., 2010; Shen et

al., 2013). A complex reactive transport code was developed to couple diffusion of CO_2-saturated brine into cement (Huet et al., 2010). The model allowed dissolution/precipitation reactions, aqueous phase speciation, and porosity-dependent transport properties. The code only studied diffusion into cement and although there is no representation of fluid advection in a fracture proximal to the cement (which is the goal of this dissertation) it does apply a constantly refreshing boundary condition (Dirichlet B.C.). The model assumes equilibrium in liquid and solid phase and thus does not capture any kinetically controlled reactions. The results show sharp reaction fronts in general agreement with experimental results (Duguid and Scherer, 2010; Kutchko et al., 2007). The modeling work shows that in the diffusion-dominated regime, cement alteration by carbonic acid is a slow process that leaves behind material that continues to restrict flow. No work (numerical or experimental) to date has adequately described the coupling of geochemical reactions and advection of CO_2-saturated fluids along a wellbore.

1.5. REACTIVE TRANSPORT

In the subsurface during active injection and until the system reaches equilibrium there is expected to be a pressure gradient present as CO_2 moves from the injection wells and into the reservoir. Any wells with a leak that connects the reservoir to an overlying hydrostatically pressured formation will then experience advection along the leak path. The batch experiments and modeling described above are thus missing a key phenomenon that affects how the CO_2 saturated brine and cement interact. Below is a summary of reactive transport processes (in porous media and in fractures) that are relevant to this dissertation.

1.5.1. Reactive transport with dissolution/precipitation in porous media

Most of the understanding on reactive transport processes (especially with dissolution and precipitation) is from experiments and mathematical models of flow in porous media. Complex reactive transport codes (Lichtner et al., 1996) and simple analytic models (Lake et al., 2002) have been developed to describe fluid flow and dissolution/precipitation processes and some base level understanding of reactive transport is assumed.

Chemical species dissolved in an aqueous phase are transported in porous media at rates proportional to the bulk fluid velocity. If a change in concentration occurs, as would happen with reactions, a front (or wave) develops (Lake et al., 2002). This front will move at a speed that is decreased relative to the bulk fluid. Depending on the kinetics the concentration across this front can form a sharp transition (a shock) or spread over some distance (a rarefaction) (Lake et al., 2002). When chemical reactions involve dissolution of a primary solid phase and precipitation of a secondary phase the flow field can be significantly altered (Lichtner et al., 1996).

Several studies on mixing-induced precipitation provide insights that are useful for this dissertation (Tartakovsky et al., 2008, 2007). The studies used a combination of smooth particle hydrodynamics, experiments, and continuum scale models to identify the controls on precipitation and transport in fractured and porous media. In the studies 2 fluids were injected next to each other into a 2D porous media domain and at the interface a solid precipitate would form. If the reaction rate was fast relative to advection precipitation occurred early in the domain. A slow reaction rate allowed more diffuse precipitation across the domain. When the reaction rate was slow, a lag time occurred before precipitation reduced porosity sufficiently to initiate a decrease in advection. In the mixing zone between fluids if the reaction rate was low, precipitate was initially more

diffuse across the boundary but sharpened with time. Faster advection allowed more mixing on the boundary, which promoted precipitation. If this continues and the fluids become isolated (and the precipitate is now soluble), the precipitation zone at the mixing front will sharpen to a finite interface.

1.5.2. Reactive transport in fractures

The key differences between flow in porous media and fracture flow are the nature of the open space, how flow moves through open fractures, and how chemical species react with the available surface area. The variability in fracture aperture is quite large, with orders of magnitude change in aperture size possible over short distance (Gentier and Hopkins, 1997). Fractures are defined as open, which have no contacting asperities, or closed, which have some fraction of asperities in contact. Because wellbores are under geomechanical confining stress, which acts to close fractures and increase contact between fracture surfaces, this dissertation studies closed fractures. Closed fractures significantly affects the local flow field and chemical reactions by forcing flow through the larger aperture pathways, reducing reactive surface area, and trapping fluid in slow flow pockets.

Fluid flow in fractures is often described using a first order approximation for flow between parallel plates to develop the cubic equation for flow (see Appendix A for more description). However, natural fractures are much more complex and the use of a hydraulic aperture (derived from parallel plate assumption) can over or underestimate actual mean aperture (Berkowitz, 2002). Indeed the assumption of a parabolic velocity profile, key in derivation the cubic equation, may break down at the local scale of a heterogeneous fracture (Berkowitz, 2002). Unfortunately, no model has provided a robust alternative to estimating aperture from fluid flow properties without *a priori* knowledge

of the fracture aperture statistics. The nature of the fracture geometry can also be quite variable. Natural fractures often have self-affine fractal patterns (Berkowitz, 2002) on the local scale and much larger jumps or discontinuities on the larger scale (as one might expect on the well scale). This complexity drastically affects the local flow field, resulting transport of aqueous species, and subsequent chemical reactions.

Park et al. (1995) performed numerical experiments that showed the effect that rough-surfaced fracture variability has on solute transport. They varied several geostatistical parameters (correlation length and standard deviation of aperture) to show how breakthrough curves are affected. They found that flow will be dominant and concentration plumes will move fastest in the regions of large fracture aperture. Where aperture is small, the flow is restricted and movement of the solute is retarded. The resulting effluent concentration curve is log-normal. A high concentration early breakthrough is followed by a long tail of low concentration that is a result of solute transport being retarded in the slow flow regions. This behavior is in contrast to a break-through curve for porous media, which should have an S-shaped behavior (Berkowitz, 2002). 2D numerical experiments showed that increasing the variability of a fracture aperture (e.g. standard deviation) caused a retardation in the arrival time, reduced the sharpness of the arrival front, and extended the post break through effluent concentration (Park et al., 1995). With larger standard deviation, there were more large apertures but they remain unconnected (because correlation length was held fixed) and thus flow communication was not enhanced. Because the number of smaller apertures also increased there were more slow flow zones to retard the concentration. When correlation length, which is a geostatistical parameter related to spatial variability, decreases the system approaches a pure random aperture distribution. As a result dispersion increases, breakthrough time is delayed, the effluent concentration profile is more spread over time,

and the fracture approaches porous media behavior. While the nature of the fracture surface will depend on the types of materials at the interface (e.g. cement-cement versus cement-earth) and mode of failure (e.g. tensile failure versus micro-annulus debonding) it will clearly play a role in local residence time and fluid transport. This is especially true when dissolution/precipitation reactions (often kinetically limited) begin to occur and alter the flow field.

In the presence of dissolution alone self-enhancing behavior can lead to wormhole development as dominant channels become the main flow path (Szymczak and Ladd, 2009). Fracture roughness, dissolution rate, and advection rate determined the behavior that developed in these fractures that lacked the self-affine character of natural fractures.

In the presence of a geochemical system that allows dissolution and precipitation in fractures complex coupling occurs that leads to conditions of self-reinforcing, either toward self-enhancing flow or self-limiting flow (Singurindy and Berkowitz, 2005). Relative concentration of aqueous species, fluid flux rate, roughness, and the fracture geometry were key parameters. Increasing the acid (dissolving) concentration led to dissolution-dominated behavior; while increasing the anion required to form the secondary precipitate promoted precipitation-dominated behavior. Increasing the residence time by altering the geometry or reducing fluid flux led to precipitation-dominated behavior. Complex coupling lead to oscillations in hydraulic aperture during the experiments (Singurindy and Berkowitz, 2005). If the sample was shorter than a 'critical fracture length' (in their work this length was between 2 cm to 14 cm) key phenomena might not be observed because fluid breaks through before reactions can occur in sufficient quantity to invoke coupling in system. From a practical standpoint this means that laboratory samples must be sufficiently long to capture phenomena expected on the well scale.

1.6. DISSERTATION GOAL

1.6.1. Problem statement

Research on diffusion-controlled reaction between carbonic acid and cement has been performed and results show that intact wellbore cement is reactive but does not pose a significant risk for total wellbore failure. However, the fate of leaky wells must be known if GCS is to be employed as a means of mitigating anthropogenic CO_2. The addition of pressure-driven advection causes a coupling between flow, dissolution, and precipitation reactions. Several key questions are:

- Are the chemical reactions observed in the diffusion-dominated regime the same with the addition of advection?
- Will the silicon-rich material remain behind to prevent wormhole development?
- Will the fracture close due to reaction and mechanical weakening of the cement?
- What role will fracture heterogeneity play on extent of reaction?
- What is the role of reaction kinetics and local residence time?
- How will dissolution/precipitation affect local heterogeneity?
- How long will it take for the system to evolve?
- Can understanding of the fundamental phenomena allow an up-scaled approximation of wellbore leakage behavior?

1.6.2. Hypothesis

This dissertation proposes that time-dependent flux of CO_2-saturated water is controlled by the coupled reactive transport processes that dissolve hydrated cement phases and precipitate secondary calcium carbonates in the fracture space leading to a condition of self-limiting. Self-sealing occurs with a pressure differential driving force and when local residence time is sufficiently long. Time to seal the leak path is a function

of the magnitude of driving force for flux, initial fracture conductivity, residence time, and system reactivity.

1.6.3. Research methods

To test the hypothesis and address the questions posed above, laboratory experiments are designed for a variety of conditions in order to observe key system couplings. Analysis using a variety of analytical techniques helps explain observations of changes in pathway conductivity. A simple analytical model is then developed to describe features of the system and project results from the laboratory experiments to simple field scale leak models. Each chapter is briefly summarized below:

Chapter 2 details simple analog experiments using HCl injected into cement fractures. These experiments were the first attempt at understanding the system and comparing it with previous work.

Chapter 3 builds on the analog experiments to study more realistic down hole conditions of high CO_2 concentration and constant pressure differential driving force.

Chapter 4 presents a mechanistic model for the evolution of a leaking well and a simple wellbore leak model is developed based on experiment results and applied to several hypothetical examples to show the model's utility.

Chapter 5 presents a summary of the dissertation and identifies the next steps to be taken in fully understanding wellbore leakage.

2. Hydrochloric acid analog experiments

2.1. SUMMARY

This chapter presents results and analysis of reactive transport experiments in cement fractures. The experiments simulate coupling between flow and reaction when acidic, CO_2-rich fluids flow along a leaky wellbore. As a proxy for carbonic acid, dilute hydrochloric acid (HCl) is used. The goal of the analog experiments is an exploratory assessment of the reactive transport processes that control the leakage flux. A subset of this work was published in Huerta et al. (2013). Some of the experiments presented in this chapter were performed and analyzed as part of a senior thesis project by Quinn Wenning and presented as a conference paper (Wenning et al., 2013). Results from those experiments are included in this dissertation, because I helped to advise the research of the undergraduate student and they add significantly to the understanding of reactive transport in the system. Detailed reports of key experiments are included in Appendix C and used as a basis for the concise arguments presented in this chapter.

In the experiments, hydrochloric acid solution between pH 2.0 and 3.15 is injected at constant rate between 0.1 mL/min and 12.0 mL/min into a fractured cement core. HCl is used as an analog fluid because it can easily be diluted to vary the injected pH to study how reactivity affects the evolution of the leakage rate. Using HCl also allows for lower experimental pressure. The pressure differential across the core and effluent pH are measured to infer dissolution/precipitation reactions within the fracture, which is analyzed with scanning electron microscopy on the fracture surface after injection.

In many experiments reaction is restricted within relatively narrow, tortuous channels along the fracture surface. Injected HCl reacts with the fracture surface to leach calcium from cement phases. Ahead of the reaction front and in lateral slow-flow regions

high-pH pore fluid mixes with calcium-rich water and induces calcium carbonate precipitation. Because the system was open to the atmosphere a small amount of aqueous carbonate is present for precipitation but is in insufficient quantity to buffer the pH. Increases in the pressure differential for 9 out of the 12 experiments indicate that precipitation can be sufficient to restrict flow. Experimental data from this study combined with published field evidence for mineral precipitation along cemented annuli suggests that leakage of CO_2 rich fluids along a wellbore may seal the leakage pathway if the initial aperture is small and residence time allows the leaching of calcium from the cement and the precipitation of minerals along the fracture.

2.2. METHODS

2.2.1. Core flow equipment

Figure 2.1 shows images of the core flow equipment. The cement core is housed in a uniaxial Hassler cell designed by Phoenix Instruments (Splendora, TX) and a confining pressure is applied to the core to ensure flow through the fracture and prevent flow between the core and Viton rubber confining sleeve. To negate the effects of variable confining stress, which is an unavoidable limitation of the equipment setup, the sample fracture surface has to be conditioned to behave in a linear elastic manner. To achieve a linear elastic fracture, weak asperities were removed using an approach based on the work by Huerta et al. (2009). The procedure consists of a cyclic loading and unloading of confining stress on the sample. An Enerpac manual hydraulic pump is used to increase confining pressure to a maximum pressure (600 psi to 800 psi) in specific increments (typically 200 psi). Deionized water is continuously injected during the buildup of confining pressure and after each increment to let the upstream pressure equilibrate. Confining pressure is then reduced in similar steps down to 200 psi. The next

cycle is performed in the same manner, while ensuring the confining pressure remains below the first cycle's maximum pressure, otherwise further inelastic deformation of the fracture would occur. A final cycle is performed and then confining pressure set at the desired experimental condition (typically around 500 psi). A high pressure liquid chromatography pump is used to inject the acidic fluid at constant rate into the core. Pressure transducers measure the confining and upstream pressure, while the downstream pressure is open to atmosphere and assumed constant. Occasionally a 5 mL sample of effluent is collected to measure pH and effluent cation concentrations.

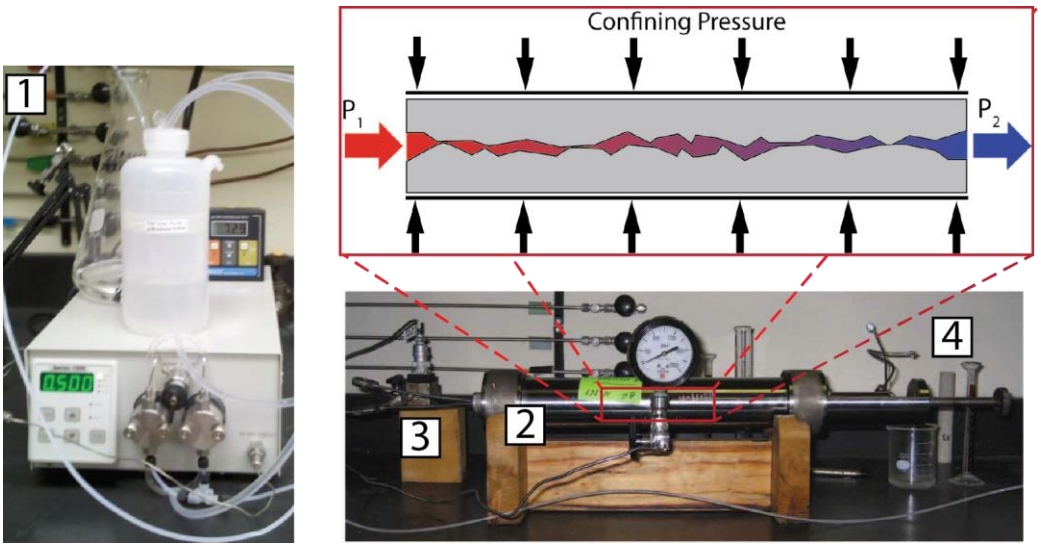

Figure 2.1 – Images and description of core flow equipment. (1) Constant flow rate liquid pump. (2) Hassler cell. (3) Upstream pressure transducer. (4) Effluent exit port.

For all experiments, deionized water is injected to get a baseline measurement of the flow rate to pressure differential relationship and to estimate initial fracture conductivity. An effective hydraulic aperture (B) is then estimated assuming the cubic equation for flow through parallel plates holds (for derivation see Appendix A):

$$B = \left(\frac{12\mu QL}{W(\Delta P)} \right)^{1/3} \qquad (2.1)$$

The liquid phase dynamic viscosity (μ) is assumed to be 10^{-3} Pa-s and the flow rate (Q) is constant during each experiment. The pressure differential (ΔP) is measured between the upstream pressure transducer and atmospheric pressure at the outlet, which is assumed constant. Since the pressure transducer was set to gauge pressure the terms upstream pressure and pressure differential are synonymous in this chapter. The sample length (L) and sample width (W) are set to the bulk core dimensions. Thus, changes in upstream pressure are related to changes in flow geometry (true flowing width and aperture distribution).

2.2.2. Sample preparation

Cement cores are prepared using API Class H neat oil well cement (Lafarge, Montgomery, TX). The cement is prepared using a modified version of the API Recommended Practice 10B (API, 1997). Samples are mixed with a water-to-cement ratio of 0.38 and poured into cylindrical acrylic molds with a diameter of 2.54 cm and a length of 12.7 cm. The samples are cured at 50 °C and ambient pressure for 3 days. The samples are then removed from their molds and allowed to cure under water and at ambient temperature and pressure for 28 days. To generate a flow path, the samples are placed into a loading frame and fractured using the Brazilian method (Guo et al., 1993). The fracture is then offset, i.e. displaced by a few millimeters in the plane of the fracture, to ensure an aperture that permits flow. The sides are sealed with latex polymer caulk (DAP KWIK SEAL) and the ends are trimmed flush. As a result of sample preparation no fracture has the exact same surface geometry or the same length. The small variation has a negligible effect on the phenomena studied here, but longer cores do increase residence

time and facilitate the observation of key dynamic phenomena. Typical oilfield cement permeability is much less than a milli-Darcy (Kutchko et al., 2009), and flow through the fracture is assumed to be the dominant pathway.

2.2.3. Analytical equipment

Upon completion of the experiment, the sample core halves are separated and stored in sealed containers until analysis. Macroscopic images are acquired with a digital camera. Electron microscopy is then used to study fracture surface alteration for changes in cement chemistry and microstructure. An FEI-Quanta 600 FEG Environmental SEM (ESEM) equipped with an Oxford INCA energy dispersive spectroscopy (EDS) system with a Large-field Secondary Electron (LFD) detector and a Back Scatter Electron detector (BSED) is used to collect images. The unpolished and uncoated samples are analyzed in low vacuum mode with an acceleration voltage of 20 keV and nominal working distance of ~10 mm for EDS mapping. Care is taken to analyze fracture surfaces that are as flat as possible. Images and EDS spot chemical analyses are collected throughout various regions of the fracture surface (varying working distance where necessary to account for surface roughness). Additionally elemental EDS maps are collected over a time period of several hours to better monitor the overall chemical alteration of the cement along the fracture pathway. Higher-magnification EDS spot analyses are used to confirm trends seen in the maps to assure that chemical trends were not a result of surface roughness effects. Micro x-ray diffraction (μXRD) is used for mineral phase identification. The sample is run on a Rigaku R-Axis micro-diffractometer equipped with an UltraX18 Cu rotating anode X-ray source and a Rapid II 180° curved imaging plate detector. Sample analysis is performed at 50 kV, 300 mA. The desired portion of the sample is brought into the focus position, and the sample is analyzed with

an exposure time of 5 minutes using a 0.1 collimator. Phase identification is performed using the JADE software equipped with the ICDD PD4 database.

2.3. RESULTS

The results for 12 samples are shown in Table 2.1. Results are grouped based on flow behavior. Controlled experiment parameters are flow rate, injected acid concentration, and total acid injected. Parameters unique to each sample are width (typically 2.54 cm), sample length, and initial hydraulic aperture. The hydraulic aperture (Eqn. 2.1) is calculated using core parameters, flow rate, and pressure differential. Initial average velocity is calculated assuming flow across the maximum available flow area. Total acid injected is calculated from the product of injected acid concentration, flow rate, and experiment time. Upstream pressure evolution, effluent pH history, post-experiment fracture surface images, electron microscopy, and μXRD of selected experiments are presented below.

Table 2.1 – Experiment parameters and key results.

Sample name	BB-9	PL-1	PN-1	BSD7	NA3-3	NA4-1	PN-3	AAT-15	BSD10	BSD1	NA4-5	QB4-4
Length, cm	5.04	5.62	6.73	3.65	3.49	7.17	7.11	4.52	5.62	4.28	3.19	6.5
Flow rate, mL/min	3.3	2.0	1.1	1.0	2.0	1.0	0.1	0.55	0.5	12.0	3.0	5.0
Injected acid pH	2.18	2.20	2.00	2.31	2.18	2.30	3.15	3.07	3.10	2.25	2.15	2.38
Initial pressure differential, psi	15.0	4.5	0.2	0.02	0.8	0.2	1.0	0.2	0.1	0.9	1.4	0.8
Initial velocity, cm/sec	9.4	4.2	0.9	0.5	2.9	0.8	0.3	0.7	0.5	9.3	4.2	7.1
Initial hydraulic aperture, μm	23	31	76	122	46	85	24	55	64	85	47	46
Total fracture volumes injected	27,106	15,756	2,351	8,081	5,728	1,029	1,382	20,413	101,714	8,719	8,040	3,391
Total HCl injected, mmol	5.30	4.33	3.03	4.50	1.59	0.83	0.04	1.10	7.38	4.53	1.53	1.07
Total HCl consumed, mmol	5.16	4.28	2.83	3.03	-	0.80	0.04	1.10	7.38	3.03	0.89	0.92
	Experiment behavior											
Upstream pressure evolution												
Case A: Spike and decay												
Case B: Continuous build												
Case C: Shallow decrease												
Effluent pH history												
Breakthrough and decrease												
No change												
Fracture surface alteration												
Channel formed												
Broad reaction												
No reaction evident												

2.3.1. Upstream pressure evolution

In each experiment, the upstream pressure follows one of 3 general trends (Table 2.1). The plot on Figure 2.2 shows an example of the most common behavior (Case A), which is an upstream pressure spike and decay which flattens out but remains above the initial upstream pressure. Early in the experiment there is a period of constant pressure differential, which typically occurs before 0.2 mmol HCl is injected and is uncorrelated to flow rate or initial hydraulic aperture. The period of constant pressure is most likely related to the displacement of fluid in the in the tubing (e.g. dead volume) before the acid begins to significantly react with cement. Upstream pressure begins to increase quickly until pressure reaches a maximum, often more than twice the initial pressure. At this point upstream pressure begins to decrease at a much slower rate. The pressure curve eventually flattens or has a small negative slope but always remains above the initial pressure. The shape of the pressure curve (maximum height, width, and curve smoothness) is uncorrelated to any single parameter. The most significant inlet pressure changes typically occur before 1.0 mmol of HCl is injected and in most experiments upstream pressure gradually decays for several more mmol of HCl injected.

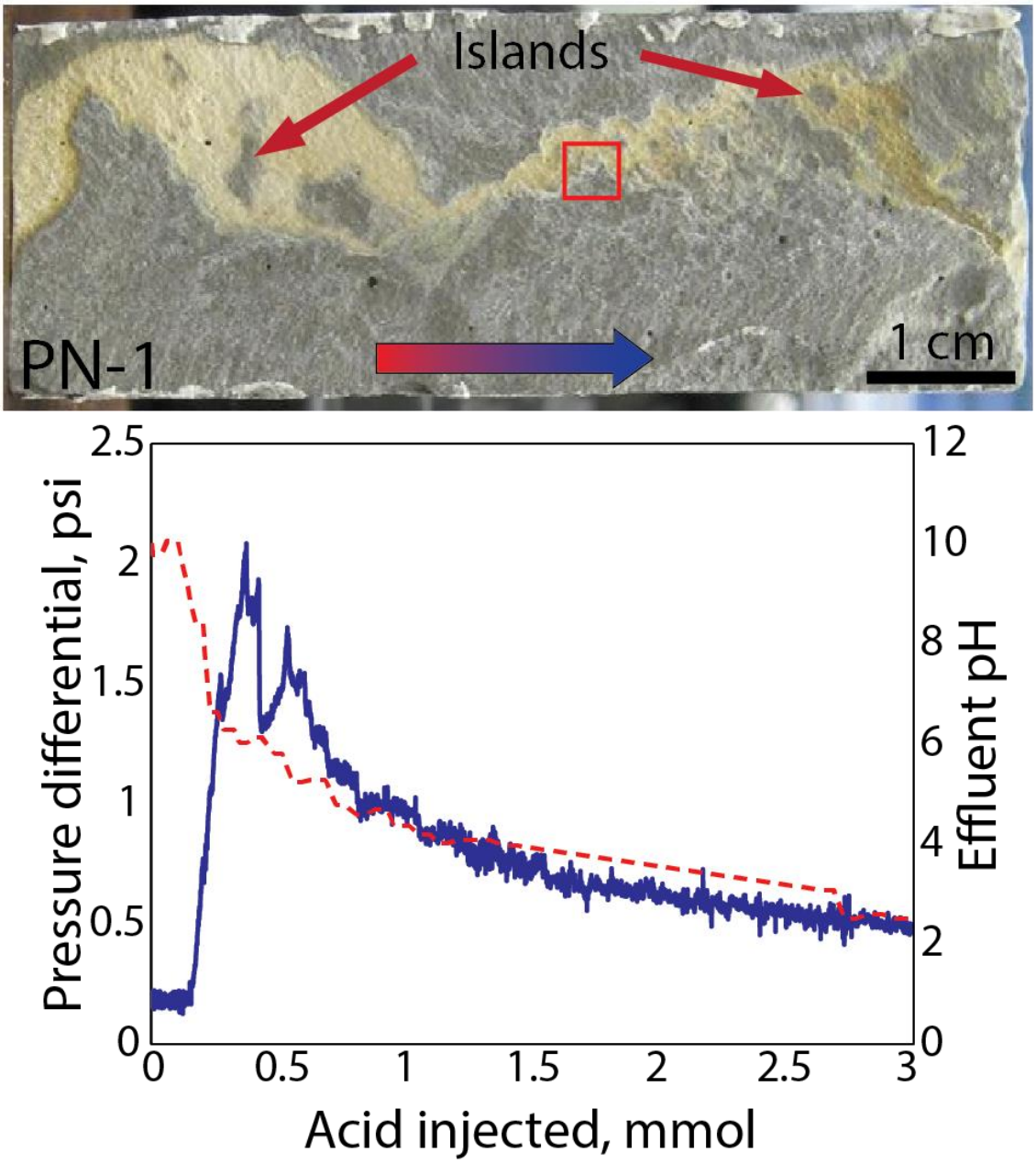

Figure 2.2 – (Top) Fracture surface of sample PN-1. (Bottom) Pressure differential (blue) and effluent pH (ref) plotted versus total acid injected.

The plot on Figure 2.3 shows an example of Case B, which is characterized by a significant monotonic increase in pressure over time. In this example, the pressure

increase was so high that the pressure transducer's upper limit was reached and the experiment was terminated. The flow path is assumed to be significantly reduced at this point and the reaction would have likely sealed the flow path if the flow would have been driven by a constant pressure differential as expected in the field. All 3 experiments that yielded this pressure history have a slow flow rate and low acid concentration, but they have a range of initial apertures. The time before initiation of the pressure increase varies widely (from ~0.02 mmol to 1 mmol acid injected) and upstream pressure increases over the initial pressure span up to 3 orders of magnitude. First order correlation to onset of pressure increase indicates low pH, slow flow rate, and a small initial aperture tends to cause an earlier pressure increase.

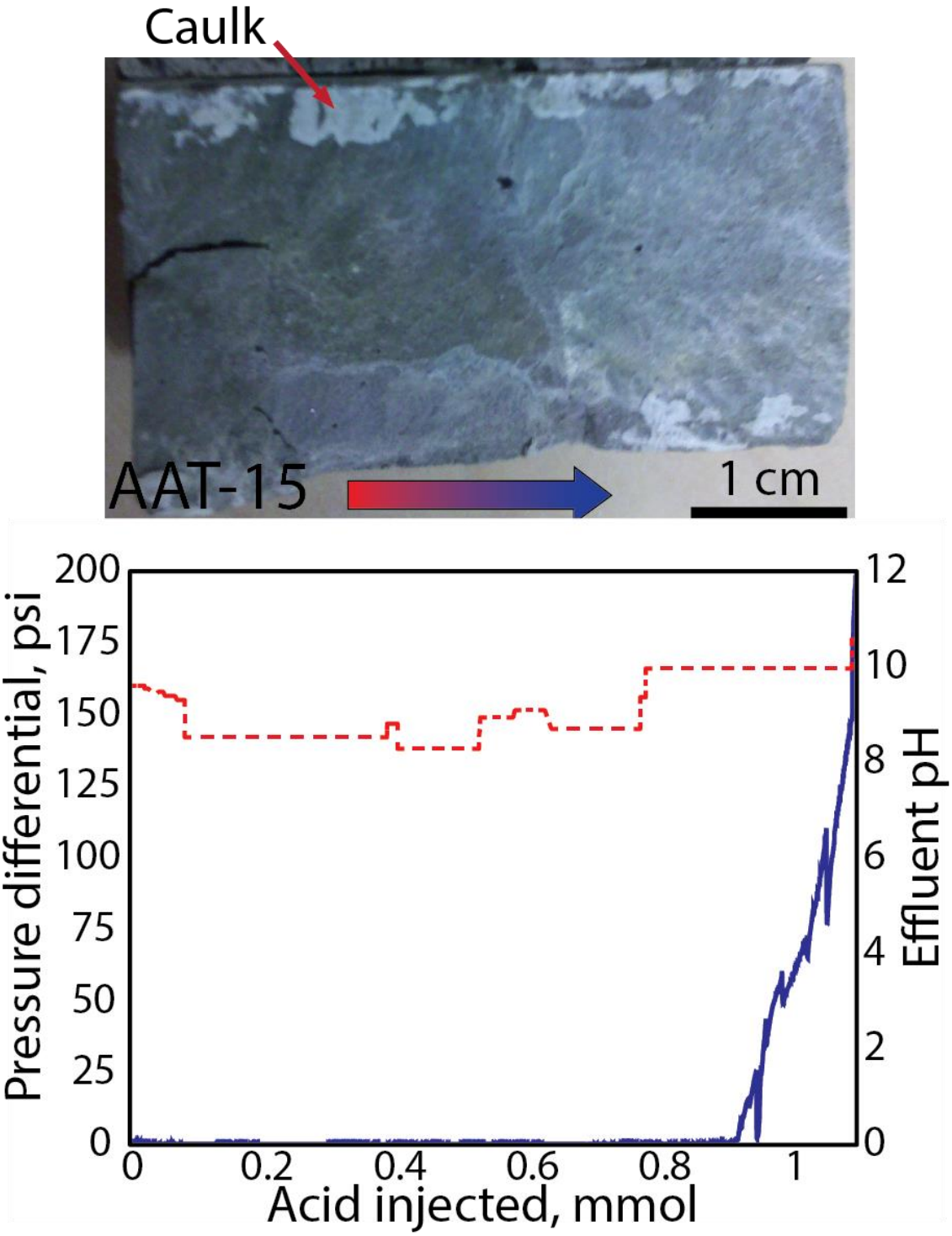

Figure 2.3 – (Top) Fracture surface of sample AAT-15. (Bottom) Pressure differential (blue) and effluent pH (red) plotted versus total acid injected.

Figure 2.4 shows the final behavior type (Case C), which is characterized by a small decay in pressure differential that flattens out or has a shallow decreasing slope. This behavior occurs in three experiments. In all three experiments there is a correlation to high flow rate, relatively high injected acid concentration, and medium to large initial aperture size.

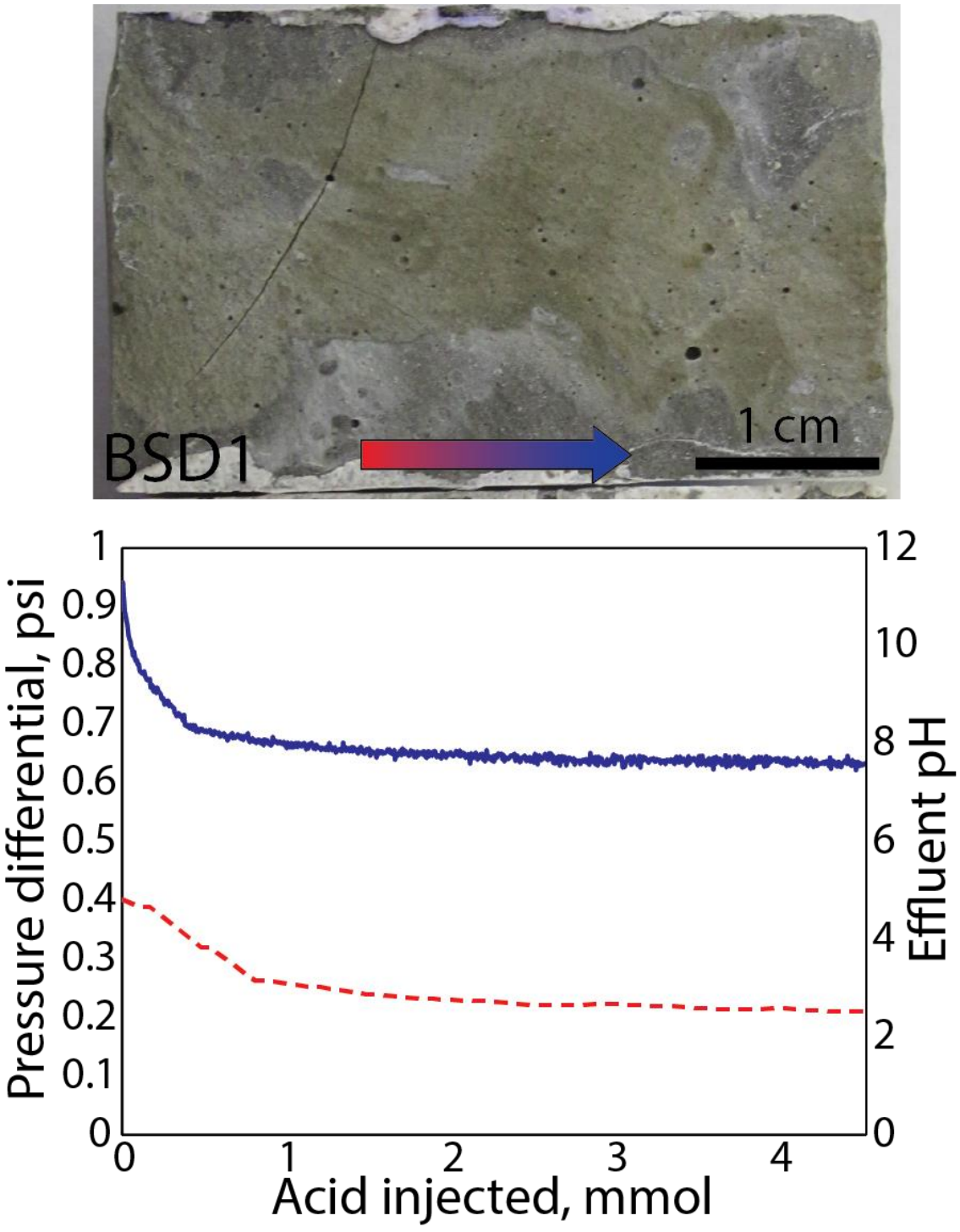

Figure 2.4 – (Top) Fracture surface of sample BSD1. (Bottom) Pressure differential (blue) and effluent pH (red) plotted versus total acid injected.

2.3.2. Effluent pH history

Effluent pH evolution is as an indication of reaction progress because effluent pH varies monotonically between the pH of fluid fully equilibrated with cement (initial value) and the pH of the injected acid (value when all reaction has completed). In the absence of flow, the pH of static fluid filling the crack is assumed to be ~12.3 based on equilibrium with solid portlandite in the cement (Kutchko et al., 2007). Prior to acid flow, the effluent pH is measured from non-acidified water injected into the fracture. For all experiments the initial effluent pH is 10. This value is a function of injected fluid pH, injection rate, residence time, diffusion from the cement's pore fluid, and equilibrium reactions in the fluid. Effluent pH history for acid injection tests falls into 2 types of behavior. The first type occurs in all experiments with flow profiles described in Case B above and an example is shown in Figure 2.3. The effluent pH remains high, near the expected pH of cement's equilibrated fracture fluid. The 3 experiments that retain an elevated pH are those that also show a significant and sustained increase in pressure differential over time.

The second type of effluent pH behavior, which is the most common, occurs in all Case A and Case C experiments. The experiments have a stable initial pH followed by a period of rapid pH decrease that approaches the injected acid pH. In none of the experiments did the effluent pH actually reach the injected acid pH, despite injecting large volumes. The shapes of the pH curve (e.g. Figure 2.2 and Figure 2.4) have no obvious correlation to parameters on Table 2.1. Some practical considerations to note when comparing the shapes of the curve are that the time between switching from deionized water flow to acid flow allows fluid in the fracture to equilibrate with the cement and determine the initial effluent pH. In some experiments the fluid lines upstream of the core were primed so that the acid reached the sample almost instantly

(e.g. BSD7). Additionally, higher flow rate and shorter cores reduce residence time and allow for faster fluid breakthrough.

2.4. DISCUSSION

2.4.1. Interpretation of fracture surface

Color images of the fracture surface were collected after the acid experiment to observe the extent and shape of reaction on the surface. Flow is from left to right in all images (Figure 2.2, Figure 2.3, and Figure 2.4). Unreacted cement is gray. Reacted surfaces have a tan to brown color, consistent with previous cement degradation studies performed in static reactors (Chandra, 1988; De Ceukelaire, 1992). A white mineral precipitate is often associated along reacted boundaries between unreacted cement and the dominant flow paths, but is not to be confused with caulk along sample edges. The nature of the reacted pathway along the surface of the fracture is quite complex. Every experiment yielded a unique reaction pathway and 3 examples are shown in Figure 2.2, Figure 2.3, and Figure 2.4 (for more examples see experiment reports in Appendix C). The nature of the pathways is different and allows us to organize the patterns into the following three groups described below and in Table 2.1.

In the first group, there was limited visual evidence for reaction (Figure 2.3). In the samples that fell into this classification there was either no apparent change, or a small length of reacted surface that did not penetrate the entire fracture length (as in the presented image). There is always evidence for white material across the surface but a lack of reacted pathway development. The second type is the broad reaction channel (Figure 2.4). This is evidenced by a general tan coloration across large areas of the fracture surface in the example shown. White material is present but less visible except along the sides. The third and most prevalent type is a distinct reaction pathway across a

subset of the total fracture surface (Figure 2.2). The channel can be a single pathway, or multiple smaller channels, and is generally wider at the inlet and narrows toward the outlet. There is often a white precipitate along the edges of the channel boundary.

Images of the fracture provide evidence for the dominant reacted channel. Inspection by microscopic methods improves understanding of the structural and elemental changes that are key to describing the reaction mechanisms in the system. The red box in Figure 2.2 was an area studied using SEM and EDS. While these techniques are qualitative in nature due to sample roughness, study areas were selected to ensure that the trends seen were not surface roughness artifacts. For example, a decrease in the fracture surface would cause poor signal response in all element channels of the EDS maps and a shadow effect on BSED images (See Appendix C – Sample BSD7). General trends have been identified (described below), and were consistent across the different samples analyzed.

Figure 2.5 shows a backscatter image of the red boxed area shown in Figure 2.2 and there are several distinct textures and zones that can be identified. Inside the orange band, the unreacted cement has a fine grained uniform texture. In between the orange and red bands is an intermediate zone with larger, well-formed crystals and more grainy texture, corresponding to the location of the white band seen in the Figure 2.2 image. Above the red line is a zone of reacted material presumed to be the dominant flow path composed of plate-like fine grained material, separated by sub-polygonal gaps.

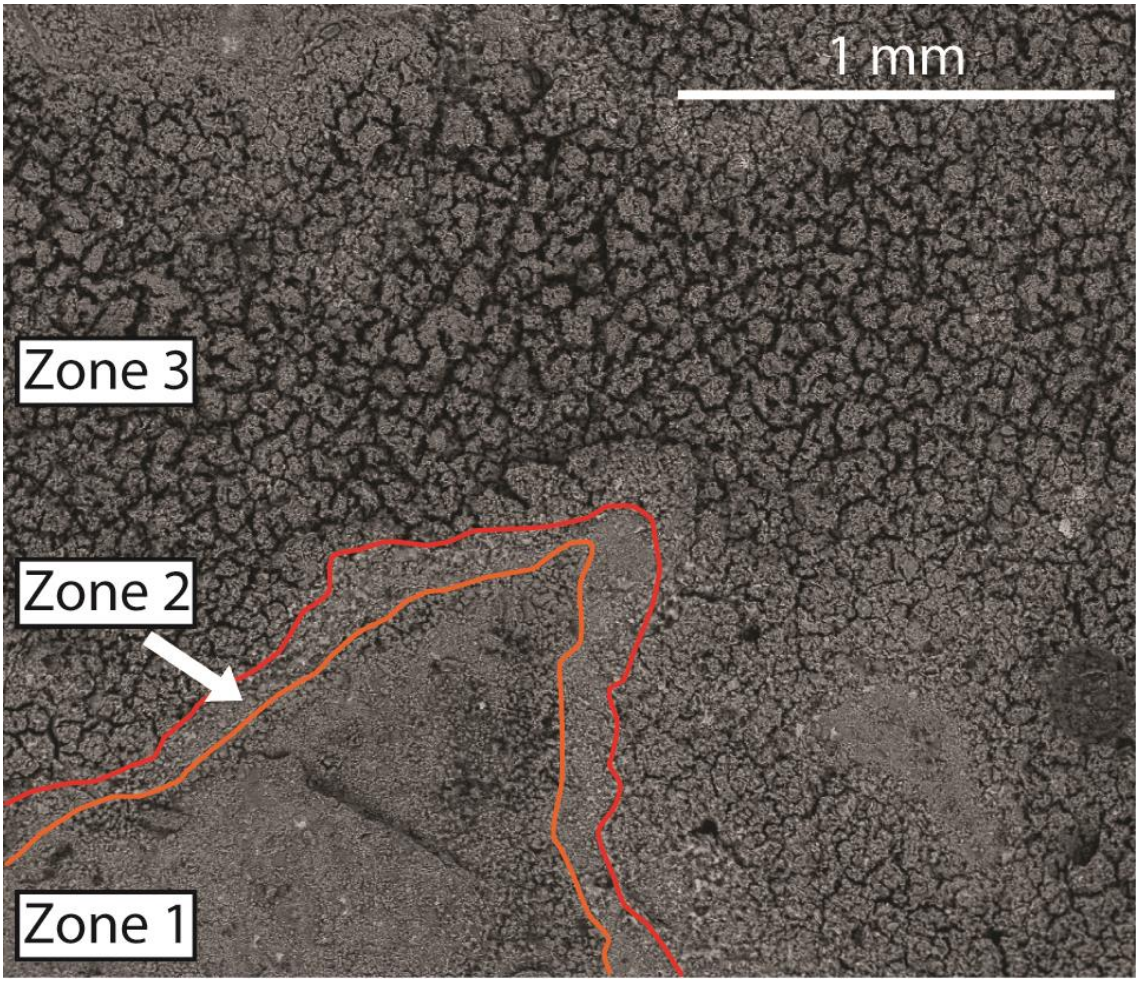

Figure 2.5 – **PN-1** SEM image identifying key zones on the fracture surface highlighted in the red box in Figure 2.2. Zone 1 consist of unreacted cement. Zone 2 is the precipitation zone. Zone 3 is the reacted channel.

EDS mapping (Figure 2.6) in the same area shows sharp element gradients across the fracture surface. Calcium is present in both the unreacted and intermediate area but is significantly depleted in the reacted zone. Higher magnification EDS spot analysis confirmed these trends (Figure 2.7). Iron and silicon are relatively more concentrated in the reacted channel, which is due to leaching of calcium from the channel. Aluminum is concentrated between unreacted (calcium rich) cement and reacted (silicon rich) areas.

Unlike silicon the aluminum is being concentrated due to transport and reaction processes to form as a secondary precipitate band. The logic for this argument is that if aluminum was totally insoluble it would have a concentration trend like silicon. In the intermediate zone calcium has concentration decrease (which would result in a relative increase in all other phases present) and therefore aluminum must be increasing in concentration relative to calcium in that zone.

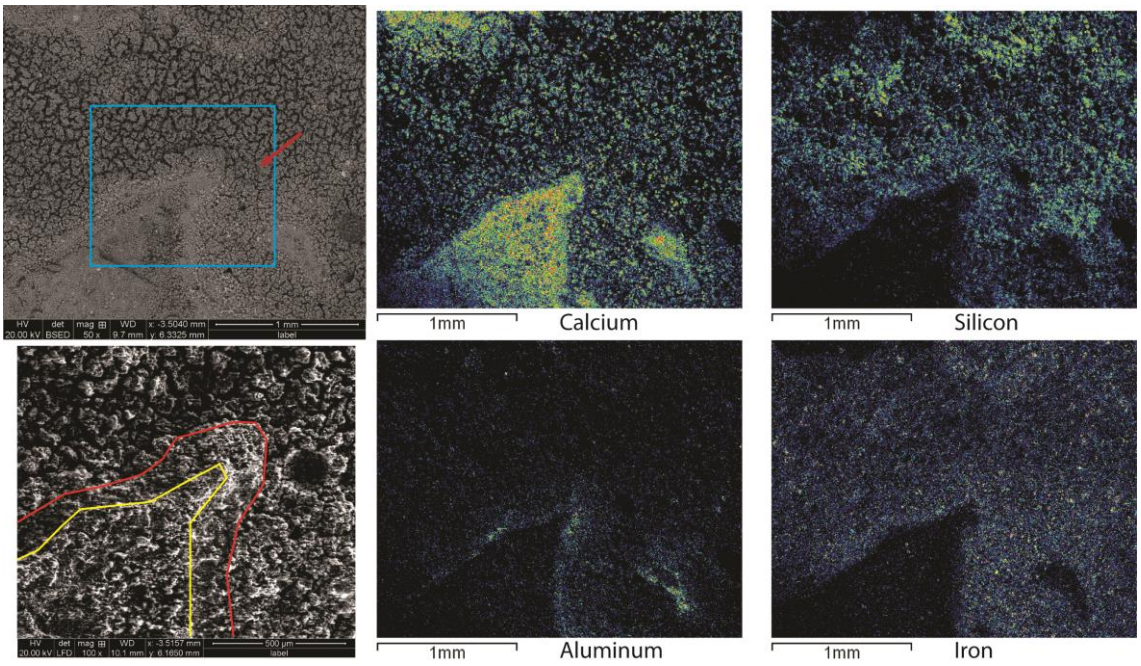

Figure 2.6 – **PN-1** BSED (top left), LFD (bottom left), and EDS element maps (center and right 4 images) for calcium, silicon, aluminum, and iron. The BSED map shows material density on the fracture surface, while LFD displaces an image of the fracture surface topography. For example note the void in large pore in the LFD image is seemingly absent in the BSED image (red arrow). In the LFD image, zone boundaries are highlighted based on surface morphology features. EDS element maps (middle two and right two images) are roughly from the area in the blue box drawn in the BSED. Warmer colors in the EDS maps correspond to greater concentrations for each element. Calcium is concentrated in the unreacted zone. Silicon has a higher relative concentration in the reacted channel. Aluminum shows a concentration increase in bands around unreacted zones. Iron correlates with silicon concentration and is relatively enriched in the degraded zones.

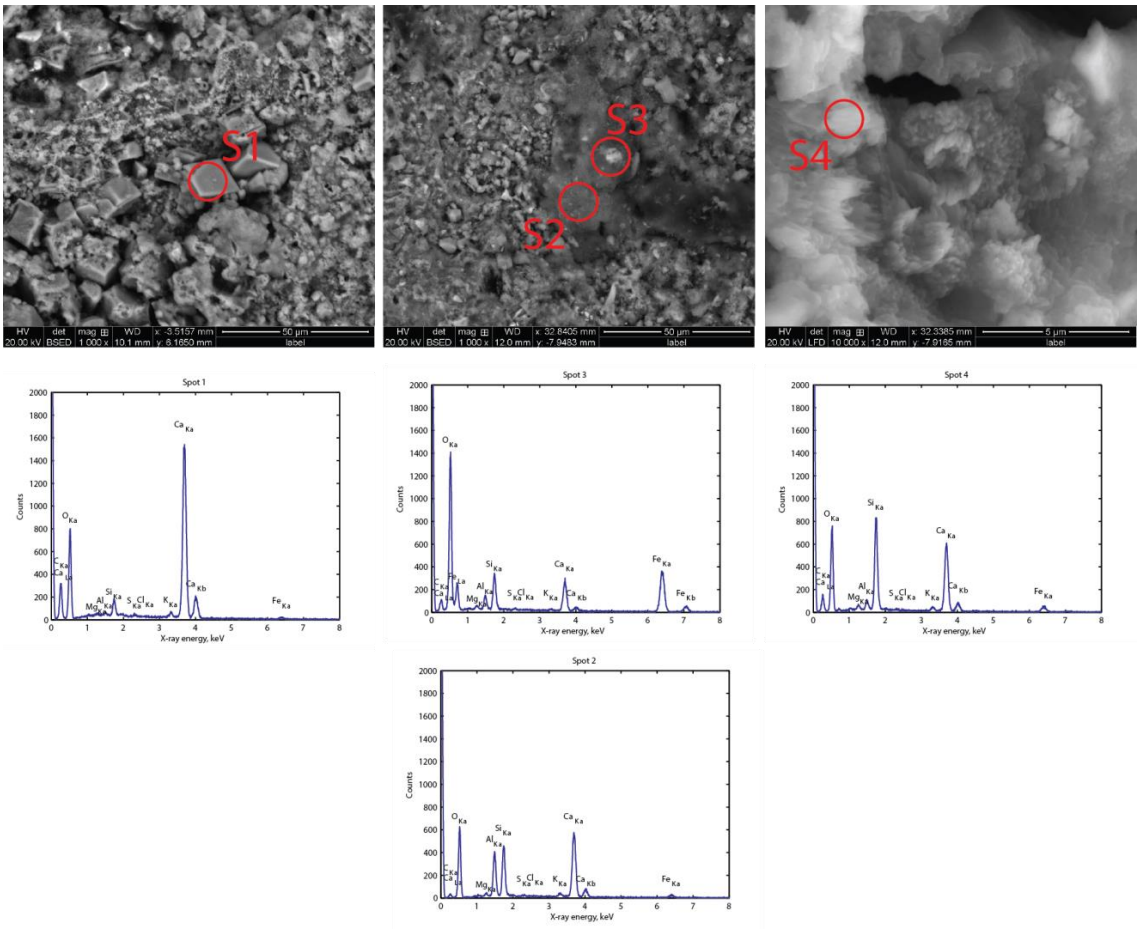

Figure 2.7 – **PN-1** Left BSED image is located just inside zone 1 (unaltered zone). Typical cement composition was measured along with larger euhedral minerals. EDS spot map was taken of a large grain (S1) and shows a large concentration of calcium and oxygen. Middle BSED image is located in zone 2 (alteration zone). Typical textures are poorly developed grains that are uniform in texture (S2). These grains are rich in calcium, silicon, and aluminum. While uncommon, relic cement grains may be present (S3). Right BSED image is a high magnification image of zone 3 (reacted zone). EDS spot map shows that calcium is not totally depleted in this material but silicon is more abundant.

2.4.2. Classification of fracture surface

Based on the fracture surface images and electron microscopy three distinct zones are identified. **Zone 1 – Unaltered zone**. This zone has typical cement phases and elemental compositions. On some samples there is indication of secondary precipitate (often calcium or aluminum rich phases) on the fracture. The unaltered zone typically remains present in experiments with little acid injected or along the sides of the fracture. When this zone is surrounded by a reacted channel, a small local aperture is inferred and thus the surface is not exposed to significant flux of acidic water. **Zone 2 – Precipitation zone**. This zone corresponds to the white material on the macroscopic images. It can occur as diffuse bands on fracture surfaces that show no or little diffuse alteration. Most commonly this zone separates Zone 1 and Zone 3. This zone is characterized by distinct euhedral mineral precipitation, concentrated in calcium and aluminum. Qualitative identification of minerals using μXRD shows this zone contains calcite and brownmillerite (Figure 2.8). The presence of calcite is due to the injected fluid container being open to the atmosphere and can contain a small amount of dissolved CO_2 that is insufficient to buffer the pH but is the source of carbonate ions. **Zone 3 – Dissolution zone**. This zone is characterized by varying shades of tan to brown and can be diffuse or form distinct channels. Dissolution of calcium rich minerals from Zone 1 and Zone 2 leads to a surface that is fine grained but has polygonal cracks on the microscopic scale and is relatively enriched in silicon and iron. Degree of coloration may be an indication of depth of penetration and progressive dissolution of initial cement phases (Chandra, 1988; Kutchko et al., 2007). Thus the dissolution zone, though significantly altered, still retains a silicon rich material that acts as a flow barrier.

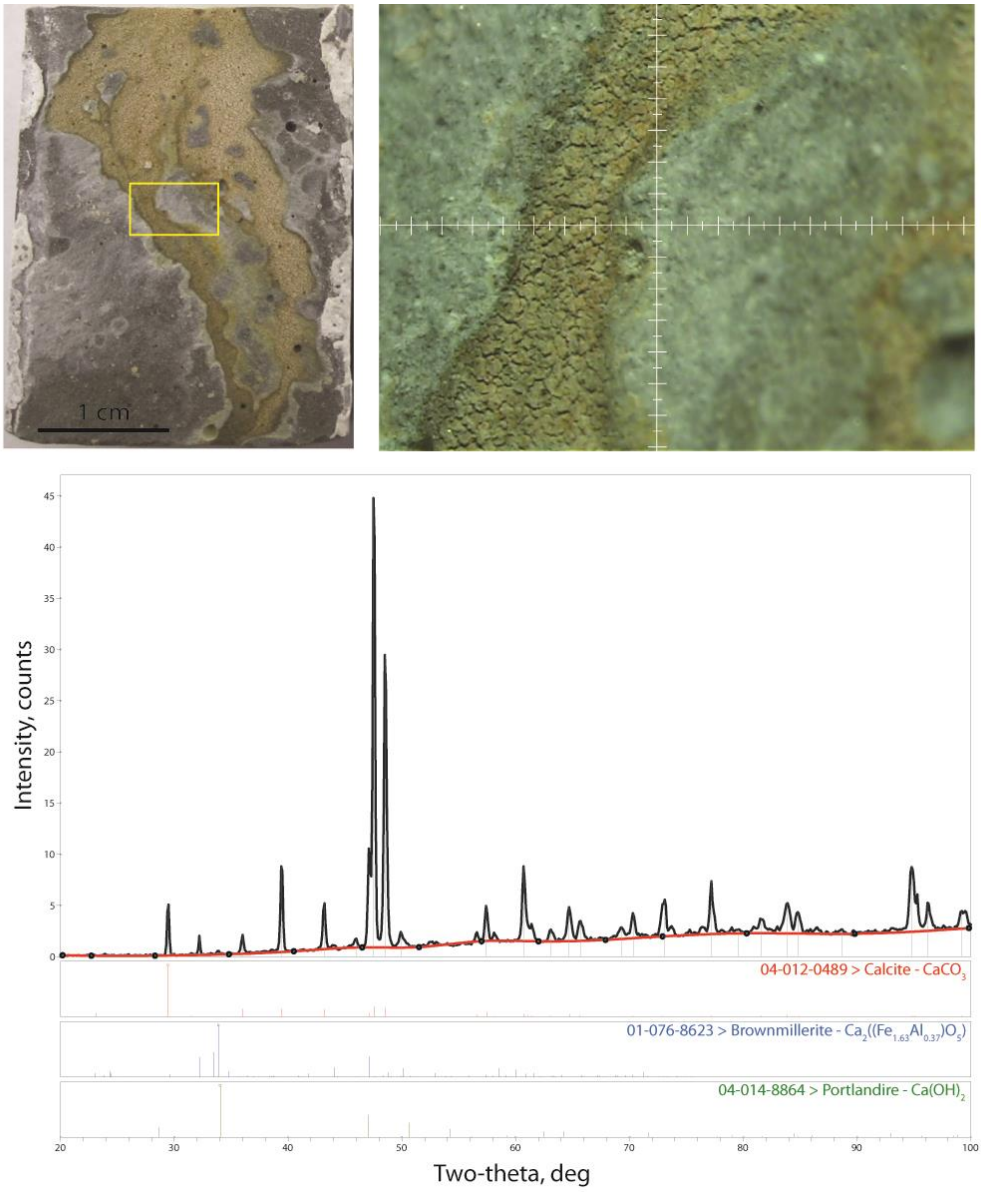

Figure 2.8 – **BSD7** The dominant phase identified was calcite. Brownmillerite was also identified but is most likely remnant and not precipitating. Portlandite seemed to have very minor, if any, occurrence. No specific steps were taken to prevent injected fluid from equilibrating with atmospheric carbon dioxide. Thus we assume the injected fluid provided the carbonate used to precipitate calcite identified. It is also possible that any portlandite precipitation was altered via carbonation to calcite as there was significant time between experiment and µXRD analysis.

2.4.3. Proposed mechanism for channeling

The occurrence of reacted channels that occupy only a fraction of the fracture surface area is remarkable. For single phase flow, there is no reason *a priori* to expect fluid to be excluded from any portion of the fracture volume. The effective apertures determined from hydraulic conductivity measurements are consistent with this expectation. Single phase unreactive flow experiments using a tracer dye independently confirm this expectation. Thus a reasonable expectation for the reactive transport response is the emergence of classical, essentially one-dimensional (in the direction of flow) zonation of chemical compositions (Helfferich, 1989; Walsh et al., 1984). According to classic reactive transport behavior, the zonation could approach a steady state, or it could evolve with time, possibly with fronts propagating in the direction of flow for suitable ratios of flow velocity and reaction rate (Lake et al., 2002; Singurindy and Berkowitz, 2005). Contrary to expectation, the location of zonation appears to be dominated by fluid dynamics, rather than by geochemical processes. Channels confine the dissolution zone; unreacted areas lie outside the channels and sometimes even form "islands" between some channels (Figure 2.2). The fronts that bound the reacted channel appear to be propagating transverse to the main flow direction, if the zones are moving at all. The zonal development is quite similar to observations from previous studies of diffusion dominated reaction into cement (Chandra, 1988; De Ceukelaire, 1992; Duguid and Scherer, 2010; Kutchko et al., 2008, 2007). The source of this unexpected complexity must be the coupling between acid/cement reactions and the flow field. The following discussion outlines features of this coupling that contribute to the emergence of these patterns.

As low-pH HCl is injected into the flow path it interacts with the hydrated (and any remaining unhydrated) cement phases. Portlandite is the first phase to be attacked and totally dissolves, releasing calcium and hydroxide ions. The next phase to be attacked is C-S-H, followed by ettringite, and then hydrated calcium aluminate phases (Chandra, 1988; De Ceukelaire, 1992). These phases also release calcium but leave behind insoluble reaction products rich in silicon, iron, and aluminum. This solid is more porous than the unaltered cement (Duguid and Scherer, 2010) and might undergo some volumetric contraction (Matteo and Scherer, 2012). Any minor amount of carbonation on the fracture surface will also be dissolved, releasing calcium and carbonate ions. As the active flow path is reacted, and available calcium is leached, the acid begins to diffuse through the reacted layer to attack the underlying cement.

Ahead (downstream) of the injected acid front (before acid breakthrough) and on the lateral edges of the active flow channel a large gradient in pH, cation, and anion concentrations occurs. The pH of cement pore fluid is significantly higher (pH ~12.3) than the injected acid and as the fluids mix several phases become insoluble and precipitation occurs along this interface. The precipitated phases are rich in calcium and aluminum and form distinct crystals that are either euhedral rhombs or elongate crystals (see Appendix C – BSD7 detailed analysis). Minerals identified in the intermediate zone were calcite and brownmillerite, with little evidence for portlandite. The source of carbonate for calcite precipitation was assumed to be either minor carbonation on the fracture surface or from the injected fluid containing atmospheric CO_2.

Because the fracture is rough-walled, the aperture distribution is spatially heterogeneous. Thus rapid precipitation at the beginning of the experiment can create numerous local dead ends near the flow inlet, diverting subsequently injected acid elsewhere. The dissolution/precipitation process yields a moving front that propagates at

a speed proportional to local flow speed. Thus the process is self-reinforcing and quickly leads to a channel at the leading edge of the fluid moving rapidly because the constant injection rate, which forces fluid to keep moving downstream. On the edges of the channel, transverse to the flow direction, the front moves much more slowly. If the flow field is slow enough and the gradient in concentration between acid and the cement pore fluid is small, precipitation at the front of the flow path is sufficient to cause elevated pressure spike as in Case B. If acid concentration is high, residence time low, and the flow path large, then a small decrease in upstream pressure was observed (Case C). This decrease could be the result of unblocking of flow restrictions via portlandite dissolution, aperture increase via volumetric contraction of the remnant amorphous silicate, or widening of the reacted channel. However, these phenomena must be balanced with the fact that in most experiments where a channel still forms (Case A) the net result is a significant increase in upstream pressure.

2.5. CONCLUSIONS

The practical result from these analog experiments is that even though acid was injected into cement, fracture opening and wormhole development did not occur. In fact, the silicon-rich phase that remains prevents fracture opening and becomes a diffusive boundary, which slows reaction into the cement. Further, evidence for self-limiting behavior is seen when calcium-rich water interacts with high-pH fluid in front of the channel tip and to the sides of the flow path. Where this mixing occurs, distinct minerals precipitate which could act as a restriction in flow. In the cases with small decrease in upstream pressure, it is hypothesized that the flow path was large and that any precipitation occurring during the duration of the experiment was insufficient to constrict flow or that flux of fluid (and core length) did not allow significant residence to promote

sufficient mineral precipitation to block the flow path. The experiments reported in this chapter are for constant flow rate. Thus even when pressure gradient increased significantly as precipitated mineral accumulated, it was possible to break through such an accumulation mechanically.

The expected down-hole conditions differ from these experimental conditions in several key respects: significantly higher dissolved CO_2 concentration (and higher reactivity), smaller fluid flux driven by a constant pressure gradient (as opposed to a constant flow rate), the presence of significantly more carbonate (and a resulting pH buffering effect), and much longer residence time within the fracture. Further the complexity of specific cement formulations, down hole conditions (e.g. pressure and temperature), and brine composition affects the coupled system. As a result, reaction rates, mineral solubility, and local channel development could vary. While the next chapter presents more realistic experiments, insights from the analog experiments have identified that self-limiting or even self-sealing behavior seems likely due to local dissolution precipitation reactions in the fracture.

3. Carbonic acid experiments

3.1. SUMMARY

Building off the previous chapter's analog hydrochloric acid (HCl) experiments, this chapter presents results and analysis of more advanced and representative reactive transport experiments in cement fractures. This set of experiments more realistically captures the subsurface conditions (higher pressures, more dissolved CO_2 concentration, and carbonic acid) expected in GCS. The goal of this chapter is to confirm reactive transport processes discovered in the analog experiments of Chapter 2, compare the results to the chemical reactions of the diffusion-dominated experiments (Kutchko et al., 2007; Mason et al., 2013), and determine the time-dependent fluid flux due to the coupled reaction and transport. A subset of this work will be submitted for review in the International Journal of Green House Gas Control.

The experiments are performed using one of 2 inlet boundary conditions. Short core constant flow rate experiments are used to compare reaction behavior to the HCl experiments. While the reaction mechanisms are comparable to the analog experiments, the reaction time scale is significantly longer.

As a consequence, longer composite cores were developed to increase residence time. Additionally, the second type of boundary condition (constant pressure differential) was used because it represents the expected subsurface driving force and any changes in fracture conductivity will have direct effect on the flux, allowing the experiments to test for coupled behavior.

In all experiments in this chapter carbonic acid progressively reacts with cement by dissolving phases which neutralize the acid and liberate calcium ions. Where aqueous calcium concentration and pH are sufficiently high calcium carbonate becomes insoluble and precipitates in the open fracture.

When the driving force for fluid flux is a constant pressure differential precipitation leads to lower fluid flux and the development of self-limiting behavior. With sufficient residence time self-limiting leads to sealing of the leaky well.

3.2. METHODS

3.2.1. Core flow equipment

All experiments are performed with core flow units (Figure 3.1) built by Coretest Systems, Inc. (Model CFS-839Z). The units are designed to perform flow experiments at elevated pore pressure, confining pressure, temperature, a range of flow rates, and flow modes. Fluid is mixed and injected using 2 L stainless steel accumulators. The cement sample is held in a bi-axial core holder or Hassler cell. Water is used as the confining fluid and elevated to confining pressure by low pressure air and a Maximator pressure intensifying pump. Quixiz QX pumps are used to drive fluid from the accumulators. Quartzdyne digital pressure transducers are used to monitor all system pressures. Back pressure is maintained by a 2 stage system. The first is a digital back pressure regulator built by Coretest Systems, Inc. to dynamically control downstream pressure. To limit instability due to Joule-Thompson cooling of the CO_2, a second heated backpressure regulator is used to step down pressure from an intermediate value to atmospheric pressure.

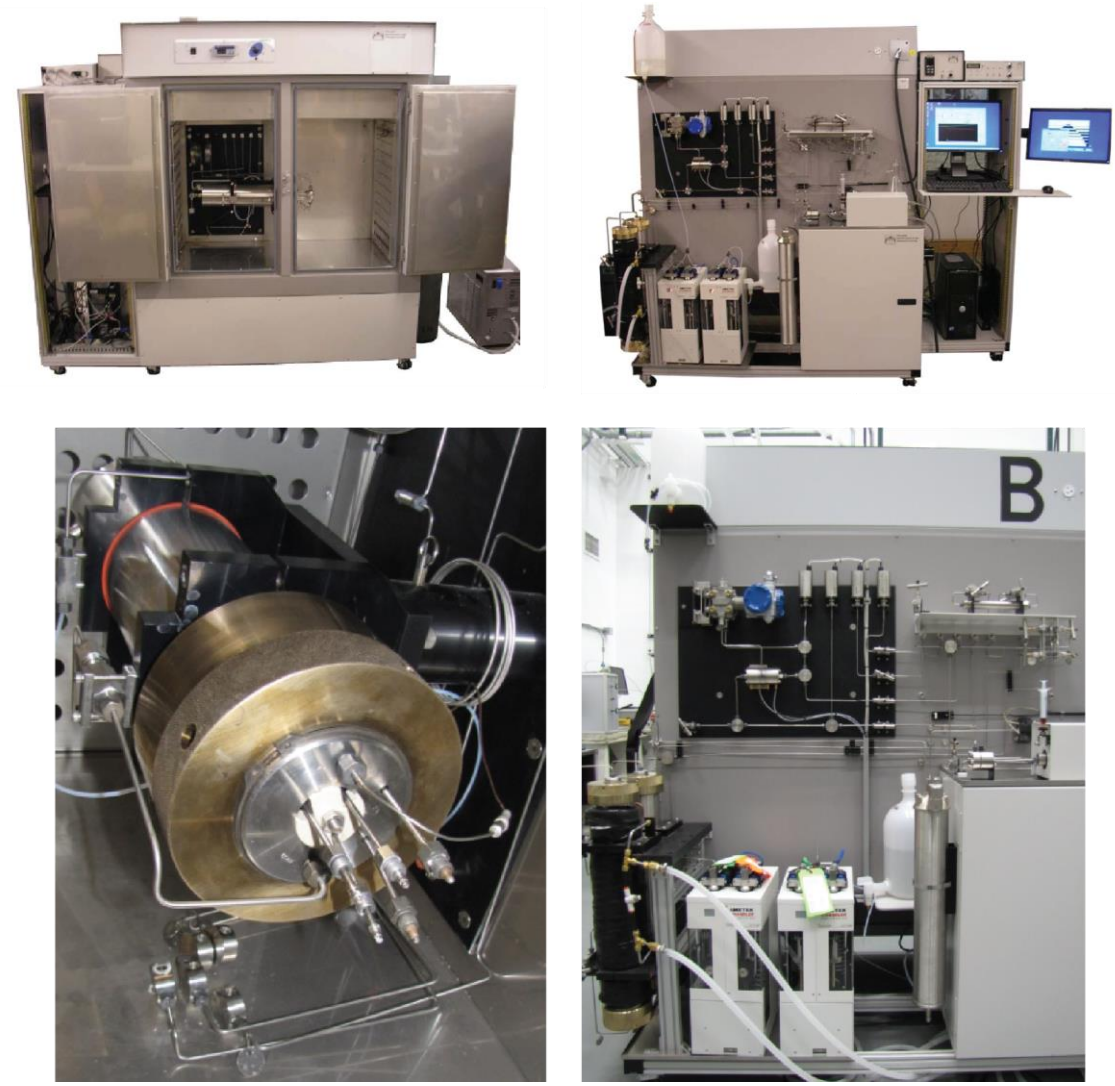

Figure 3.1 – Images of core flow unit used in experiments. (Top left) Inside of the oven and Hassler cell. (Top right) Image showing pumps, pressure transducer manifold, accumulators, confining pressure system, back pressure regulators, and computer control system. (Bottom left) Close up of Hassler cell and inlet tubing manifold. (Bottom right) Close up of fluid control system.

The sample is placed in the core holder, the confining system is filled with water, and confining pressure is applied. Prior to reactive fluid injection, distilled water is injected into the fracture to achieve the required experimental pressure, measure a base

line flow rate to pressure differential relationship, and estimate the initial hydraulic aperture.

3.2.2. Sample preparation

Cores of class H neat cement are prepared according the methodology of Huerta et al. (2013) and summarized in Chapter 2. Natural fractures are created via the Brazilian method in order to obtain irregular, rough walled fractures similar to fractures in a wellbore. This technique generates a single tensile fracture by applying stress down the length of the core. The equipment used is either a loading frame with two flat platens or a core splitter with one flat platen and a dull blade that concentrated the load along a single line and improved the success rate of creating fractured samples. The re-assembled core, when slightly offset, provides a so-called closed natural fracture that is propped open by locally touching asperities.

Some limitations of the approach are that each fracture is unique and local fracture aperture heterogeneity cannot be accounted for *a priori*. The fractures tend to deviate from the applied stress lines, typically along local heterogeneity, and move off center of the core. This is especially true as the length of the core is increased. As a result, fractured cores are typically less than 10 cm in length.

For the constant flow rate experiment, a single fractured core is used and a range of flow rates used similar to the rates used in Chapter 2. For experiments with large residence time, individual cores are stacked end-to-end to lengthen the overall core. To ensure a continuous flow path between cores, the fracture plane of each core is rotated 90° to the proceeding core. While the junction between points represents a significant flow restriction, the experiments still show behavior similar to the single core experiments. It is also not unrealistic that in the wellbore a fracture will be subject to

significant junctures, splitting, and flow path narrowing as the fractures propagate along a well.

3.2.3. Fluid conditions and mixing method

3.2.3.1. CO_2 saturated water

The goal of these experiments is to study the simplest chemical system and maximize the amount of CO_2 dissolved. Thus distilled water with no added salinity is used and experiments are conducted at ambient temperature. These conditions maximize the concentration of dissolved CO_2 in the water. Using distilled water also allows the fundamental processes to be studied and is independent of reactions that would be unique to individual brine composition.

3.2.3.2. Calculation of theoretical CO_2 saturation

Due to laboratory safety protocols fluid sampling at experimental pressure to measure CO_2 concentration is not possible, so CO_2 saturation is estimated using the equation of state (EOS) of Duan and Sun (2003). For more background on the EOS see Appendix B. To ensure complete saturation, the water is mixed with an excess (typically 10%) of the amount of CO_2 needed.

3.2.3.3. Fluid mixing method

CO_2 is mixed with the distilled water by first filling the one accumulator with a volume of water (typically 1.5 L). A second accumulator is chilled to 5 °C and the calculated volume of liquid CO_2 is metered in. The chilled accumulator is brought up to ambient temperature and experiment pressure and the water is pushed into the CO_2 filled accumulator. The system is allowed to equilibrate and the volume change is monitored

while applying constant pressure to identify when CO_2 had stopped dissolving. Equilibration is typically reached within 24 hours.

3.2.4. Analytical equipment

To analyze changes on the fracture surface a Philips/FEI XL3 scanning electron microscope (SEM) is used. Analysis is performed in environmental SEM (ESEM) mode on uncoated and unpolished samples. Secondary electron (SE) images, back scattered electron (BSE) images, and energy dispersive x-ray spectroscopy (EDS) maps are collected. Specific experiment conditions are noted on the respective image.

To identify secondary precipitated phases a Rigaku R-Axis micro diffractometer (μXRD) with an UltraX18 Cu rotating anode X-ray source and Rapid II 180° curved imaging plate detector is used on select samples. The X-rays are collimated to a 100 μm spot size. Phase identification is performed using Rigaku PDXL software with the ICDD PD4 database.

Effluent samples are collected at varying intervals and durations for the constant rate experiments to observe the evolution of the chemical reactions occurring in the fracture. A Perkin Elmer model Optima 3000 XL coupled plasma atomic emission spectrometer (ICP-OES) is used to measure key cations.

3.2.5. Experiment method

3.2.5.1. Constant flow rate short core experiments

The purpose of constant rate experiments with CO_2-saturated water is to emulate conditions of Chapter 2 with more representative fluid and chemical interactions. Specifically chemical reactions due to dissolution of cement phases and precipitation of secondary phases are compared to the previous case where an HCl solution is the reactive fluid. To observe change in chemistry, texture, and mineralogy, the change in pressure

differential is recorded, effluent cation concentration measured, and the altered fracture surface is analyzed.

3.2.5.2. Constant pressure differential composite core experiments

Based on the results from the constant flow rate experiment and in an attempt to more realistically model down-hole conditions, longer cores are used under constant pressure differential driving force. Extended core length allows longer residence time and also increases the ability to detect small changes in conductivity due to precipitation on the fracture surface. A constant pressure differential driving force also captures the subsurface condition and allows self-limiting behavior to develop as a decrease in fluid flux, which could lead to self-sealing. This approach is a direct experimental test of the hypothesis that these fractured cement pathways seal given sufficient residence time.

3.3. RESULTS

Table 3.1 contains summary statistics for all experiments. Appendix C has detailed reports for each experiment but key results are presented and discussed below. Length in the constant pressure differential experiments refers to total length of the composite core. Flow rate is the initial stable rate reported by the pump software. Pressure differential is taken as the difference between upstream and downstream pressure transducer readings. Temperature and confining pressure are measured by the core flow equipment software. CO_2 saturation is estimated as described above using the upstream pressure, temperature, and pure water assumption. Hydraulic aperture is estimated using the cubic equation (for derivation see Appendix A):

$$B = \left(\frac{12\mu QL}{W(\Delta P)} \right)^{1/3} \qquad (3.1)$$

Where Q is the flow rate, B is the aperture, W is the sample width, ΔP is the pressure differential ($P_{in} - P_{out}$), μ is the fluid viscosity, and L is the sample length.

Permeability is a unit of measure more appropriate for flow through porous media however because it is used as convention in leakage estimate models (Nordbotten et al., 2005; Tao et al., 2011) the results will also be presented in those units. Permeability (k) can be related to aperture through equating Darcy's equation and the cubic equation using (see Appendix A for more discussion):

$$kA = \frac{WB^3}{12} \qquad (3.2)$$

The choice of the area (A) for these experiments is the cross sectional area of the sample. So the equation for equivalent sample permeability is:

$$k = \frac{B^3}{3W} \qquad (3.3)$$

Total time is presented for constant flow rate experiments as the entire experiment time while time is presented for the constant pressure differential experiments as total time and time used in the analysis section below.

Moles of CO_2 injected (n_{CO2}) are calculated during each experiment and at the experiment end. Plotting with this parameter normalizes for flow rate and experiment conditions (temperature and upstream pressure), which control amount of dissolved CO_2 ($wt.\%_{CO2}$) that contacts the core. Also included in the calculation are the density of the fluid (ρ_f) and molecular weight of CO_2 (MW_{CO2}). The equation is:

$$n_{CO_2} = \frac{tQ\rho_f wt.\%_{CO_2}}{MW_{CO_2}} \qquad (3.4)$$

Fluid flux is calculated by dividing the flow rate by the cross sectional area of the fracture and residence time is calculated by dividing the sample length by the fluid flux. Because these fractures are not open smooth walled channels the fluid flux and residence times are most likely over estimates of the true value but provide insight in the scale of transport occurring within the fracture.

Table 3.1 – Summary of experiment parameters.

Constant flow rate experiments				
Sample name	**NA7-11**	**NA9-3**	**QB4-3**	**QB6**
Length × Width, cm	6.25 × 2.54	5.37 × 2.54	7.24 × 2.54	6.17 × 2.54
Flow rate, mL/min	1.0	0.5	0.25	0.25
Pressure differential, psi	0.9	0.35	0.2	5.7
Temperature, °C	21	22	21	21
Confining pressure, psi	1,519	1,653	1,528	1,540
CO_2-saturation, wt. %	6.38	6.25	6.34	6.33
Hydraulic aperture, µm	43	44	47	33
Sample permeability, mD	317	351	415	148
Total time, hr	8	47.1	50.6	7.9
Residence time, s	4	7	21	1
Constant pressure differential experiments				
Sample name	**JA1-Frank1**	**JA5-Frank2**	**JA8-Frank4**	**JA9-Frank3**
Length × Width, cm	23.4 × 2.54	24.03 × 2.54	21.9 × 2.54	24.38 × 2.54
Flow rate, mL/min	0.011	0.13	0.011	0.006
Pressure differential, psi	2.0	7.4	21.3	55.1
Temperature, °C	21	22.5	23.5	22
Confining pressure, psi	1,986	1,896	2,457	2,385
CO_2-saturation, wt. %	6.57	6.42	6.39	6.52
Hydraulic aperture, µm	12	17	5	3
Sample permeability, mD	6	19	0.52	0.12
Total time, hr	77.2	72.3	25.5	71.2
Residence time, s	360	48	126	193

3.3.1. Constant flow rate short core experiments

3.3.1.1. Flow rate and pressure differential history

Flow rate is selected over a range of values to observe changes in pressure differential due to dissolution of cement phases and precipitation of secondary phases which were identified in the analog HCl experiments in Chapter 2. A key result for the current experiments is that the pressure differential remains essentially constant, especially compared to results in the analog system. Although there is no change in pressure differential, analysis of effluent fluid samples and inspection of the post experiment fracture surfaces shows that there was significant reaction on the fracture surface.

3.3.1.2. Effluent history

Figure 3.2 shows effluent concentrations of the key cations plotted versus amount of dissolved CO_2 injected. Several cations (calcium, iron, and silicon) that make up a significant portion of cement are used to describe the experiment evolution. Because of dead volume (estimated to be several mL) the first effluent sample can contain a mixture of pre-experiment fluid and effluent from injection of the CO_2 saturated water.

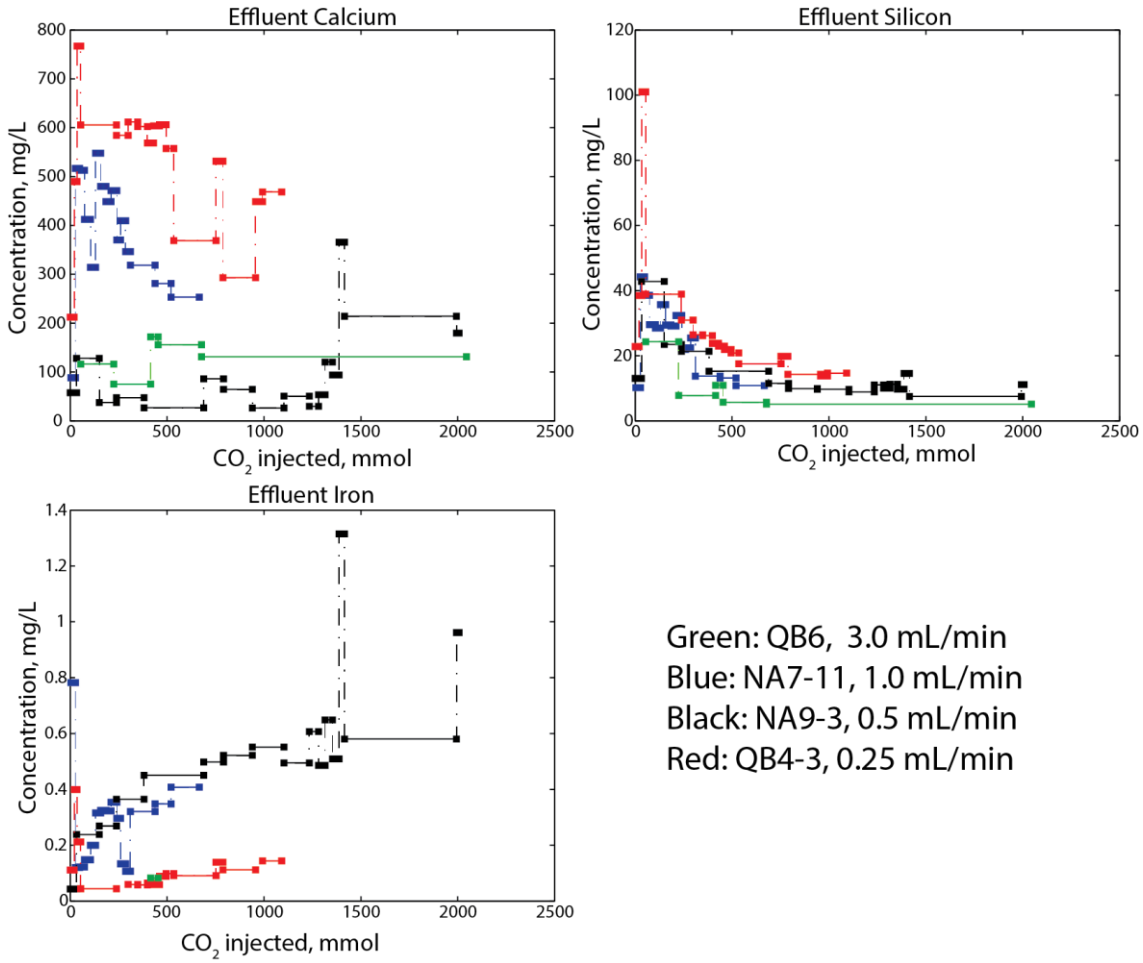

Figure 3.2 – Effluent concentrations plotted versus total dissolved CO_2 injected for 4 constant rate experiments. (Top left) Calcium concentration. (Top right) Silicon concentration. (Bottom left) Iron concentration.

Calcium is the most abundant cation in all effluent samples with 2 distinct types of behavior. In QB4-3 and NA7-11 there is an early concentration spike followed by a general decay as the experiment progresses. In QB6 and NA9-3 there is a low sustained effluent concentration profile. While the slowest and fastest flow rates have a large and small effluent concentration respectively, there is no direct correlation between bulk flow rate and effluent calcium behavior.

Silicon has a low but measureable concentration in effluent samples. The low effluent concentration considering its relative abundance in cement is evidence that silica remains generally insoluble. In all experiments silicon concentrations have a distinct spike followed by an asymptotic decay. When plotted versus total CO_2 injected all curves are nearly identical, with a minor trend showing that faster flow rate yields lower effluent concentration.

Total iron concentrations in the effluent are low compared to the iron concentration in cement. Iron displays a general trend that shows effluent concentration increasing with time, except with QB6 (the fastest) which is above detection limit in only one sample. There is no correlation with flow rate, as the fastest (QB6) and slowest (QB4-3) show the lowest effluent concentration. At intermediate rates (NA9-3 and NA7-11) effluent concentrations rise at a similar rate. Aluminum is below detection limits in the effluent samples and is further evidence that certain key elements remain immobilized during the experiments.

Based on effluent concentrations of calcium it is clear that no simple relationship exists between fluid flux and effluent concentration profile and thus complex coupled transport and reaction processes are occurring within the cement fracture.

3.3.1.3. Fracture surface, SEM, and μXRD analysis

Figure 3.3 shows photographs of one reacted surface for each sample. Shown to the right of each image is an illustration identifying the caulk (white), unreacted cement (grey), and reacted flow path (black). In all images flow is from top to bottom. Key regions of interest are also labeled and discussed below. In all experiments a distinct reacted pathway forms. In most experiments the pathway is broad and covers most of the available flow area, though there are lateral flow restrictions in all samples. At the

boundary between reacted channel and unreacted cement there is either a sharp zone of white precipitate or a broader zone that is medium grey.

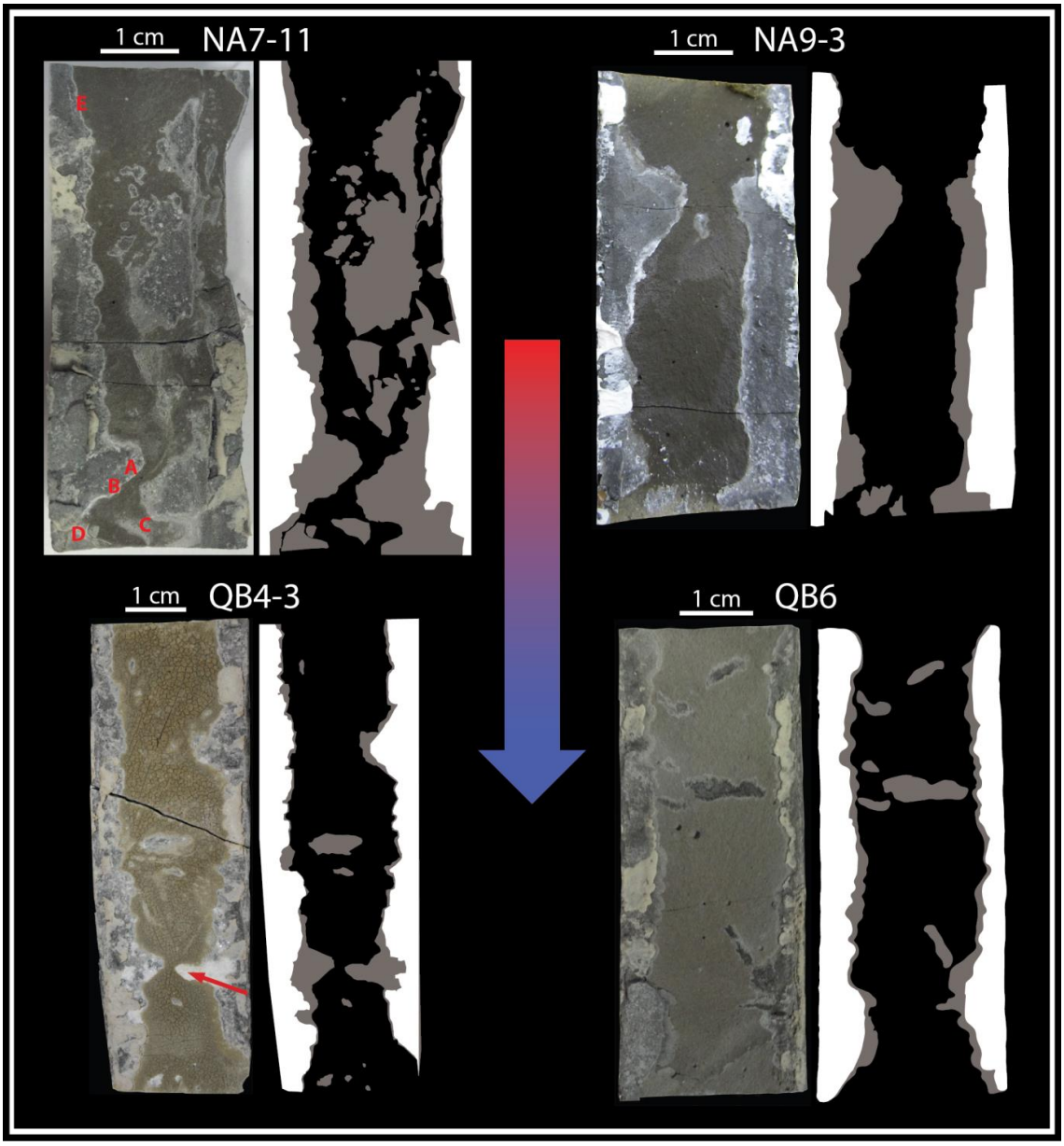

Figure 3.3 – Images of one half of the fracture surface for the constant rate experiments. Flow is from top to bottom in all experiments. The left side of each sample is an image of the surface while the right side identifies the location where caulk (white), unreacted cement (grey), or reacted cement (black) was identified on the fracture surface. Letters (NA7-11) and the arrow (QB4-3) indicate locations selected for analysis with SEM and µXRD.

Sample NA7-11 was selected for further analysis by SEM/EDS to characterize textures and changes in relative element concentration in the zones identified in Figure 3.3. Figure 3.4 shows BSE images taken at Location A, which is an example of a sharp transition between the reacted channel (above blue line) and unreacted cement (below blue line). The reacted channel has a visually distinct cracked texture, while the transition and unreacted zone contains micron scale euhedral grains. Figure 3.5 shows BSE images acquired at Location B which shows the transition between reacted and unreacted cement. An enlarged BSE image (Figure 3.5 – right) shows most of the material in the reacted channel is very fine grained and lacks distinct crystal shapes. Figure 3.6 is a BSE image near the outlet (Location C) and is an example of the more gradational texture associated with a broad boundary. Much larger euhedral crystals are immediately next to reacted cement. Location D is also near the outlet and Figure 3.7 shows BSE images progressively zoomed in to illustrate the distinct crystal shapes in a complex relationship with the reacted channel. Zoomed in images show the crystals actually contain imperfections to the bulk crystal habit that seem to be along cleavage planes (Figure 3.7 – red arrows). Figure 3.8 shows BSE, SE, and EDS element maps for Location E. In the reacted channel (left side of images and maps) calcium is depleted, which leaves silicon relatively enriched. Iron and aluminum also remain in the reacted channel, which explains their low concentration in the effluent samples.

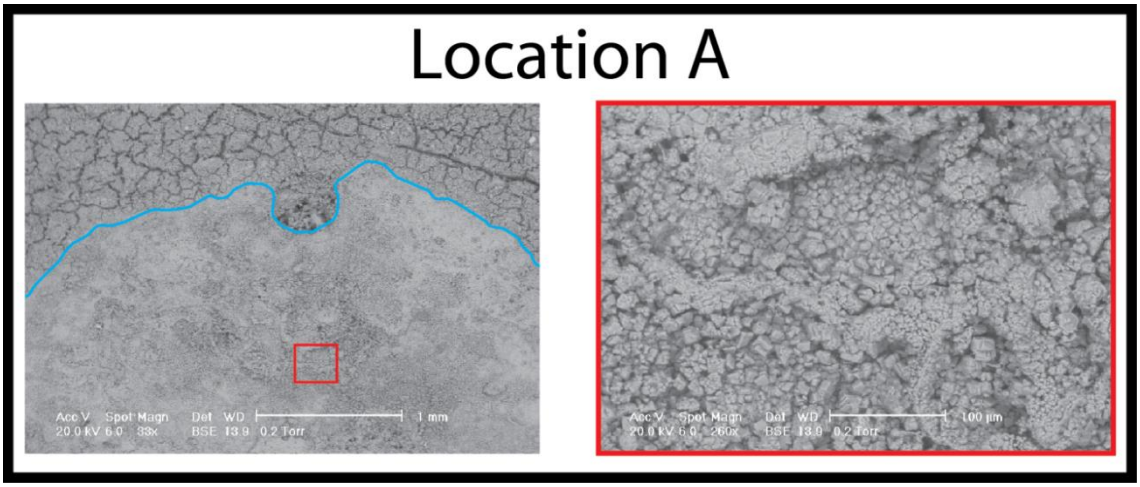

Figure 3.4 – **NA7-11**(Left) BSE image of location showing sharp transition between reacted (above blue line) and unreacted areas (below blue line). (Right) A zoomed BSE image shows distinct euhedral crystals present in the unreacted zone.

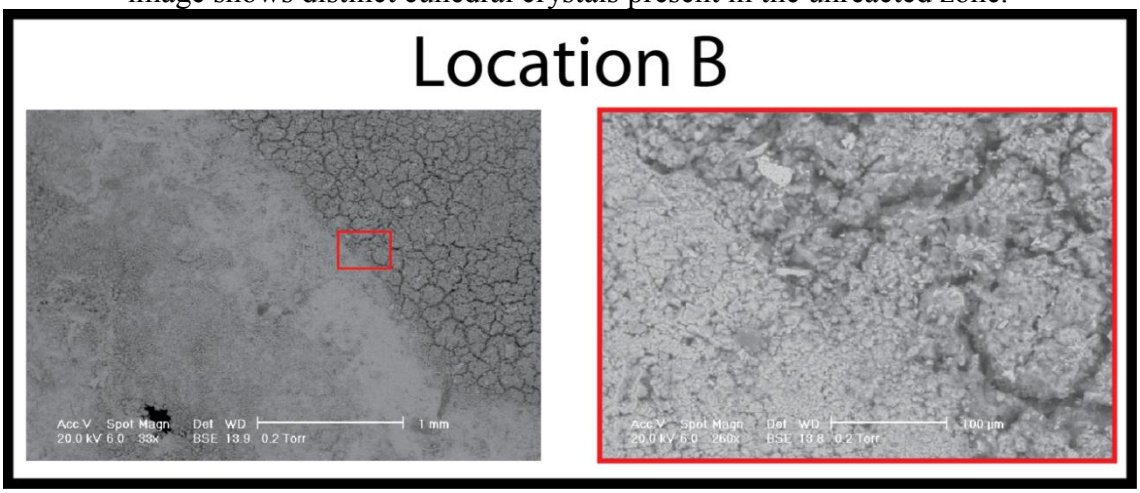

Figure 3.5 – **NA7-11** (Left) BSE image of transition between reacted and unreacted cement. (Right) A zoomed BSE image of transition zone showing fine grained solids.

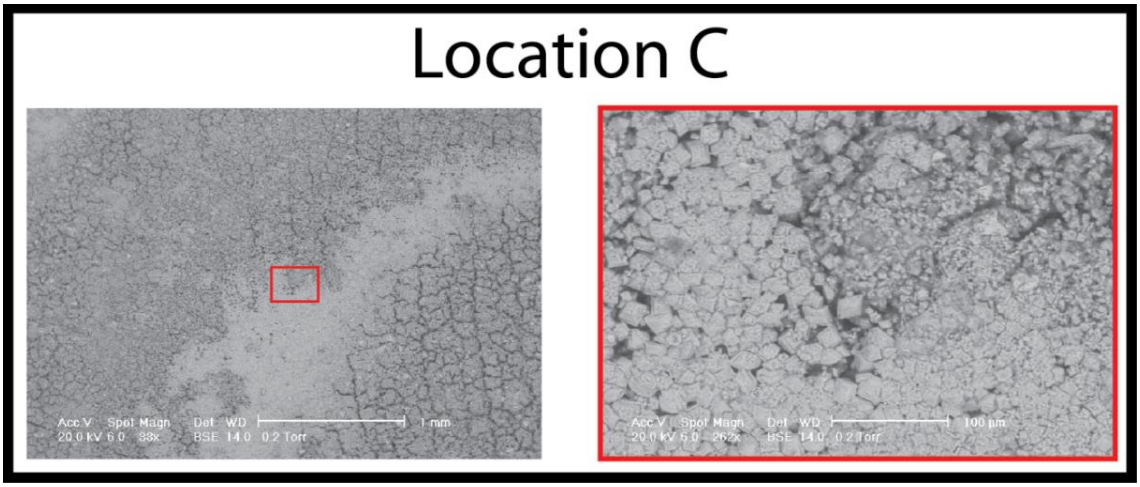

Figure 3.6 – **NA7-11** (Left) BSE image near the core outlet shows reacted cement surrounding a core of large euhedral crystals. (Right) a zoomed in BSE image shows the crystals typically display a rhombohedral habit.

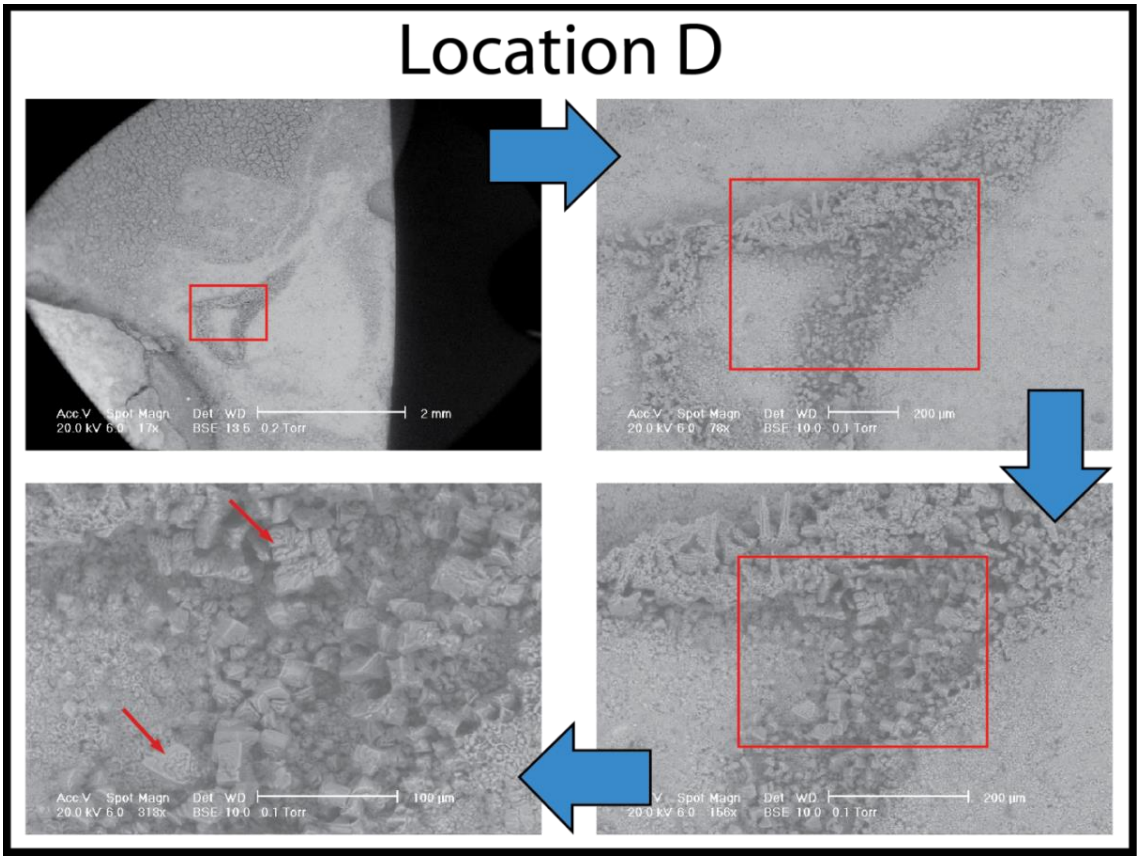

Figure 3.7 – **NA7-11** BSE images that progressively zoom in on a location to show the dissolution of the large euhedral crystals (red arrows).

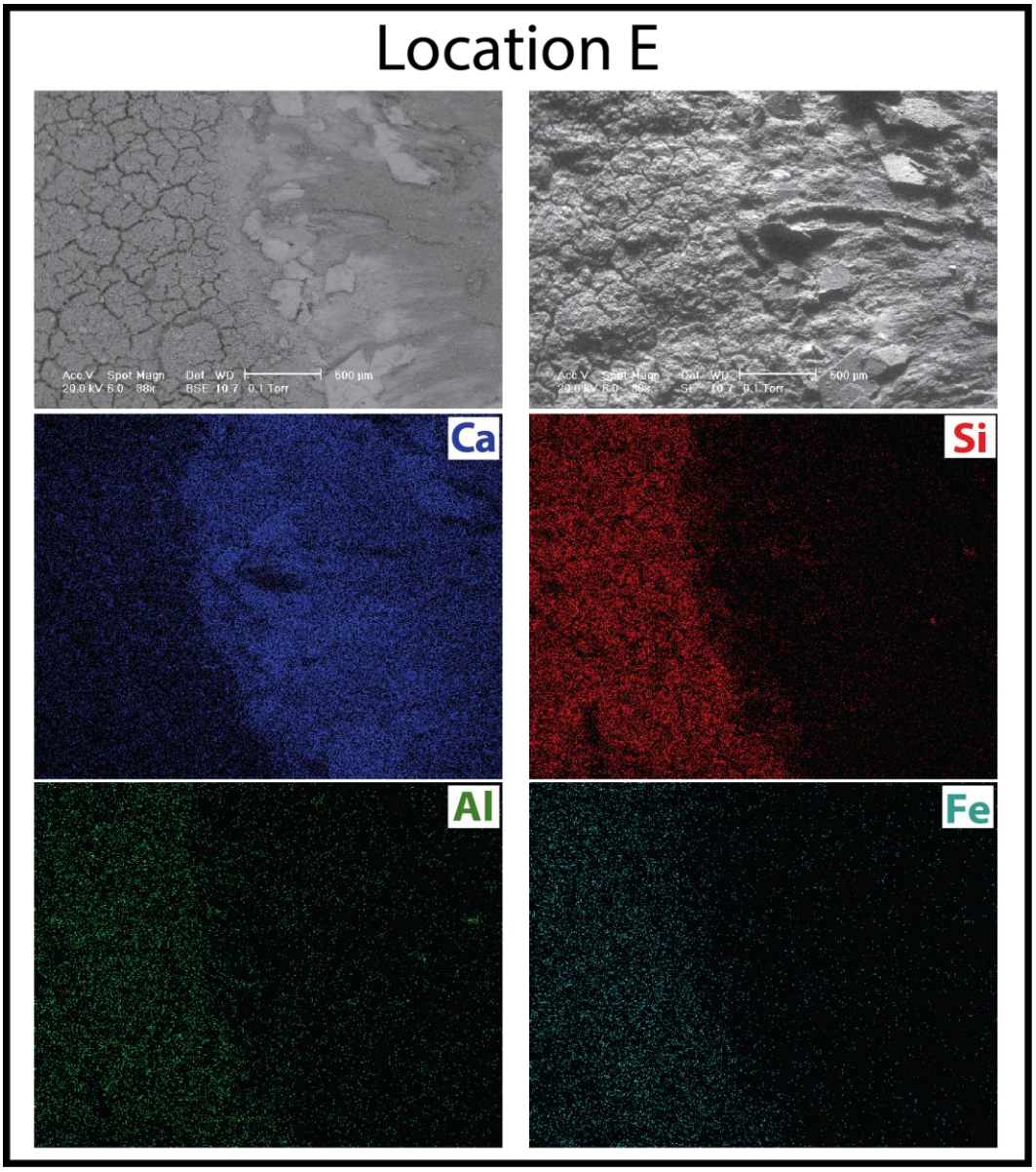

Figure 3.8 – **NA7-11** Flow direction in these images is from the bottom up. (Top left) BSE image showing distinct textural differences between reacted (left side) and unreacted (right side) zones. (Top right) SE image showing the morphology of the fracture surface. (Middle left) Calcium EDS map showing that calcium is more abundant in the unreacted zone. (Middle right) Silicon EDS map showing that in the reacted zone silicon is relatively enriched. (Bottom left) Aluminum EDS map and (Bottom right) iron EDS map also show that they remain in the reacted zone and are generally low concentration.

Figure 3.9 shows μXRD analysis of a large area of secondary precipitate on the fracture surface of sample QB4-3. The location is highlighted by the red arrow in Figure 3.3. Identified phases are calcite, portlandite, and perhaps trace vaterite.

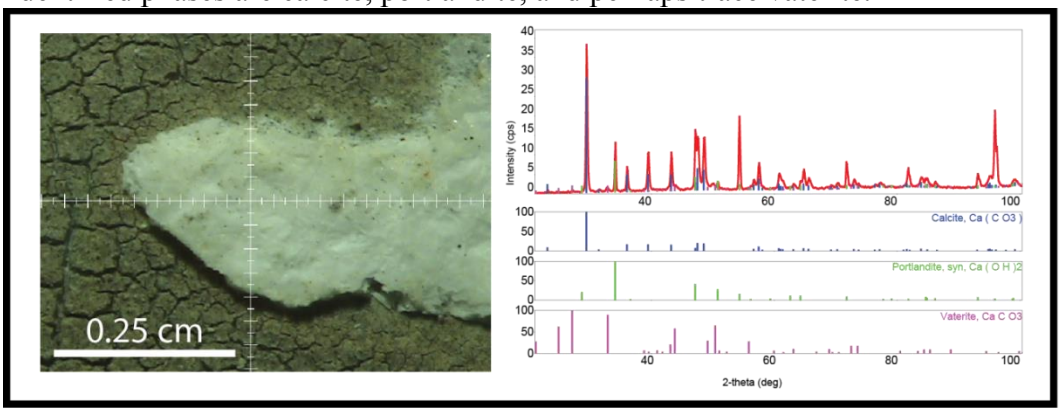

Figure 3.9 – **QB4-3** (Left) Image of precipitate analyzed with μXRD. (Right) Identified precipitate phases were calcite, portlandite, and vaterite.

3.3.2. Constant pressure differential composite core experiments

3.3.2.1. Flow rate and pressure differential history

Figure 3.10 shows flow rate history for each of the 4 constant pressure differential composite core experiments. Flow rate and pressure differential is recorded every 30 seconds and is smoothed using a 5-point average to dampen noise.

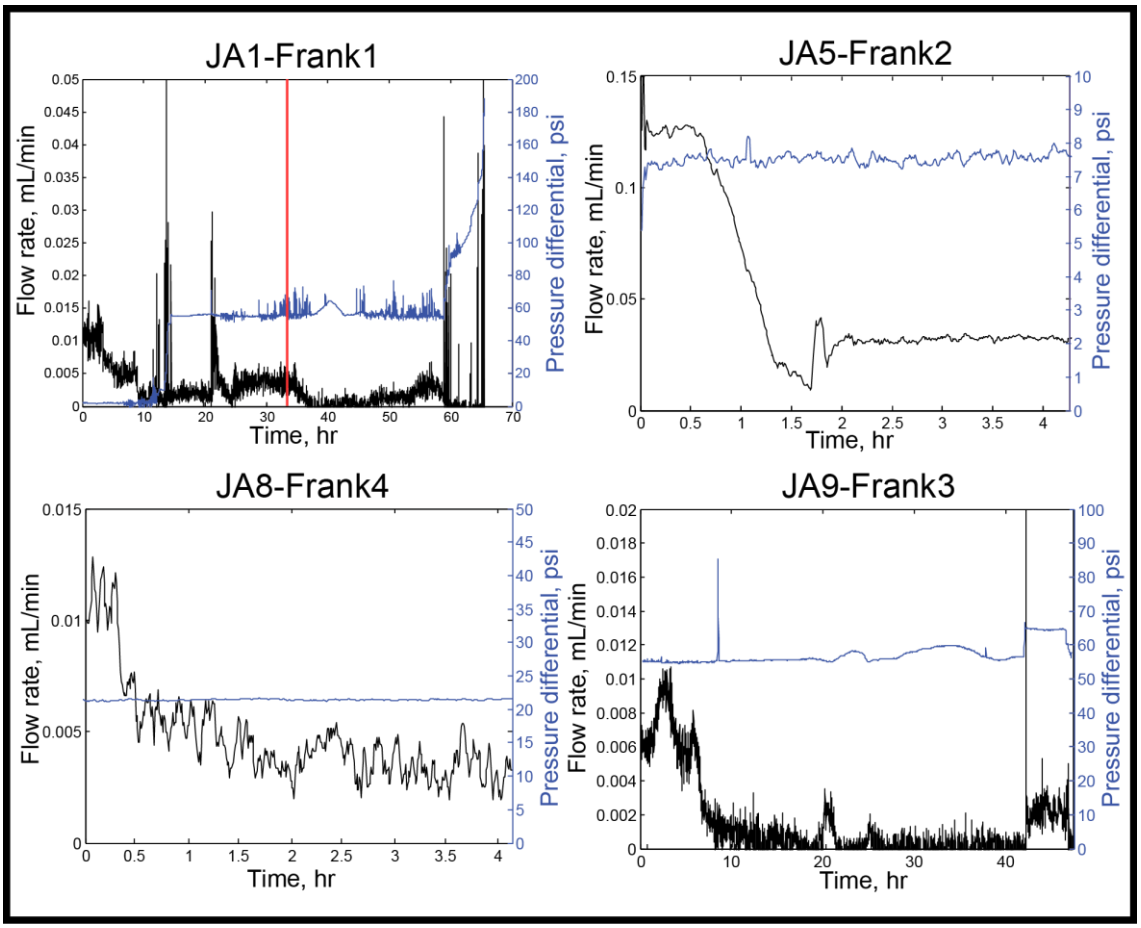

Figure 3.10 – Pressure differential (blue line) and flow rate (black line) plotted versus time for the 4 constant pressure differential experiments.

Sample JA1-Frank1 (Figure 3.10 – Top left) is the first attempt to conduct constant pressure differential experiments on a composite core. The flow rate for the first few hours is below 0.005 mL/min as the pressure of the fluid in the fracture equilibrates. During this interval less than 1 mmol CO_2 is injected. After 3 hours the pump cylinders switched and there is a rapid decrease in upstream pressure that corresponded with flow establishment at a steady flow rate of 0.011 mL/min. Fluid has passed through the dead volume (calculated at 6.872 mL) by 11.6 hours. After 15 hours, flow rate begins to decrease. Flow rate continues to decrease until just before 21 hours where flow was near

the lower limit for detection. Upstream pressure is increased by 10 psi in an attempt to reestablish a steady flow rate. After no significant flow is established, upstream pressure is increased until the pressure differential across the core is 50 psi. A flow rate below 0.005 mL/min did periodically occur but equivalent sample permeability remains very small. These conditions are held for 50 hours. At the end of the experiment the pressure differential is increased to 200 psi for a short time with no development of significant flow. For the comparative analysis in section below the experimental data is plotted from the time acid reaches the core face at 11.6 hours to 33.4 hours (indicated on Figure 3.10 by a vertical red line) and incorporates part of the 50 psi pressure differential time.

For sample JA5-Frank2 (Figure 3.10 – top right) residence time is 48 seconds and much less than the previous experiment. Pressure differential is 7.4 psi, which corresponded to an initial flow rate of 0.13 mL/min. Because the residence time was short, the important behavior occurred within the first 2 hours and time up to 4.27 hours was used for the comparative analysis section below. The acid seems to react the core well before the dead volume amount has been injected (see experiment report for details). Within this time flow rate is constant at its initial value for 40 minutes then rapidly decreases and settles at 0.03 mL/min. The flow rate remains constant at 0.03 mL/min (lower than the initial value) for 25 hours. The tubing begins to plug from precipitation after 32 hours but did not affect results. The sample was removed after 72.3 hours and a total of 151 mmol CO_2 injected. This experiment does not exhibit self-sealing behavior based on flow rate data.

Sample JA8-Frank4 (Figure 3.10 – bottom left) has a very small equivalent sample permeability of 0.7 mD so to get the desired initial flow rate of 0.015 mL/min a pressure differential of 20.7 psi was set. For the first 5 minutes, as upstream and correspond pressure differential are increasing to their set point, flow is 0.3 mL/min.

Flow rate decreases and stabilizes at 0.015 mL/min for the first 6 hours and then flow rate begins to decay. Acid is estimated to travel through the dead volume (6.872 mL) and reach the core by 7.58 hours. By 11.7 hours flow rate decreases to 0.003 mL/min. This time is used as the final time for the comparative analysis section. The experiment ran for a total of 12.4 hours before a leak from the confining fluid system to the fluid pore system raised upstream pressure and shut off flow, effectively ending the experiment.

Sample JA9-Frank3 (Figure 3.10 – bottom right) has a very low initial equivalent sample permeability of 0.12 mD so a large pressure differential (55.1 psi) is required to yield an initial flow rate of 0.006 mL/min, which is just within the equipment's lower flow rate limit. It takes 23.75 hours for flow to travel through the dead volume (6.872 mL) of the core reach the core face. After this point flow rate begins to decrease by 31.97 hours flow rate has nearly shut off. At the end of the experiment the upstream pressure is increased to attempt to reestablish flow but no significant flow rate is generated.

3.3.2.2. Fracture surface, SEM, and μXRD analysis

Figure 3.11 shows the reacted surface of the constant pressure differential experiments. In this figure both halves of the cement core are shown and flow is from left to right. Each paragraph below refers to the respective sample shown in Figure 3.11.

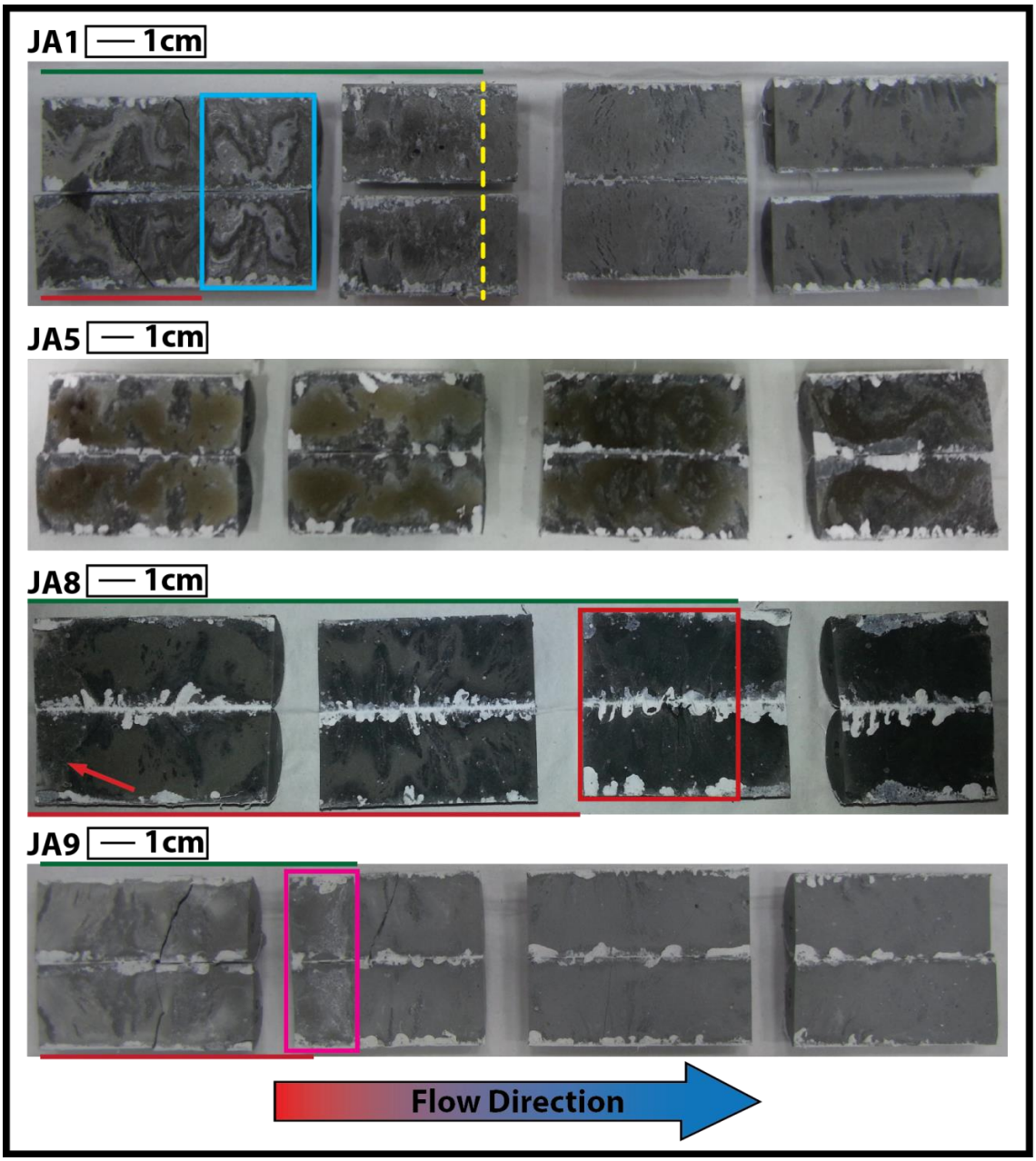

Figure 3.11 – Both fracture halves for the 4 constant pressure differential experiments. Flow is from left to right. Colored boxes, lines, and red arrow indicate location of interest discussed in the text.

JA1-Frank1 has a distinct reacted channel at the inlet, similar the reaction patterns observed in the constant flow rate experiments. A distinct secondary white mineral

precipitate is highlighted in the blue box and appears to be located within a previously developed reacted channel. Precipitation within a reacted channel does not occur on other samples and could have occurred because the upstream pressure was raised several times, which resulted in short surges of new acid into the fracture. Secondary precipitate also occurs in the second core but it is distributed across the entire surface. The yellow dashed line indicates a sharp boundary beyond which no precipitate is visible. Thereafter the fracture surface has a texture that is indicative of reaction with fluid that has dissolved away some cement material (either from carbonic acid or distilled water).

Similar to the constant flow rate experiments, each core section in JA5-Frank2 has a distinct reacted channel. The formation of reaction patterns similar to those observed in single cores across the entire composite core suggests the narrow cross over sections between individual cores do not impart significantly different behavior to the overall sample. There is significant narrowing of the reacted channel toward the outlet. Evidence for a reacted channel down the entire length of the sample corroborates the flow rate data that indicated breakthrough of the precipitation front before the system could completely seal.

In sample JA8-Frank4, the observed reaction pattern is more complicated. The reacted zone propagates into most of the second core and minor secondary mineral precipitation is indicated by white material near the inlet of the first core (red arrow) and across the surface of the third core (red box).

Sample JA9-Frank3 is overall lighter in color because the sample is dry when the photograph is taken. Some minor reaction occurs across the first core. In the second core, a distinct band of precipitation crosses the core and is highlighted by the magenta box. Beyond this band there is no evidence for reactive fluid injection and only evidence for minor dissolution upstream of the precipitation zone.

3.4. DISCUSSION

3.4.1. Discussion of experiment results

3.4.1.1. Constant flow rate experiments

The processes of combined leaching and precipitation that are observed in the constant flow rate experiments with CO_2-saturated water reported here are similar to the ones identified in our previous work with analog systems using HCl (Huerta et al., 2013) and similar to current understanding of the system (Kutchko et al., 2007; Mason et al., 2013). In the current experiments a distinct but broader reacted channel develops on the fracture surface. The reacted channel is calcium-depleted and relatively enriched in silicon. This matches observations from both the reacted surface of the analog experiments (Huerta et al., 2013), what occurs in diffusion experiments (Kutchko et al., 2008, 2007), and in short core experiments (Mason et al., 2013). Absence of aluminum in the effluent and growing iron concentration with time of all experiments supports the conceptual model of (Mason et al., 2013) in which the amorphous zone iron-rich calcium-aluminate phases are dissolved, freeing the iron but trapping the aluminum into a zeolite phase. Not only does silicon remain on the reacted surface but the silicon-rich solid phases also are relatively insoluble. When plotted versus total CO_2 injected effluent silicon (Figure 3.2 – top right) is nearly identical in all experiments and with a progression that shows slower flow allows more diffusion of silicon into fluid phase. The presence of the remaining silicon as solid phases and their nearly insoluble nature explains why no significant decrease in differential pressure differential due to increasing aperture is observed.

Despite using natural fractures that impart local aperture variability and thus flow variability, the reaction patterns (e.g. channelization) and effluent histories are very

consistent. Effluent calcium is always the dominant cation, silicon is a minor component, and both iron and aluminum are trace. Lateral flow restrictions and unreacted 'islands' on the fracture surface show that both heterogeneous flow and non-uniform reaction across the sample width is occurring (Wenning et al., 2013). These heterogeneities provide low-velocity regions where local residence time is increased, which allows for favorable precipitation conditions. Unreacted cement, protected by a layer of secondary precipitate, might form geomechanical supports that will resist closure due to stress which seemed not to occur in the short residence time experiments of (Mason et al., 2013).

The constant flow rate experiments do not exhibit the significant increase in pressure differential that was observed in the HCl experiments and was correlated to secondary mineral precipitation. The dissolution reaction is comparable in both HCl and CO2 experiments, where higher acid concentration and residence time enhance reaction on the surface. For example, QB4-3 has the longest residence time, the most reacted texture, and the largest calcium concentration in the effluent. While QB6 has the shortest residence time, there is less visible reaction on the fracture surface, and it features a low calcium concentration in the effluent.

A significant difference between the HCl and CO_2 experiments is how the reaction affects channel development and secondary calcite precipitation. NA7-11 and NA9-3 had similar residence times (4.1 and 5.4 seconds respectively) but almost three times as much CO_2 was injected into NA9-3 which has a much broader reaction pathway. In NA7-11, SEM analysis indicates that the secondary precipitation bounding the reacted channel is dissolving and the reacted channel is growing laterally and is less stable than the HCl experiments. Significant channeling of the flow (NA7-11), the formation of narrow reacted channel zones (NA9-3 and QB6), and precipitation of secondary minerals (QB4-3) are apparently insufficient to cause an increase in the pressure differential during

these experiments. Overall mineral precipitation is less dominant than it was in the analog experiments and is often only well-developed next to where the caulk was located in the fracture (zones of minimal velocity and high local residence time). The suppressed precipitation is caused by the enhanced reaction capacity for the CO_2-saturated water, which acts as a pH buffer that suppresses changes in pH and calcite precipitation. In the HCl system, once the acid is consumed the pH rises and affects mineral solubility to promote precipitation. For example in a HCl system with a pH of 3 the acid concentration is 0.001 M but in a CO_2-saturated water system the CO_2 concentration can be several orders of magnitude larger (1.42 M assuming a 6.3 wt.%$_{CO2}$). With the CO_2 saturated water system, once carbonic acid is consumed the carbonate system adjusts to create more acid and keep minerals insoluble. Enhanced reaction potential occurs because much more CO_2 is present as dissolved species that adjust to produce more carbonic acid as it is consumed reacting with cement, hence the buffering capability. To capture the coupling between fluid flow and reaction, the CO_2 system therefore requires an increase in residence time by extending core length as we have done in the composite cores discussed next.

3.4.1.2. Constant pressure differential experiments

Constant pressure differential experiments clearly show self-limiting behavior caused by precipitation-induced flow restriction. Figure 3.12 shows that in all experiments as CO_2 is injected the sample permeability remains constant for some time before rapidly decreasing until no flow occurs (in all but JA5-Frank2). In fact, after effectively sealing the fracture, two samples (JA1-Frank1 and JA9-Frank3) are able to withstand significantly higher pressure differentials across the sample without reestablishing fluid flow. Precipitation need not occur as a thick uniform band to seal (as

in JA9-Frank3) but needs to only seal sufficient portion of the fracture to prevent flow (JA1-Frank1 and JA8-Frank4). Given sufficient time and diffusion across the precipitate zone a more uniform band would develop, as in the diffusion dominated experiments (Kutchko et al., 2007 and 2008) or what was observed in the field (Carey et al., 2007; Crow et al., 2010). There is a strong correlation between where sealing occurs and residence time. A longer residence time would allow the precipitation band terminating closer to the sample's inlet.

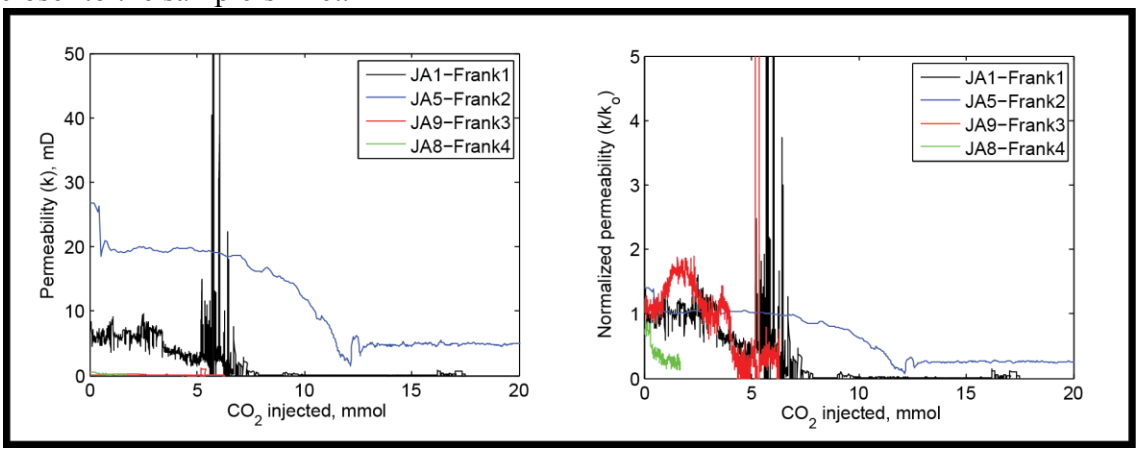

Figure 3.12 – Permeability evolution for constant pressure differential composite core experiments. (Left) Permeability plotted versus total CO_2 injected into the core. (Right) Permeability normalized to initial permeability plotted versus total CO_2 injected into the core.

In the sample (JA5-Frank2) with residence time that was too short (48 seconds) to fully seal the fracture before the precipitation zone was advected out of sample there is still evidence for self-limiting behavior. The experiment still exhibits a reduction in flow rate before breakthrough, which is equivalent to a pressure spike in the constant rate HCl experiments. This experiment's residence time was more than double the constant rate CO_2 experiments, which did not exhibit a pressure differential spike. The post-breakthrough permeability is lower than the initial permeability and the reacted zone is

narrow in the last section of core, which is evidence for lateral restriction in flow also occurring.

3.4.1.3. Coupled reaction and flow mechanisms

While similar to the analog HCl experiments, the experiment results and observations in this chapter are more representative of what would occur in GCS. Thus a discussion of the reactive transport processes is presented. At the beginning of the experiment, where the carbonic acid concentration is high, the reaction of CO_2-saturated water with cement releases calcium and hydroxide ions from dissolution of portlandite and alteration of C-S-H (and reaction with other phases to form the orange amorphous zeolite) and consumes carbonic acid. In front of this reacted zone is a calcite precipitation zone that acts to retard diffusion of acid into the cement. However, as the reaction fronts penetrate deeper into the cement, the process quickly becomes diffusion limited as the ions must diffuse through the remaining amorphous zeolite and low porosity calcium carbonate zone to react with cement and diffuse back out into the fracture channel. And thus the cement's ability to raise pH diminishes with time. This behavior is similar to the diffusion limited boundary condition (Kutchko et al., 2008; Mason et al., 2013).

In lateral zones with small local aperture, fluid flow is slow and residence time is longer. Longer residence time allows more carbonic acid to react with cement phases and the resulting pH increase leads to the precipitation of calcite. The precipitation of calcium carbonate next to the regions of high flow leads to a strong localization of the flow.

Carbonic acid is consumed at the leading tip of the reaction front along the fracture. This leads to a rise in pH relative to the infiltrating fluid and calcium carbonate ions precipitate in the open fracture space. However, once precipitated the calcite becomes immobile and fresh fluid passes over the solid, which will allow subsequent

dissolution and transport of the ions down the fracture. This process generates a zone where calcite is precipitating at the front end, while dissolving at the back end. These zones advance at speeds much slower than the injected fluid speed, hence many fracture volumes of fluid can be injected before precipitation can be sufficient to begin to affect flow rate. Evidence for the precipitation zone is best seen in the magenta box of sample JA9-Frank3 (Figure 3.11), where the precipitate is bound in a discrete interval and followed by the reacted zone. For the constant flow rate experiments, if precipitation is sufficient to close a portion of the fracture, there would be a spike in the pressure differential. However if the fluid flux is too fast the front of calcium and carbonate ions will exit the core before pH is high enough to initiate precipitation. Further calcium release (and pH neutralization) would come by much slower processes, e.g. via diffusion through the reacted channel or through mixing of fluids with lateral slow flow regions. Thus there is a critical length scale or residence time that must be achieved to begin the process of precipitation leading to a pressure differential spike. The ability of the system to buffer the pH and remain below saturation of calcite is also important in these experiments.

Even if a critical length is satisfied under constant flow rate conditions (and assuming pore pressure does not exceed confining pressure) there will come a point where the precipitation zone is advected out of the system. Hence the need to study the condition that is actually present in the subsurface, that of a constant pressure differential driving force. By the time calcite precipitation in the fracture reaches a critical size and begins to restrict fluid flow, diffusive penetration into the sample (behind the precipitation zone) has slowed down. Once plugging begins the flow rate constantly decreases with time and thus injection of CO_2-satuated water slows.

3.5. CONCLUSIONS

Experiments performed using more realistic down hole conditions of pressure, chemistry, flow rate, and residence time were performed to identify coupled reactive transport processes. Chemical reactions were found to be similar to analog acid experiment and previous work presented in the literature. Self-sealing of composite cores under conditions of constant pressure differential was observed as a decrease in the fluid flux for 4 experiments. Because of high buffering capacity of the carbonate system (high CO_2 saturation) precipitation induced channeling was less pronounced in short core, constant rate experiments.

4. Conceptual and empirical leak model

4.1. SUMMARY

The one goal of this dissertation is to develop an understanding of time-dependent wellbore leakage from laboratory experiment observations. Using those observations and other published work a conceptual model of the coupled reactive transport process is developed. An empirical model is then presented that matches experiment observations and applies the behavior to field scale wellbore leakage. Finally, several case studies are presented to highlight the utility of this model.

4.2. DESCRIPTION OF CONCEPTUAL MODEL

A conceptual model is presented that discusses the chemistry, transport, and system couplings that affect time dependent leakage of CO_2 along a well.

Chemical reactions occur when an acidic fluid phase (CO_2-saturated brine) that is introduced at the leak source is out of chemical equilibrium with the initial aqueous and solid phases. Kinetics plays a major role in dissolution/precipitation reactions and must be accounted for when modeling the system. Reactive surface area, mineral solubility, and reaction order for mineral dissolution are important to accurately capture the correct release of ions into the aqueous phase. For example, portlandite is most the soluble component of cement and readily dissolves to release hydroxide ions to neutralize pH. When calcium silicate hydrate (C-S-H) begins to dissolve it does so at a slower rate and via a solid solution change to increasing silicon content (Mainguy et al., 2000). Precipitation of secondary minerals that occurs as a result of super-saturation of dissolved ionic components and the subsequent dissolution of secondary minerals must also be accounted for.

The effect that spatially varying pressure and temperature has on the chemistry must be accounted for. As fluids move from the leak source to an overlying formation temperature and pressures will decrease according to the geothermal gradient, overburden pressure gradient, and pressure differential driving force. Temperature and pressure changes affect reaction rates, aqueous phase equilibrium, and mineral saturation states.

The specific cement formulation and invading fluid composition will affect the reactivity of cement and chemical reactions. For example, in the analog HCl experiments, a small concentration of dissolved CO_2 from exposure to the atmosphere was apparently sufficient to promote calcium carbonate precipitation on the cement factures. However, the concentration was insufficient to actively buffer pH and suppress mineral precipitation as observed in the constant rate carbonic acid experiments. In cements that contain pozzolan (or fly ash), which is a common additive used to reduce cement slurry density, the mechanism and rate of reaction were distinctly different (Kutchko et al., 2009). While the rate of alteration was faster when compared to class H, the petrophysical properties of the altered pozzolan cement were less degraded. The precipitated calcite was more evenly distributed throughout the sample, less calcium leaching occurred, and the permeability remained low. While it had a beneficial effect when considering total wellbore degradation that might not be the case for a leaky well. It is possible that less portlandite is available to release calcium, neutralize acid, and thereby suppressing precipitation in the leak path. This would extend the distance leaking fluid may be able to move along a well. If the sequestration reservoir is a carbonate or has significant carbonate cements buffering of the system to a near neutral pH might already have occurred (Gaus, 2010).

The initial condition should be such that fracture and cement pore fluid is in equilibrium with solid cement phases. The boundary condition for the leak source would

most easily be modeled as a constant concentration flux consisting of the formation brine and dissolved CO_2 species. However, if long-term modeling (tens to hundreds of years) was the goal, the use of a time-evolving boundary condition with fluid chemistry determined from a reactive transport reservoir simulation would be more appropriate.

In the experiments presented in this dissertation the fluid was always a single liquid phase. In the field there is the potential for multiphase leakage along a well. Indeed most leakage models assume multiphase flow (Nordbotten et al., 2005; Viswanathan et al., 2008). This flow can occur either by invasion of free-phase CO_2 at the leak source or by effervescence of CO_2 from the brine as it advects along the wellbore. The latter is unlikely because only a small amount of CO_2 is dissolved in brine and chemical reactions are likely to consume carbonate ions. The former leads to a discussion in multiphase reactive transport that is outside of the focus of this dissertation. The movement of fluid by advection should be via a discrete fracture model (as opposed to an equivalent porous media approximation) that properly captures the effect that local aperture variability imparts on the flow field and solute transport. Even a model based on the approximate cubic equation may not be adequate (Zheng et al., 2008). For example, the parabolic velocity profile assumption typical of flow in parallel plates roughly holds but might break down at local scale (Berkowitz, 2002). On the lab scale aperture anisotropy (Thompson and Brown, 1991), percent of closed fracture surface (Watanabe et al., 2008), and fracture roughness controls fluid flow (Brown, 1987). However, on the field scale flow might be controlled by local discontinuities or jumps in the fracture aperture.

Dispersion is determined in fractures by the Peclet number, which is the ratio of mean solute velocity and molecular diffusion. Mean solute velocity is, in turn, controlled by local aperture. The smaller the Peclet number, the greater the effect of dispersion (Detwiler et al., 2000). Diffusion must be considered for two different cases. The first is

diffusion in the fluid phase in the fracture and the second is the diffusion that occurs into the cement pore fluid. For the former typical Fickian diffusion can be assumed. However, for the latter the diffusion is significantly more complex. Diffusion has been shown to follow non-Fickian behavior due to changes in the cement's structure (Kutchko et al., 2008). As the cement is altered, the reacted zone becomes more porous and permeable (allowing faster diffusion). However, as the carbonation front develops it acts as a barrier that retards diffusion and slows the overall penetration rate into cement.

The coupling phenomena occur when mineral precipitation in the fracture alters the flow field and local residence time. We can define a specific local Damköhler (Da) number that captures the relation between characteristic fluid advection time (or residence time T_{res}) and characteristic chemical reaction time (T_{rxn}). The characteristic reaction rate must account for initial fluid concentration, strength of carbonate buffering, dissolution rate for portlandite and C-S-H, diffusion rate for transport through cement, and reaction rate for precipitation. If the reaction rates are assumed fast then T_{rxn} is principally controlled by how long it takes to diffuse an amount that neutralizes pH sufficiently to promote precipitation. The saturated fluid need not precipitate in place but can be advected into zones with faster local residence time (and thus a Da that would not promote precipitation) and precipitate. This leads to emergent behavior in that the source of precipitation is slow flow mixing zones but is sufficient to seal the fracture (Tartakovsky et al., 2008, 2007).

Simple one dimensional model

A simple one-dimensional model for portlandite dissolution and calcite precipitation/dissolution is presented to illustrate the reactive transport processes occurring in the fracture. The model was developed using PFLOTRAN, a multi-

component reactive transport numerical simulation software (Lichtner et al., 1996). Model parameters are shown on Table 4.1. This model assumes constant fluid flux and upstream pressure boundary conditions. This model also decouples the effect that mineral volume fraction has on local flux rate. In this model CO_2-saturated liquid is injected at constant rate into a sample that originally contains only 0.1 portlandite volume fractions (the system has an inert porosity of 0.5). As the simulation progresses portlandite dissolves and calcite precipitates. This model simulates large Da, hence the sharp reaction fronts. While this model is a simplification of the processes occurring in the laboratory experiments (and what is expected to occur at the field scale), there are some fundamental similarities. These similarities help illustrate the evolution of the system. The system is controlled by the reaction between aqueous and mineral phases in the following reactions. Portlandite will dissolve according to the equation:

$$Ca(OH)_2 + 2H^+ \rightleftarrows Ca^{2+} + 2H_2O \qquad (4.1)$$

Calcite precipitation/dissolution reaction is controlled by the equation:

$$CaCO_3 + H^+ \rightleftarrows Ca^{2+} + HCO_3^- \qquad (4.2)$$

Figure 4.1 shows the mineral volume fractions and Figure 4.2 shows chemical concentrations at four times during the simulation. At time 0 h (blue line) chemical equilibrium between portlandite and initial fluid controls the amount of calcium ions and the pH. No carbonate species are present initially. After 60 hr and 10 pore volumes (red line) of fluid have been injected distinct dissolution/precipitation zones begin to form. Portlandite has dissolved up to 0.2 m from the inlet and calcite is precipitated within a zone from 0.2 m to 0.1 m. Eqn. 4.1 controls the portlandite dissolution as an increase in

the H^+ ions from the injected fluid drives the reaction to dissolve portlandite, neutralize the acid, and liberate calcium ions. The presence of a large concentration of calcium and bicarbonate ions drives Eqn. 4.2 to promote the precipitation of calcite at an intermediate pH. Behind this calcite precipitation zone (upstream of 0.1 m) high acid concentration drives Eqn. 4.2 to redissolve the calcite. Calcium remains low in this zone because portlandite is not present and there is no calcium being injected. At 240 hr the profile has moved down the domain. The width of the precipitation zone has increased from 0.1 m to 0.4 m. By the experiment end (yellow line) portlandite has completely dissolved in the domain and the calcite precipitation zone spans from the end of the domain to 0.8 m. The concentration profiles remain in the respective zones but most of the domain is representative of the injected fluid concentrations.

This high Da numerical experiment illustrates the general trend of behavior occurring in the experiments. The key similarities between laboratory and numerical experiment are the large lag between the tracer front and the calcite precipitation zone, consumption of most of the readily available portlandite required to move the calcite front, growth of the width of the precipitation zone, and that a significant portion of the dissolved CO_2 is consumed during the calcite precipitation.

Table 4.1 – Parameters used in the numerical model.

Chemistry of system					
	Initial concentration, M	Constraint	Inlet concentration, M	Constraint	
Primary					
H^+	1×10^{-8}	Z	1×10^{-2}	Z	
HCO_3^-	5×10^{-4}	M (calcite)	1×10^{-1}	T	
Ca^{2+}	5×10^{-4}	M (portlandite)	1×10^{-10}	T	
Secondary					
OH^-					
CO_3^{2-}					
Gas species					
CO_2					
Minerals	Initial fracture volume				Reaction rate constant, $molcm^{-2}s^{-1}$
Calcite	0.0				5×10^{-1}
Portlandite	0.1				7×10^{-1}

Geometry of system	
Length, m	1×10^{0}
x-dir. grids	300
Width, m	1×10^{-1}
y-dir. grids	1
Height, m	1×10^{-1}
z-dir. grids	1
Diffusion coefficient, m^2s^{-1}	1×10^{-8}
Porosity, -	0.5
Permeability, m^2	1×10^{-12}
Flux, ms^{-1}	2.3139×10^{-5}

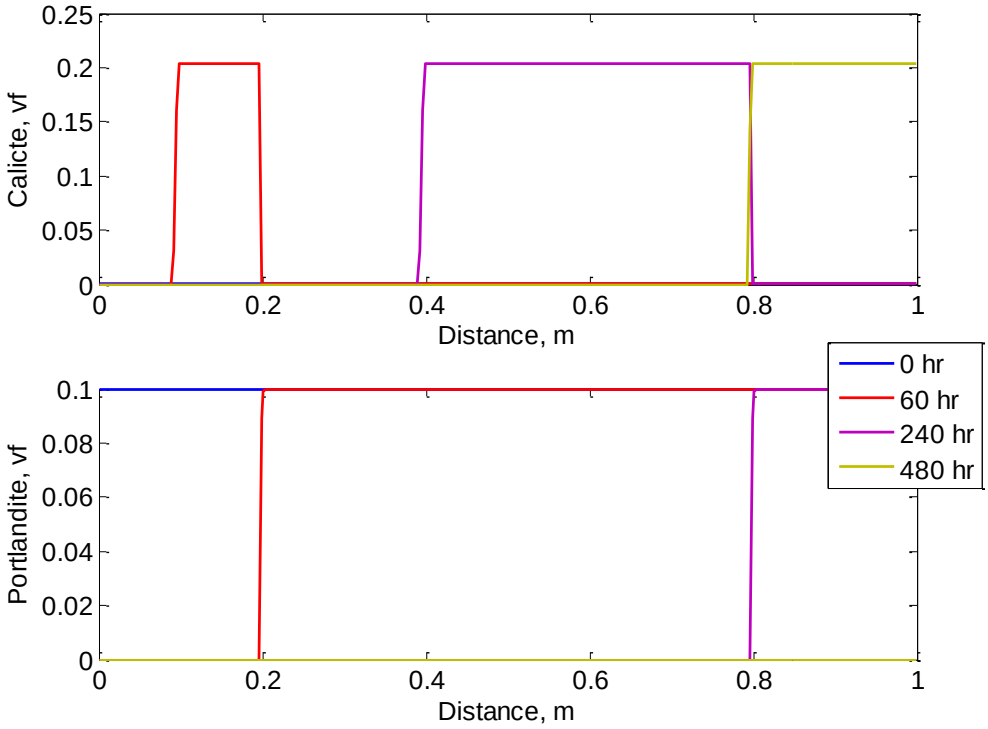

Figure 4.1 – Numerical simulation results showing mineral volume fraction (vf) at four times. As injection progresses portlandite (lower panel) is dissolved and calcite (upper panel) precipitates directly behind it. Calcite then dissolves when the immobile mineral reacts with fresh acid advecting over it.

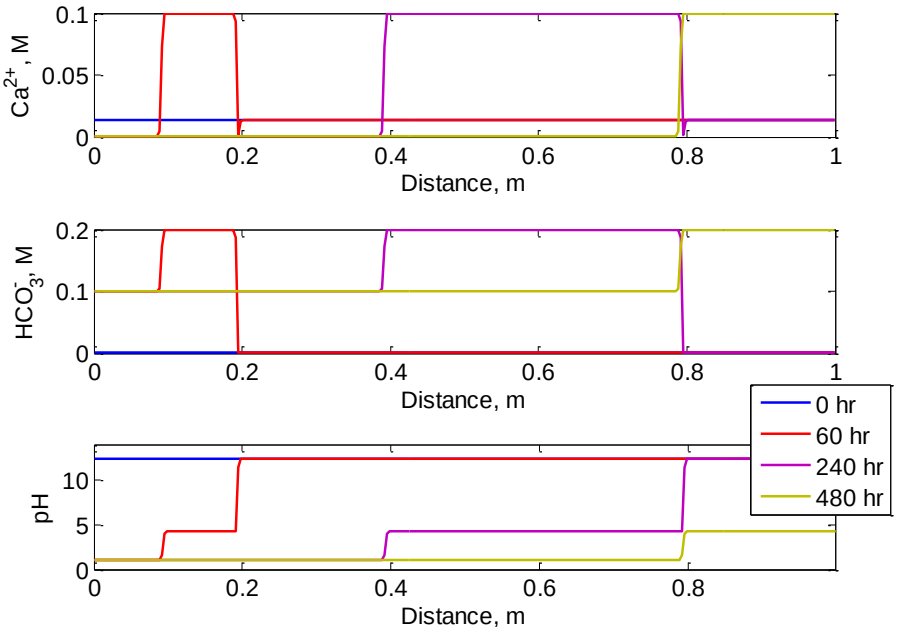

Figure 4.2 – Numerical simulation results showing profiles of calcium ion concentration, bicarbonate concentration, and pH at four times. The concentrations and pH are driven by the presence of portlandite initially, by the concentration of calcium and bicarbonate in the intermediate zone where calcite has precipitated, and finally by the injected acid concentration.

Several distinctions between this simple numerical model and the experiments must be emphasized. Decoupling the mineral volume fraction (and porosity) from the fluid flux misses two different effects depending on the driving force. For constant flow rate experiments, a smaller porosity (due to mineral volume fraction increase) would increase local velocity and reduce Da. This would slow the precipitation and dissolution of the calcite zone and reduce the rate at which the zone advances. For constant pressure differential driving force, a reduction in fracture volume would reduce total flux across the sample and increase Da. This effect is seen in the laboratory experiments when, as the system seals, an increasingly longer time is required to inject a given volume of fluid.

Thus the simple numerical model does not match the actual system because the simulation shows that the precipitation zone advances and grows in constant proportion to time and fluid volume. Finally, the numerical model assumes a finite quantity of portlandite that is immediately available to react. This assumption is incorrect for the following reasons. First the numerical model contains no C-S-H or other less soluble cement phases that would continue to react with the acid after portlandite has been consumed. Additionally, the amorphous silicate material remains behind and acts as a diffusive barrier for further reaction with fresh cement.

Taking the insights from the simple numerical experiments with observations from the laboratory experiments a conceptual model for fracture sealing can be developed. Figure 4.3 shows an illustration of the model for three times.

Time t=1 represents very early time behavior. At this time the injected fluid displaces the initial fluid along a fluid front (black dashed line). and the calcite precipitation front (green dashed line) and calcite dissolution front (red dashed line) have not significantly separated. The only difference between the initial fluid and the injected fluid downstream of the calcite precipitation front is the presence of a very small amount of bicarbonate remaining in equilibrium with portlandite. At the precipitation front portlandite dissolves and drives the system to release calcium ions while neutralizing pH (Eqn. 4.1). In the presence of the liberated calcium and the injected bicarbonate, the system is driven to precipitate calcite (Eqn. 4.2) but because a sufficient quantity of calcite has not precipitated the zone is small. Upstream of the dissolution front the cement has been reacted such that further reaction becomes diffusion limited (black arrows moving from the fracture channel into the cement matrix).

At time t=2 the injected fluid has traversed the entire domain and the precipitation zone has moved downstream along the fracture. In this zone calcite is precipitating at the

front end due to the release of calcium from portlandite in the presence of high bicarbonate concentration. At the calcite dissolution front (red dashed line), fresh acid drives calcite dissolution and advects the dissolved ionic species downstream along the fracture. The precipitation zone has grown principally in width but also some height.

At t=3 calcite has precipitated in sufficient lateral width and also in height to almost seal the open fracture. Since the driving force is constant pressure differential this decrease in permeability reduces fluid flux. The reduced fluid flux increases Da and residence time which promotes further precipitation. In addition, the time required to inject a given volume of fluid (and move the precipitation zone) would increase as the fracture closes. This feedback makes the flow self-sealing.

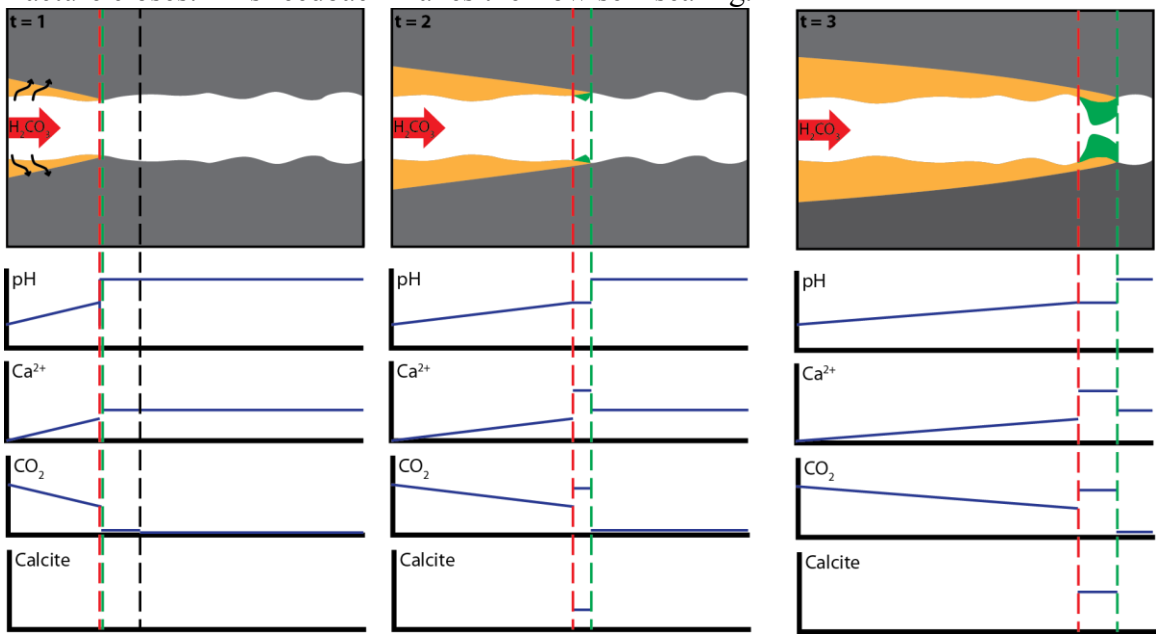

Figure 4.3 – Conceptual model for fracture sealing by mineral precipitation driven by dissolved CO_2.

This conceptual model captures much of the relevant process but a simple one-dimensional model cannot fully account for the true complexity. In the laboratory experiments the flow field was heterogeneous (irregular, branching paths within the

fracture) and lateral slow flow zones (from a main flow channel across a reacted zone into an unreacted zone) with longer residence time were observed. Reaction in the fracture probably violates the local equilibrium assumption because of kinetically limited reactions and reactive surface area constraints. If the calcite precipitation reaction was slower than the dissolution reactions, higher residence time will be needed to promote precipitation. Thus the concept of a precipitation zone should be thought of as an average of a low Da in the main flow channels and higher Da regions (with small local aperture) that allow precipitation. For constant pressure differential driving force, once restriction in flow begins in part of the fracture the entire domain's Da increases and precipitation becomes favored, which leads to self-sealing.

4.3. SIMPLE LEAK EVOLUTION MODEL

This section presents a simple empirical model that captures key aspects of the coupling between transport and reaction that were identified in laboratory experiments and projects them to estimate leakage at the field scale. An advantage of this empirical model is its modular derivation and analytic solution. It does not require complex reactive transport numerical simulations, which would have difficulties with the large scale difference between the micron size fractures and the leak path, which can be hundreds of meters. This model is useful for field-scale risk assessment to forecast a range of leakage behavior. The modular nature of the model can be utilized to improve the model with additional experiments that further constrain the model parameters. The full derivation of this model is presented in Appendix D.

4.3.1. Description of model

The model assumes one-dimensional flow of a single incompressible isothermal phase. The model uses the flux version of Darcy's equation (Eqn. 4.3) and relates

permeability to aperture by using the equivalent fracture permeability (Eqn. 4.4), which normalizes for the fracture area perpendicular to the flow direction.

$$q=\bar{k}\frac{\Delta P}{\mu L} \qquad (4.3)$$

$$k=\frac{B^2}{12} \qquad (4.4)$$

Figure 4.4 shows a schematic of the model at two time steps. The model defines a fluid (or salinity) front (x_f) which advances with time at the speed of the injected fluid. Behind this front is a precipitation front (x_p) and dissolution front (x_d) that move at a speed proportional to x_f. The proportionality constants are retardation factors α and β respectively. As the three fronts advance, the precipitation zone between the precipitation and dissolution front grows. To model the precipitation/dissolution and fracture sealing process the concept of flow in series (Bear, 1972) for three zones is used. The first 'minimally altered' zone (Zone 0) lies between x_f and x_p and has the initial permeability (k_0) of the leak path. The second 'precipitation' zone (Zone 1) lies between x_p and x_d and has permeability (k_1) that is less than the initial permeability. The final 'reacted' zone (Zone 2) comes after x_d and had a permeability of k_2.

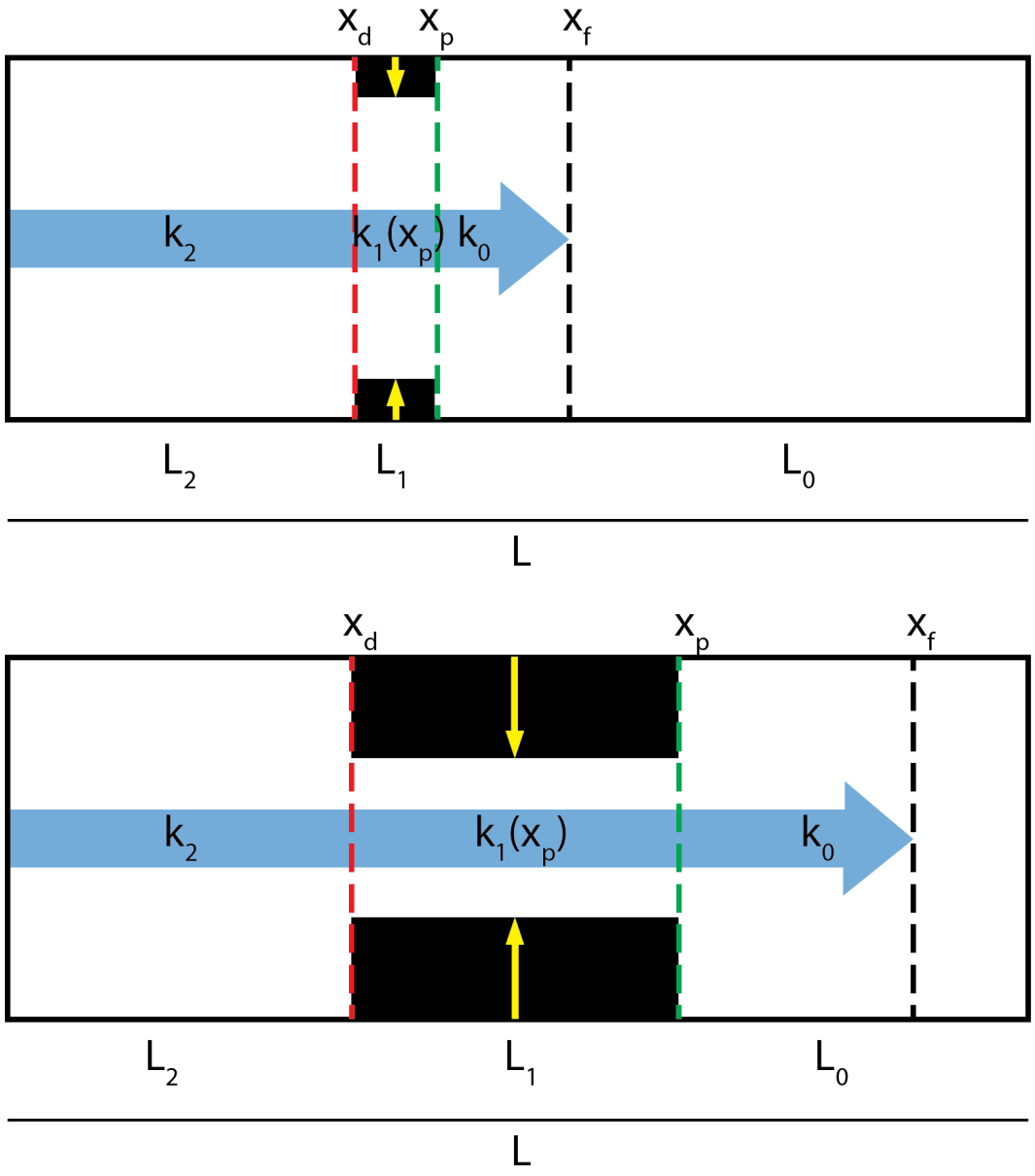

Figure 4.4 – Illustration showing relation between front positions, zones, and lengths in the model. Zone 0 is between the fluid front and the precipitation front and has the same permeability of the pathway before acidic fluid was injected. Zone 1 is between the precipitation front and the dissolution front and has a permeability that evolves as the precipitation front moves along the length. Zone 2 is between the dissolution front and the inlet of the pathway. Evolution of this pathway for two time steps (upper and lower panels) is shown.

An important postulation in this model is that permeability in the precipitation zone decreases as additional fluid is injected and precipitate accumulates. To match the experiment results it is insufficient that the precipitation zone simply grows in width and has constant permeability. A constant k_1 would result in an immediate asymptotic decay of average permeability which contradicts experiment observations (see Appendix D for analysis).

The choice of a logistic function to describe k_1 evolution is favored because it is consistent with two experiment observations (Figure 4.5). The first observation is that average permeability remains constant for a significant amount of time and fluid injected. The second observation is that once average permeability begins to decrease there is a sharp and asymptotic decay to low permeability. After defining relations to get all distances in terms of x_f and solving the differential equation (See Appendix D) the following equation describes the time evolution of a fluid front.

$$t = \frac{1}{F}\left[Ix_f + \frac{M}{2}x_f^2 + \frac{(\alpha-\beta)}{k_o}\left[\frac{x_f^2}{2} + \left(\frac{a}{b^2\alpha^2}\right)e^{b\alpha x_f}\left(b\alpha x_f - 1\right) + \left(\frac{a}{b^2\alpha^2}\right)\right]\right] \qquad (4.5)$$

The constants F, I, and M are lumping parameters defined as:

$$F = \frac{\Delta P}{\mu} \qquad (4.6)$$

$$I = \frac{L}{k_0} \qquad (4.7)$$

$$M = \frac{(\beta k_0 - \alpha k_2)}{k_0 k_2} \qquad (4.8)$$

Other parameters, like precipitation zone permeability, average permeability, and front locations, can be solved for based on fluid front position.

$$k_1 = \frac{k_0}{1+ae^{b\alpha x_f}} \qquad (4.9)$$

$$\bar{k} = \frac{L}{\frac{L-\alpha x_f}{k_0} + \frac{(\alpha-\beta)x_f}{k_1} + \frac{\beta x_f}{k_2}} \qquad (4.10)$$

$$x_p = \alpha x_f \qquad (4.11)$$

$$x_d = \beta x_f \qquad (4.12)$$

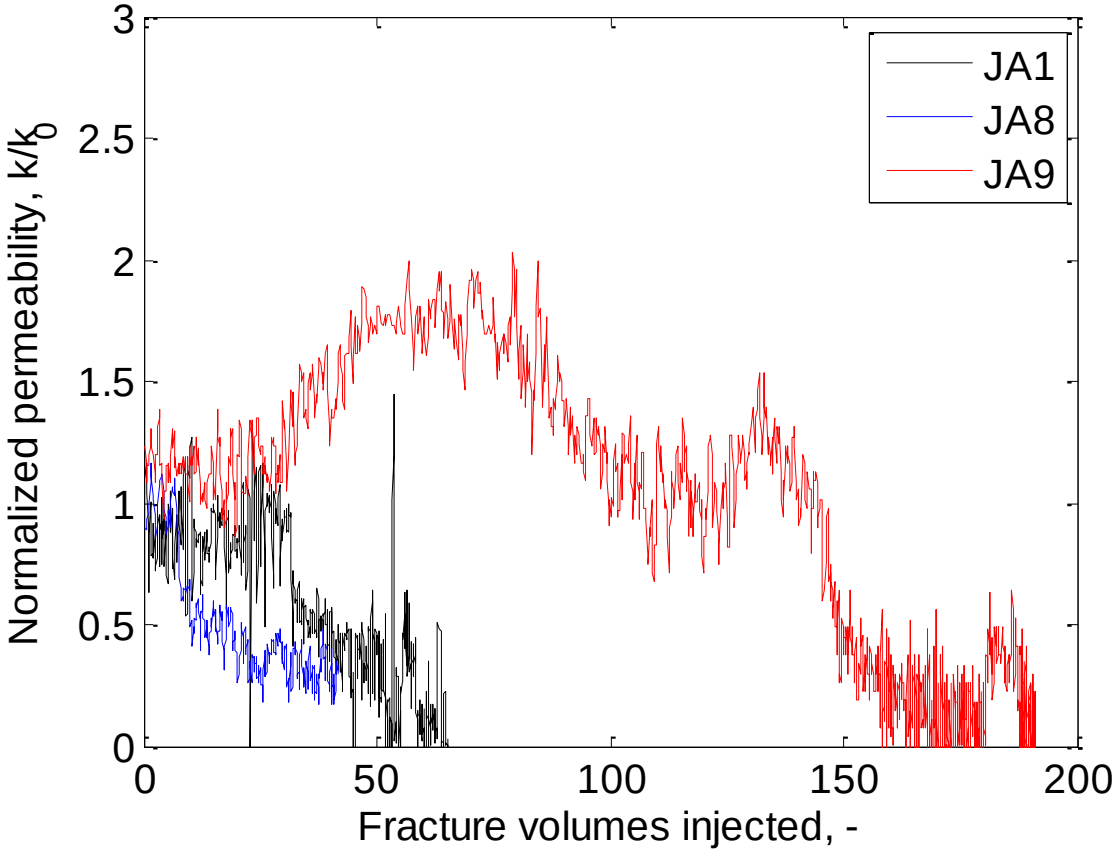

Figure 4.5 – Normalized permeability versus fracture volumes injected.

4.3.2. Application to experiments

The model is applied to three constant pressure differential experiments to test the quality of the model fit, determine the magnitude of parameters to use in the well scale model, and attempt to infer a physical interpretation of fitting parameters.

4.3.2.1. Model parameters

Table 4.2 shows parameters determined from experiments that are used in the model. Sample length was measured for the composite core and the entire width of the core sample (1 inch) was used. Initial pressure differential and flow rate were determined from the initial stable values. Initial hydraulic aperture was calculated using from Eqn. 4.13 and related to permeability using Eqn. 4.4.

$$B = \left(\frac{12\mu QL}{W\left(P_{in} - P_{out}\right)} \right)^{1/3} \qquad (4.13)$$

Dead volume was estimated at 6.872 mL and accounted for in these experiments. Fracture volumes injected is calculated as the total volume of fluid injected during the experiment interval divided by the initial fracture volume. Dividing fracture volume injected by the fracture cross-section (the product of aperture and fracture width) gives the position of the fluid front (x_f) of the model. The retardation factors (α and β) were calculated from the ratio of the precipitation and dissolution front length divided by the fluid front length respectively. To determine the length of the precipitation zone, the linear distance from the core inlet to the extent of precipitation was measured. This extent is shown on Figure 4.6 as a green line at the top of the image of each core. The length of the dissolution zone was determined as the location where the well-developed reaction channel ended and precipitation began. The red line below the image of each sample on

Figure 4.6 shows the location. Note that the gap between cores was not included in the length.

For this analysis I assume k_2 is equal to k_0, although there is evidence that k_2 is typically less than k_0 (e.g. experiment JA5-Frank2 and most HCl experiments that show final permeability lower than initial). However, without data from a breakthrough an estimate of k_2 is pure conjecture and in any case assuming $k_2 = k_0$ yields a more aggressive leakage estimates.

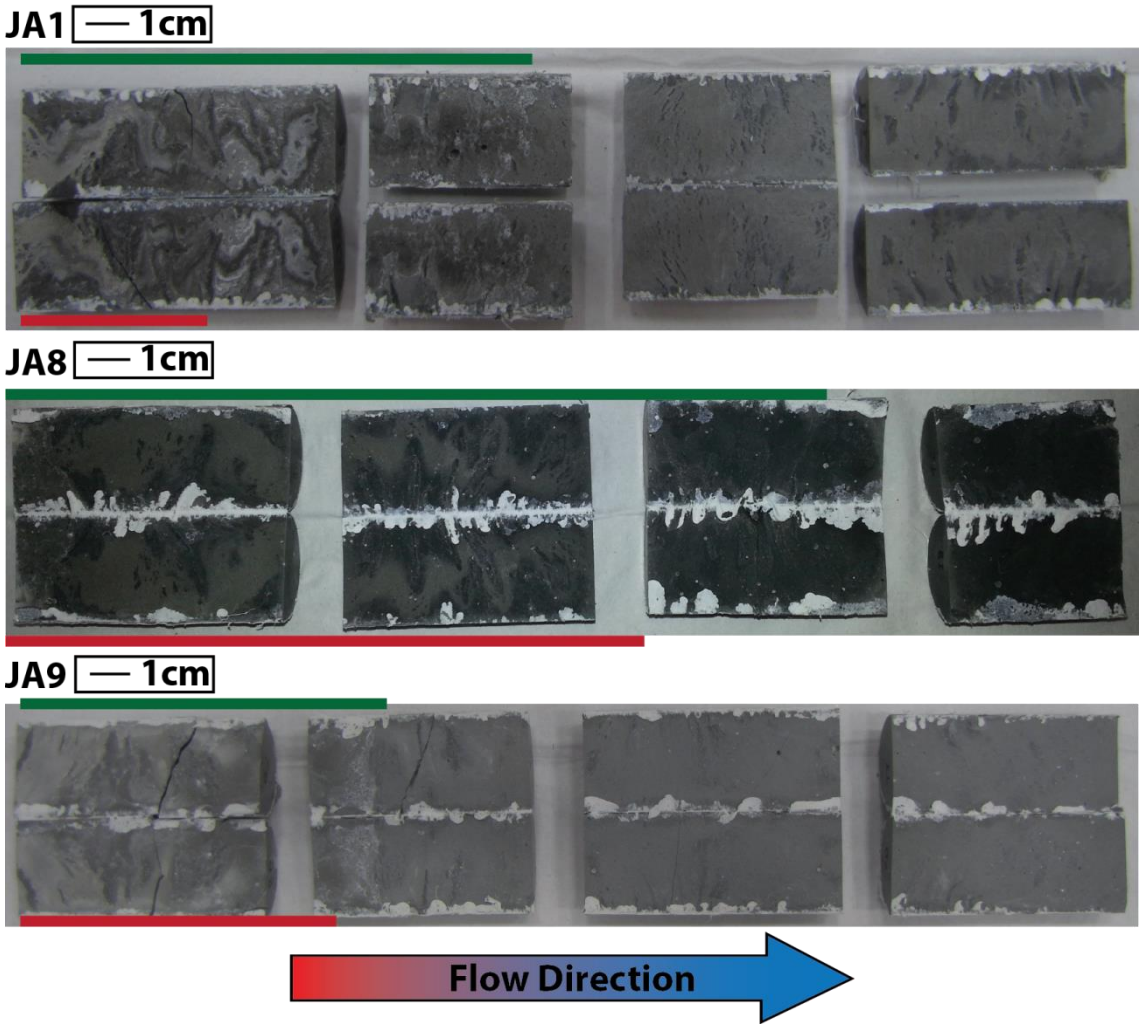

Figure 4.6 – Constant pressure differential composite core experiment fracture surfaces. Green line shows where x_p was measured to red line shows where x_d was measured to. Note the space in between cores was not included in the length measurement.

Figure 4.7 shows the behavior of the logistic function for different a and b values. The a parameter is unit-less and controls the onset of permeability reduction in the precipitation zone. A smaller a yields longer volume injected before sealing initiates. The parameter b has units of inverse length and affects how quickly permeability decreases once it begins to affect system. A larger b yields a sharper permeability decrease. Thus

the *a* and *b* parameters are chosen to match the experiments and then used to predict behavior at the field scale.

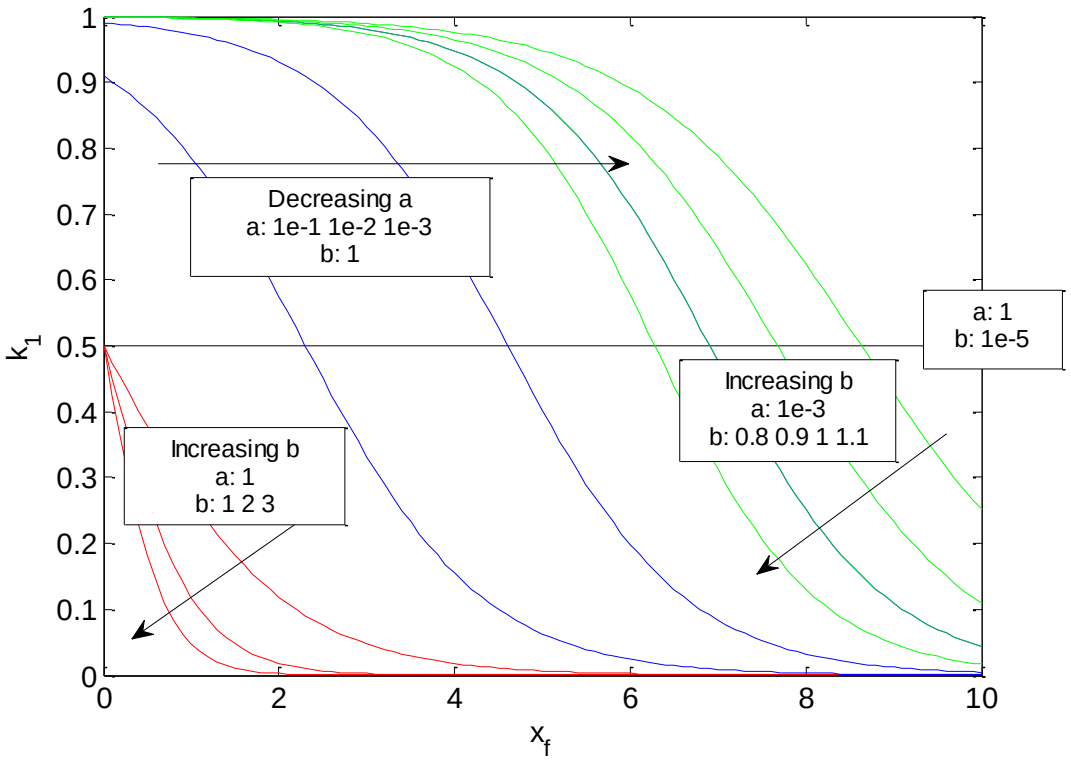

Figure 4.7 – Behavior of the logistic function (Eqn. 4.9) for several different *a* and *b* values.

4.3.2.2. Results for each experiment

Sample JA1-Frank1 is used to illustrate the curve fitting process. The goal of curve fitting is to provide a model that matches the experiment data for a given set of input parameters (*a* and *b*). On Figure 4.8 is the experiment data (black) and model (red) plotted versus fracture volumes injected and versus time. Determining measures that quantify the goodness of fit between model and data is not trivial. The experiments produce a set of three data (time, volume injected, and effective fracture permeability - which is calculated from measured pressure differential and flow rate at each time). The

model is highly sensitive to changes in the values of *a* and *b*. For example, a small change in *b* for a given value of *a* has an exponential effect on the timescale of the model. Because the model treats time as a function of fluid front position, forcing the model time interval (from beginning to end of flow) to match the measured time interval (duration of the flow experiment) is an important means of constraining the value of *a*. This is done by minimizing the t_{err}, the error between experiment and model end time. The equation is:

$$t_{err} = \left| t_{model}^{end} - t_{data}^{end} \right| \qquad (4.14)$$

With time constrained, adjusting *a* and *b* to minimize the mismatch between volume injected and permeability based on a minimization scheme such as an l^2-norm of the residual between model and data would seem attractive, this equation is:

$$k_{norm} = \sqrt{\sum \left(k_{model} - k_{data} \right)^2} \qquad (4.15)$$

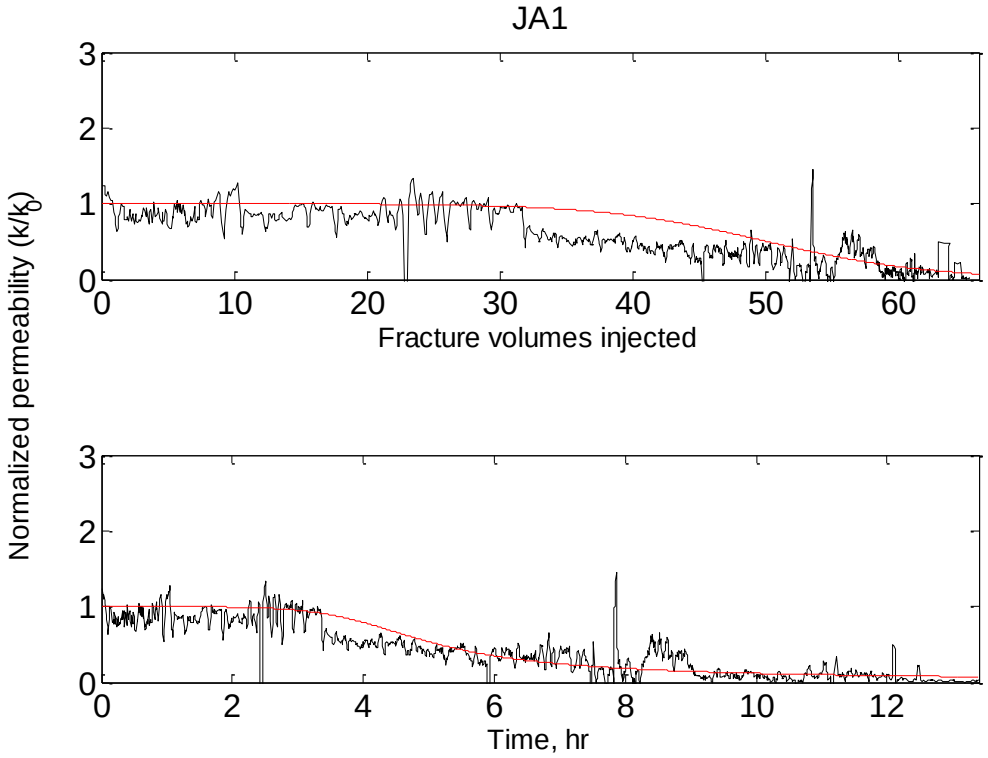

Figure 4.8 –Plot of data (black) and model (red) as a function of fracture volumes injected (top) and time (bottom). In this plot $a = 4 \times 10^{-3}$ and $b = 1.266$ cm^{-1}.

Figure 4.9 shows contour plots for t_{err} (top) and k_{norm} (bottom) for a range of a and b values. The shape of the contour plots for t_{err} and k_{norm} do not coincide and a good fit is not necessarily the one with the lowest t_{err} and k_{norm}. The colored dots represent four example fits where t_{err} is minimized. On the bottom plot the dots do not coincide with a minimized k_{norm}. To further illustrate this point, the colored dots are plotted on Figure 4.10 and show the model fit versus the experiment data. When a is large the model has an exponential decay that flattens to a non-zero permeability and cannot accurately model the experiment's decay in permeability toward zero. When b is larger the model over

estimates time and volume required to match permeability evolution. Visual 'best fits' are used to estimate parameters for the experiments.

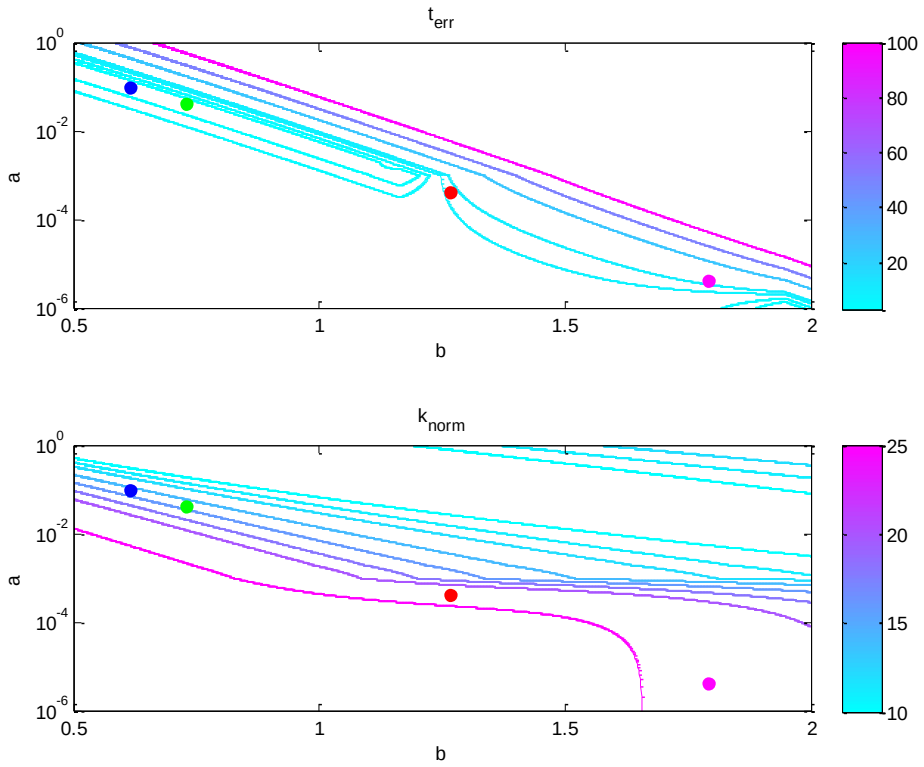

Figure 4.9 – (Top) Plot of error measure t_{err} for a range of a and b values; t_{err} units are in hour. (Bottom) Plot of k_{norm} for a range of a and b values. The colored points are select a and b values that minimize t_{err} but as shown in the bottom plot do not minimize k_{norm}.

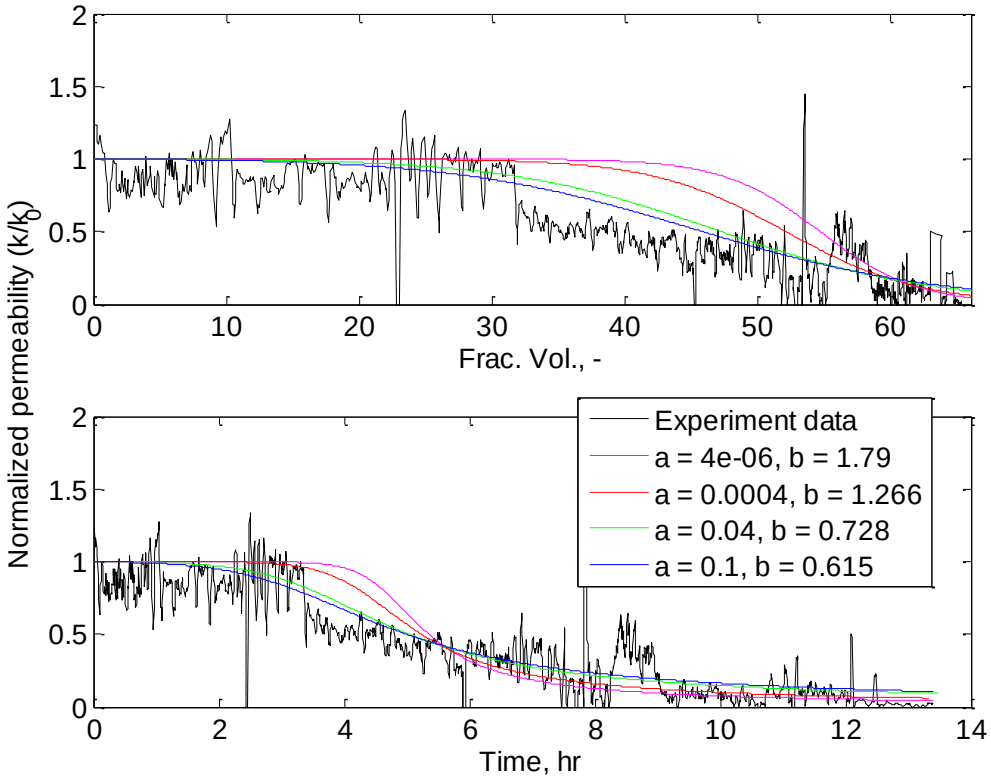

Figure 4.10 – Plot of four minimized t_{err} fits for different a and b values. Colors match dots on Figure 4.9.

For JA1-Frank1 the best fit parameters are $a = 4 \times 10^{-3}$ and $b = 1.266$ cm^{-1} (Figure 4.8). These parameters produce a model curve that matches early time behavior well but overestimated time and fluid volume required to initiate core sealing. The curve also slightly overestimates permeability toward experiment end but overall provides a good match.

Figure 4.11 shows experiment data and best model fit for sample JA8-Frank4. The fitting parameters are $a = 1 \times 10^{-1}$ and $b = 0.4$ cm^{-1}. This experiment ran for a very short time and the amount of fluid injected and did not have a long time period of constant permeability that is characteristic of other experiments. Figure 4.12 shows

experiment data and best model fit for sample JA9-Frank3. The fitting parameters are a = 2.0×10^{-3} and b = 1.55 cm^{-1}.

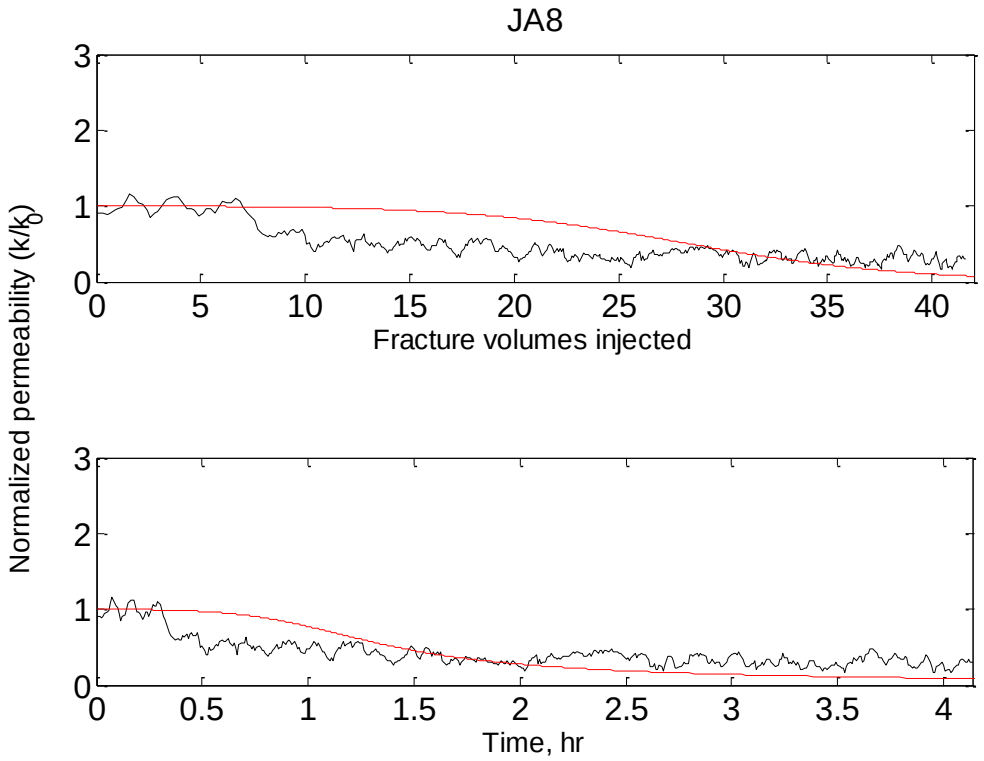

Figure 4.11 – Plot of data (black) and model (red) as a function of fracture volumes injected on top and time on the bottom graph. In this plot a = 1×10^{-1} and b = 0.4 cm^{-1}.

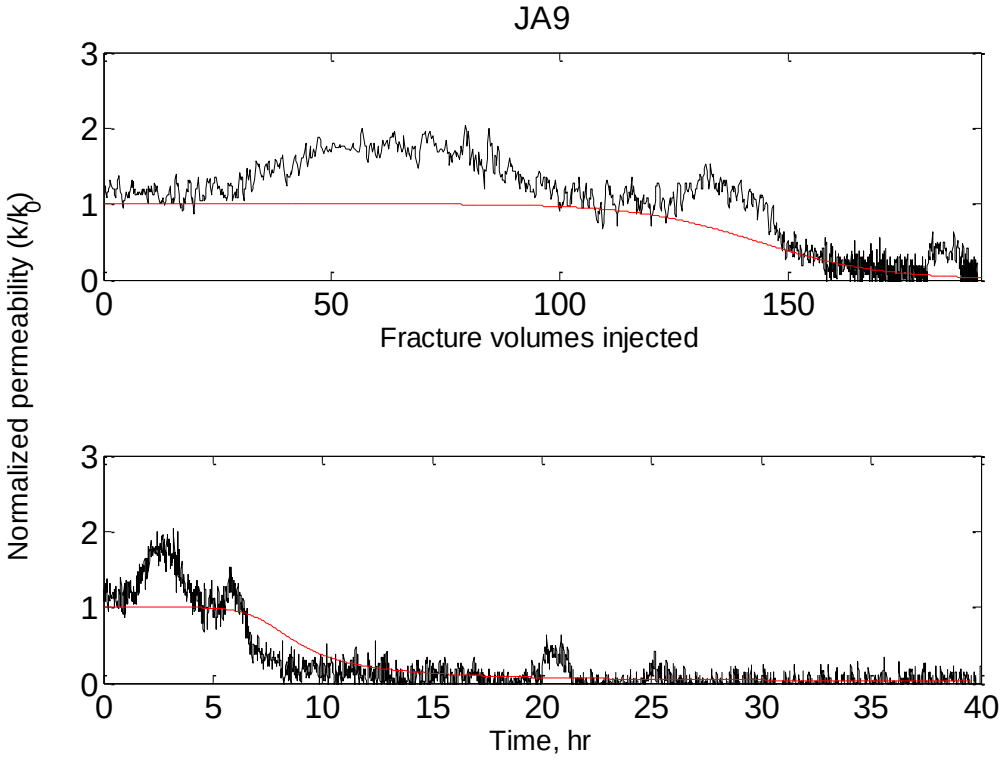

Figure 4.12 – Plot of data (black) and model (red) as a function of fracture volumes injected on top and time on the bottom graph. In this plot $a = 2 \times 10^{-3}$ and $b = 1.55$ cm^{-1}.

Table 4.2 – Parameters used in model.

	JA1-Frank1	JA8-Frank4	JA9-Frank3
Length, cm	23.4	21.9	24.38
Width, cm	2.54	2.54	2.54
Pressure differential, psi	2.0	21.3	55.1
Initial flow rate, mL/min	0.011	0.011	0.006
Initial hydraulic aperture, μm	12	5.06	3
Initial equivalent fracture permeability, D	12	2.1	0.75
Time, hr	21.8	4.14	42.18
Fracture volumes, -	91	42	188
Viscosity, Pa-s	0.001	0.001	0.001
α term	6.1×10^{-3}	1.8×10^{-2}	1.8×10^{-3}
β term	2.2×10^{-3}	1.4×10^{-2}	1.6×10^{-3}
Best fit parameters			
a	4×10^{-3}	1×10^{-1}	2×10^{-3}
***b*, cm^{-1}**	1.266	0.4	1.55

4.3.2.3. Discussion of experiment curve fitting results

All 3 experiments show evidence for sealing soon after the CO_2-saturated water reaches the core face (after passing through the dead volume). No simple correlation to an experiment parameter (flow rate, pressure differential, initial aperture size, etc.) was identified. JA9-Frank3 had the smallest aperture and took the most fracture volumes injected (150) before the permeability began to decrease, while the other two samples took between 10 and 40 fracture volumes before showing a permeability decrease. In sample JA8-Frank4 the experiment is not well fit with the logistic type behavior (permeability constant for some time followed by an asymptotic decay) but the permeability evolution does seem to match a shallow exponential decay. This behavior could be because the confining system was already leaking into the pore fluid system or it could be that the α and β parameters were not properly identified. Indeed on JA8-Frank4

there is not a distinct zone of precipitation as in other samples (Figure 4.6). More experiments are needed to determine the nature of the *a* and *b* parameters and how they relate to experiment parameters.

4.4. ESTIMATION OF FIELD SCALE LEAKAGE

Some examples of how the model developed above is useful for risk assessment are presented. For these examples the case of a single leaking well is studied. First the parameters determined for the three experiments are applied to field scale geometry and driving force to observe the evolution of the leak path. Next individual parameters are adjusted to predict how this affects amount of fluid leaked (or how far fluid travels up leak) and timescale to leak.

4.4.1. Geometry of system

The parameters needed to implement the well leak model on the field scale are described below and shown on Figure 4.13.

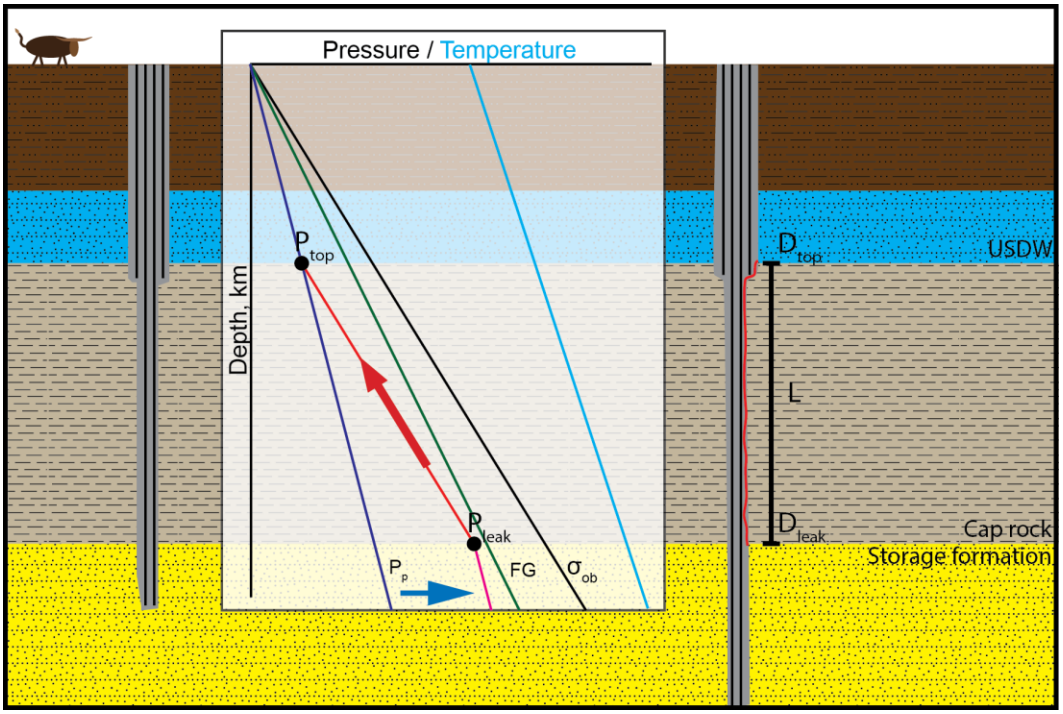

Figure 4.13 – Subsurface leakage scenario for a single leaking well.

The leaking well is assumed to have a leak source depth (D_{leak}) at the top of the storage formation. Fluid exits the top of the leaky well at a vital asset (e.g. USDW or oil/gas reservoir) of some depth (D_{top}). The leakage path length is the difference between these two depths:

$$L = D_{leak} - D_{top} \qquad (4.16)$$

Pressure differential is the driving force for fluid flux and is the difference in pressure from the leak source (P_{leak}) to the pressure of an overlying formation (P_{top}).

The pressure differential is then:

$$\Delta P = \left(P_{leak} - P_{top}\right) \qquad (4.17)$$

Fluid pressure at the leak source will be determined by the injection history of the GCS operation and is assumed constant in this study. To prevent fracturing, the maximum injection pressure will be significantly less than the overburden (σ_{ob}) pressure (Figure 4.13 – black line). Overburden gradient is assumed to be 1.0 psi/ft. An engineering factor (0.8 for this scenario) is used to reduce the allowed injection pressure below the overburden gradient because the least principal stress is the actual limiting condition for formation fracture initiation (Figure 4.13 – green line). Pressure at the leak top is determined by a freshwater hydrostatic gradient (0.45 psi/ft) and depth of the leak top. Table 4.3 shows the parameters of the well that are used in the case studies below.

4.4.2. Single well leak using experiment parameters

The model of the permeability evolution described above for the experiments is applied to this wellbore leakage path by setting the fracture length to the leakage path length and the pressure gradient to that of the leakage scenario. Parameters from modeling each experiment (Table 4.2) (fracture aperture, a b α and β) were applied to the extended length and lower pressure differential of the wellbore scenario. The no reaction residence time (Table 4.3) refers to the time it would take for brine to move from the leak source to the leak top if there were no dissolution or precipitation reactions, i.e. no change in the permeability of the leakage path. Figure 4.14 shows plots of the fluid front (x_f) moving from the leak source for 1 year. If no reactions occurred, a leakage pathway having the same aperture as sample JA1 would allow brine to reach the leak top in 109 days (black dashed line). Accounting for precipitation induced permeability evolution, the fluid front position reaches about 25 m within three days and then moves very slowly (solid black line). This indicates that the leak is essentially sealed, as the black line remains horizontal on the longer time scale in the right-hand plot. Leakage paths with

parameters corresponding to experiments JA8 and JA9 would also seal before 100 days of leakage of CO_2-saturated brine. While this study uses a limited number of experiments the observation that the wells tend to seal quickly and near the leak is a characteristic feature of the system. Accounting for this behavior is important for improving risk assessment of wellbore leakage.

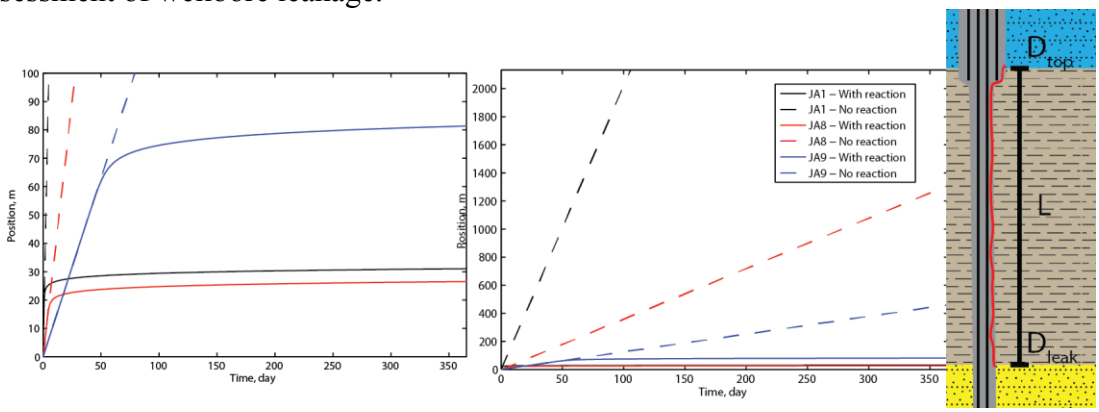

Figure 4.14 – Wellbore leakage predictions for one year using parameters from the three experiments. Lines represent fluid front (x_f) as a function of time. Dashed lines represent the no reaction leakage front and solid lines represent leakage with precipitation induced sealing. Left plot is a zoomed in graph of the early time behavior.

Table 4.3 – Parameters for single leak.

Leak top (D_{top}), ft	1,000
Leak top pressure (P_{top}), psi	250
Leak source (D_{leak}), ft	8,000
Leak source pressure (P_{leak}), psi	6,400
Pressure gradient, psi/ft	0.85
No reaction residence time, day	
JA1	106
JA8	594
JA9	1,690

4.4.3. Single well leak varying individual parameters

It is useful to perform a simple parameter study to identify and discuss the conditions that might lead to a leaky well. This parameter study uses the JA8 experiment as a basis.

The first parameter varied was the initial aperture, which is increased from 5.06 μm to 10 μm. The result of varying this parameter was that the leak sealed much faster. Precipitation began to affect the pathway permeability after 5 days in the base case and after 2 days with the larger aperture. A larger initial permeability reduces the time required to move a given distance for the same pressure differential driving force.

Next, the retardation factors (α and β) were reduced by 50%. The result was that the fluid traveled twice the distance before beginning to seal. If the retardation factors were reduced by two orders of magnitude the fluid front would reach the leak top at 1,272 days but would be well on the way to shutting off flow so no CO_2-saturated brine would leave the leak and the well would still become self-sealing.

The next parameter that was varied is the *a* term in the logistic function. This parameter controls the onset of permeability decrease in the precipitation zone. Reducing a by 10 orders of magnitude had a correspondingly small effect on the leakage. The leak travelled along the same path as the base case and began sealing at two weeks and 50 m up the leak path. Altering the *a* parameter created behavior similar to varying the retardation factors.

The final parameter that was varied is the *b* term in the logistic function. A reduction in *b* by an order of magnitude changes the behavior of the logistic function to behave more like an exponential decay (reduces effect of the *a* parameter but also reduces how quickly the logistic function approaches zero). While this behavior runs counter to experiment observations of a distinct time period of no permeability change, and then an

asymptotic decrease in permeability toward zero, leakage with a smaller *b* is still negligible. After 100 years the fluid front (while still technically moving) has essentially stopped below 300 m.

4.5. CONCLUSIONS

A full reactive transport code would be required to attempt to explicitly model all of the key phenomena and is outside of the scope of this dissertation. However, a simple analytic and empirical model is developed to provide a tool for risk assessment models. Risk assessment models combine multiple aspects of GCS over many length scales and require computationally cheap modules to describe each component. Thus the attractiveness of combining the complex phenomena occurring in wellbore leakage into a simple form that can be adjusted based on improvements to the theoretical understanding and empirical observations.

From the limited experimental dataset and adjusting individual parameters it was difficult to get a hypothetical well to leak brine into an overlying aquifer. Further experiments with less reactive systems may provide insights into the conditions that would permit a leak and are left for future work.

5. Conclusions and future work

5.1. CONCLUSIONS

The goal of this dissertation is to study the issue of wellbore leakage by using experiments. Specifically, it is important to understand the time-dependent behavior of the leak to help assess the risk of wellbore leakage during and after GCS operations. Results from the laboratory experiments have shown that complex and coupled processes occur when reactive fluids are transported along a cement fracture. The fluid (either HCl

or carbonic acid solution) reacts with cement to neutralize pH and liberate calcium. When carbonate ions are present and pH is sufficiently high, precipitation of calcium carbonate occurs.

The results show that a whole class of behavior can be eliminated. Self-reinforcing behavior that leads enhancing of the flow path (e.g. wormhole development) does not occur because a silicon-rich zeolite phase remains in the reacted zone and continues to act as a flow barrier. This is especially true when one considers the length scale of a well. This is a very important result for understanding time-dependent leakage. While a leaky well might not seal (e.g. if the residence time is too short or reactivity of the system is small) reactions will not lead to an ever widening aperture and increased leakage rate.

Self-limiting was shown to occur in systems with sufficient residence time to allow dissolution/precipitation processes to create calcite precipitation zones in slow flow regions. In the constant rate HCl experiments self-limiting was evidenced by an increase in pressure differential. With the constant pressure differential driving force experiments utilizing CO_2-saturated fluid the precipitation reaction was further retarded due to pH buffering by the carbonate system. With longer residence time self-limiting behavior lead to self-sealing of fractures.

An empirical model that matches experiment observations was developed to estimate leakage rates and time-dependent leakage flux on at the well scale. A simple parameter study showed the utility of the model and also showed (based on the limited experimental dataset) that wells tend to seal given a large range of parameters. This model can be used in a stochastic manner to project leakage for a single well or for an entire field. While more work is needed to validate and improve the model it is a useful tool to aid in risk assessment of GCS.

5.2. FUTURE WORK

Additional research to fully understand wellbore leakage is already occurring and some of the next steps are detailed below. The composite core experiments have worked well and will continue to be used for the analysis of different conditions.

The first parameter to be studied is the role of dissolved CO_2 concentration. Lower CO_2 concentration will reduce the pH buffering capacity of the system and promote earlier precipitation. Lower CO_2 concentration will also reduce the total reactivity of the system, which may retard sealing. Thus there is a trade-off between enhanced precipitation conditions and retarded sealing due to lack of sufficient reaction that must be studied. I hypothesize that the role of CO_2-saturation will manifest itself in the logistic and retardation terms in the simple empirical model.

In this dissertation temperature was held fixed and experiments are planned to include elevated temperatures that are more representative of down hole conditions. The increased temperature will have two effects, both of which should promote precipitation. First there will be less dissolved CO_2 in the fluid and second higher temperature will accelerate chemical reactions.

Experiments with brine (first NaCl then more complex formulations) will also be conducted. The role of brine composition will be unknown as there could be profound effects on the solubility of aqueous and solid species, especially when natural brines with many cations that can form insoluble salts are used.

Finally experiments studying more exotic cement formulations and the cement-to-earth interface should also be performed. Cement formulation plays an important role in the availability of calcium phases for acid neutralization and is quite varied in actual wellbores. Additionally, the cement-to-earth interface is a leak path that has highly

variable chemistry and the observations in the dissertation might not hold under certain interfaces.

There are two goals of the proposed additional lab work. The first is to identify any new phenomena that might occur in ever more realistic systems. The second is to provide additional parameters for the simple leak model. Giving a physical interpretation of the retardation and logistic parameters is important for applying the model to a specific scenario. If there is a dependence on a single parameter or combination of parameters (e.g. aperture geometry, residence time, or CO_2 concentration), then more experiments will help identify this relationship.

Capturing the development of the precipitation front in situ will also provide valuable evidence for the mixing induced hypothesis. Experiments are still in development to flow CO_2-saturated fluids along a cement fracture and non-destructively image at discrete intervals. The role of multiphase flow in the fracture is necessary to understand leakage early on or very near the injection wells and is a significant challenge.

Finally, efforts should be made to develop a robust reactive transport code to identify mixing induced precipitation and self-sealing under constant pressure differential driving force. The fracture should be treated explicitly, instead of using a flow through porous media assumption. The chemistry should account for pH buffering by the carbonate system and the mineral reaction kinetics. The flow field and chemistry should be coupled such that precipitation on the fracture surface alters the flux and local residence time. As precipitation occurs the fluid flux should decrease correspondingly. Reaction of the cement fracture surface (and into cement) needs to match previous batch reaction experiments. Any additional insights from new experiments or models should be incorporated into the model. While this robust model will probably not have the

capability to capture fracture scale phenomena with a well length scale, results from this model can be used to improve the simple leak model presented in Chapter 4.

Appendices

SUMMARY

To keep the main body of the dissertation a concise argument, the appendix is liberally used to give further details on material presented in the chapters. Specifically Appendix A contains equations, derivations, and definitions used in the dissertation. Appendix B contains a summary of the equation of state used for CO_2 saturation calculations. Appendix C contains detailed experiment reports on all laboratory experiments. Appendix D presents the derivation of the simple well scale leakage model.

Appendix A

SUMMARY

This appendix contains derivation of the cubic equation used for flow in a fracture. The hydraulic aperture is defined and related to permeability.

DERIVATION OF CUBIC EQUATION FOR FLOW IN A FRACTURE

The cubic equation for flow between two parallel plates is used to estimate the size and conductivity of a fracture (Bear, 1972). This measure is often determined from experiments that measure the flow rate to pressure drop relationship. The cubic equation can be derived from the single phase incompressible version of the Navier-Stokes equation (Bird et al., 2002):

$$\rho\left(\frac{d\mathbf{v}}{dt}+\mathbf{v}\bullet\nabla\mathbf{v}\right)=-\nabla P+\mu\nabla^2\mathbf{v}+\mathbf{f} \qquad (A.1)$$

Where ρ is the fluid density, $\boldsymbol{v}$ is the velocity vector, t is time, P is pressure, μ is fluid viscosity, $\boldsymbol{f}$ represents body forces (i.e. gravity). If inertial terms and body forces are ignored the following terms are equal to zero:

$$\rho\left(\frac{d\mathbf{v}}{dt}+\mathbf{v}\bullet\nabla\mathbf{v}\right)=0 \qquad (A.2)$$

$$\mathbf{f}=0 \qquad (A.3)$$

The resulting equation retains the divergence of stress terms and is referred to as Stokes equation:

$$\nabla P=\mu\nabla^2\mathbf{v} \qquad (A.4)$$

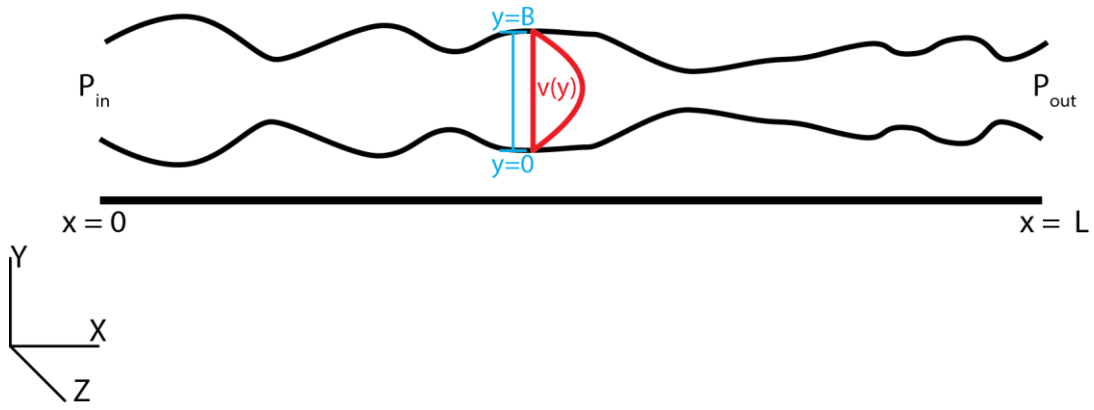

Figure A.1 – Geometry of flow through a fracture.

Assuming no flow in the z-direction and bulk flow in the x-direction, velocity will vary in the y-direction (Figure A.1). The equation becomes:

$$\frac{dP}{dx}=\mu\left(\frac{d^2v}{dy^2}\right) \qquad (A.5)$$

Next the differential equation is solved for the velocity profile using the variable substitution:

$$\theta = \frac{dv}{dy} \qquad (A.6)$$

The differential equation becomes:

$$\frac{dP}{dx} = \mu\left(\frac{d\theta}{dy}\right) \qquad (A.7)$$

Solving the equation for θ and y by separation of variables:

$$\int dy \frac{dP}{dx} = \mu \int d\theta \qquad (A.8)$$

$$y\frac{dP}{dx} = \mu\theta + C_1 \qquad (A.9)$$

Plugging θ back in to the equation yields:

$$y\frac{dP}{dx} = \mu\frac{dv}{dy} + C \qquad (A.10)$$

To solve for the constant (C) assume a boundary condition (BC) where velocity is maximized at the center point between the two surfaces (and a parabolic velocity distribution):

$$\frac{dv}{dy} = 0 \text{ at } y = \frac{B}{2} \qquad (A.11)$$

Plugging in the BC the constant of integration is:

$$C = \frac{B}{2}\frac{dP}{dx} \qquad (A.12)$$

Plugging in for the constant the differential equation becomes:

$$y\frac{dP}{dx} = \mu\frac{dv}{dy} + \frac{B}{2}\frac{dP}{dx} \qquad (A.13)$$

This simplifies to:

$$\frac{dv}{dy} = \frac{1}{\mu}\left[y - \frac{B}{2}\right]\frac{dP}{dx} \qquad (A.14)$$

Solving the differential equation by separation of variables gives:

$$\int dv = \frac{1}{\mu}\int\left[y - \frac{B}{2}\right]\frac{dP}{dx}dy \qquad (A.15)$$

$$v = \frac{1}{2\mu}\left[y^2 - By\right]\frac{dP}{dx} + C \qquad (A.16)$$

To solve for the second *C*, a no slip BC is assumed at the fluid solid interface:

$$v=0 \text{ at } y=0 \qquad (A.17)$$

Plugging the BC into the equation and the second constant is zero:

$$C=0 \qquad (A.18)$$

Thus the x-direction velocity changes in the y-direction according to:

$$v = \frac{1}{2\mu}\left[y^2 - By\right]\frac{dP}{dx} \qquad (A.19)$$

Next, the average velocity is solved for by integrating across the y-direction from 0 to B:

$$\int_{y=0}^{y=B} v\,dy = \int_{y=0}^{y=B} \frac{1}{2\mu}\left[y^2 - By\right]\frac{dP}{dx}\,dy \qquad (A.20)$$

After integrating over the aperture the equation becomes:

$$v(B-0) = \frac{1}{2\mu}\left[\frac{(B-0)^3}{3} - \frac{B(B-0)^2}{2}\right]\frac{dP}{dx} \qquad (A.21)$$

This equation simplifies to an equation relating the fluid flux to the differential change in pressure.

$$v = \frac{-B^2}{12\mu}\frac{dP}{dx} \qquad (A.22)$$

Solving the pressure along the x-direction from 0 to L with corresponding pressure P_{in} and P_{out} respectively we have:

$$\int_0^L v\,dx = \int_{P_{in}}^{P_{out}} \frac{-B^2}{12\mu}\,dP \qquad (A.23)$$

Which gives the cubic equation for average velocity:

$$v = \frac{B^2}{12\mu}\frac{(P_{in} - P_{out})}{L} \qquad (A.24)$$

To get the volumetric flow rate the next step would be to integrate over the fracture aperture (B) and fracture width (W), which is equal to the flow area A:

$$\int_0^B \int_0^W v\,dz\,dy = \int_0^B \int_0^W \frac{B^2}{12\mu} \frac{\left(P_{in} - P_{out}\right)}{L}\,dz\,dy \qquad (A.25)$$

The ***cubic equation for volumetric flow rate*** ($Q = vA$) is then:

$$Q = \frac{WB^3}{12\mu} \frac{\left(P_{in} - P_{out}\right)}{L} \qquad (A.26)$$

The equation above can be rearranged to solve for the aperture of the parallel plates.

$$B = \left(\frac{12\mu QL}{W\left(P_{in} - P_{out}\right)} \right)^{1/3} \qquad (A.27)$$

When used to describe flow in a rough walled fracture B is often referred to as the ***hydraulic aperture*** to denote its determination by measuring the flow rate to pressure differential relationship, as opposed to another direct measurement method like X-ray CT imaging (Ketcham et al., 2010).

RELATION BETWEEN APERTURE AND PERMEABILITY

The cubic equation and Darcy's equation have similar forms and the conductivity terms can be related. First both equations are rearranged to place all shared terms on the left side. The cubic equation is:

$$Q \frac{L\mu}{\left(P_{in} - P_{out}\right)} = \frac{WB^3}{12} \qquad (A.28)$$

And Darcy's equation is:

$$Q \frac{L\mu}{\left(P_{in} - P_{out}\right)} = kA \qquad (A.29)$$

The two equations are then related by:

$$kA=\frac{WB^3}{12} \qquad (A.30)$$

The choice of the area (A) has important implications and two distinct definitions for the scale of the equivalent permeability. If A is defined as the flowing fracture area (BW) then the equation yields an ***equivalent fracture permeability***:

$$k=\frac{B^2}{12} \qquad (A.31)$$

If A is defined as the cross sectional area of a core used in experiments ($0.25\pi W^2$) the equation yields an ***equivalent sample permeability***:

$$k=\frac{B^3}{3W} \qquad (A.32)$$

The difference between these values is several orders of magnitude for work in this dissertation. The equivalent fracture permeability is typically a very large value (many Darcys). This value is useful when the flux version of flow equations is used or with larger areas, for example in the well scale modeling in Chapter 4. The equivalent sample permeability yields permeability in the milli-Darcy range. This measure takes into account the flow restriction from the low permeability porous media surround the fracture. The experiment results in this dissertation are typically presented as equivalent sample permeability.

Appendix B

SUMMARY

This appendix summarizes the methodology used to calculate dissolved CO_2 concentration. The model is based on a robust Equation of State (EOS) model for the CO_2-H_2O-Salt system (Duan and Sun, 2003; Duan et al., 2006, 1992; Li and Duan, 2007). It is strongly encouraged to review their work for full understanding of the EOS. This approach accounts for the effect of brine (NaCl) composition, pressure, and temperature. This model is used throughout the dissertation in experiments to determine the amount of CO_2 to mix with water.

MODEL DERIVATION

Estimation of dissolved CO_2

The model calculates the amount of CO_2 dissolved in water from the following equation:

$$\begin{aligned} \ln m_{CO_2} = & \ln y_{CO_2} f_{CO_2} P - \frac{\mu_{CO_2}^{l(0)}}{RT} \\ & -2\lambda_{CO_2\text{-}Na} m_{Na} \\ & -\zeta_{CO_2\text{-}Na\text{-}Cl} m_{Cl} m_{Na} \end{aligned} \qquad \text{(B.1)}$$

The fraction of CO_2 in the vapor phase is:

$$y_{CO_2} = \frac{\left(P - P_{H_2O}\right)}{P} \qquad \text{(B.2)}$$

The pure water pressure is:

$$P_{H_2O} = \left(\frac{P_c^{H_2O} T}{T_c^{H_2O}}\right)\left[1 + c_1(-t)^{1.9} + c_2 t + c_3 t^2 + c_4 t^3 + c_5 t^4\right] \qquad \text{(B.3)}$$

The critical pressure for water is 220.85 bar and critical temperature is 647.29 K. The constants *c1* to *c5* are given in

Table B.1. The parameter *t* is:

$$t=\frac{\left(T-T_c\right)}{T_c} \qquad \text{(B.4)}$$

The fugacity coefficient of CO_2 can be calculated using a cubic equation of state with an iterative solution (Duan and Sun, 2003) or by a non-iterative approximation that is valid over a range of pressure and temperature (Duan et al., 2006). The iterative equation for the fugacity coefficient is:

$$\begin{aligned}\ln\phi=&\frac{PV}{RT}-1-\ln\left(\frac{PV}{RT}\right)+\frac{c_1+\frac{c_2}{T_r^2}+\frac{c_3}{T_r^3}}{V_r}\\&+\frac{c_4+\frac{c_5}{T_r^2}+\frac{c_6}{T_r^3}}{2V_r^2}\\&+\frac{c_7+\frac{c_8}{T_r^2}+\frac{c_9}{T_r^3}}{4V_r^4}\\&+\frac{c_{10}+\frac{c_{11}}{T_r^2}+\frac{c_{12}}{T_r^3}}{5V_r^5}+\frac{c_{13}}{2T_r^3c_{15}}\\&\times\left[c_{14}+1-\left(c_{14}+1+\frac{c_{15}}{V_r^2}\right)\times\exp\left(-\frac{c_{15}}{V_r^2}\right)\right]\end{aligned} \qquad \text{(B.5)}$$

The parameters c_1 to c_{15} are listed on

Table B.1. Using the above equations we can calculate the total amount of CO_2 dissolved in a brine for a given salinity at a given pressure and temperature. The reduced volume is:

$$V_r = \frac{VP_c}{RT_c} \qquad \text{(B.6)}$$

The chemical potential and interaction parameters are modeled using a Pitzer equation to account for temperature and pressure dependence:

$$\begin{aligned}\frac{\mu_{CO_2}^{l(0)}}{RT} &= c_1 + c_2 T + \frac{c_3}{T} + c_4 T^2 \\ &+ \frac{c_5}{(630\text{-}T)} + c_6 P + c_7 P \ln T \\ &+ c_8 \frac{P}{T} + c_9 \frac{P}{(630\text{-}T)} \\ &+ c_{10} \frac{P^2}{(630\text{-}T)^2} + c_{11} T \ln P\end{aligned} \qquad \text{(B.7)}$$

$$\begin{aligned}\lambda_{CO_2\text{-}Na} &= c_1 + c_2 T + \frac{c_3}{T} \\ &+ c_8 \frac{P}{T} + c_9 \frac{P}{(630\text{-}T)} \\ &+ c_{11} T \ln P\end{aligned} \qquad \text{(B.8)}$$

$$\xi_{CO_2\text{-}Na\text{-}Cl} = c_1 + c_2 T + c_8 \frac{P}{T} + c_9 \frac{P}{(630\text{-}T)} \qquad \text{(B.9)}$$

Using the above equations we can calculate the total amount of CO_2 dissolved in a brine for a given salinity at a given pressure and temperature.

Table B.1 – Fitting parameters for EOS equations.

	P_{H_2O}	$\ln\phi$	$\frac{\mu^{l(0)}_{CO_2}}{RT}$	$\lambda_{CO_2\text{-Na}}$	$\xi_{CO_2\text{-Na-Cl}}$
c_1	-38.640844	8.99288497e-2	28.9447706	-0.411370585	3.36389723e-4
c_2	5.8948420	-4.94783127e-1	-0.0354581768	6.07632013e-4	-1.98298980e-5
c_3	59.876516	4.77922245e-2	-4770.67077	97.5347707	
c_4	26.654627	1.03808883e-2	1.02782768e-5		
c_5	10.637097	-2.82516861e-2	33.8126098		
c_6		9.49887563e-2	9.04037140e-3		
c_7		5.2060088e-4	-1.14934031e-3		
c_8		-2.93540971e-4	-0.307405726	-0.0237622469	2.12220830e-3
c_9		-1.77265112e-3	-0.0907301486	0.0170656236	-5.24873303e-3
c_{10}		-2.51101973e-5	9.32713393e-4		
c_{11}		8.93353441e-5		1.41335834e-5	
c_{12}		7.88998563e-5			
c_{13}		-1.66727022e-2			
c_{14}		1.398e0			
c_{15}		2.96e-2			

VARIABLES AND UNITS

t – Parameter used in pure water pressure equation, -

T – Temperature, K

T_c – Critical temperature, K

T_r – Reduced temperature, -

P – Pressure, bar

P_c – Critical pressure, bar

P_r – Reduced pressure, -

P_{H2O} – Pure water pressure, bar

R – Universal gas constant (8.3144621e-2), $m^3 bar K^{-1} mol^{-1}$

V_r – Reduced volume, $molm^{-3}$

m_i – Molality of component i dissolved in water, $molkg^{-1}$

y_{CO2} – Mole fraction of CO_2 in vapor phase, -

ϕ_{CO2} – Fugacity coefficient of CO_2, -

$\mu^{1(0)}_{CO2}$ – The standard chemical potential of CO_2 in the liquid phase

$\lambda_{CO2\text{-}Na}$ – The interaction parameter between CO_2 and Na^+

$\xi_{CO2\text{-}Ca\text{-}Cl}$ – The interaction parameter between CO_2, Na^+, and Cl^-

Appendix C

SUMMARY

This appendix contains detailed reports for key experiments used in this dissertation. The reports delve more deeply into the analysis and experiment technique than the chapters.

EXPERIMENT REPORT: BB-9

Summary

Sample BB-9 was the first experiment that attempted to coupled reaction and transport by injecting hydrochloric acid (HCl) into a fractured cement core under confining stress. A new High Pressure Liquid Chromatography Pump (HPLC) was added to the core flow equipment used in previous work (Huerta et al., 2009). The pump was designed to handle low pH corrosive fluid, which allowed the injection of HCl directly into the samples. Pressure, effluent fluid volume, and effluent fluid pH data was recorded manually and the experimental methodology was not fully developed. However, the experiment produced useful results.

During the experiment effluent pH decreases rapidly and then flattens out to remain above injected acid pH. The upstream pressure increases from its initial value to a maximum and then decreases asymptotically and remains above the initial value. On the fracture surface is a set of distinct reacted channels which narrow towards the outlet. The observations of reacted channel development and pressure differential increase imply apparently contradictory behavior for the coupling of reaction and transport in this system.

Experiment design

The cement sample was cast in a 1 inch diameter by 5 inch length flexible acrylic cylindrical mold. After curing the sample was fractured using the Brazilian method, offset, the sides of the core were sealed with caulk, and the ends shaved flush. The standard low pressure core flow equipment was used. The upstream pressure was monitored with a 200 psi (maximum) pressure transducer. Pump, pH probe, and pressure transducers were not calibrated before acid experiment.

Results

Pressure differential and effluent fluid history

Table C.1 contains a summary of experiment conditions and results for sample BB-9. Throughout the experiment confining pressure remains flat (Figure C.1) with a mean of 487 psi (9.6 psi standard deviation). Figure C.2 shows the evolution of pressure differential (as pressure was measured at psig) and effluent pH during the experiment. As acid is injected into the core, inlet pressure increases from 15 psi to a maximum of 37 psi. After this peak, pressure decays along an asymptotic slope and by the experiment end the inlet pressure is 26 psi, which is 11 psi above the initial value. The effluent pH is initially above 9 and also asymptotically decreases during the experiment. By the end of the experiment the effluent pH is 3.3, which is well above the injected value of 2.18. Figure C.3 shows hydraulic aperture plotted versus acid injected. The plot shows a sharp initial decrease in aperture which then begins to rebound and increase at 0.5 mmol injected but flattens out by the end of the experiment.

Fracture surface analysis

Figure C.4 (left) shows an image of the fracture surface post experiment. A distinct reacted channel is developed with fingering that decreases in width from inlet to outlet and is dominated by a few reacted pathways in the middle.

Discussion

As this was the first experiment many more questions were raised than answered. The most intriguing result was that, as opposed to previous work where flow and reaction were decoupled and the entire fracture surface was reacted (Huerta et al., 2009), reaction occurred along discrete pathways in the cement. The reacted channels look like they were visibly etched. Reacted channel development can become self-reinforcing (to become self-enhancing) in fractures if wormholes develop (Szymczak and Ladd, 2009). However, in this experiment the pressure differential actually increases to a peak and then decreased but remained above the initial value. If wormholes were forming, the expected behavior would be a decrease in the pressure differential. The observation that there is channel development down the length of the core and at the end of the experiment while there is an overall increase in pressure differential implies a flow restriction has developed. Furthermore, the effluent pH remained above the injected acid pH, so reaction was occurring in the sample up to the end of the experiment but was less than the reaction initially was, implying a stabilization of the reacted pathway.

It is unknown how the pressure differential and reacted channel would have evolved had the experiment ran until the injected and effluent pH were equal.

Additional information

The original data file was lost and data had to be extracted from a partial excel file and image plots to reconstruct the experiment.

Tables and figures

Table C.1 – **BB-9** experiment summary.

Core dimension (Width × Length), cm	2.54 × 5.04
Flow rate, mL/min	3.3
Average confining pressure (std. dev.), psi	487 (9.6)
Total acid injection time, min	245
Total volume injected, mL	808.5
Acid (pH, concentration), mmol/mL or M	2.18, 6.6 E-3
Acid injection rate, mmol/min	0.02178
Total acid (injected, consumed), mmol	5.3, 5.16
Pressure differential (initial, maximum, final), psi	15, 37, 26

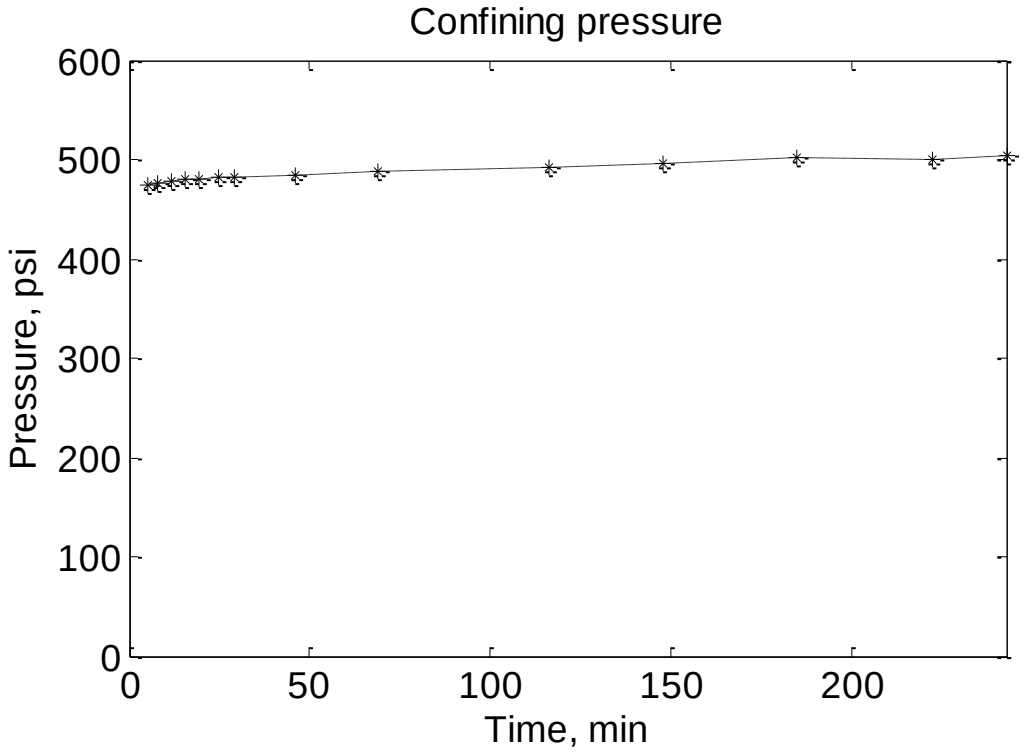

Figure C.1 – Confining pressure versus time. Pressure is stable during the experiment.

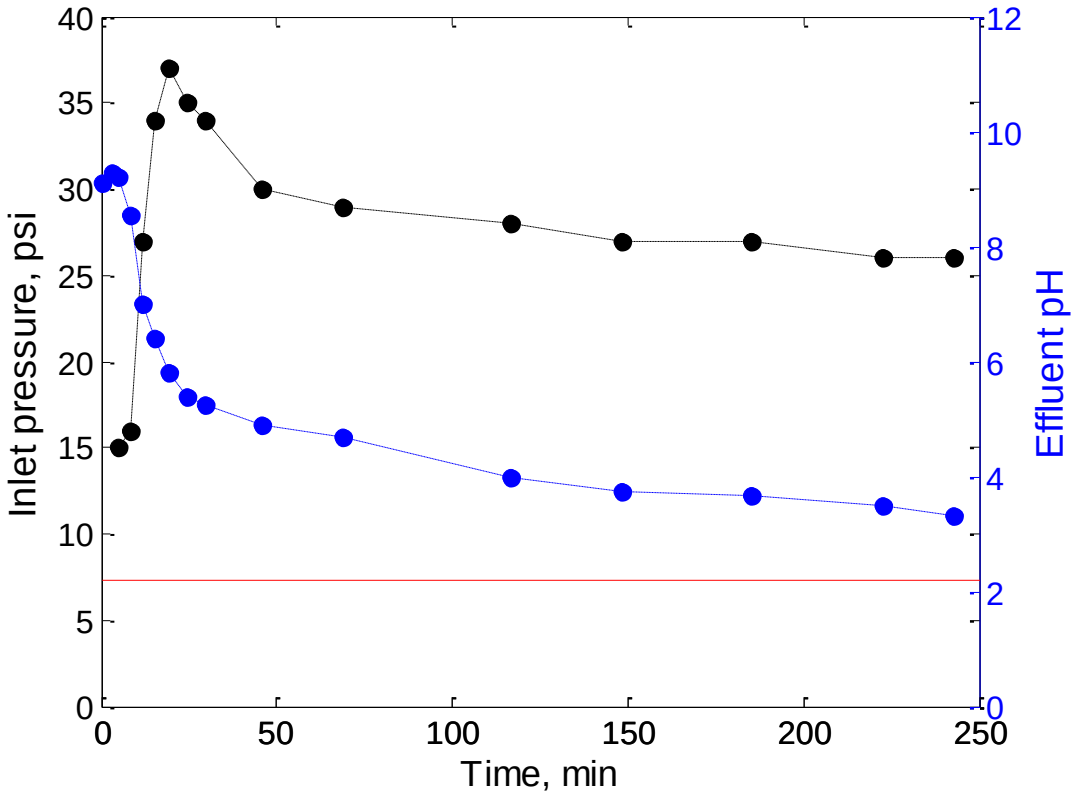

Figure C.2 – Inlet pressure (black) and effluent pH (blue) as a function of time. Injected acid concentration is also plotted (red). At the end of the experiment the inlet pressure remains above the initial pressure. Effluent pH also remains above injected acid pH at the experiment end.

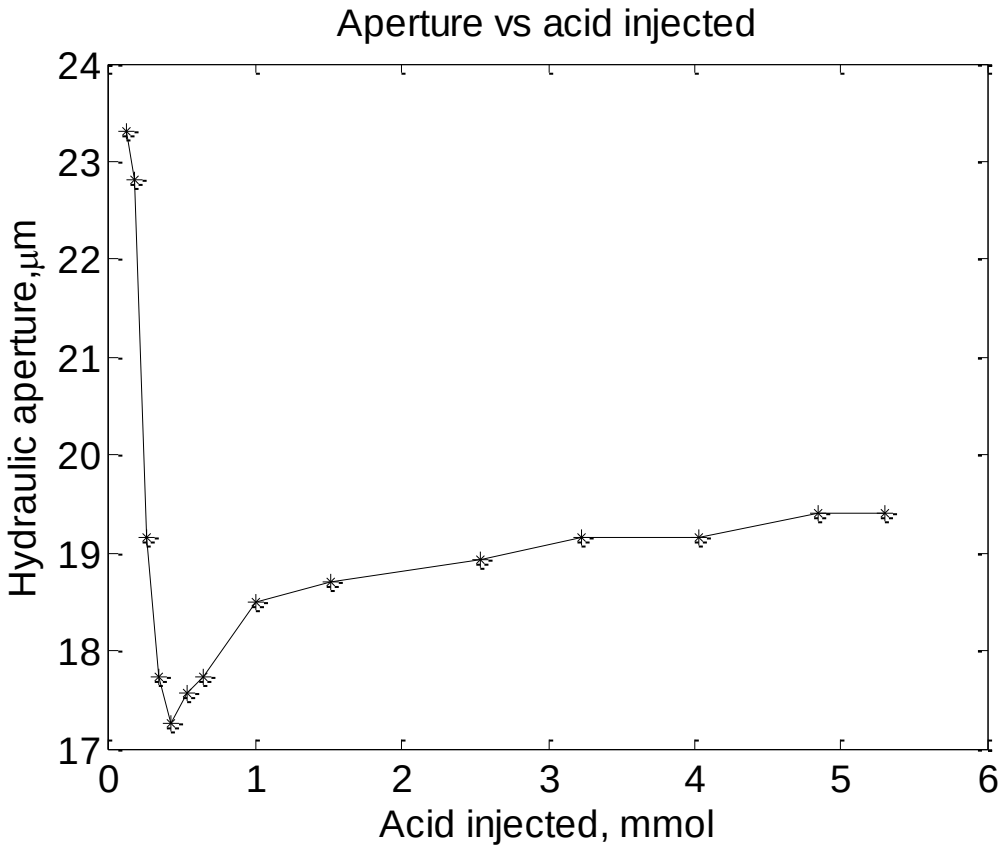

Figure C.3 – Hydraulic aperture plotted versus acid injected. Aperture at the end of the experiment is lower than the initial value.

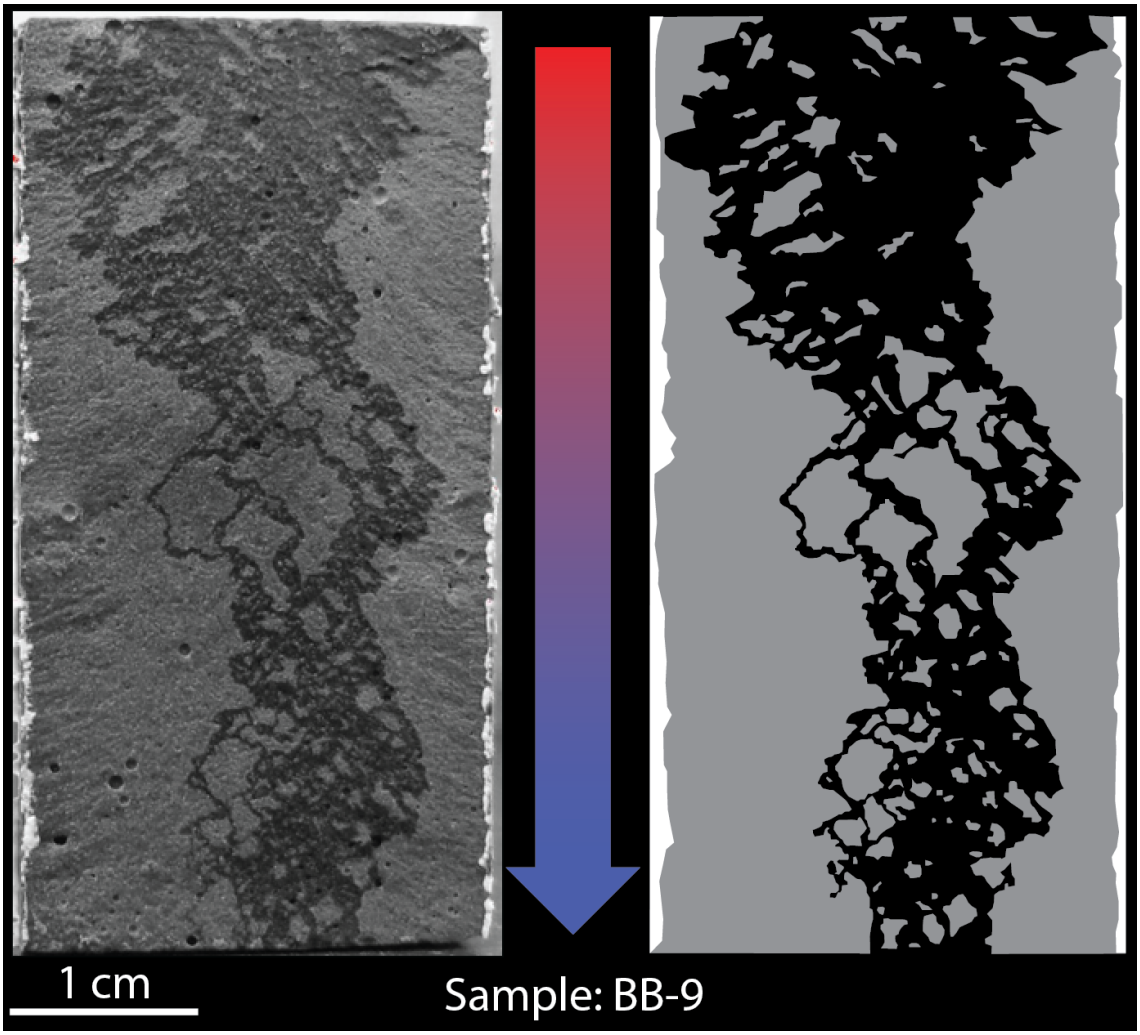

Figure C.4 – (Left) Grey scale image of fracture surface post experiment. Flow is from top to bottom. (Right) Illustration of caulk (white), unreacted cement (grey) and reacted channel (black).

EXPERIMENT REPORT: AAT-15

Summary

This experiment tested the case of slow flow rate (0.55 mL/min) and low acid concentration (pH 3.07) injected into a fractured core. The experiment ran for 32 hours before inlet pressure began building. Thereafter, the inlet pressure continually increased until the inlet pressure was near the confining pressure and the experiment was

terminated. Effluent pH remained between 8.5 and 10 for the entire experiment. Images of the post reaction fracture surface indicate reaction across the width of the sample up to a point and a white precipitate present downstream across the fracture past the reaction point.

Experiment design

The experiment consisted of 2 steps. The first step was performed to strain harden the sample, saturate the sample's facture space, and measure the initial hydraulic conductivity. The second step was to inject acid at a constant flow rate and observe changes in inlet pressure and effluent pH.

To prepare the pump for the experiments the pump lines were purged of air. The HPLC pump was also calibrated before the baseline and acid experiments to ensure the flowrate set on the pump was actually being delivered. The calibration consists of setting a flow rate and measuring the volume of liquid collected for different flow rates (3 for the baseline and 5 for the acid experiment). The offset between the values reported on the pump display and the volume of effluent measured in a 10 mL graduated cylinder were small and any error was assumed to be due to measurement using the graduated cylinder. The pH probe was calibrated before the acid experiment.

The cement sample was mixed and cured according to the standard API method (API, 1997) and a single tensile fracture was created using the Brazilian method (Guo et al., 1993) in a loading frame. The sample was slightly oblong on one end and was shaved to fit inside the core holder.

Results

Pressure differential history

Figure C.5 shows confining pressure during the experiment. The large increase at 900 minutes was caused by pumping the Enerpac pump by 1 stroke to maintain confining pressure. Confining pressure has no significant effect on pressure in the fracture. Figure C.6 shows inlet pressure, effluent pH, and injected pH during the experiment. Inlet pressure remains constant for 32 hours before beginning to increase. Once initiated, the pressure continues to build until the experiment was terminated. Figure C.7 shows the hydraulic aperture plotted versus amount of acid injected. Hydraulic aperture is 55 μm at the beginning, rises slightly, and then decreases as inlet pressure increases.

Fracture surface analysis

Figure C.8 shows the post experiment fracture surface. Flow is from top to bottom. The entire width from inlet to half way down the core has a tan color that is similar to reacted cement (Chandra, 1988). The rest of the fracture surface has a white color. There is no evidence for a distinct reacted channel and any reaction and precipitation is spread evenly across the sample.

Discussion

This experiment showed no change in flowing properties for many fracture volumes injected before suddenly and continuously increasing in upstream pressure. The high pH effluent implies that all of the acid is being reacted during this slow flow experiment. It is unknown if the inlet pressure would have eventually decreased once the precipitation zone was transported out of the core, i.e. after breakthrough of the precipitation front. Slow flow experiments with dilute acid concentrations seem to lead to

self-limiting behavior. Onset of self-limiting behavior might be caused by acid concentration, fluid flux, and aperture size.

Additional information

X-ray CT was performed on this sample but it was taken with the sample unconfined and does not represent the in situ fracture geometry.

Tables and figures

Table C.2 – **AAT-15** experiment summary.

Core dimension (Width / Length), cm	**2.54 / 4.52**
Flow rate, mL/min	0.55
Average confining pressure (std. dev.), psi	222 (48.8)
Total acid injection time, min	2,324
Total volume injected, mL	1,282
Acid pH (concentration, mmol/mL or M)	3.07 (8.6 E-4)
Acid injection rate, mmol/min	4.73E-04
Total acid (injected / consumed), mmol	1.091 / 1.091
Pressure differential (initial / maximum / final), psi	0.23 / 263 / 263

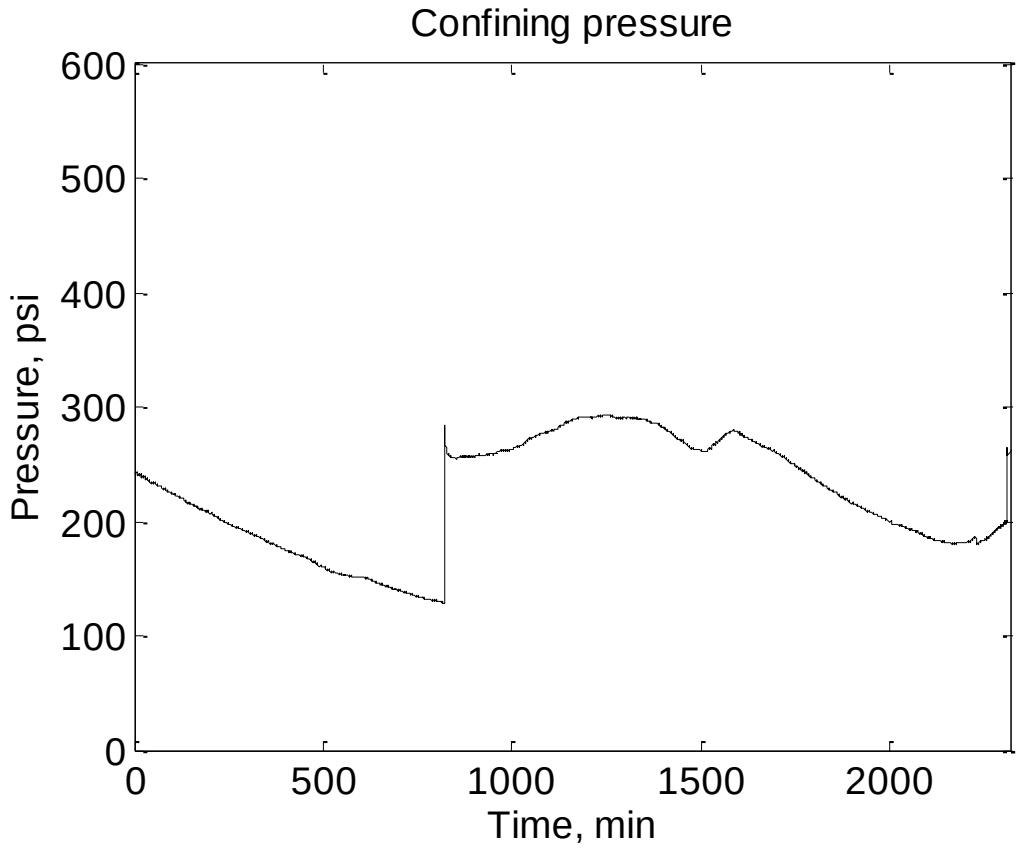

Figure C.5 – Confining pressure versus time. The rapid increase in confining pressure before 1,000 minutes is caused by a manual increase in confning pressure from a stroke of the Enerpac pump.

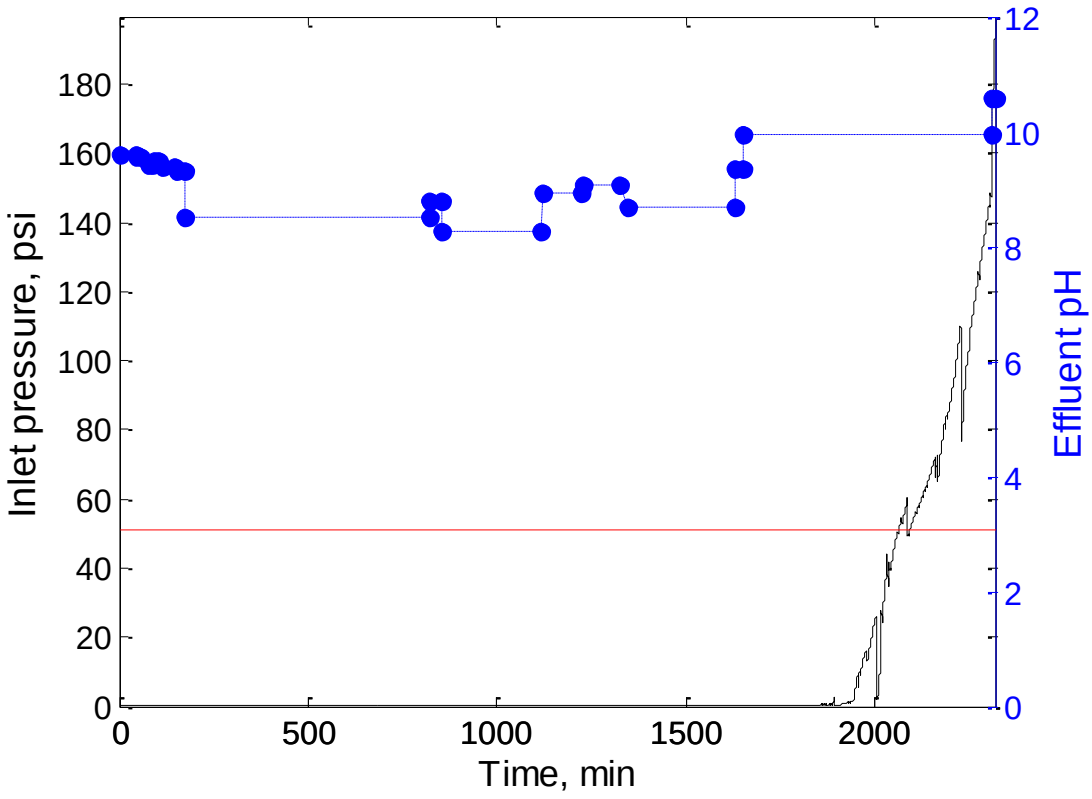

Figure C.6 – Inlet pressure (black) and effluent pH (blue) as a function of time. Injected acid concentration is also plotted (red).

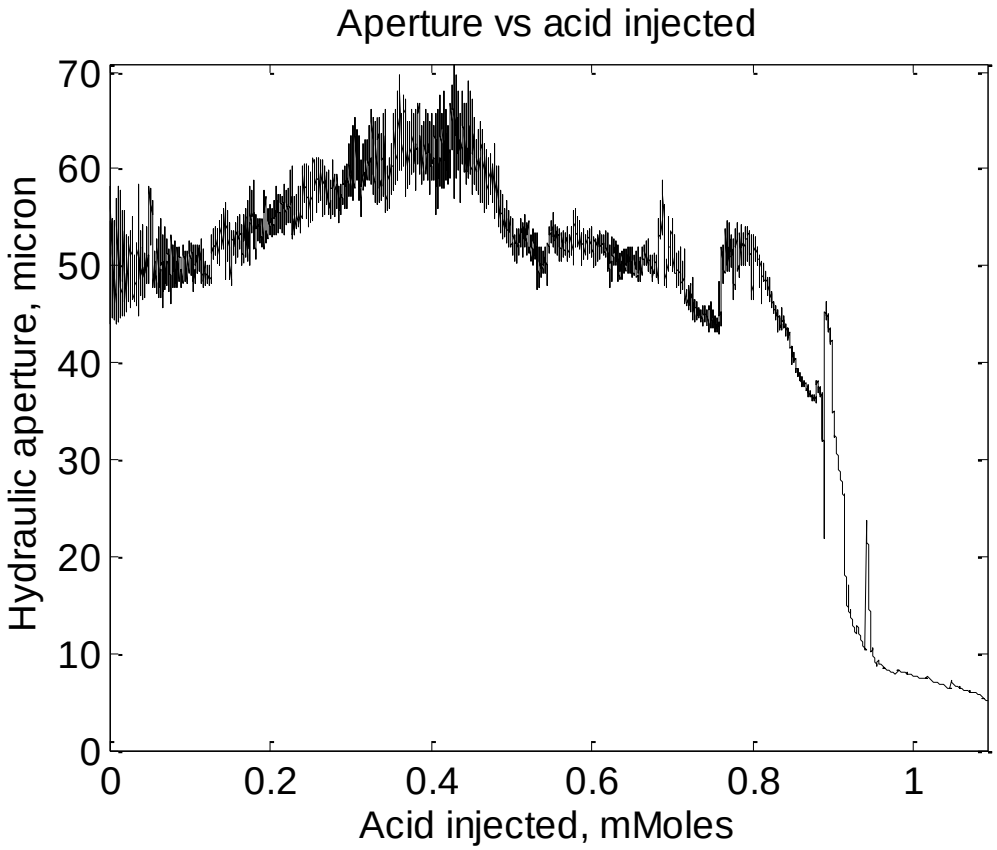

Figure C.7 – Hydraulic aperture versus acid injected.

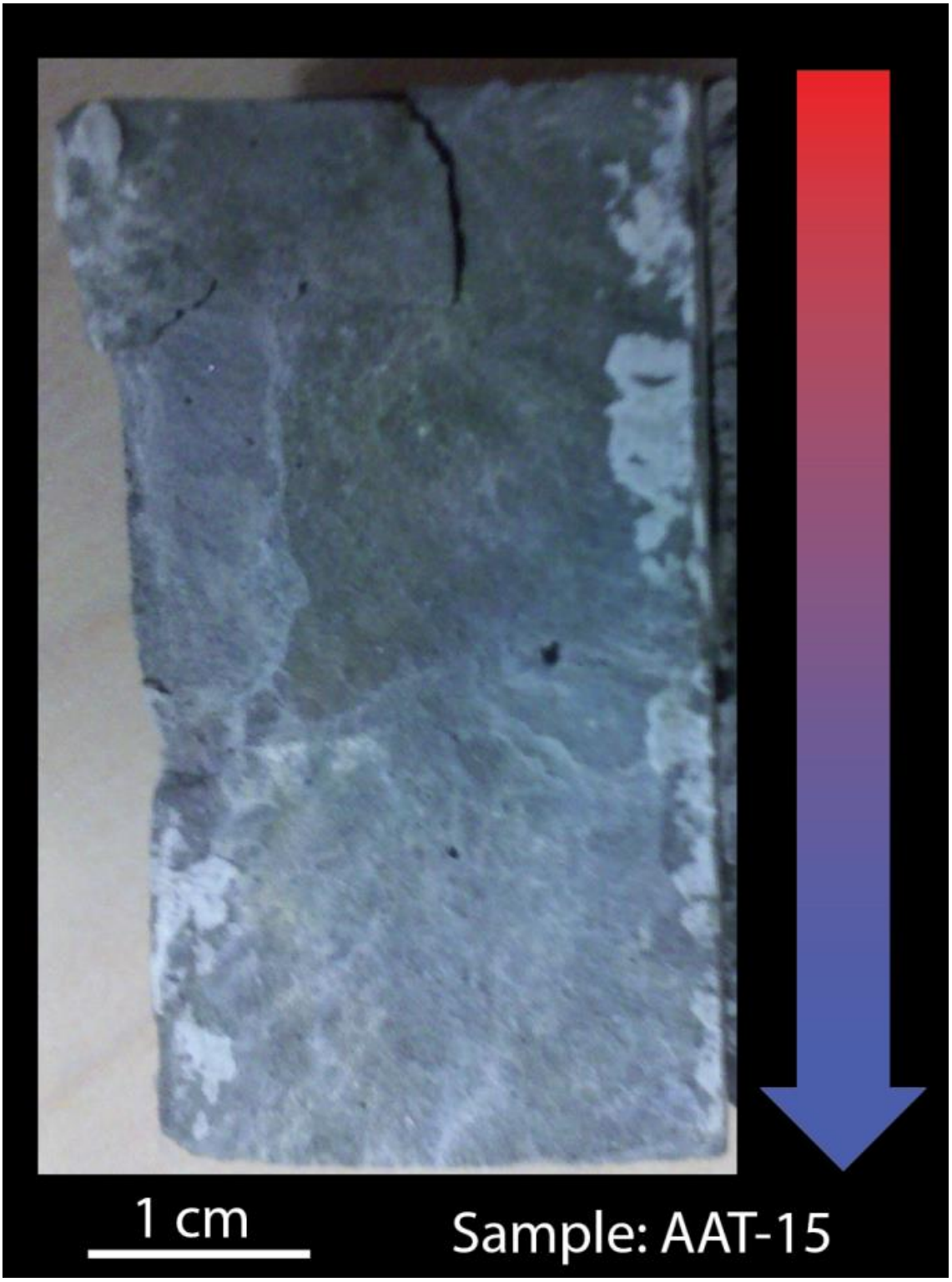

Figure C.8 – Image of fracture surface post reaction. Flow is from top to bottom.

EXPERIMENT REPORT: BSD7

Summary

The experiment goal for sample BSD7 was to inject a relatively high concentration of HCl into a cement core to study pressure differential, effluent chemistry, and surface reactions. This sample had the largest initial aperture of all HCl experiments, moderate flow rate, and highest injected acid concentration. Pressure differential increased to a peak during the experiment and then began to decrease as the experiment progressed. At the end of the experiment the pressure differential was above the initial value. Beginning effluent pH was neutral and much lower than the value of water equilibrated with cement (~12). Effluent pH decreased asymptotically toward injected value pH of 2. Effluent chemistry showed an initially high value of calcium that decreased as the experiment progressed.

The facture surface showed significant alteration along a discrete channel that narrowed towards the outlet. Unreacted cement and white precipitate bound the reacted channel. SEM/EDS analysis of the fracture surface showed calcium depletion in the reacted channel and relative enrichment of silicon. Aluminum is concentrated along reacted channels and across parts of the unreacted surface. Iron is trace but remains in the reacted channel.

This experiment is an example of a very reactive system. The reacted channel that develops is bounded by precipitate, which constricts flow into a discrete pathway.

Experiment design

Sample preparation

The sample was from batch BSD, was prepared using the standard technique, and was fractured using the Brazilian method in a loading frame with flat parallel platens. The sample was offset to ensure a flow pathway, caulked, and the core end shaved flat.

Baseline period

The sample was strain hardened using 3 confining pressure loading-unloading cycles. The maximum confining pressure applied during the baseline study was 633 psi. The fluid pump was not calibrated for baseline or acid test but pH probe was calibrated.

Results

Pressure differential and effluent fluid history

Key experiment parameters are shown on

Table C.3. Figure C.9 shows the confining pressure during the experiment, which was stable and had an average of 423 psi (standard deviation of 8 psi). Figure C.10 shows the pressure differential and effluent pH history for the experiment. The pressure was near the lower limit of the 50 psi pressure transducer's resolution, so a 5-point average was applied to smooth the data. The upstream flow line was primed to remove any water and to ensure acid reached the core face quickly (i.e. minimize dead volume). Pressure differential doubled (from 0.025 psi to 0.05 psi) during the first 100 min. Pressure had a small decrease thereafter but remained well above the initial value at the end of the experiment. Effluent pH was near neutral and asymptotically decayed during the experiment but did not reach the injected value by the experiment end.

15 effluent samples were collected during the acid injection. The samples were analyzed for cation concentration using an ICP-OES Optima 7300DV at NETL Pittsburgh. A sample of the injected acid was also analyzed and is shown on Table C.4. The water used to mix with the HCl was supposed to be deionized water but clearly contamination occurred somewhere during the process. The cations present suggest mixing with tap water or use of a beaker that was not properly cleaned. However analysis of the effluent still yields useful observations. Figure C.11 shows the effluent concentration for 4 dominant cations. Calcium concentration is high in the effluent (above 100 mg/L), has a small spike, but generally decreases during the experiment. Silicon has a much lower concentration (below 15 mg/L). Silicon has an early spike in concentration then the concentration becomes flat for the remainder of the experiment. Aluminum is initially near or below detection limits but then rises to above 3 mg/L and remains constant. Iron behaves similarly and rises to below 2 mg/L.

Fracture surface analysis

Figure C.12 shows an image of one half of the fracture surface and an illustration highlighting the reacted channel (black), unreacted cement (grey), and caulk sealed sections (white). Flow is from top down and the reacted channel decreases in width toward the outlet.

Figure C.12 also shows the 5 locations selected for analysis by SEM/EDS. The instrument used was an FEI-Quanta 600 FEG Environmental SEM equipped with an Oxford INCA energy dispersive spectroscopy system with a large-field secondary electron detector and backscatter electron detector. Each zone is described below.

Location A was selected for analysis because it was near the inlet and contained both unreacted and reacted layers. The interface between zones is sharp and parallel to

the bulk flow direction. Figure C.13 shows the reacted channel (bottom and left side of image) and unreacted zone (top left and into middle of image). Not that the image is rotated so that bulk flow is from right to left. The reacted channel consists of fine grained material and contains polygonal cracks. This zone is relatively enriched in silicon and depleted in calcium. Iron has an overall low concentration but remains in the reacted channel and become relatively enriched like silicon. Aluminum is also minor but is concentrated along the interface between zones. Figure C.14 shows SEM image and EDS spot maps for several phases in the transition zone. The euhedral crystals are dominated by calcium (S1, S3), while the anhedral material also contains aluminum and silicon (S2, S5).

The second location studied (Location B) was farther down the core and also contained both reacted channel and unreacted cement. Figure C.15 shows a BSED image, EDS spectrum of the area, and EDS maps for selected elements. The images are rotated clockwise so that bulk flow is from right to left. The same trend of calcium depletion and relative increase in silicon signal is present in the reacted channel. Iron is present in the reacted channel and carbon is more concentrated in the unreacted zone. At the far left edge of the sample is a material that has elevated concentrations of aluminum and oxygen and low concentration of calcium. The density is less than the unreacted material (darker on the BSED image) but is texturally more like the unreacted cement than the reacted channel. Figure C.16 shows progressively zoomed in BSED images of the aluminum rich zone. There are distinct thread-like minerals on top of subhedral minerals. The specific mineralogy is unknown but occurs within the aluminum rich phase.

Location C was selected because it is within one of the narrow channels. Figure C.17 shows another example of the distinct textural and chemical differences between the reacted, transition, and unreacted cement zones. The blue and yellow boxes were selected

for higher magnification analysis. Figure C.18 contains zoomed in images of both the yellow and blue box with spot EDS spectra. In the yellow box is fine grained material that is still rich in calcium and also contains some aluminum. The blue box contains images and a spectrum that shows more silicon rich material (S1).

Figure C.21 shows BSED images of Location D. Flow is from right to left and images show well developed secondary precipitation of minerals parallel to the bulk flow direction.

Location E was selected for SEM analysis because it was near the outlet. Figure C.22 shows SEM images for a typical spot far from the reacted zone. Present are distinct but very small euhedral grains that are rich in calcium. The minerals could be a mixture of reprecipitated portlandite or calcite precipitated from the mixing of calcium rich fluid from cement pores with carbonate rich injected fluid that has been depleted of its acid.

X-ray diffraction was used to identify the precipitate growing proximal to the reacted channel and in parts of the unreacted zone (Figure C.23). The sample was run on a Rigaku R-Axis micro-diffractometer (μXRD) equipped with an UltraX18 Cu rotating anode X-ray source and a Rapid II 180degree curved imaging plate detector. Sample analysis was performed at 50 kV, 300 mA. The desired portion (white precipitates) of the sample was brought into the focus position, and the sample was analyzed with an exposure time of 5 minutes using a 0.1 collimator. Phase identification was performed using the JADE software equipped with the ICDD PD4 database. The dominant phase identified was calcite. Brownmillerite was also identified but is most likely remnant and not precipitating. Portlandite seemed to have very minor, if any, occurrence. The aluminum rich precipitate did not show up as a distinct mineral phase on μXRD. No specific steps were taken to prevent injected fluid from equilibrating with atmospheric CO_2. Thus we assume the injected fluid provided the carbonate used to precipitate calcite

identified. It is also possible that any portlandite precipitation was altered via carbonation to calcite as there was significant time between experiment and μXRD.

Discussion

A key finding in this system is that aluminum is concentrated on interfaces and not relatively enriched like silicon and iron are in the reacted channel. This indicates that it is mobilized but quickly precipitates to form a secondary phase with distinct crystal shapes. The precipitate increases toward the outlet and is present over the 'unreacted' cement (left side of fracture image). The restriction in flow observed from the elevated pressure differential was surprising given the large size of the initial hydraulic aperture. The pervasive precipitation could explain why the HCl systems seem so much more responsive to precipitate inducted blockage than the CO_2 systems.

Effluent analysis shows the system is less reactive as more acid is injected. Less calcium rich (acid buffering) species are readily available. As a consequence calcium and pH both approach their injected concentration. Silicon signal remains relatively constant and seems to be immobile. Aluminum signal is actually lower than the injected concentration. If the injected acid concentration is to be believed this would imply aluminum is being immobilized during before 1 mmol of acid is injected. After this time period the reacted channel has broken through and the aluminum signal is a combination of cations from injected fluid and dissolution of Al rich species. Iron also has a similar signal but the initial and injected are much closer. The increase in iron could be due to dissolution of iron bearing species in the reacted channel.

Additional information

None for this experiment.

Tables and figures

Table C.3 – **BSD7** experiment summary.

Core dimension (Width / Length), cm	2.54 / 3.65
Flow rate, mL/min	1
Average confining pressure (std. dev.), psi	423 (8)
Total acid injection time, min	914
Total volume injected, mL	914
Acid pH (concentration, mmol/mL or M)	2.31 (4.9 E-3)
Acid injection rate, mmol/min	0.0049

Table C.4 – Injected acid cation concentration.

Element	Concentration, mg/L
Al	2.5
B	2.9
Ca	25
K	0.6
Mg	0.5
Na	4.7
S	0.8
Si	2.3
Z	39

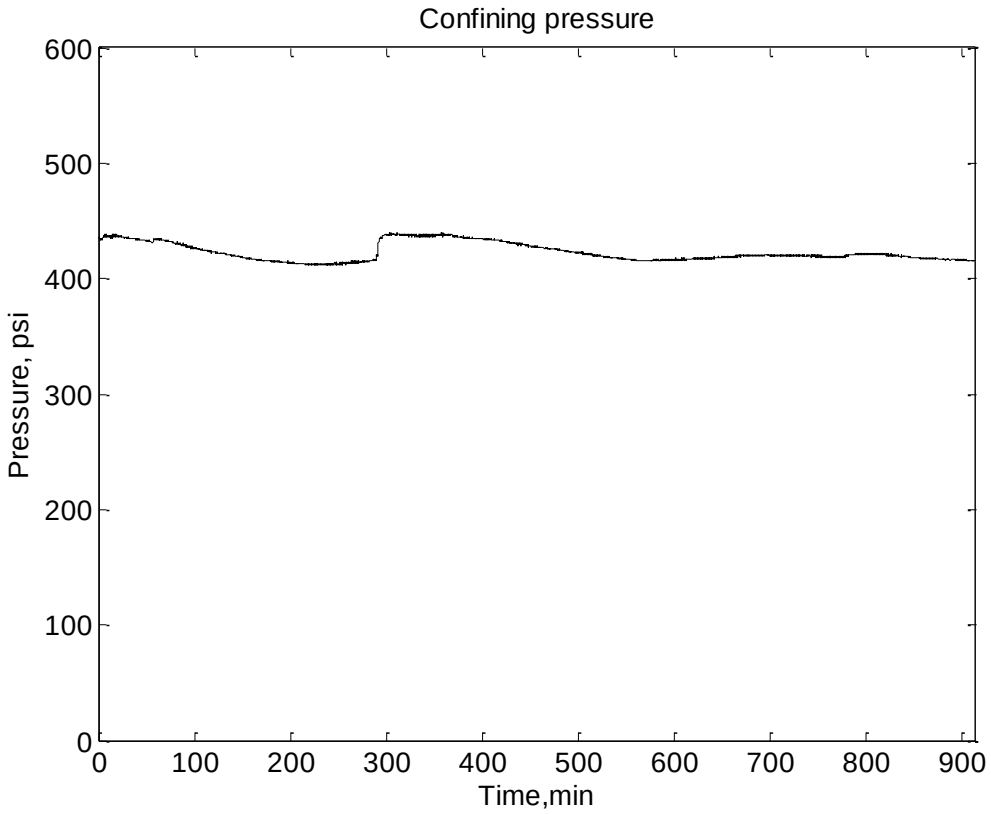

Figure C.9 – Confining pressure versus time. Confining pressure is well behaved during the experiment with an average pressure of 423 psi (standard deviation of 8 psi).

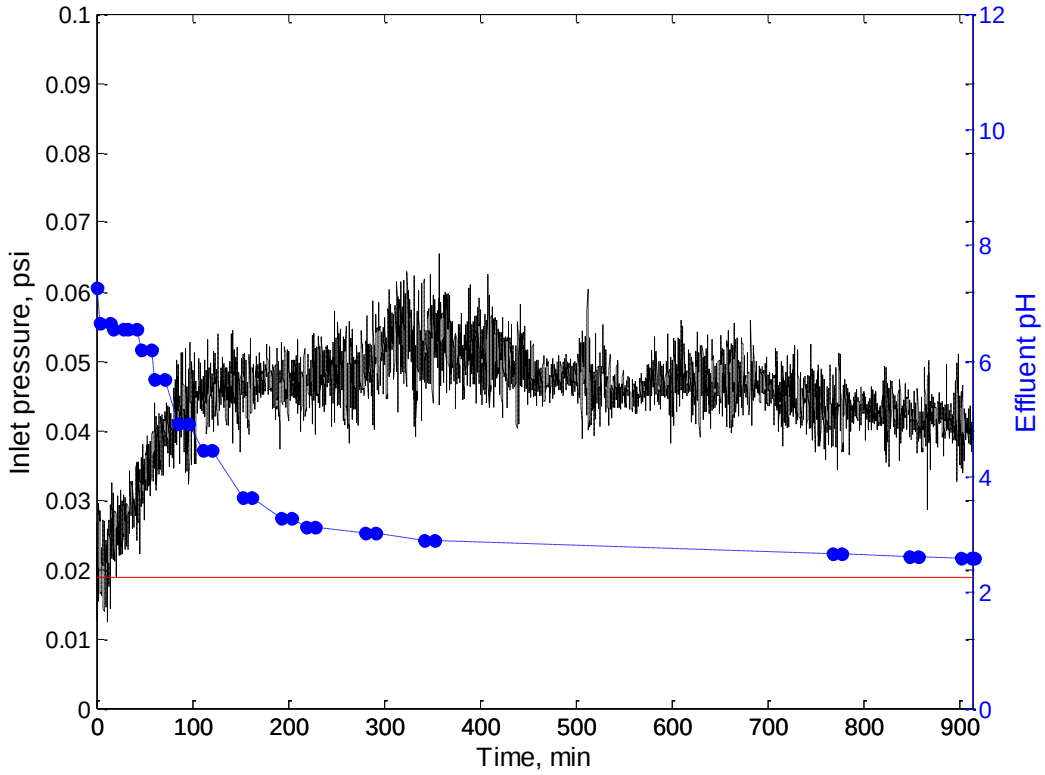

Figure C.10 – Pressure differential (black), effluent pH (blue), and injected pH (red) plotted versus time. Pressure differential increases during the first 100 minutes then remains high until 400 minutes where is begins to decrease but remains well above the initial value. Effluent pH is neutral at the experiment start but asymptotically decreases during the experiment to be just above the injected acid pH at the experiment end.

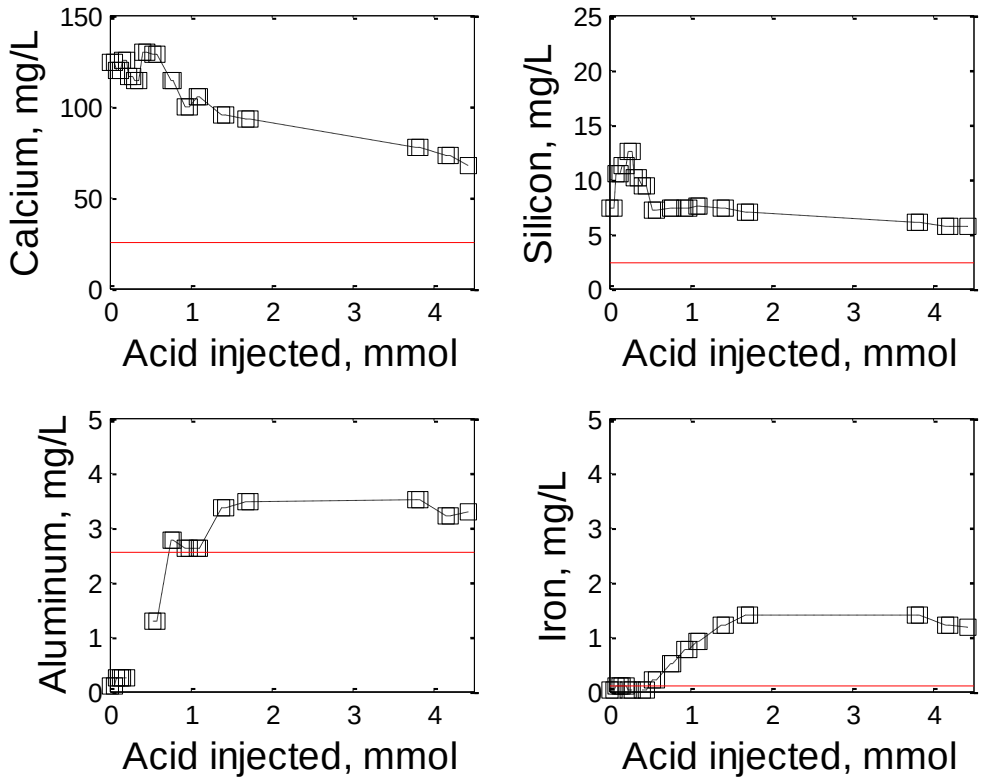

Figure C.11 – Effluent cation concentration plotted versus acid injected. Black squares represent sample collection start and stop time and red lines represent injected acid concentration.

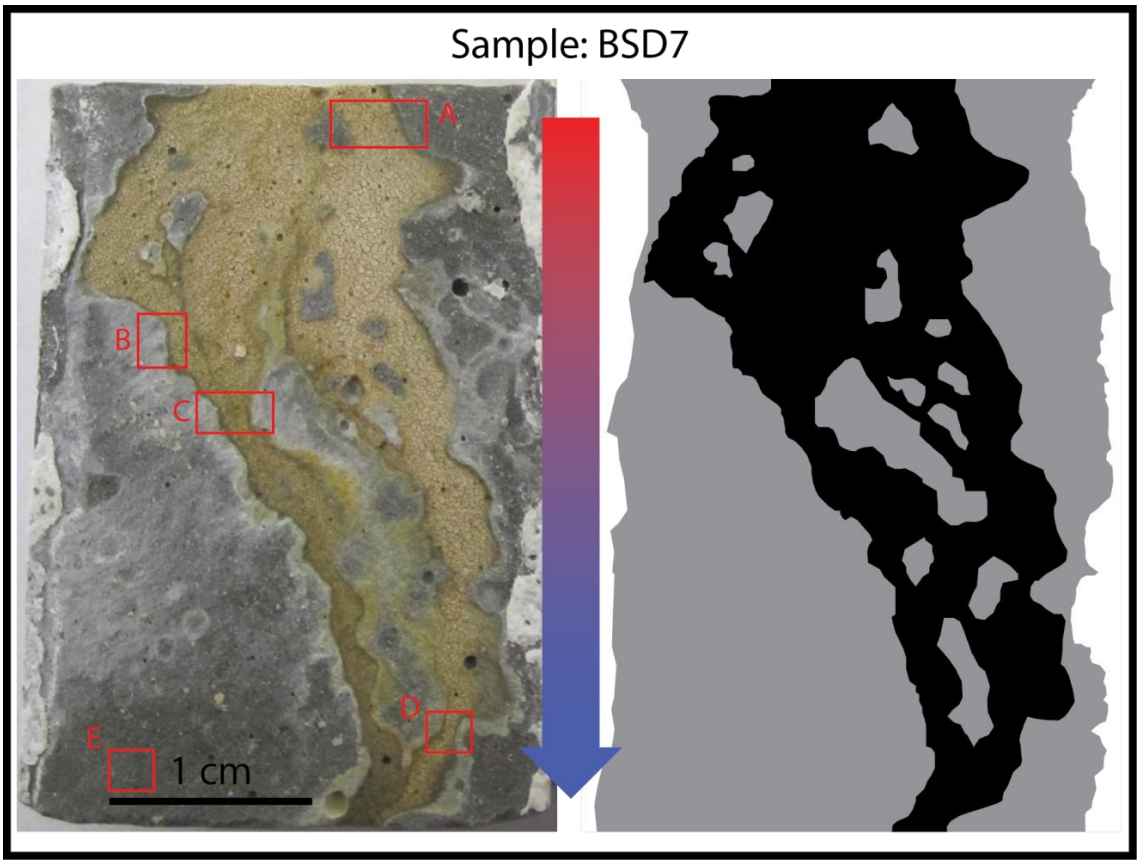

Figure C.12 – (Left) Post acid injection reacted fracture surface of one core half. Locations A to E were studied with SEM. (Right) Illustration identifying caulk (white), unreacted cement and precipitation zone (grey), and reacted channel (black). Flow is from top to bottom.

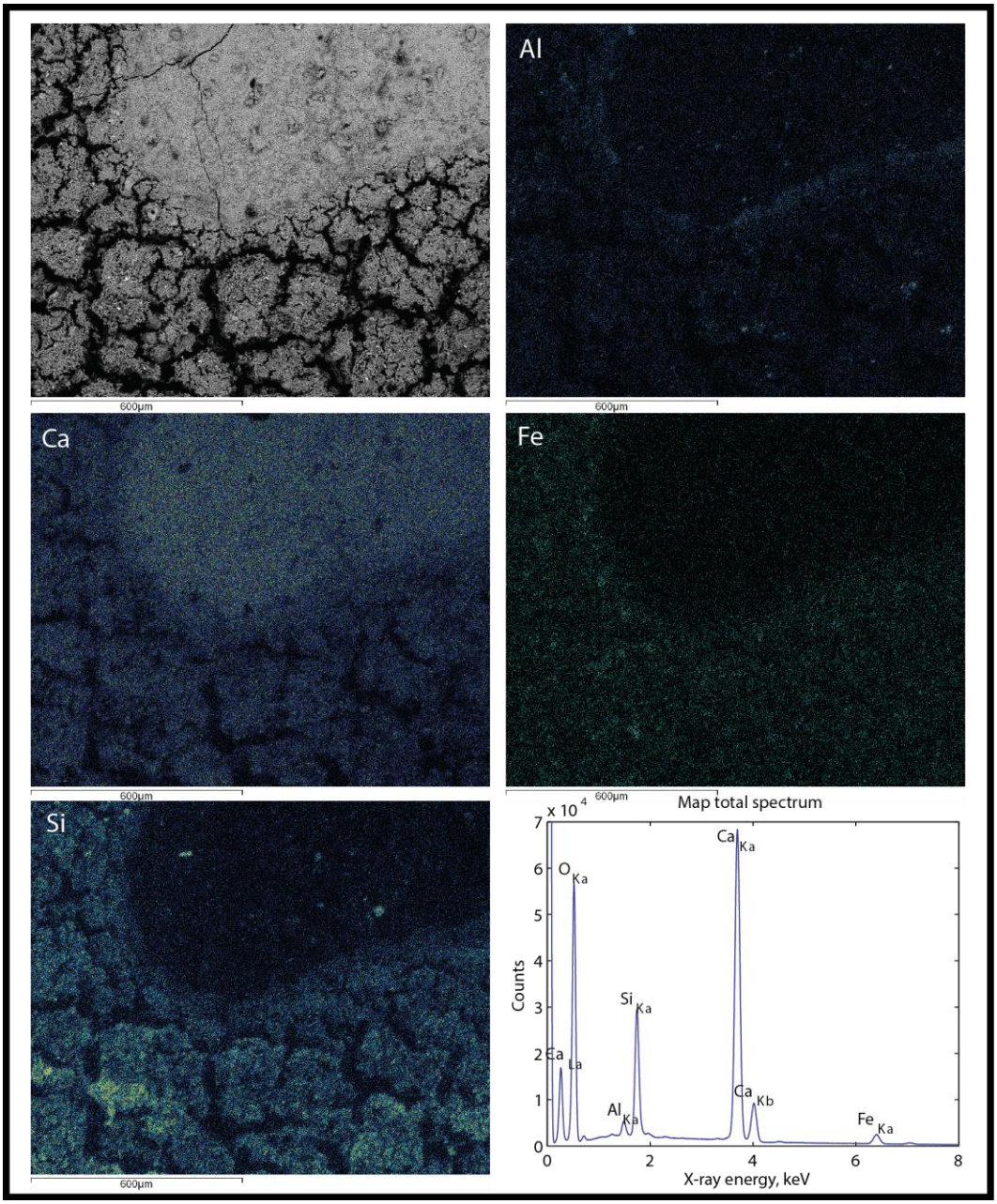

Figure C.13 – (Location A) BSED Image and EDS maps of key elements. Also shown is a plot of the full field EDS spectrum.

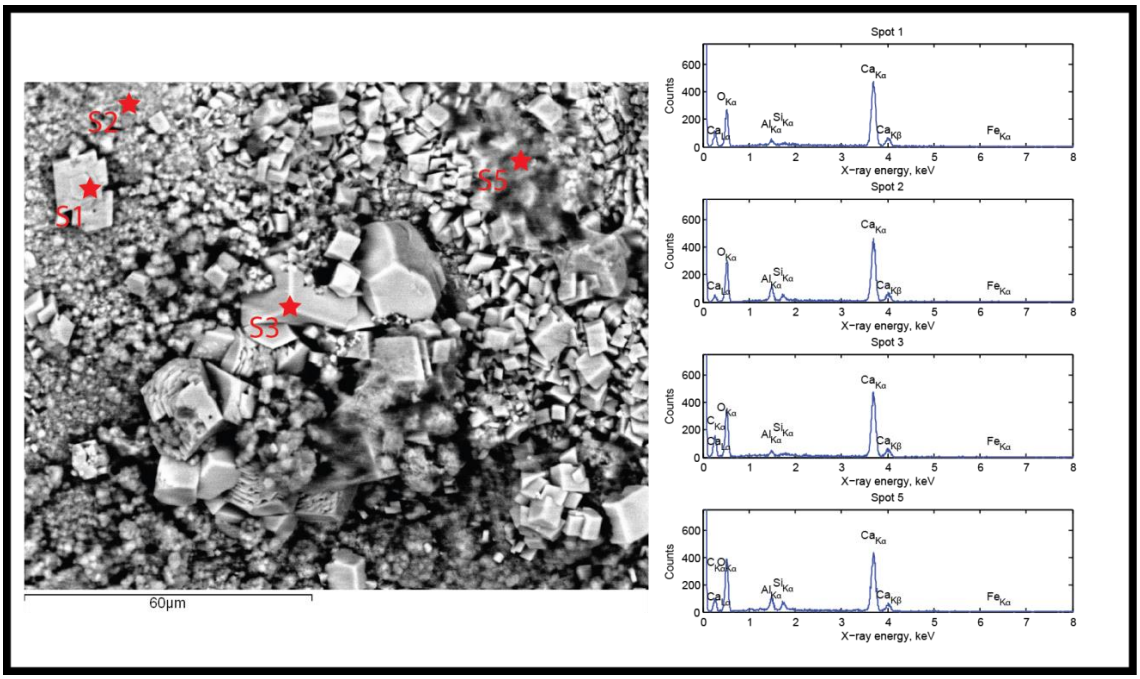

Figure C.14 – (Location A) SEM image and EDS spot measurements of precipitation zone between unreacted cement and reacted channel. In the image are distinct calcium rich euhedral crystals (S1 and S3) anhedral phases that are more aluminum and silicon rich (S2 and S5).

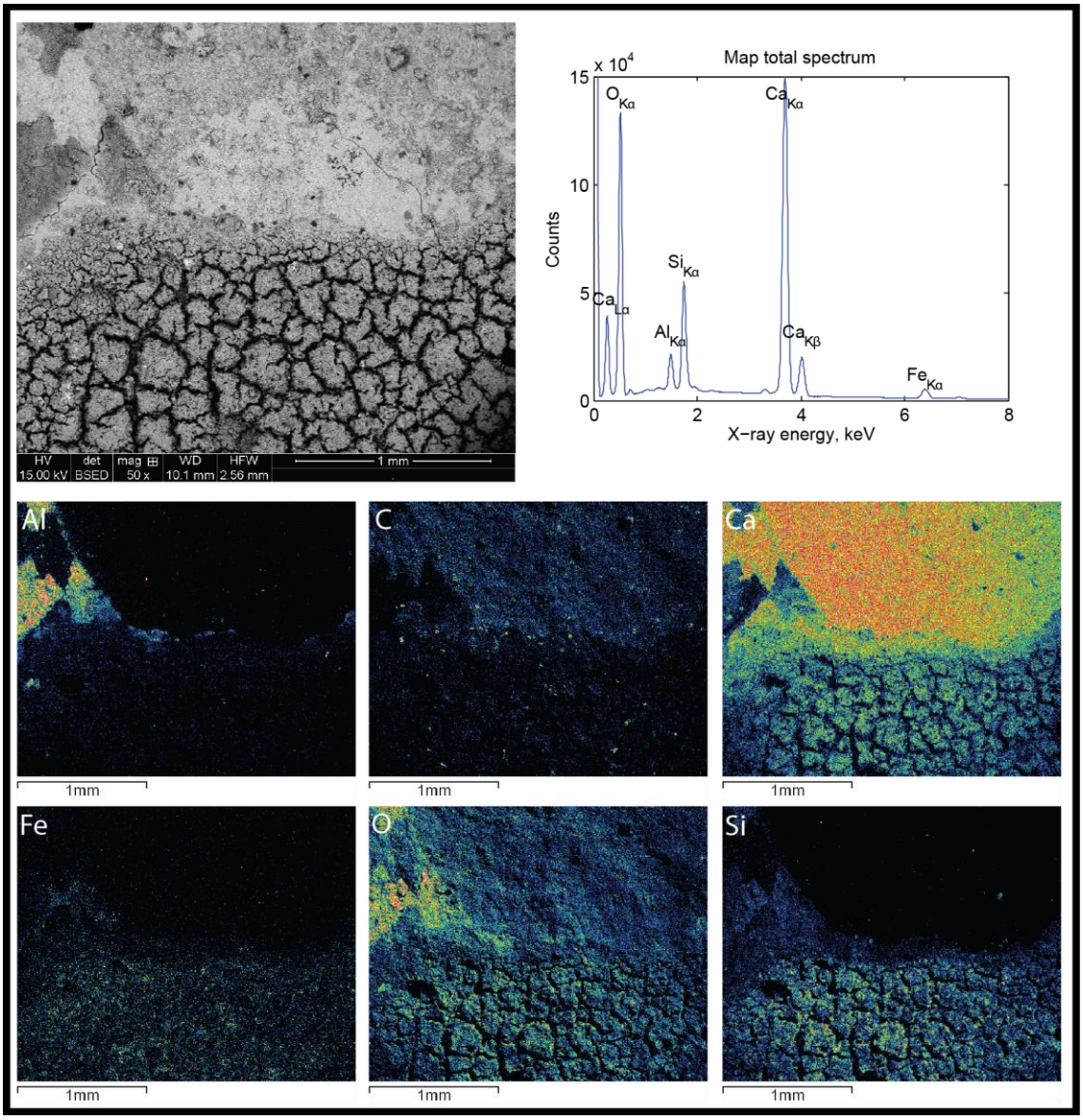

Figure C.15 – (Location B) BSED image of reacted channel and unreacted cement. EDS maps for key elements are also shown. Not that images are rotated so that flow is from right to left.

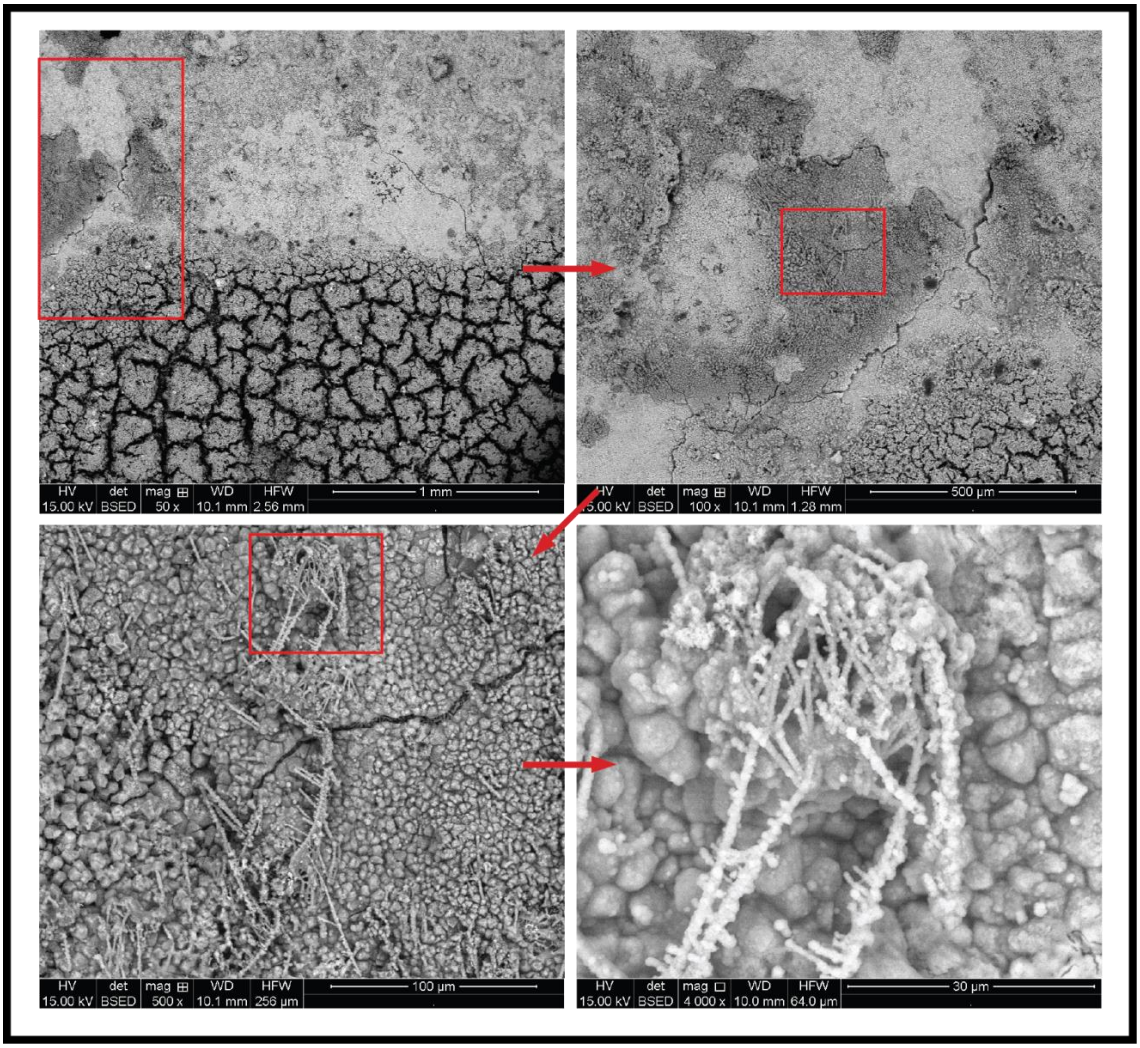

Figure C.16 – (Location B) BSED images of the aluminum rich zone.

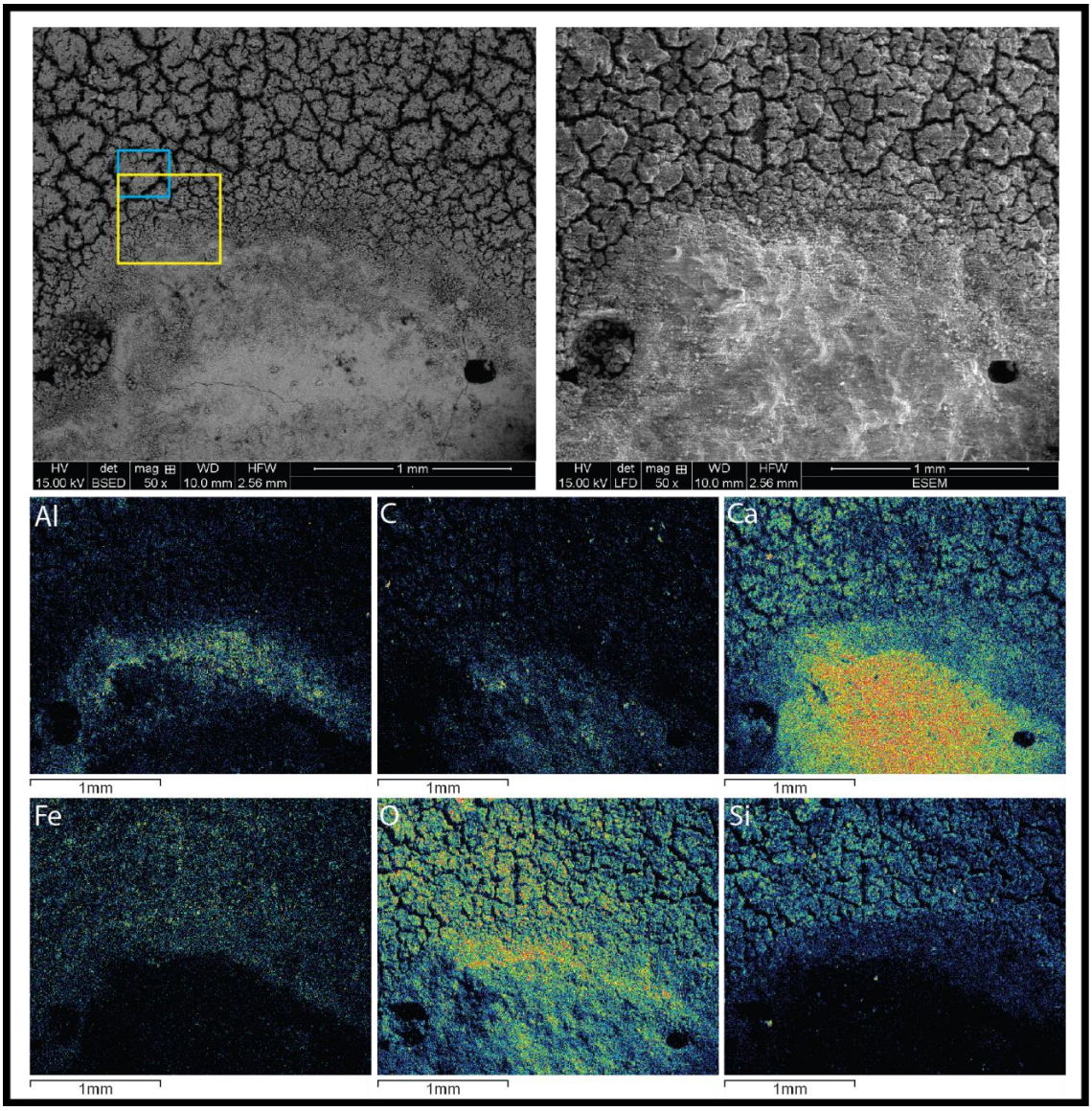

Figure C.17 – (Location C) BSED, LFD, and EDS maps of the reacted channel on the right side of the red box in Figure C.12. Note that the image and maps are rotated 90° clock-wise from the macro scale image.

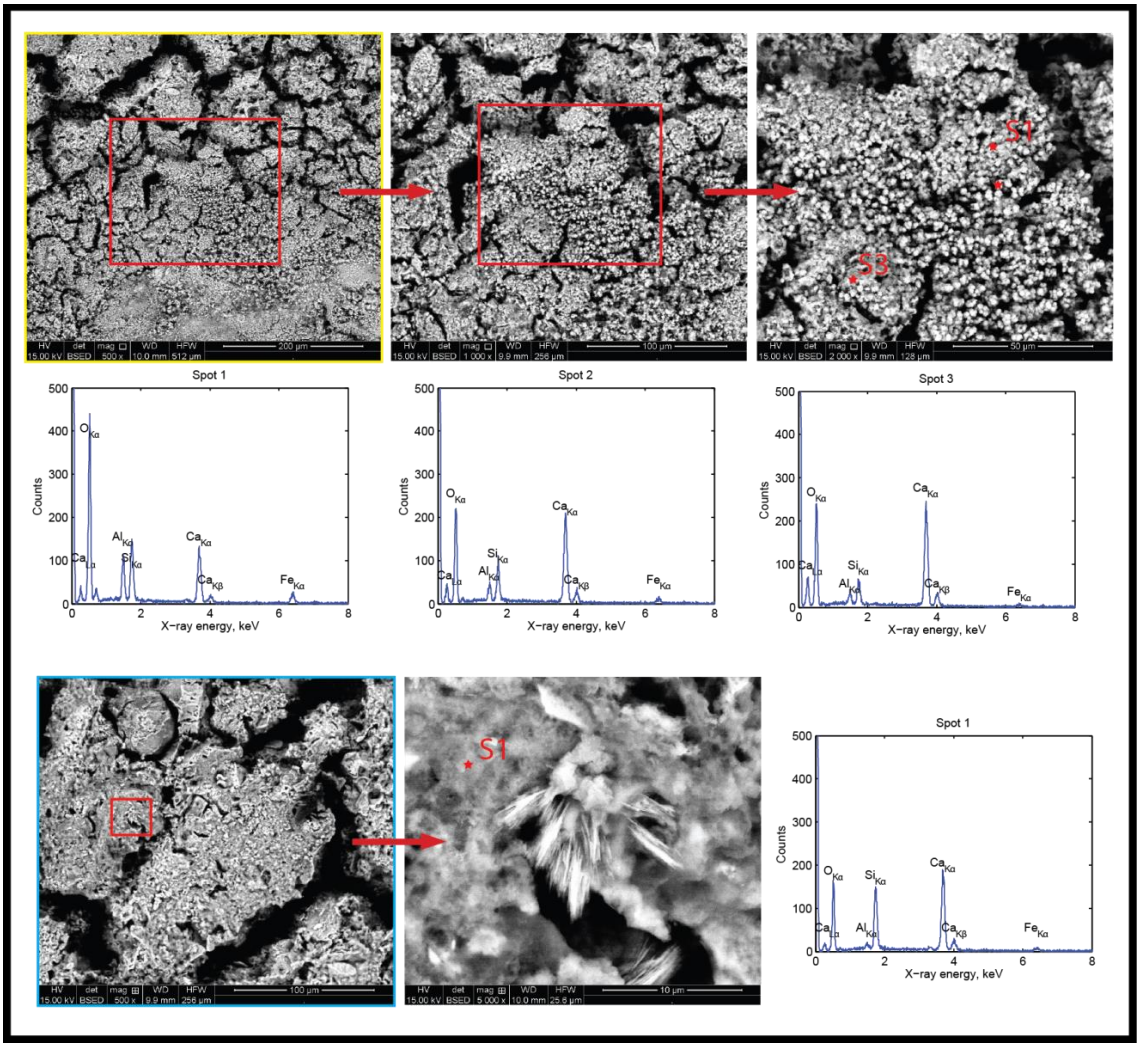

Figure C.18 – (Location C) The location for the yellow box (top) and cyan box (bottom) are shown on Figure C.17. The BSED images show progressively zoomed in section of the transition (yellow) and reacted zone (cyan). Spot EDS analysis show in the transition zone that calcium is dominant but some phases are enriched in aluminum. Silicon is also present in Spot 1 of the transition and reacted zone.

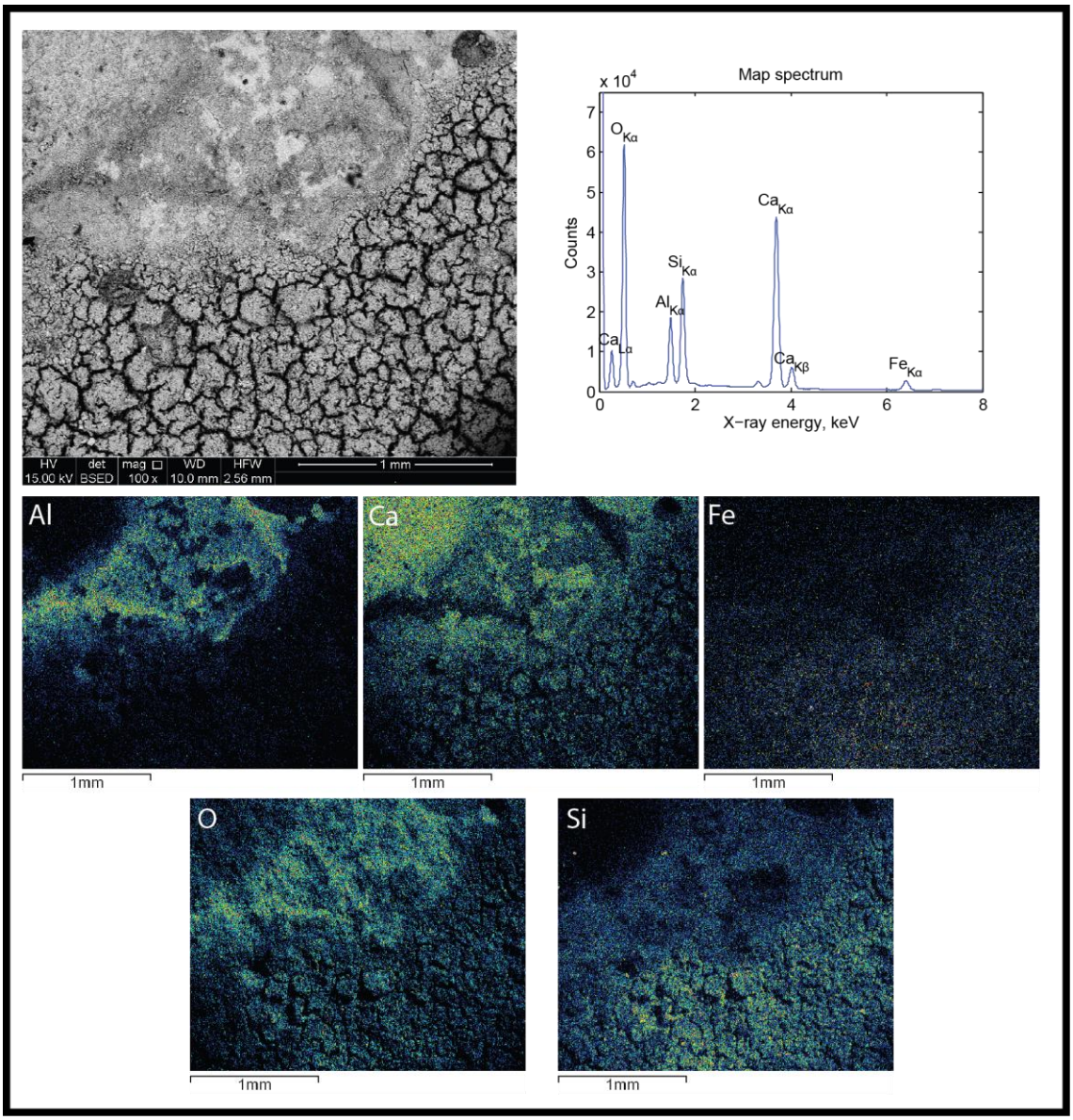

Figure C.19 – (Location C) The BSED image and EDS maps were collected in the upper left corner of Figure C.12. Note that the image and maps are rotated 90° clock-wise from the macro scale image.

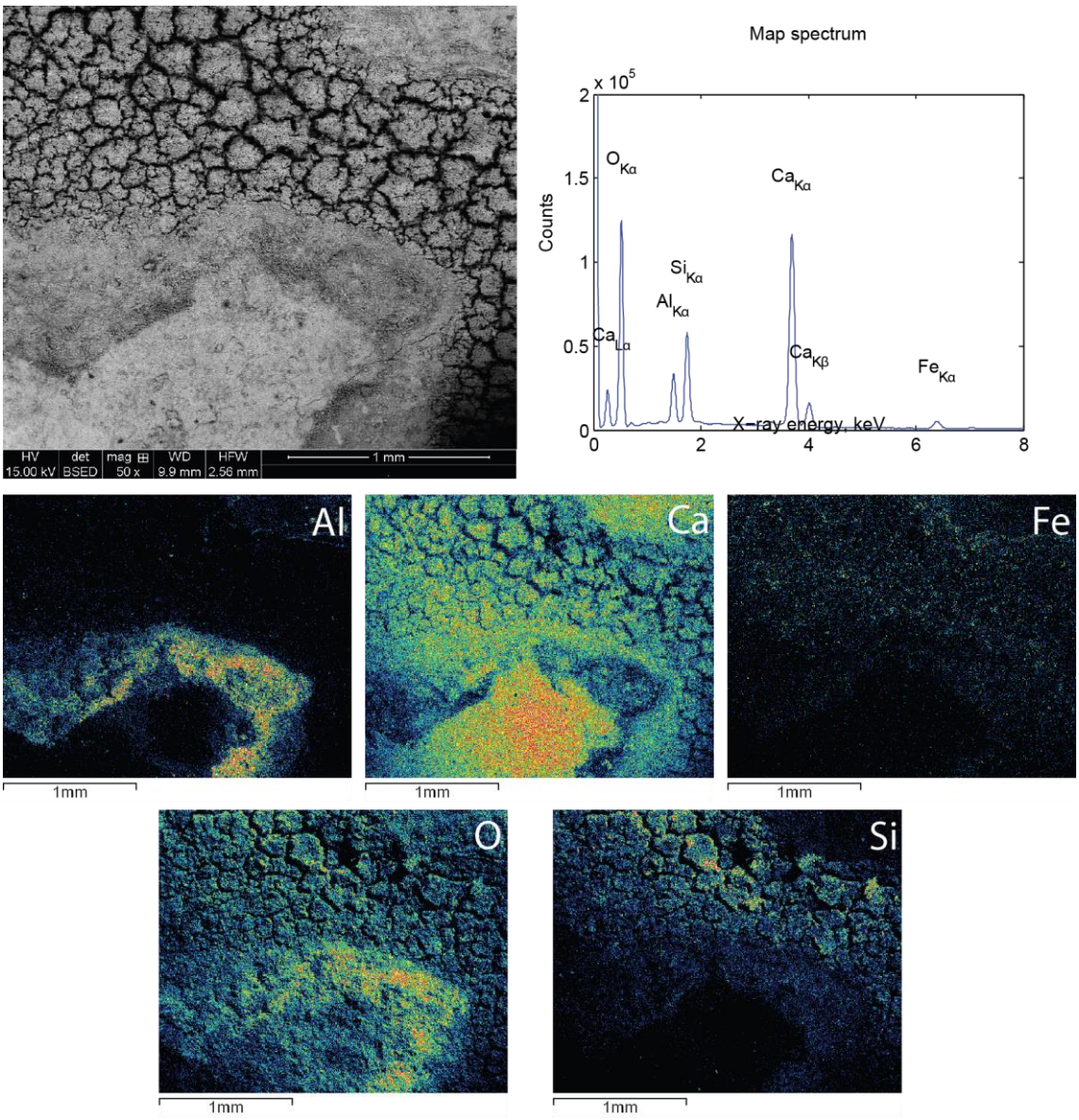

Figure C.20 – (Location D) BSED Image, EDS whole field spectrum and maps showing concentration for select elements.

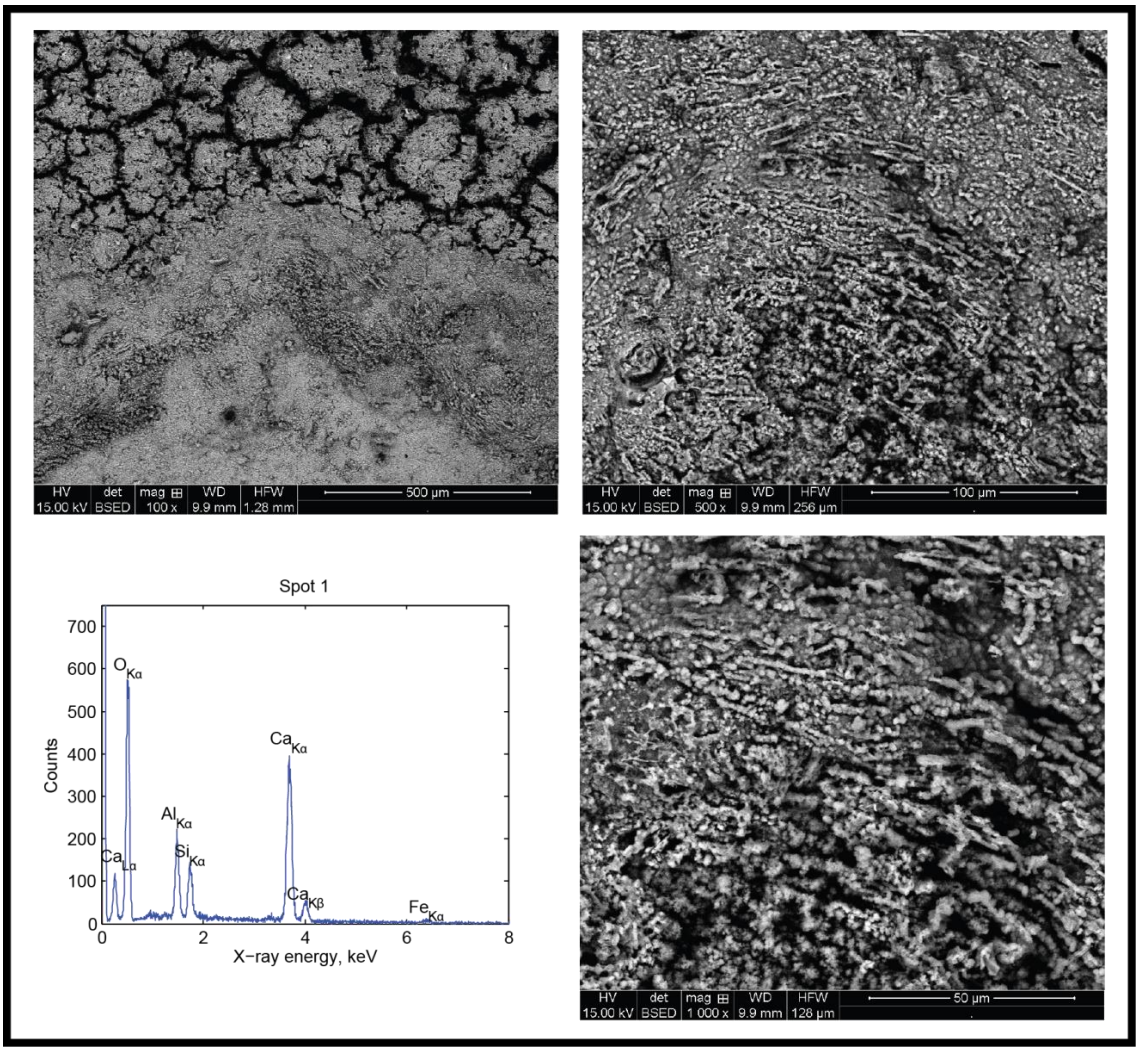

Figure C.21 – (Location D) BSED images of transition zone with distinct mineral precipitation in parallel direction as bulk fluid flow.

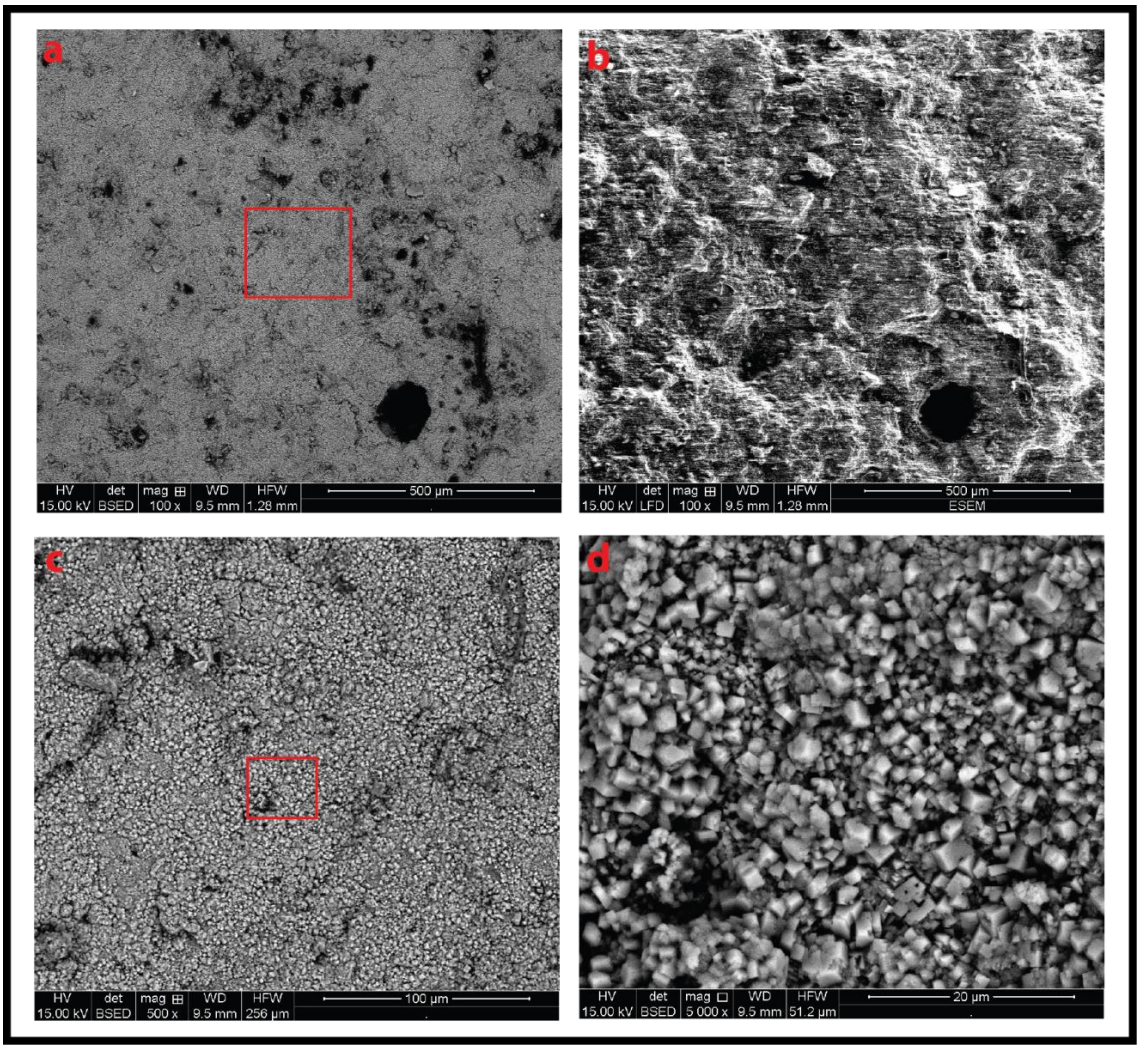

Figure C.22 – (Location E) SEM Images of fracture surface far from reacted channel. (a) Large field BSED image showing unreacted area. Shading indicates relative density with lighter being denser solid. (b) LFD (SE) of same fracture area as a. This image illustrates the local topography of the fracture surface with lighter areas being topographic highs. (c) Zoomed in BSED image from red box in a. Distinct euhedral grains are now visible. (d) Zoomed in BSED image from red box in c. Closer image of euhedral grains. Grains are distinct but very small

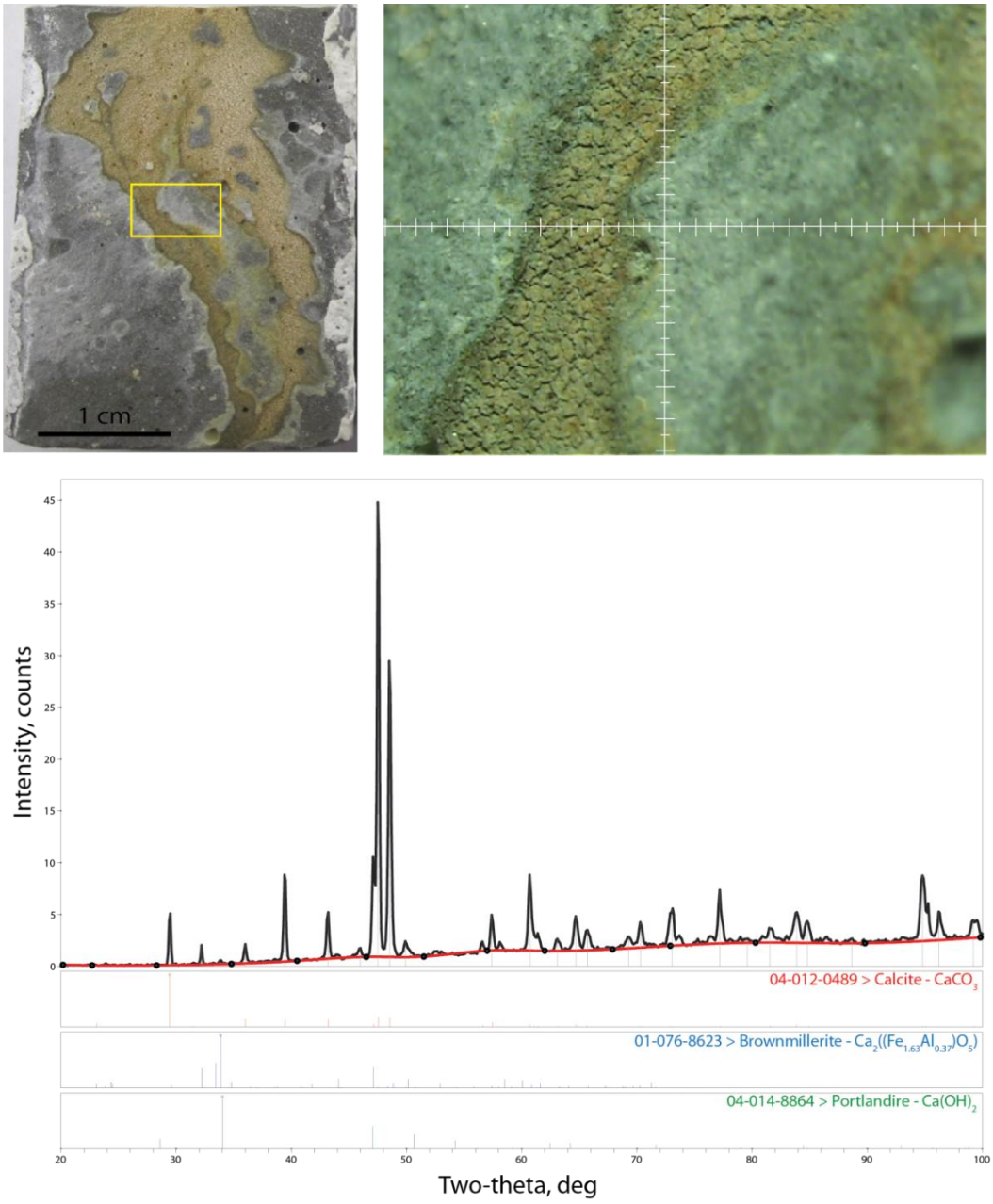

Figure C.23 – μXRD of precipitate just outside of reacted channel. Identified phases were calcite, brownmillerite, and portlandite.

EXPERIMENT REPORT: NA7-11

Summary

Sample NA7-11 was the first experiments where CO_2 rich water was injected into a fractured cement core at elevated pressures. The goal was to test the system and compare behavior the analog HCl experiments. CO_2 rich water (6.38 wt.%) was injected at a constant flow rate of 1.0 mL/min. Pressure differential showed an initial decrease that flattened out during the experiment. Effluent concentrations show an initial spike that decays through the experiment. Calcium is the dominant cation coming out of the cement, with minor silicon and iron. Significant alteration of the fracture surface occurs along a discrete channel. SEM analysis shows three texturally distinct zones and EDS analysis shows a corresponding change in relative elemental concentrations. The most significant change is the relative decrease in calcium in the reacted channel and the relative enrichment of silicon left behind.

Experiment design

The experiment was performed at NETL PGH on the unit A CFS-839Z. The core was sealed using the Teflon tape / heat shrink tubing / aluminum foil / heat shrink tubing approach.

Sample preparation

CO_2 and water mixing procedure

Mixing CO_2 with water was achieved by pushing fluids between two accumulators. First a theoretical maximum CO_2 saturation is estimated for experiment temperature (21 °C), minimum pore pressure (1,100 psi), and brine concentration (0 M or distilled water in this case). Based on the equation of state model developed by Duan and Sun (2003) we expect a saturation of 6.38 wt.% or 1.4486 mol-CO_2/kg-H_2O.

A known volume of water (1,295 mL) was first placed in accumulator 1 based on amount of space needed for the liquid CO_2 before dissolution. Assuming a water density of 1 kg/L, the minimum mass of CO_2 that we need to mix is 82.6 g. Assuming we pull liquid CO_2 using a dip tube cylinder, the CO_2 will have a density of 0.75 kg/L. The theoretical minimum volume of liquid CO_2 we would need is 110 mL.

For this experiment we metered in 500 mL of CO_2 into accumulator 2, though we expect to draw liquid from the via a dip tube CO_2 cylinder (at 21 °C pressure is 850.61 psi. density of liquid is 17.323 mol/L and gas is 4.5971 mol/L) some phase change might occur in drawing from the cylinder to the accumulator. To minimize phase change we used a chiller on the second accumulator at 5°C. After metering in the CO_2 we turned the chiller off and proceeded to mix the fluids.

For mixing purposes we have the pressure of both accumulators at 1,100 psi. We first drive the water into accumulator 2, then both fluids back into the accumulator 1, and finally pushed the fluids back into the accumulator 2. To mix we used two Quizix pumps to drive the fluid from one accumulator and hold back pressure on the receiving accumulator. During mixing it was not uncommon for the accumulator pistons to get stuck and cause pressure spike faulting on the pumps but it is not expected to affect mixing.

On the final change over from the water accumulator to the CO_2 accumulator the piston got stuck and the full amount of water was not transferred into the CO_2 accumulator. Because the water accumulator pushed from the bottom up, all free phase CO_2 was pushed into the CO_2 accumulator thus we assume full saturation of the water used in the experiment. Before conducting the experiment we isolated the accumulators and opened the water accumulator to measure the amount of water not pushed into the

CO_2 accumulator. This mass was 686 g and so we have a maximum of 609 g of water in the CO_2 accumulator to inject during our experiment.

Results

CO_2 saturated water was injected at a flow rate of 1.0 mL/min for 477 min and a total of 477 mL of CO_2-rich water. Confining pressure was an average of 1,519 psi and had standard deviation of 95 psi (Figure C.24). Pore pressure was around 1,100 psi (Figure C.25) and temperature was 21 °C. Based on a theoretical saturation of 6.38% by weight, we inject a total of 691 mmol of CO_2. Pressure differential was recorded during the experiment and effluent was collected for chemical analysis. Alteration on the fracture surface was also photographed and studied using microscopy methods.

Pressure differential and effluent fluid history

Figure C.26 shows the plot of pressure differential, which is the difference between upstream and downstream pressure transducer reading, plotted versus mmol CO_2 injected. Initially the pressure differential is about 0.9 psi which gradually rises to 1.0 psi but is within the signal noise. After about 25 mmol injected the pressure signal begins a constant decrease to about 0.6 psi. After 200 mmol injected the pressure differential begins to slowly build, until ending up at 0.7 psi at experiment completion. Figure C.27 shows estimated hydraulic aperture for the experiment. Hydraulic aperture begins around 43 μm, grows to about 48 μm, and finishes at about 46 μm.

Effluent was collected in 15 intervals of various volume and time. The first measurement collected will contain most of the dead volume in core from DI water flow prior to the experiment starting. Cation and anion concentrations were analyzed and key species are plotted and trends identified below. Figure C.28 shows effluent calcium concentration as a function of total CO_2 injected. Concentration spikes to above 500

mg/L early, then drops to above 300 mg/L, rises back up to a maximum at 550 mg/L and then begins to decrease at a roughly constant trend until finishing above 250 mg/L. Effluent calcium concentration is the dominant species at 500 to 250 mg/L and is typically an order of magnitude higher than other cations. Figure C.29 shows effluent silicon concentration during the experiment. Silicon behaves in a similar matter to calcium, where is its initially low (at 10 mg/L), rises up to a peak (45 mg/L), then begins to decrease until about 300 mmol injected, where there is a significant drop in concentration. Other species following this trend are magnesium, sulfur, and sulfate – though with less significant drops at the 300 mmol mark. Effluent sodium and chloride show initially high concentrations, which quickly drop off and remain fairly flat but also show a drop in concentration at 300 mmol (more so for sodium) and are flat thereafter. Iron (Figure C.30) is anomalously low in overall effluent concentration (0.8 mg/L max at initial reading). Concentration quickly drops down but then builds up to above 0.3 mg/L. Just before the 300 mmol mark it falls off, only to shoot back up after and remain flat at 300 mmol injected. Aluminum is anomalously absent from effluent considering the overall concentration in cement.

Fracture surface analysis

After reaction the sample was removed from the core holder and the core end were separated. During separation it is not uncommon for the cement cores to crack either normal to the core length or at the edges where the sample was caulked. Figure C.31 shows an image of fracture surface taken with a digital camera. The right side illustration shows three distinct zones, where the white area was sealed from flow by caulk, grey is identified by unreacted cement, and black is the reacted zone.

In this sample a distinct reacted channel forms in which the flowing pathway is smaller than the overall width of the fracture. The reacted zone is broad toward the inlet and narrows as it reaches the outlet. There are two types of transition zones. On the left side the reaction zone is narrow while on the right side the transition zone is broader. (Narrow zone like HCl did not see broad zone in HCl experiments) (Also in SEM the narrow zone often looks like ppt while the broad zone looks like dissolution).

SEM imaging shows the textural and elemental changes occurring at key locations on the fracture surface. Figure C.32 shows BSE images at a bend in the reacted channel (Figure C.31 – Location A) that distinctly shows the transition from reacted zone into transition zone (blue line). Key textural differences are that in the reacted zone fine grained material is separated by sub-polygonal cracks on the surface, in the transition zone the minerals are much larger and often form euhedral to sub-euhedral rhombs that sometimes show distinct lineation (Figure C.32 – Right image). Figure C.33 shows BSE images taken little farther toward the outlet on the same side as previous figure (Figure C.31 – Location B). These images are a good example of the sharp transition in texture that can occur between reacted and transition zone. Figure C.34 shows BSE images taken near outlet (Figure C.31 – Location C). These images show a good example of textures that are more indicative of the broad transition zone. Here the minerals, while still being well developed, look flat on the surface. Figure C.35 shows BSE images from another location near outlet (Figure C.31 – Location D). In this transition zone the minerals have a distinctly chewed texture and what might be cleavage planes are shown as the minerals are eroded (red arrows). Figure C.36 shows BSE (Top left) and SE (Top right) images of near the inlet (Figure C.31 – Location E). Note that these images are flipped from the standard convention so that flow is upward. Top left BSE image shows the sharp transition between zones. In transition and unreacted zone large euhedral crystals are

present. Lineations that move through transition zone in a direction normal to bulk fluid flow are also present. SE image (top right) gives a better estimate of the topography and roughness of the fracture surface. EDS maps for key elements show that calcium (middle left) is relatively depleted in channel, while silicon (middle right) is relatively enriched compared to the unreacted cement. Minor elements aluminum and iron have same behavior as silicon.

Discussion

Results show that reaction is occurring despite being dominated by advection (residence time is only 4.08 sec). There is much evidence for dissolution of cement phases, from development of a distinct reacted channel that is bounded by narrow and broad reaction zones to large amount of calcium leaving system. However there is less evidence for precipitation. There is less development in the reacted zones and no pressure signal. One possible reason for the lack of a pressure signal is the presence of portlandite in the fracture surface before the experiment began. The sample was kept in water after fracturing and caulking but before reaction and portlandite was likely to have precipitated in the fracture. This would have given a channel that was initially more restricted to flow than an open fracture and since portlandite would easily dissolve and not leave behind the silica rich material it would have easily looked like the pathway was opening up or not altering because of precipitation would balance dissolution. There is the additional issue that while the pH is relatively higher than most of the HCl experiment, there was much more CO_2 in the system that can act as a buffer to keep pH in the low range where secondary minerals are still soluble and thus prevent significant precipitation before the calcium is flushed from the system.

Additional information

None for this sample.

Tables and figures

Table C.5 – **NA7-11** experiment parameters.

Core dimension (width × length), cm	2.54 × 6.25
Temperature, °C	21
Average confining pressure (std. dev.), psi	1,519 (95)
CO_2-saturation, wt. %	6.38
Flow rate, mL/min	1.0
Pressure differential, psi	0.9
Hydraulic aperture, μm	43
Sample permeability, mD	317
Total time, hr	8
Residence time, sec	4

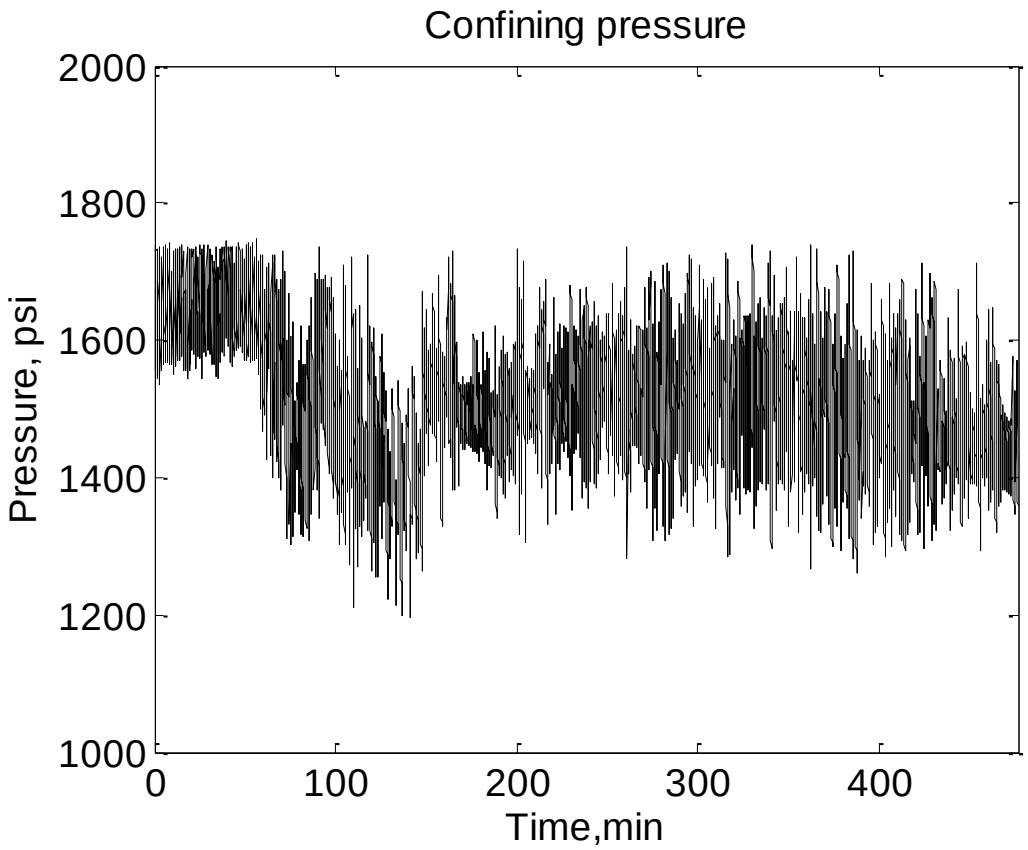

Figure C.24 – Confining pressure as a function of time. Average confining pressure during this experiment was 1,519 psi with a standard deviation of 95 psi.

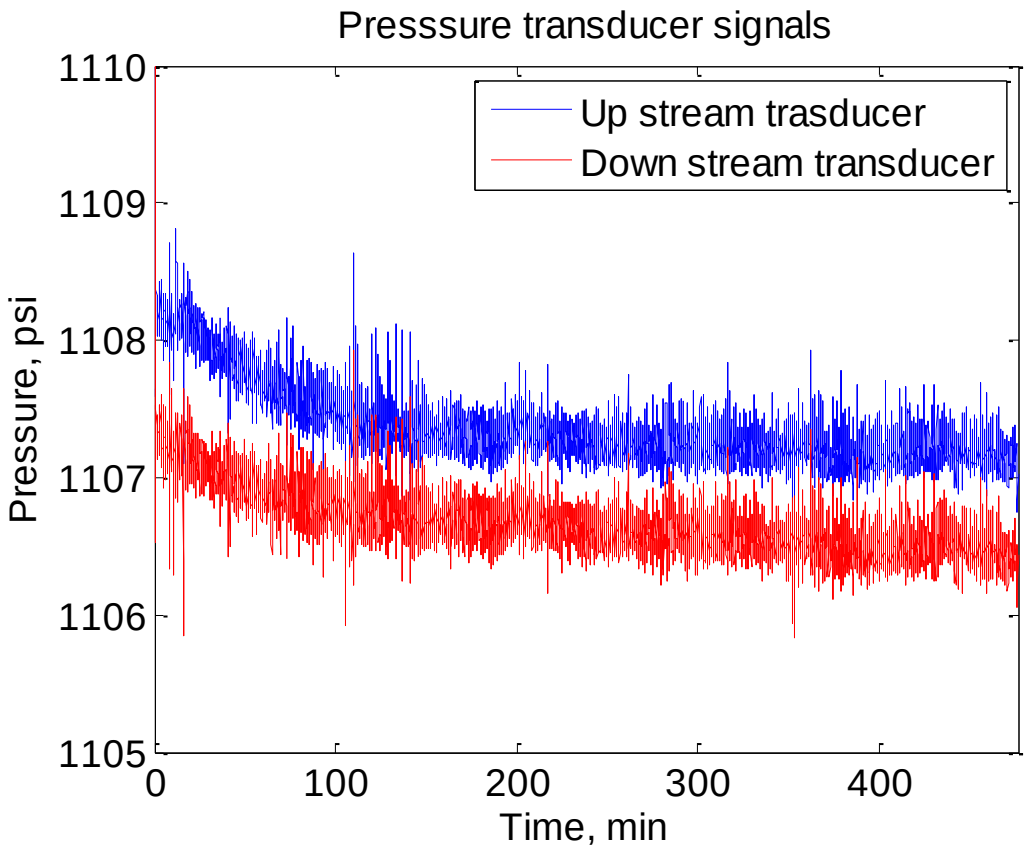

Figure C.25 – Upstream (blue) and downstream (red) pressure as a function of time during experiment. The shallow decrease in pressure signals is probably related to the digital back pressure regulator but does not affect experiment.

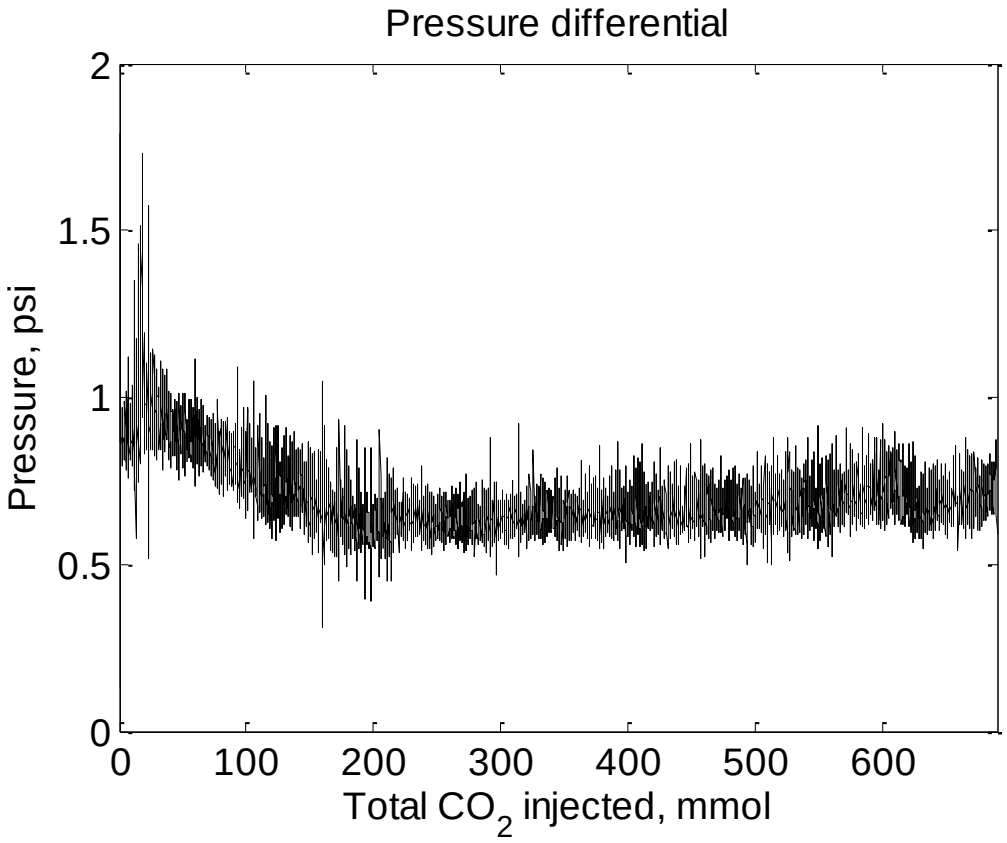

Figure C.26 – Pressure differential as a function of total CO_2 injected. While there is a small decrease in the signal which flattens out the overall signal doesn't change much overall.

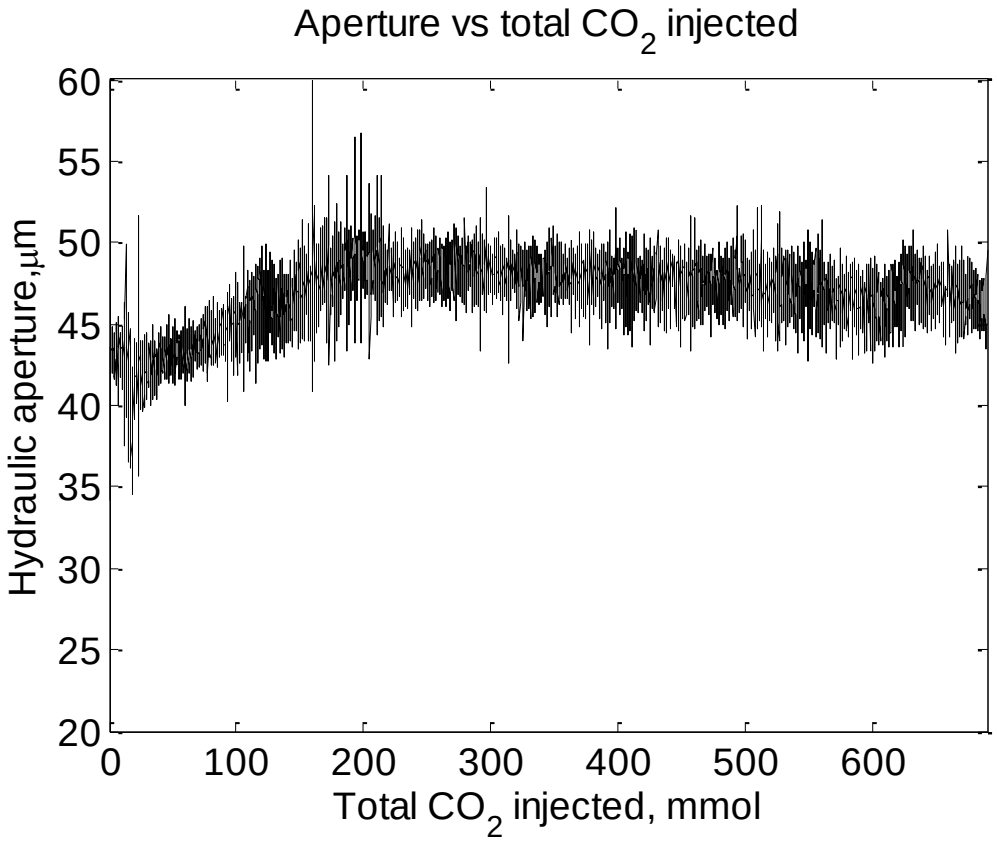

Figure C.27 – Estimated hydraulic aperture as a function of total CO_2 injected.

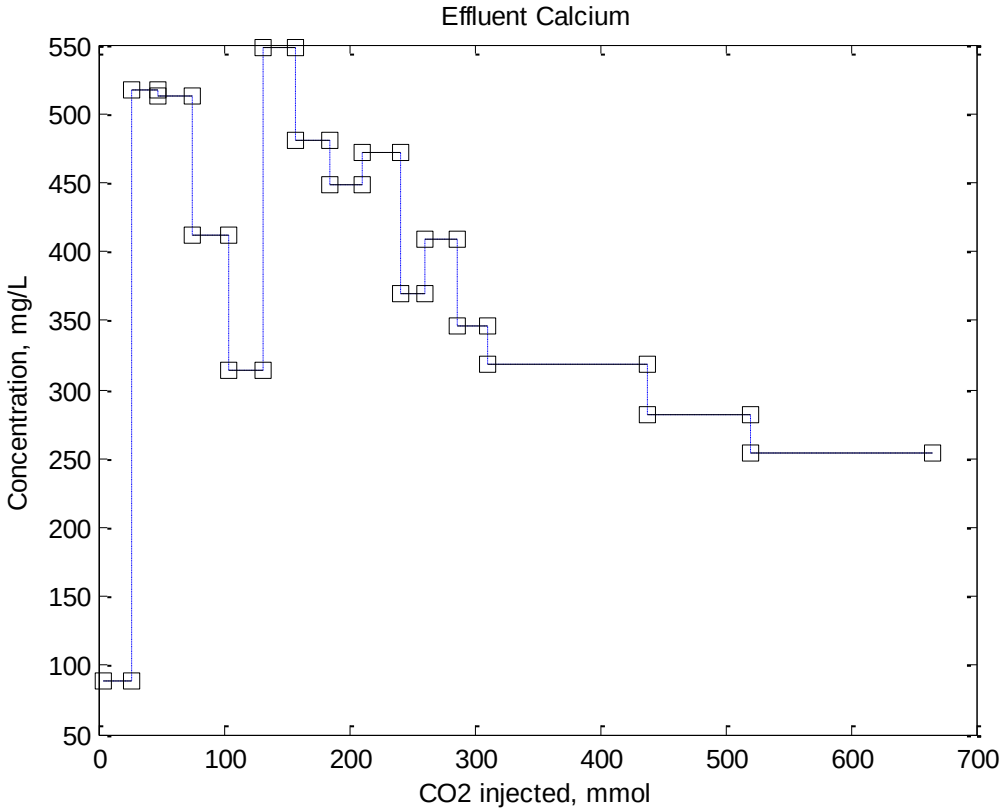

Figure C.28 – Effluent calcium concentration as a function of total CO_2 injected.

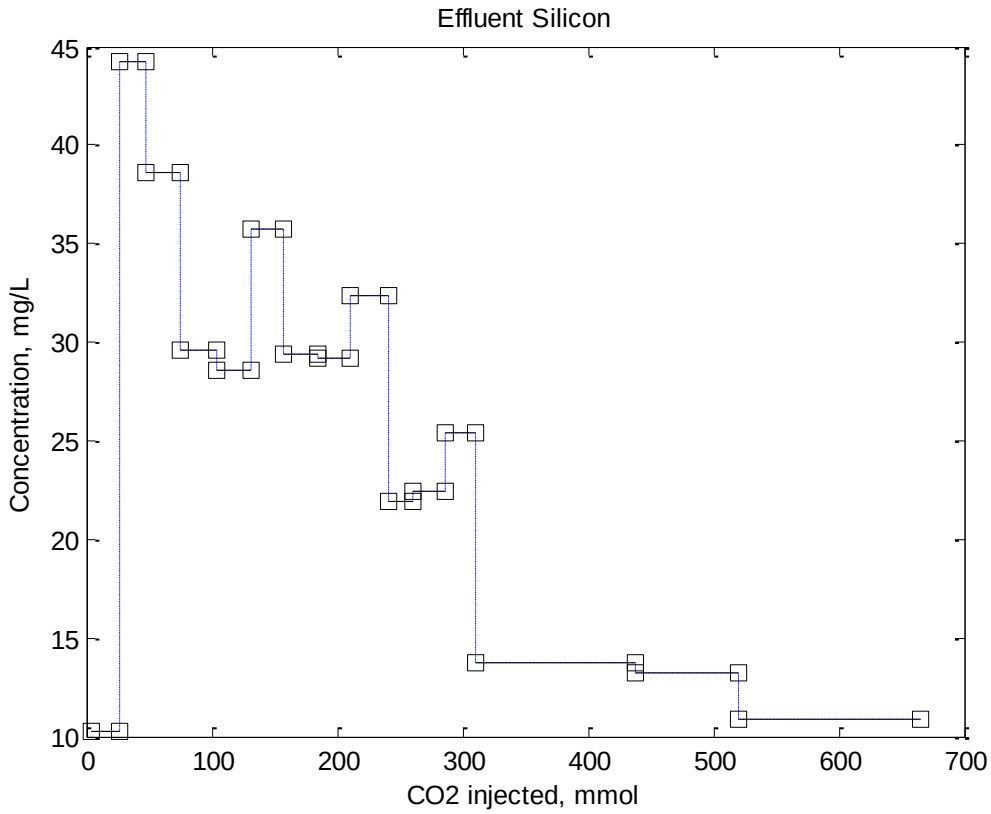

Figure C.29 – Effluent silicon concentration as a function of total CO_2 injected.

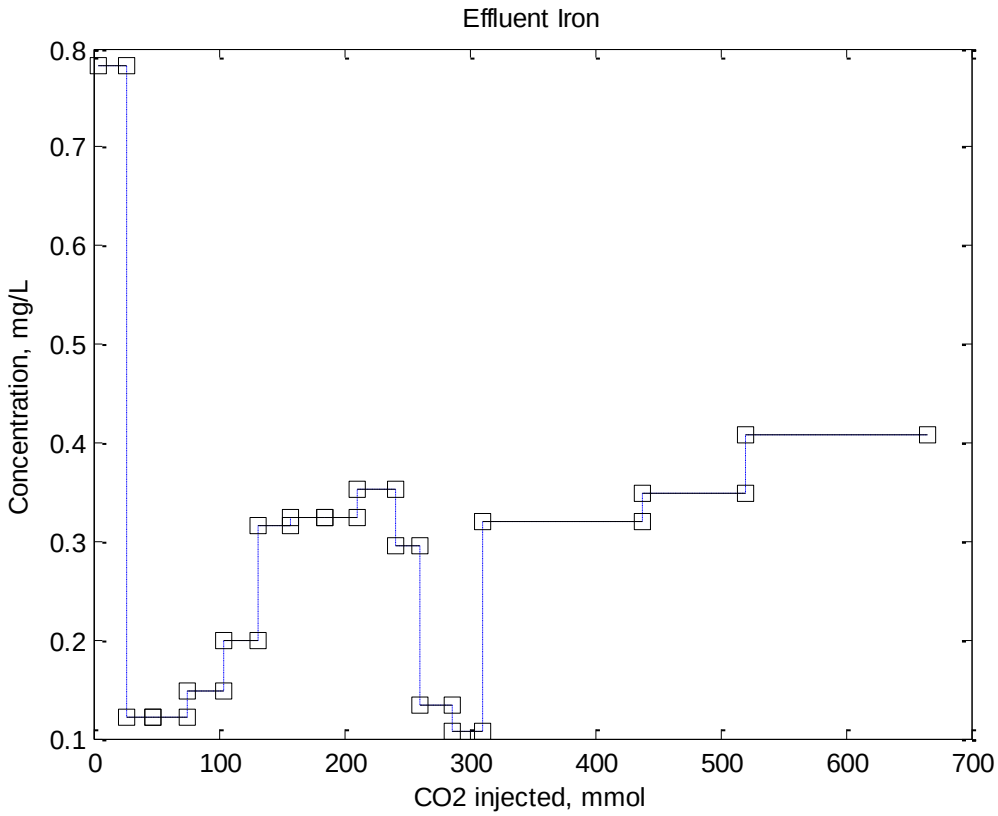

Figure C.30 – Effluent iron concentration as a function of total CO_2 injected.

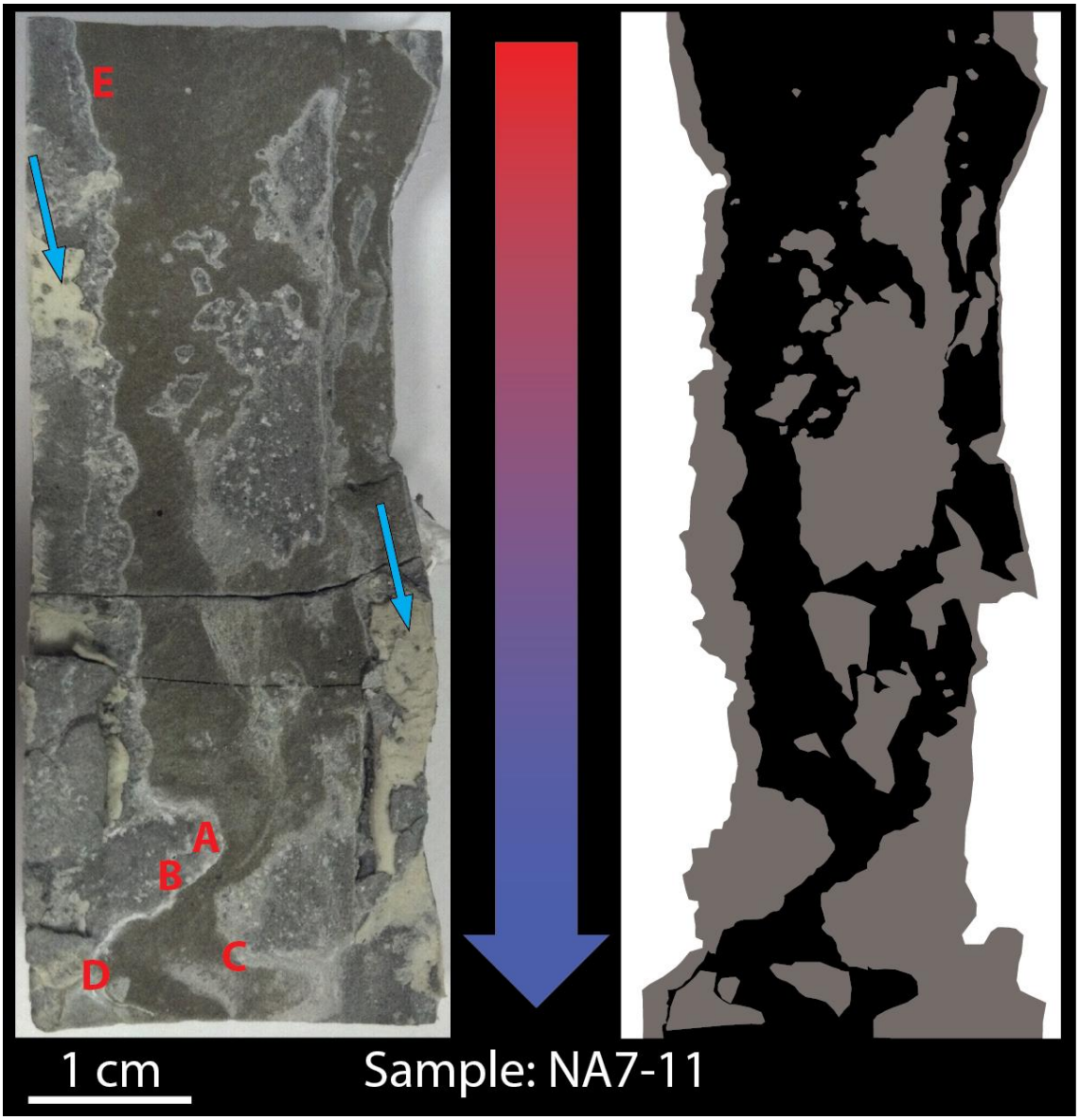

Figure C.31 – (Left) Image of fracture surface showing reacted pathway. Blue arrows show caulk used to seal fracture sided. Red letters show locations looked at with SEM. (Right) Manual identification of zone with caulk (white), unreacted cement (grey), and reacted channel (black).Flow is from top to bottom.

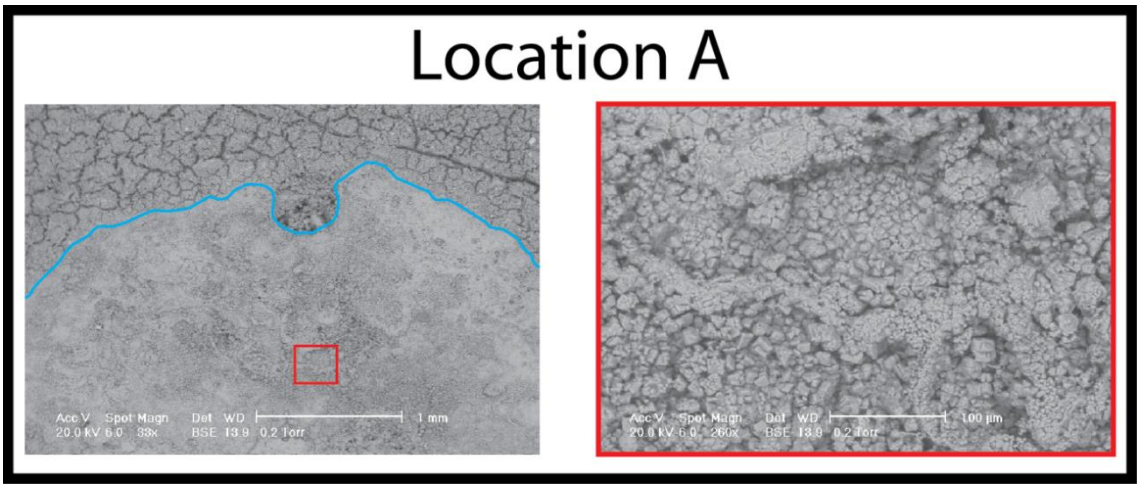

Figure C.32 – BSE images of fracture surface at Location A. Left image shows the boundary (blue line) between the reacted zone on the top of the image and the transition zone below. Red box is zoomed in on figure to right which shows distinct rhombohedral minerals.

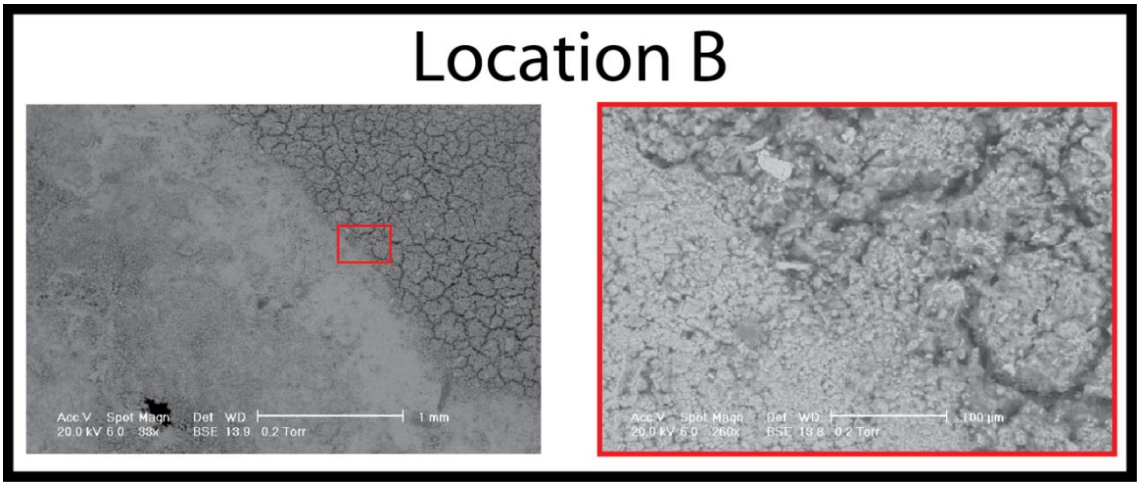

Figure C.33 – BSE images of fracture surface at Location B. Left image shows boundary between reacted zone on right and transition zone to the left. Red box is zoomed in on the image to the right. Reacted zone material is more fine grained and characterized by distinct sub polygonal cracks on surface.

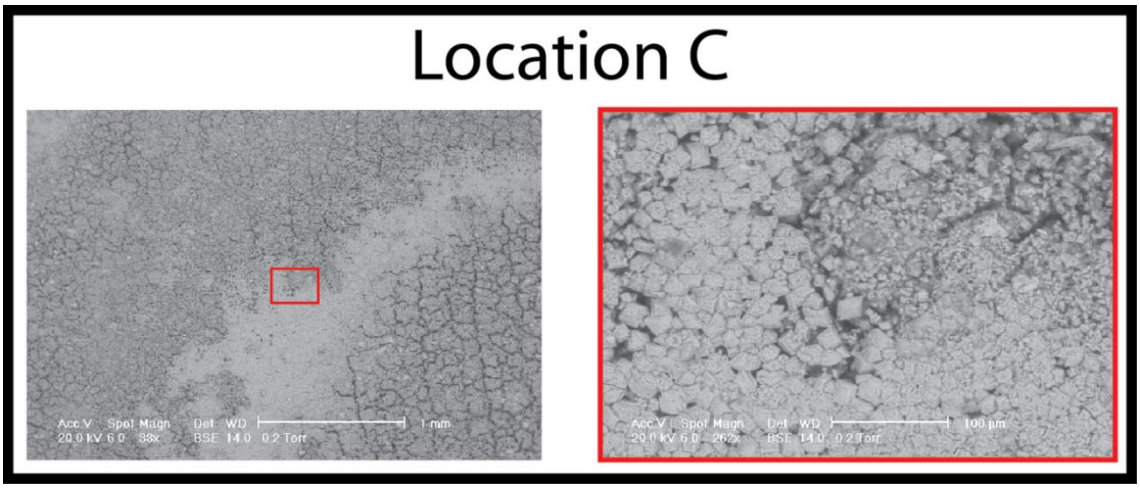

Figure C.34 – BSE image of fracture surface at Location C. This image is from near the outlet and shows active alteration occurring. The red box is shown in the zoomed in image to the right. In this image the rhombohedral grains looks like they are flat on the surface.

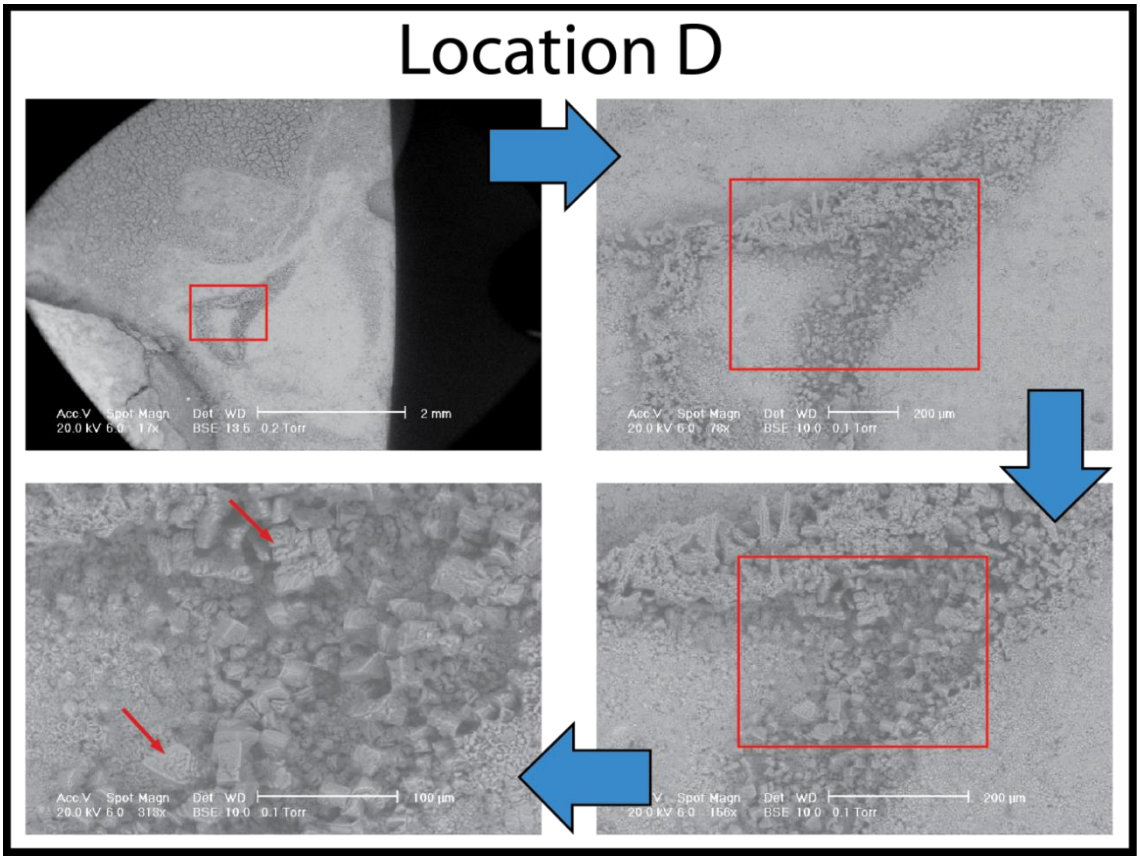

Figure C.35 –BSE images near outlet (Location D). Top left image is a low magnification image of the reacted zone. The red box is blown up in the top right image and shows a zone of distinct minerals. Zooming further into the red box we have the bottom right image and zooming one more time we have the bottom left image. In this final image we can see evidence of minerals being eroded from their euhedral crystal shape and possibly still showing cleavage planes of mineral (red arrows).

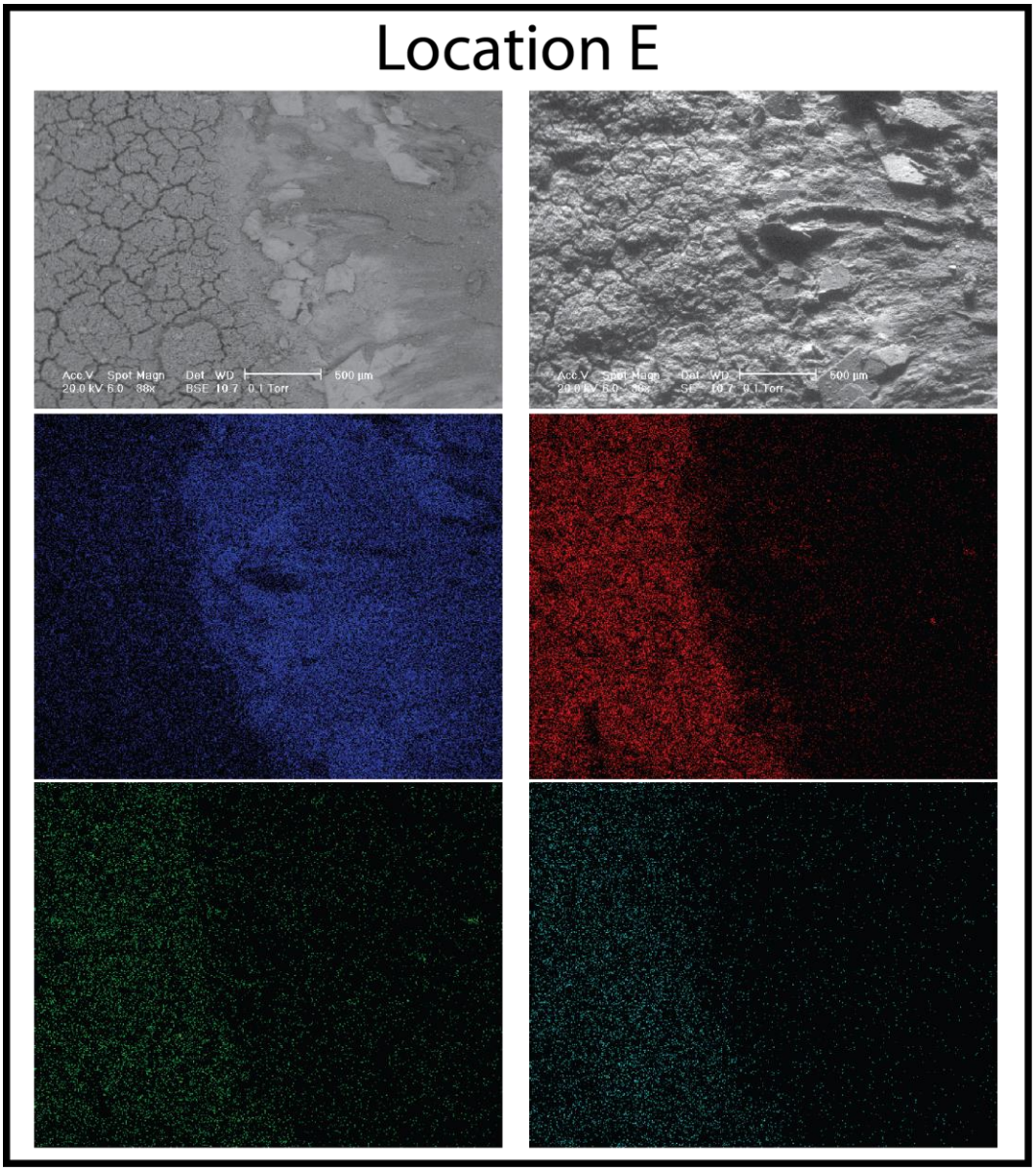

Figure C.36 – Top left is a BSE image near inlet and flow is from bottom to top. In this image distinct reacted channel is shown on left, with unreacted zone on right and transition zone in between. Distinct euhedral minerals are present in these latter two zones as is a streaking texture running normal to the bulk flow direction. Top right image is a SE image of same area. The topography of the fracture surface is much more distinct. ESD image maps of key elements are calcium (middle left), silicon (middle right), aluminum (bottom left), and iron (bottom right). In the reacted channel calcium becomes relatively depleted, while silicon becomes relatively enriched. Iron and aluminum are more minor components but show same trend as silicon.

EXPERIMENT REPORT: QB4-3

Summary

Sample QB4-3 was an experiment where CO_2 saturated water was injected into a fractured cement core at constant rate. The cement was mixed and prepared according to the standard method. The resulting core was split using the Brazilian method and contained a single fracture. Injection of CO_2 rich water was at a constant flow rate of 0.25 mL/min. Experiment lasted 3,034 minutes with 759 mL of fluid injected. Downstream pressure was fixed at 1,025 psi and anomalously increased up to 1,250 psi before falling back down to 1,025 psi. Upstream pressure changed correspondingly so the overall pressure increase did not affect the pressure differential. Confining pressure was stable with an average of 1,528 psi with a standard deviation of 68 psi. Sample and fluid were kept at temperature of 21 °C, brine (NaCl) concentration was 0 M (distilled water), and CO_2 saturation was calculated to be 6.34 wt.% or 1.4402 mol-CO_2/kg-H_2O. A total of 1,093 mmols of dissolved CO_2 was injected during the experiment.

Pressure differential showed noisy but constant pressure and was only slightly affected by the large pore pressure increase during the experiment. Effluent concentrations show large initial spikes that generally decay through the experiment. Calcium is the dominant species coming out of the cement, with minor silicon and iron. Significant alteration of the fracture surface in a discrete channel occurs.

During the experiment calcium is progressively leached from the cement phases and transported out of the core as we have seen in the previous experiments using HCl.

Experiment design

The experiment was performed at NETL Pittsburgh on the CFS-839Z 'B unit'. The core was sealed using the Teflon tape / heat shrink tubing / aluminum foil / heat shrink tubing approach.

Sample preparation

CO_2 and water mixing procedure

For this experiment CO_2 mixing was achieved by pushing fluids between 2 accumulators. First a theoretical maximum CO_2 saturation was calculated for a given temperature (21 °C), minimum pore pressure (1,025 psi), and brine concentration (0M or distilled water in this case). Based on the equation of state model developed by Duan and Sun (2003) a saturation of 6.34 wt.% or 1.4402 mol-CO_2/kg-H_2O is expected.

Distilled water (1,000 mL) was placed in 1 accumulator based on amount of space needed for the liquid CO_2 before dissolution. Assuming a water density of 1 kg/L, the minimum mass of CO_2 that is needed to mix is 63.4 g. Also assuming liquid CO_2 is pulled into the accumulator using a dip tube cylinder, the CO_2 will have a density of 0.75 kg/L at (21 °C). The theoretical minimum volume of liquid CO_2 needed to achieve saturation is 84.4 mL.

In this experiment the 2nd accumulator was not chilled and because there is a small pressure decrease when moving the CO_2 from the tank to the accumulator a phase change did occur, i.e. some CO_2 became gas phase during the transfer. Because of this issue, in this experiment 503 mL of (mixed phase) CO_2 was drawn into the 2nd accumulator. After metering the CO_2 the cylinder was compressed to 1,000 psi and the remaining volume left was 137.8 mL, so more than enough to achieve CO_2 saturation.

For mixing purposes we have the pressure of both accumulators at 1,000 psi. We first drive the water into the CO_2 accumulator, then both fluids back into the brine accumulator, and finally pushed the fluids back into the CO_2 accumulator. To mix we used 2 Quizix pumps to drive the fluid from one accumulator and hold back pressure on the receiving accumulator. During mixing it was not uncommon for the accumulator pistons to get stuck and cause pressure spike faulting on the pumps but it is not expected to affect results.

Results

CO_2 saturated water was injected at a flow rate of 0.25 mL/min for 3,034 min and a total of 759 mL of CO_2-rich water. Confining pressure was an average of 1,528 psi and had standard deviation of 68 psi (Figure C.37). Up and down stream pressure were stable for most of the experiment (~1,025 psi) except from 430 to 840 minutes, where pore pressure increased to 1,240 psi (Figure C.38). Based on a theoretical saturation of 6.34 wt.%, a total of 1,093 mmol of CO_2. Pressure differential was recorded during the experiment and effluent was collected for chemical analysis. Alteration on the fracture surface was also photographed. Mineral phases were identified using μXRD analysis.

Pressure differential and effluent fluid history

Figure C.39 shows the plot of pressure differential, which is the difference between upstream and downstream pressure transducer reading, plotted versus mmol CO_2 injected. The small signal to noise ratio yielded some negative values of pressure differential. Those values were made positive, as the equation for calculating aperture does not allow for a negative pressure differential. Hence there is a slight skew of the noisiest data to the positive spikes. Initially the pressure differential is 0.1 psi to 0.2 psi. The data shows no clear change in pressure differential during the experiment. The small

overall rise in signal around 200 mmol CO_2 injected is related to the overall rise in pore (and therefore effective) pressure. Noise in the system spans from below measureable values to up near 0.4 psi. Figure C.40 shows estimated hydraulic aperture for the experiment. Hydraulic aperture is between 40 μm and 80 μm (average 50 μm) for most of the experiment. The magnitude of the noise yields a large aperture estimations, though the true aperture was not swinging by orders of magnitude change during the experiment and was subject only to changes smaller than the system noise.

Effluent was collected in 16 intervals of various volume and time. The first measurement collected contained most of the dead volume in the equipment core from water flow prior to the acid experiment starting. Cation and anion concentrations were analyzed and key species are plotted and trends identified below. Figure C.41 shows effluent calcium concentration as a function of total CO_2 injected. Concentration spiked early to 770 mg/L and then dropped to above 600 mg/L until about 500 mmol CO_2 injected. Effluent calcium concentration then went through a series of oscillations between low values below 400 mg/L and high values at 500 mg/L or above. Calcium is the dominant cation in the effluent samples. Figure C.42 shows effluent silicon concentration during the experiment. Silicon behaved in a similar matter to calcium, where it was initially low (at 23 mg/L), rose to a peak (101 mg/L), then begins to decrease until flattening out around 20 mg/L. Other species (not plotted) following this trend were magnesium, nickel, chloride, and sulfur – with the first 2 actually having concentrations above the silicon spike concentration. The iron concentration (Figure C.43) had a high initial concentration like other cations but after the spike, slightly increased during the remainder of the experiment and had a generally low concentration. Aluminum was anomalously absent (concentration below detection limit) from effluent considering the overall concentration in cement.

Fracture surface analysis

After reaction the sample was removed from the core holder and the core halves were separated. During separation it was not uncommon for the cement cores to crack either normal to the core length or at the edges where the sample was caulked. Figure C.44 shows an image of fracture surface taken with a digital camera. The right side illustration shows 3 distinct zones, where the white area was sealed from flow by caulk, grey is identified by unreacted cement, and black is the reacted zone.

This sample has a broad reacted channel that is nearly the entire width of the fracture. There is one constriction in the reacted channel width about 75% the way down. On this constriction there is significant white material.

Figure C.45 shows the location on the fracture chosen for μXRD analysis and resulting minerals identified. Calcium carbonates and portlandite were identified as precipitates on the fracture surface.

Discussion

Despite significant evidence for reaction based on effluent concentration there was no significant change in the pressure differential during the experiment. Even though there is also significant reaction across the entire width of the flow path for most of the sample and several tight flow restriction points, it had no apparent effect on hydraulic aperture. Precipitation seems restricted to the zones where flow is very low (small aperture or no flow sides where the fracture was sealed with caulk.

This experiment can be considered a very reactive case where large volumes of acidic fluid was injected into the core and the fact that there was no significant decrease in pressure differential was evidence that self-enhancing of the flow path did not occur. While the pressure differential was low and near detection limit (large amount of noise), the mean of the pressure differential was well above detection limit.

Additional information

None for this sample.

Tables and figures

Table C.6 – **QB4-3** experiment summary.

Core dimension (width × length), cm	2.54 × 7.24
Temperature, °C	21
Average confining pressure (std. dev.), psi	1,528 (68)
CO_2-saturation, wt. %	6.34
Flow rate, mL/min	0.25
Pressure differential, psi	0.2
Hydraulic aperture, μm	47
Sample permeability, mD	415
Total time, hr	50.6
Residence time, sec	21

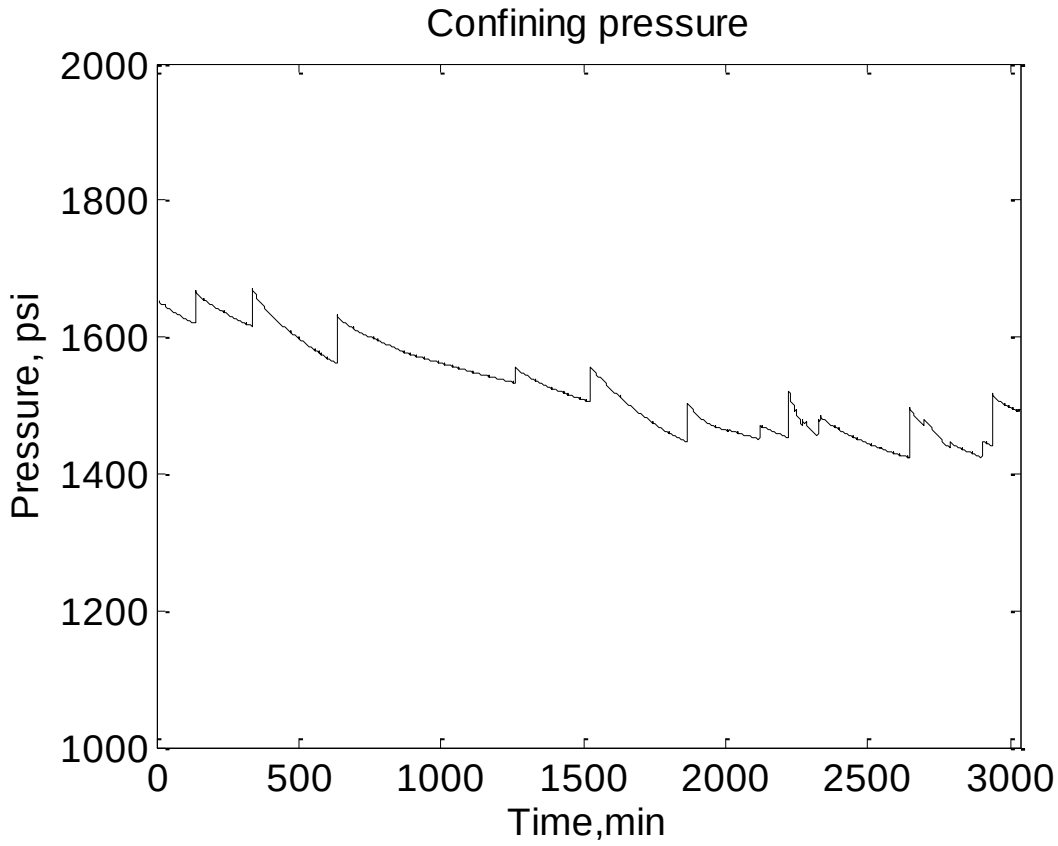

Figure C.37 – Confining pressure as a function of time. Average confining pressure during this experiment was 1,528 psi with a standard deviation of 68 psi.

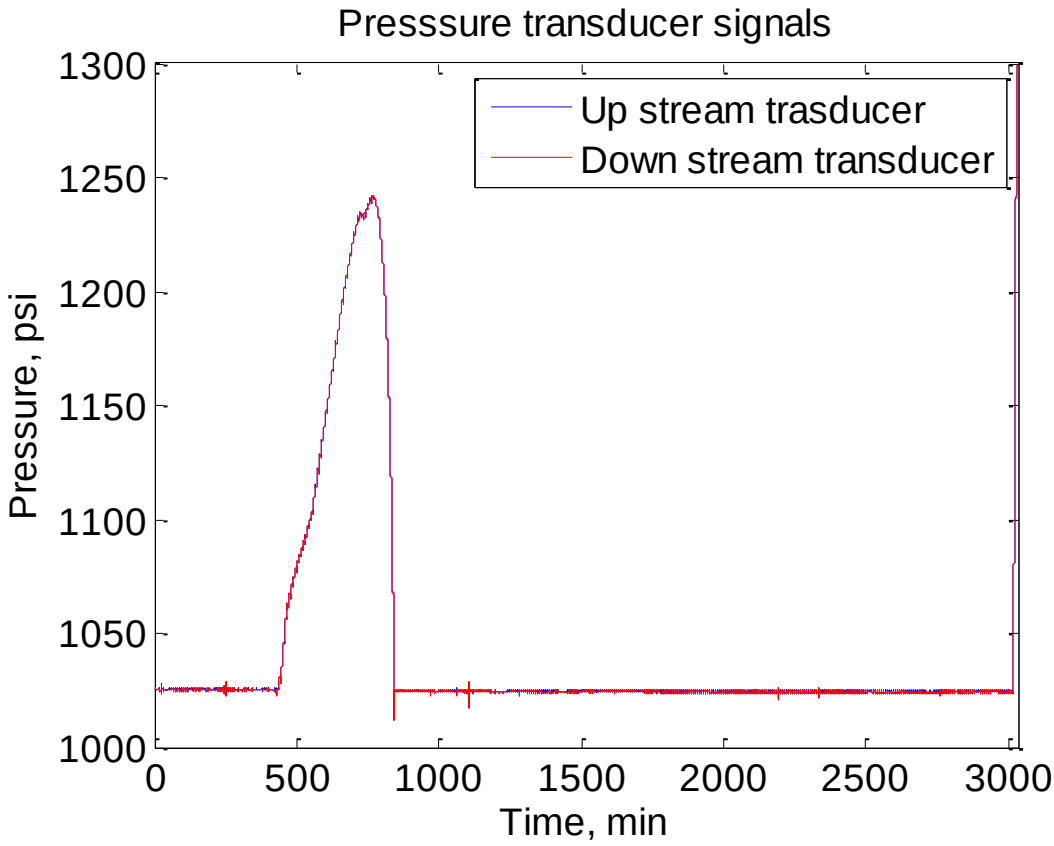

Figure C.38 – Upstream (blue) and downstream (red) pressure as a function of time during experiment. The sharp spike is due to some blockage in the D-BPR that eventually works its way out. This had no significant effect on pressure drop but did occur at the end of the experiment, causing the test to stop.

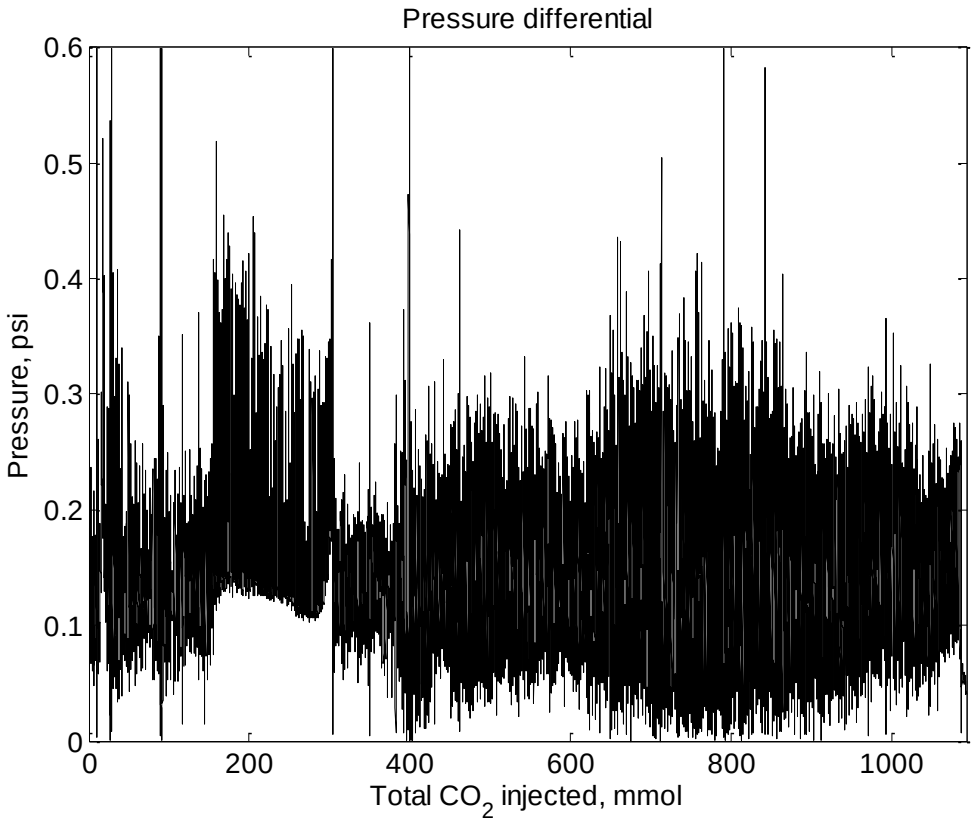

Figure C.39 – Pressure differential as a function of total CO_2 injected. While there is a small decrease in the signal which flattens out the overall signal doesn't change much overall.

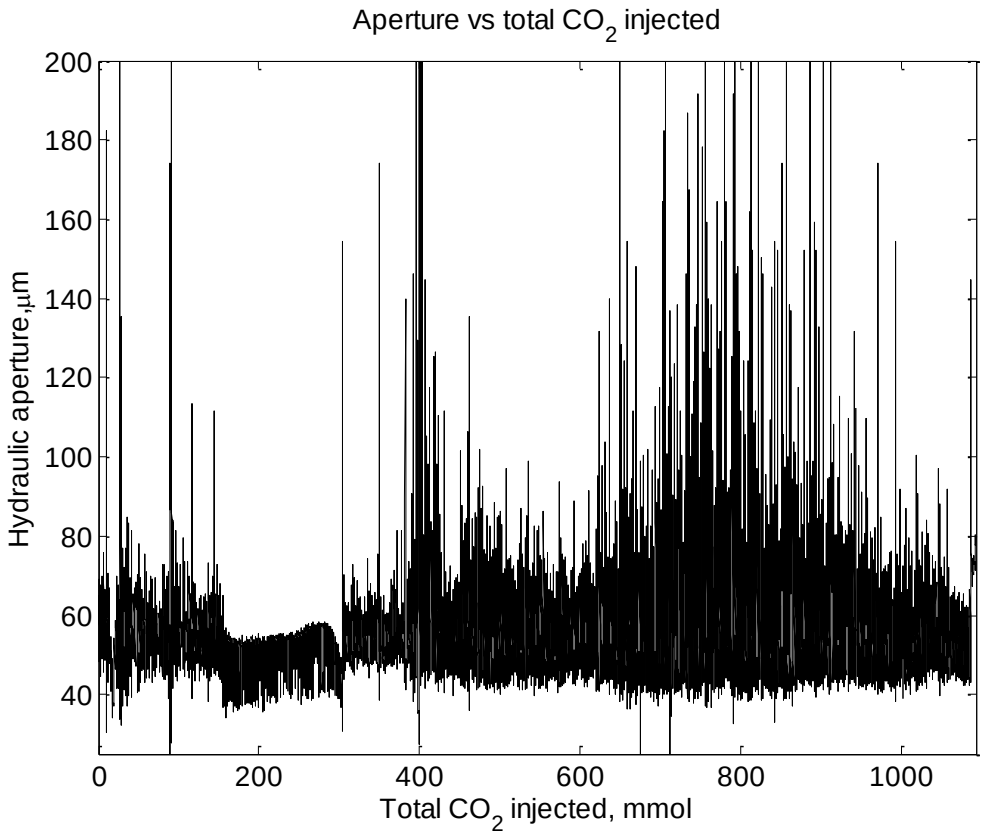

Figure C.40 – Estimated hydraulic aperture as a function of total CO_2 injected.

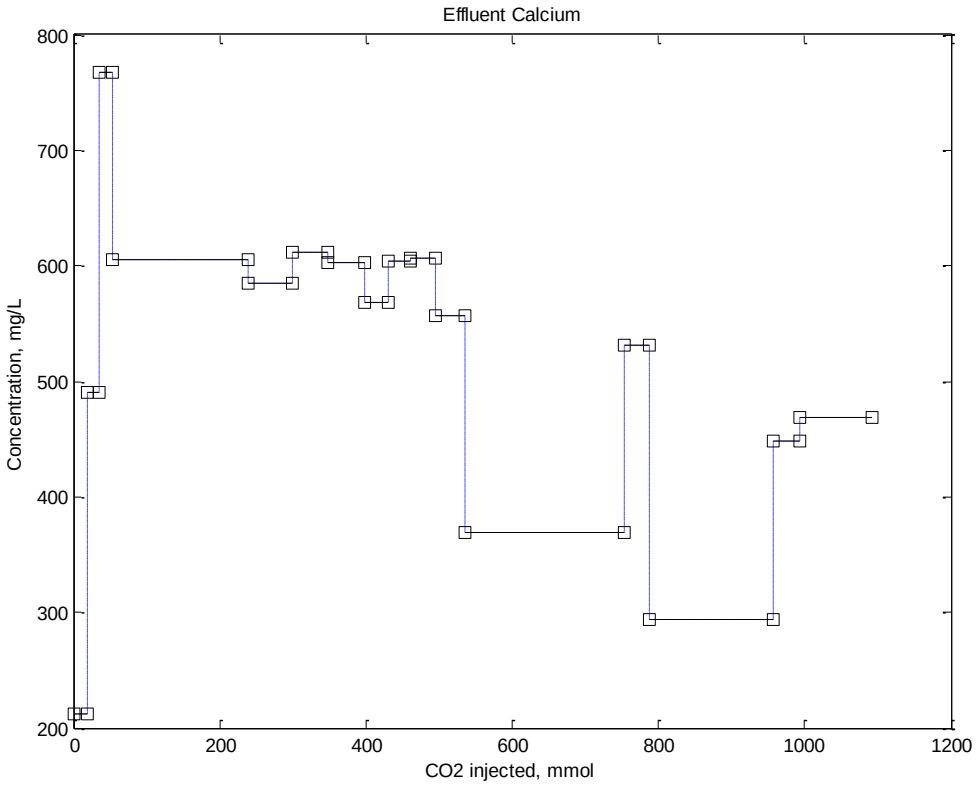

Figure C.41 – Effluent calcium concentration as a function of total CO_2 injected.

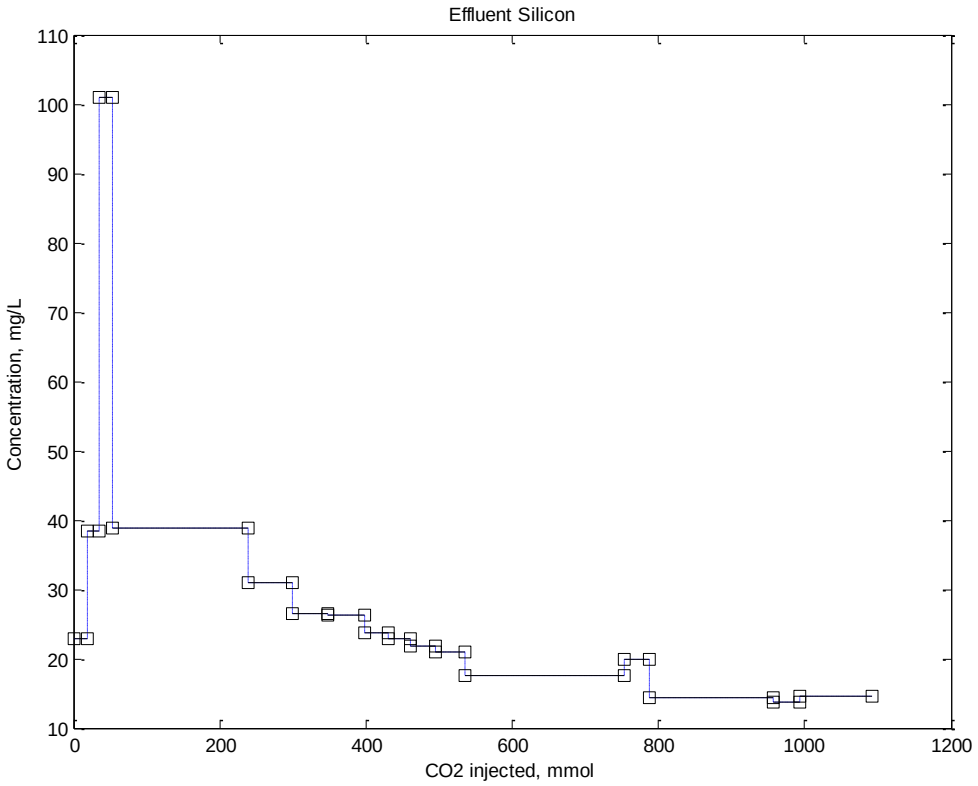

Figure C.42 – Effluent silicon concentration as a function of total CO_2 injected.

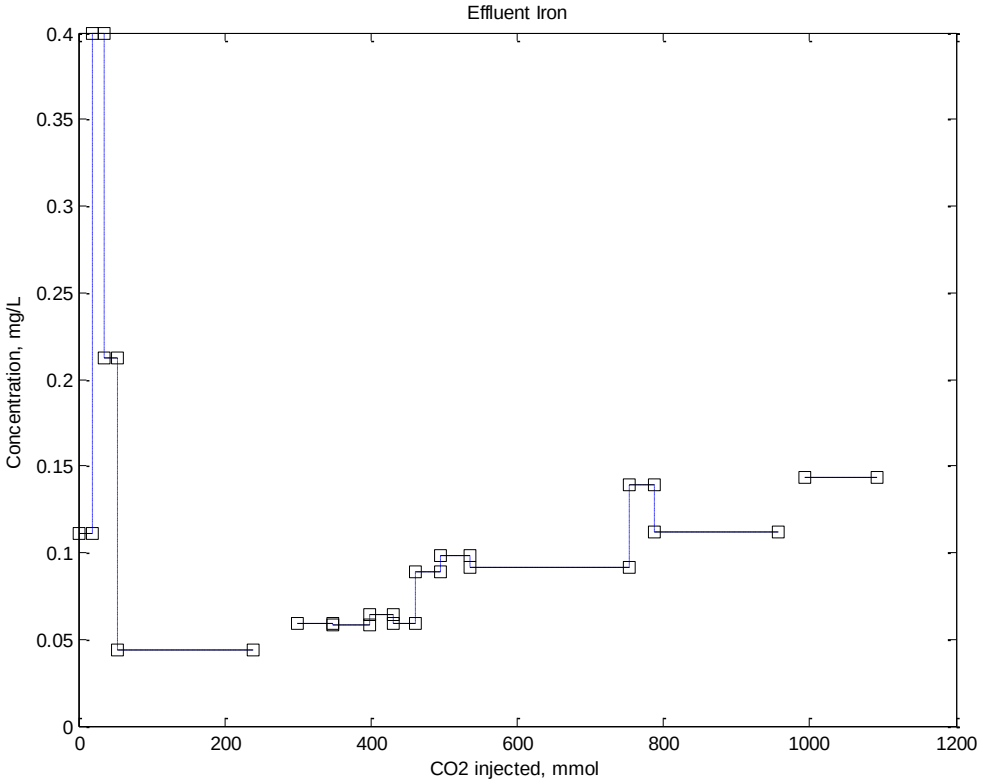

Figure C.43 – Effluent iron concentration as a function of total CO_2 injected.

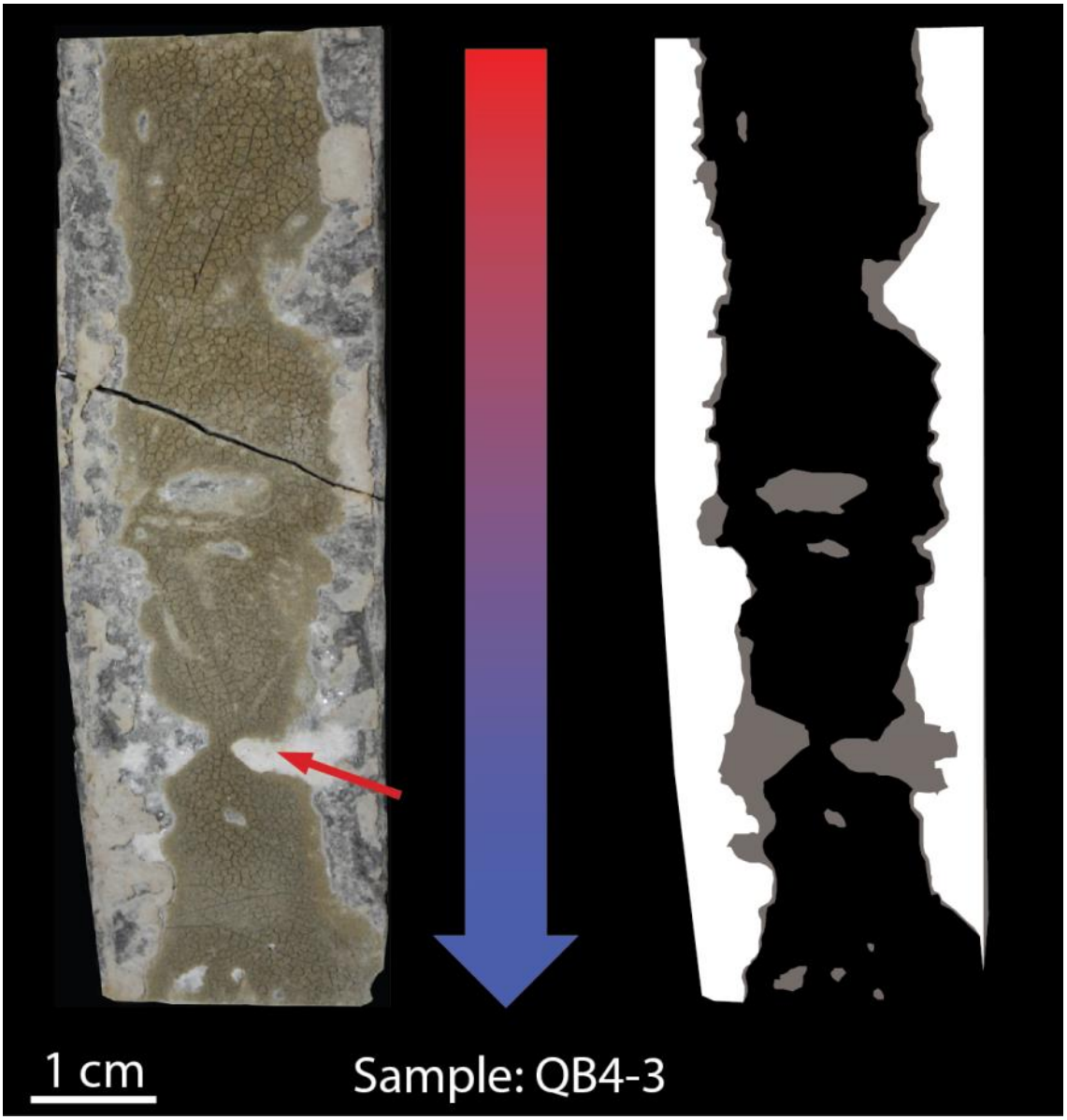

Figure C.44 – (Left) Image of fracture surface showing reacted pathway. Red letters show locations looked at with μXRD. (Right) Manual identification of zone with caulk (white), unreacted cement (grey), and reacted channel (black).Flow is from top to bottom.

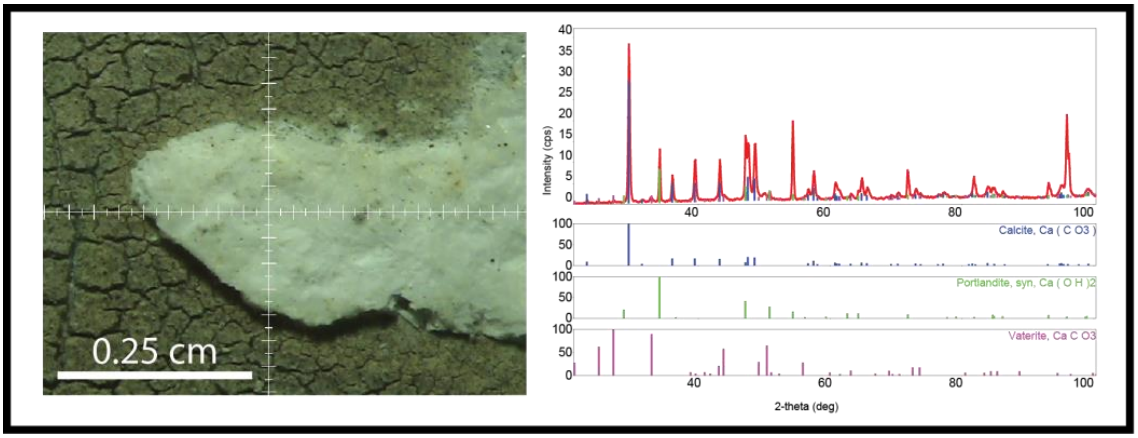

Figure C.45 – µXRD analysis of precipitate at constriction on fracture surface. Phases identified was calcite and portlandite.

EXPERIMENT REPORT: JA1 – FRANK1

Summary

Experiment JA1-Frank1 was the first attempt to extend core length by placing cores end-to-end so that a much longer composite core was generated. To ensure continuous flow, each core's fracture was placed 90° to the next core so that an open channel was maintained at each interface. A small pressure differential was used to replicate down hole conditions.

The experiment ran for over 77 hours but significant flow occurred for only the first 24 hours. Injection occurred at fixed upstream and downstream pressure. After significant time with negligible flow, upstream pressure was raised to initiate flow. Pressure differential was raised to 200 psi and no significant flow developed.

The fracture surface shows significant reaction at the inlet and no breakthrough of a reacted channel. Evidence for dissolution/precipitation matches previous HCl and carbonic acid experiments and a distinct precipitation front is observed.

While a single experiment cannot prove self-sealing, results indicated sealing and even the ability of the precipitate to maintain a higher pressure differential and warrant further experiments using the same methodology to validate the observations.

Experiment design

Sample preparation

The composite core (JA1-Frank1) was constructed from 4 cores of cement prepared in the same batch. Cores were poured and cured according to the standard method used for other experiments. They were also fractured and sealed according to the standard method. Cores were assembled so that each fracture was perpendicular to the next fracture. The purpose of this assembly was to guarantee an open flow pathway from one core to the next. Cores were then sealed around the joint at each interface with caulk. To seal the composite core and provide some strength the sample was wrapped in a layer of Teflon tape, sealed in heat shrink tubing, wrapped in a layer of aluminum foil, and sealed in a second sleeve of heat shrink tubing. Figure C.46 shows images of the fracture surface, core sections, and the wrapped composite core.

Experiment conditions

Ambient temperature (22 °C) and distilled water were used to maximize dissolved CO_2 concentration. Pore pressure was initially at 1,500 psi, which gives a theoretical saturation of 1.4747 mol-CO_2/kg-H_2O (6.49 wt.%). The sample was not strain hardened due to the elevated confining pressure and complex geometry of the composite cores. Confining pressure was kept at an average of 1,986 psi with standard deviation of 51 psi. The sample was flushed with distilled water prior to the experiment to get the system pressure up to experiment conditions and to remove any air in the fracture. The

dead volume between pump and core was calculated to be 6.87 mL based on length of tubing and inner diameter of tubing.

CO_2 and water mixing procedure

CO_2 and water was mixed by first filling the accumulator with distilled water (1.5 L) and chilling the accumulator to 5 °C. Next 144 mL of liquid CO_2 was injected into the accumulator from the bottom by driving from bottle pressure and receiving fluid from the accumulator at a constant rate. The accumulator was then isolated from the CO_2 tank and pressurized to experiment pressure (1,509 psi). The accumulator was raised to room temperature slowly and the pressure on the fluid held constant. Dissolution of CO_2 into the water was complete after 24 hours and the experiment began.

Results

Flow rate and pressure differential history

Table C.7 shows experiment conditions and parameters. Table C.8 shows the experiment history broken down into intervals and discussed below. Throughout all intervals confining pressure remained stable (Figure C.47). Interval 1 runs from the experiment start to 3.12 hours. Figure C.48 shows the pressure transducer signals and during this interval pressure differential was on average 5.4 psi (Figure C.49). Flow rate was between 0 and 0.005 mL/min with average 0.002 mL/min and during that time only 0.372 mL was injected (Figure C.50).

At the start of interval 2 the upstream pressure decreased from 1,509 psi to 1,503 psi and pressure differential correspondingly decreased to 2.1 psi. The decrease coincided with a flow rate increase to 0.012 mL/min and a switch in the Quizix pump from one cylinder to another. This phenomenon is representative of pump issues and not related to

behavior in the core. When the pump switches cylinders, especially at such slow rates and when the pump begins running, there can be small pressure perturbations. The system was stable through 11.6 hours where the acidic fluid is estimated to have moved through all the dead volume (6.872 mL) and begin interacting with the core.

Interval 3 ran from 11.6 hours to 15 hours, when flow rate begins to decrease. During this interval flow rate is constant at 0.011 mL/min, pressure differential is 2.0 psi, and by the end of the interval the pump had injected 9.15 mL of fluid. Interval 4 ran from 15 hours to 23.7 hours. Flow rate decreases from 0.011 mL/min to 0.001 mL/min. By the end of this interval 11.4 mL had been injected.

Since flow had essentially shut off I wanted to test to make sure the equipment was not stuck and to try to reestablish flow through the core. To do this, the upstream pressure was raised at the start of interval 5 by first 5 psi at 23.7 hours, then by 5 psi more at 24.09 hours, and then by 40 psi more at 25.61 hours. Thus the pressure differential was raised from 2.45 psi to 50.24 psi with no significant flow being established. By the end of this interval only 17.73 mL of fluid was injected. High amplitude noise in the digital back pressure regulator beginning at the24 hour mark (Figure C.48) did not affect results. The cumulative volume plot (Figure C.50) shows that flow was not affected by these very quick spikes in pressure signal.

The final time period, interval 6, ran from 70.5 hours to experiment end at 77.1 hours. Upstream pressure was progressively raised so that by the experiment end the pressure differential was 200 psi. During this time flow remained essentially zero, except for small spikes that account for the small volume changes associated with raising the upstream pressure. The cumulative volume remains flat and shows that there was essentially no flow during this time period.

Figure C.51 shows equivalent sample permeability plotted versus total CO_2 injected into the fracture. This plot has been normalized to subtract the dead volume. Since the pressure differential is constant for the flowing time period, permeability matches flow rate data. Once the flow rate was effectively stopped, pressure differential increases had no effect and effective permeability remains below detection limits.

Fracture surface analysis

Figure C.52 shows a post experiment photo of the fracture surface. Flow is from left to right. Three distinct zones are identified. In the cyan box the fracture surface shows minor alteration across most of the fracture surface. Distinct unreacted that are darker gray are distributed throughout and are often normal to the bulk flow direction. In the purple box there is evidence for more significant reaction and secondary mineral precipitation that is not visible past the yellow dashed line. The red box contains evidence for a well-developed reaction channel at the inlet that narrows and in the yellow box is evidence for precipitation immediately next to and within the reacted channel.

Figure C.53 shows photos of the inlet and outlet for each individual core that was stacked to create the composite core. Visual observations did not identify any significant buildup of precipitate and sealing at the junction point between cores was unlikely.

Discussion

Key results from this initial experiment are that flow rate and pressure differential are constant for many fracture volumes injected. After some time flow rate begins to decrease toward zero. Despite attempts to reestablish flow a very high pressure differential was able to be maintained across the core with no flow. Several phenomena that could sustain this pressure differential are discussed below.

Fracture closure due to geomechanical stress or failure of the construction of the composite core. A small shift in the geometry of the core could close off a cross over point in the core. Since the aperture size is a function of effective stress, a drop in the fluid pressure in the fracture might allow for closure of a segment of the core. This is unlikely as downstream and upstream pressure do not show any characteristic drop that would permit fracture closure. There was no evidence for the core breaking during the experiment.

Failure of the accumulator system. If the accumulator piston became stuck and the upstream pressure was increased (like was performed in this experiment) the pump pressure would rise but the upstream pressure transducer would remain unchanged. There was no evidence for this phenomena.

The most likely option is that secondary precipitation within the fracture caused sealing. There is significant evidence for precipitation on the fracture surface. Sealing of the tubing exiting the core hold due to precipitation is unlikely as the pressure differential was maintained by something in between the two main transducers.

The lag in onset of precipitation induced flow rate decrease was not expected and more experiments are needed to verify this behavior and begin to understand the fundamental physics.

Additional information

None for this experiment.

Tables and figures

Table C.7 – **JA1-Frank1** experiment summary.

Core dimension (width × length), cm	2.54 × 23.4
Temperature, °C	21
Average confining pressure (std. dev.), psi	1,986 (51)
CO_2-saturation, wt. %	6.57
Flow rate, mL/min	0.011
Pressure differential, psi	2.0
Hydraulic aperture, μm	12
Sample permeability, mD	6
Total time, hr	77.2
Residence time, sec	363

Table C.8 – Important intervals during experiment.

Interval	Time, hr	Flow rate, mL/min	Pressure differential, psi	Volume, mL
1	0 to 3.12	0.002	5.4	0.372
2	3.12 to 11.6	0.012	2.1	6.872
3	11.6 to 15	0.011	2.0	9.15
4	15 to 23.7	0.011 to 0.001	2.45	11.4
5	23.7 to 70.5	0.0022	50.24	17.73
6	70.5 to 77.1	0	50 to 200	18.41

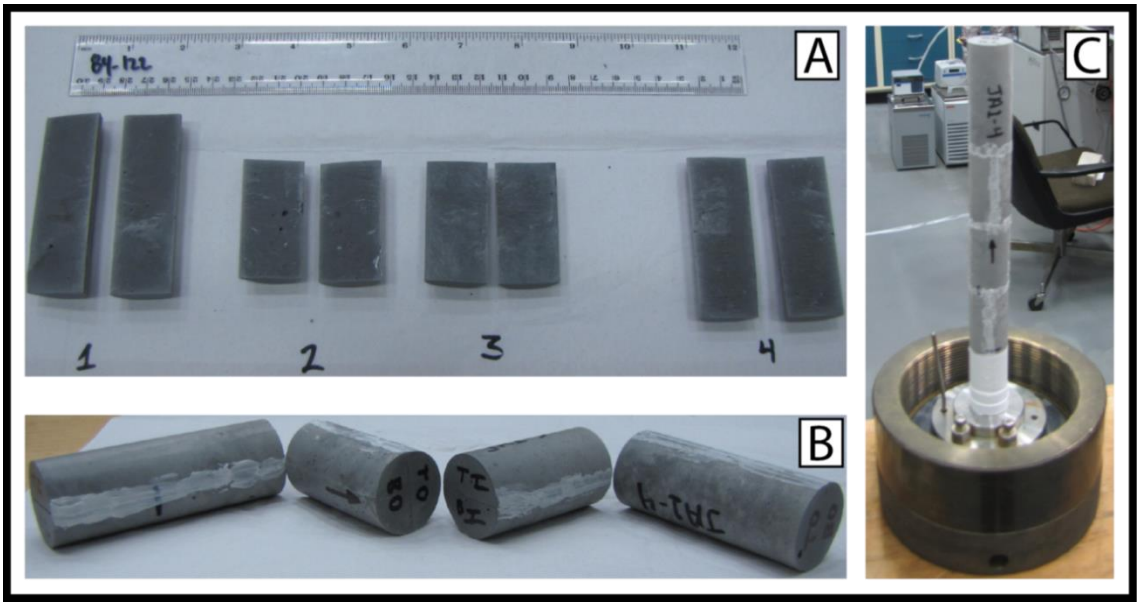

Figure C.46 – Images of JA1 cores before reaction. A) Image of fracture surface of each individual core before assembly. B) Image of each core after the sides have been sealed with caulk and showing order of assembly into one core. Note that fractures are oriented normal to each other to ensure flow. C) Complete core assembled and placed on core holder stand. Note that the joint between each individual core has been sealed with caulk.

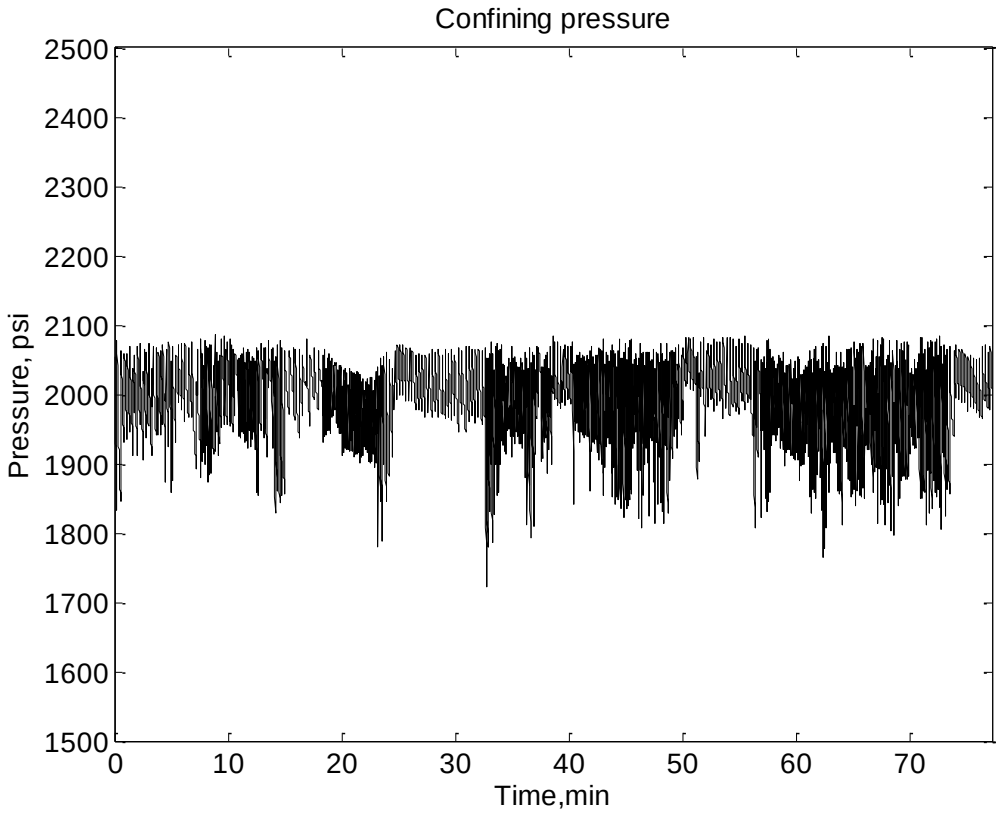

Figure C.47 – Confining pressure during experiment. Average confining pressure for the experiment was 1,986 psi with a standard deviation of 51 psi.

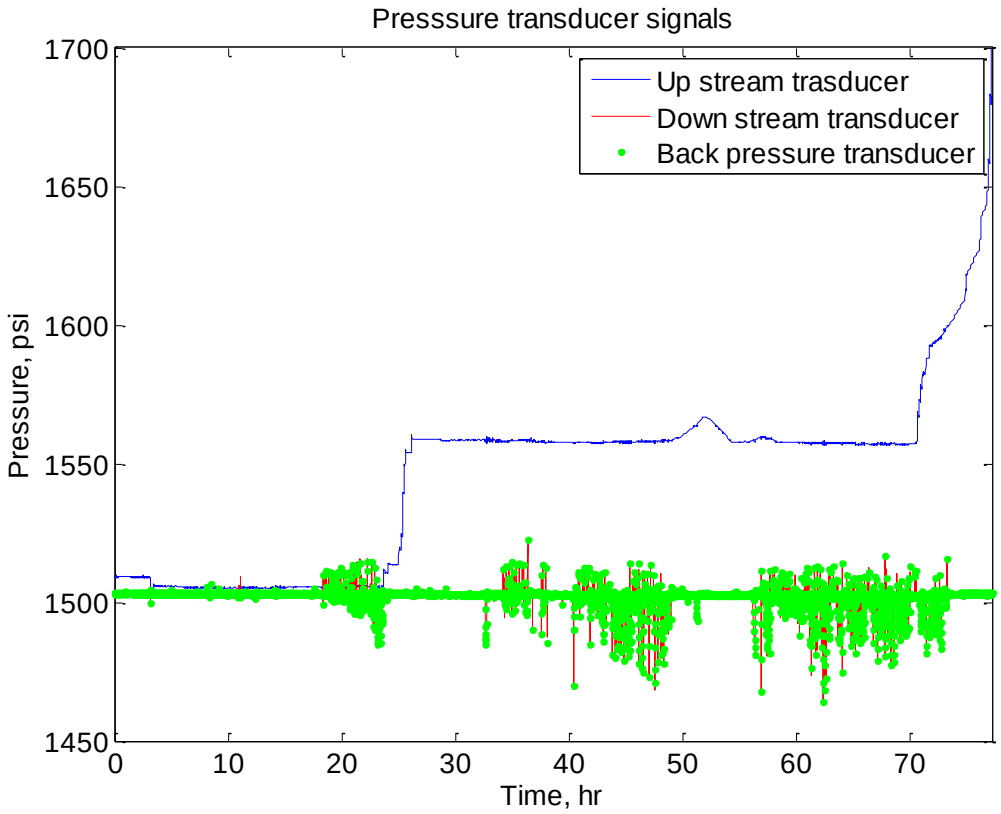

Figure C.48 – Pressure transducer signals during experiment. Driving force for flow is the difference between upstream (blue) and downstream (red) curves. High amplitude signal is in the back pressure regulator and does not affect results.

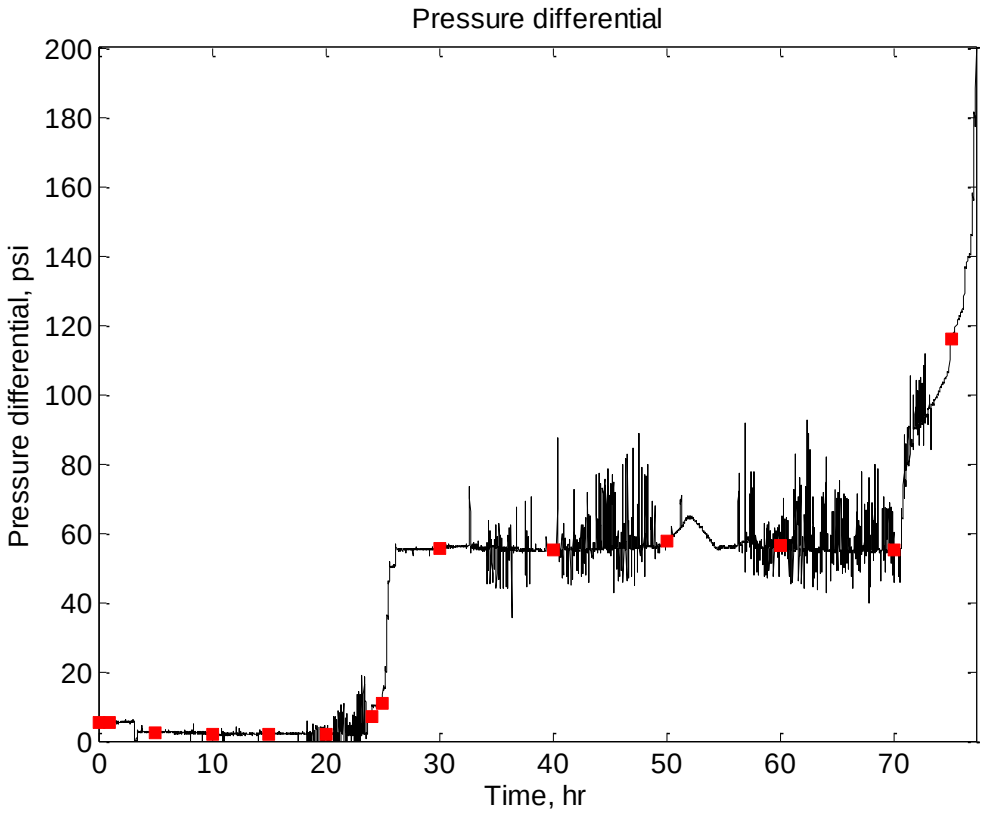

Figure C.49 – Pressure differential as a function of time. For much of the experiment the pressure differential remains constant. Drops in differential occur as a result of the D-BPR failure or due to operator manually increasing the back pressure. Red squares represent 5-point average measurement of pressure differential.

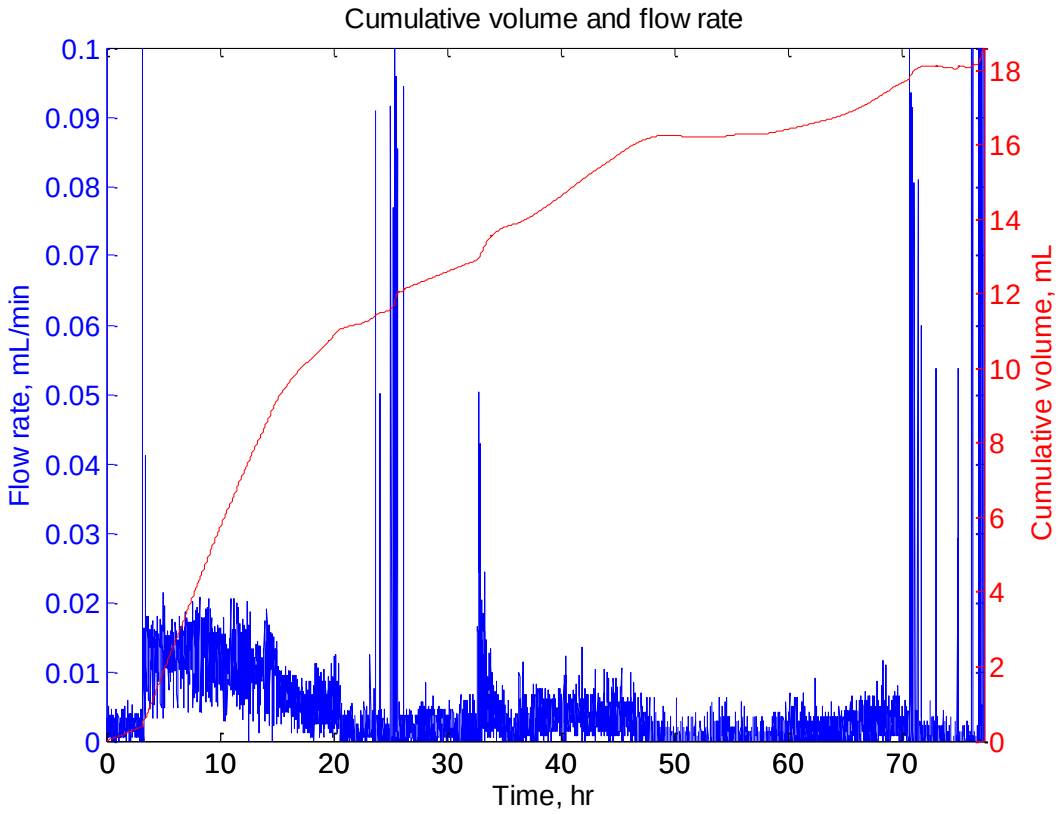

Figure C.50 – Pump flow rate (blue) and cumulative volume injected (red) as a function of time.

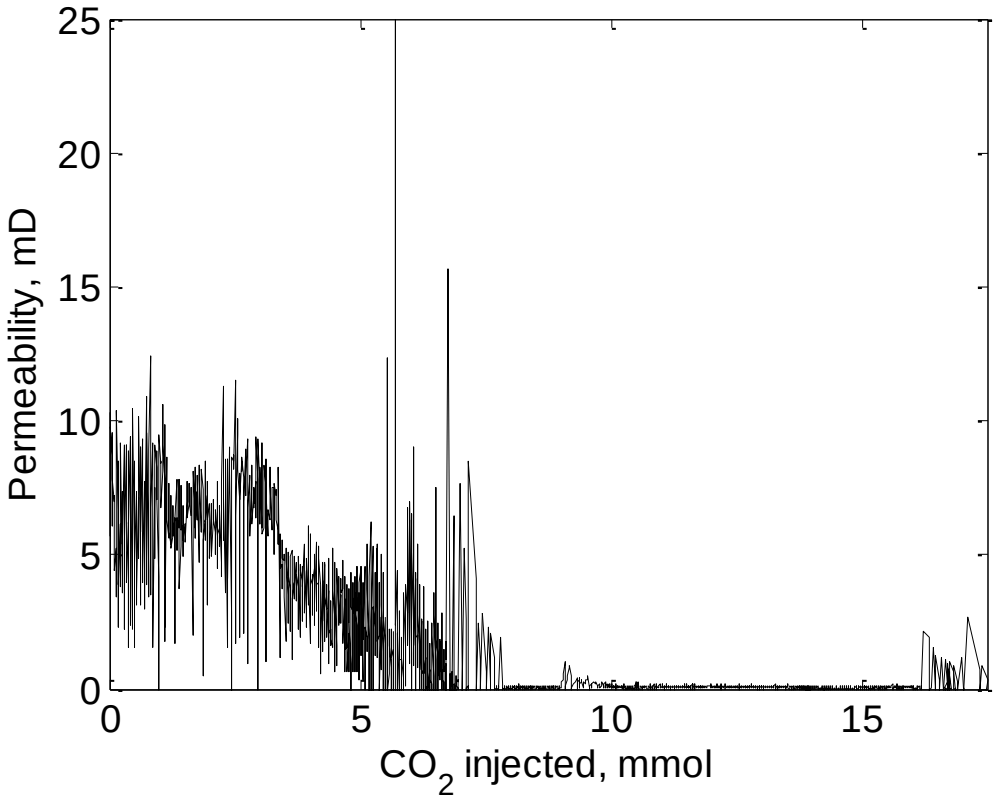

Figure C.51 – Equivalent sample permeability versus CO_2 injected. This plot has been normalized to account for dead volume.

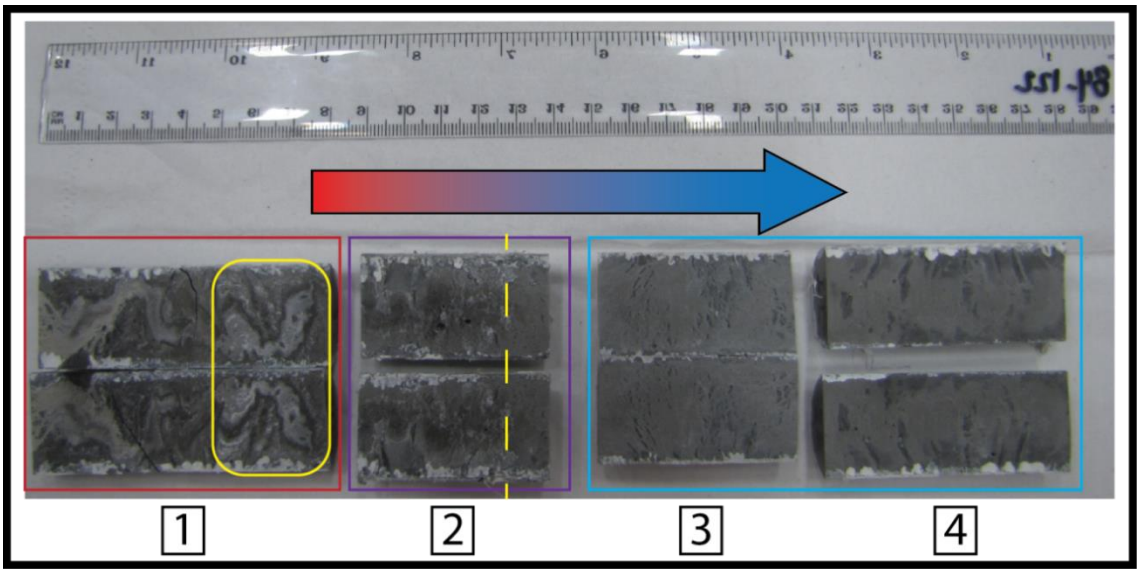

Figure C.52 – Post experiment photos of JA5-Frank1. Flow direction is from left to right.

Figure C.53 – Post experiment core ends of JA1-Frank1. Flow would enter at the top left come out at the bottom right and enter at the top of the next core to the right. No evidence for plugging at the interface was seen.

EXPERIMENT REPORT: JA5 – FRANK2

Summary

The goal of this experiment was to simulate pressure conditions of the first experiment (JA1-Frank1) with a faster flow rate to look for the same sealing behavior at much higher flows. Target flow rate and pressure differential were 0.1 mL/min and 6 psi respectively. The experiment was stopped before 80 hours but since the low rate was fast, most behavior occurs early on. During the experiment flow rate began at 0.12 mL/min but rapidly decreased to 0.03 mL/min with a corresponding pressure differential of 7.5 psi. Bubbles in the effluent were observed as early 15 minutes into the experiment. At 25 hours the flow rate increased to 0.043 mL/min. After 30 hours equipment issues began to affect the experiment. A restriction in flow downstream of the core developed driving flow rate down and pushing up the downstream pressure up.

Reaction on the fracture surface showed significant alteration down the length of the core. It is possible that breakthrough of the reaction front occurred before the system was able to setup a feedback that leads to self-sealing. The early arrival and sharpness of the flow rate decrease and the later jump in flow rate are troubling were not expect as the first experiment behaved more gradually. It is possible that loose material precipitated and plugged a local area that caused flow rate to drop.

Experiment design

Sample preparation

The composite core was created using 4 fractured cement cores (batch name JA5) prepared in the same batch. Cores were poured and cured according to the standard method used for other experiments. They were also fractured and sealed according to the standard method. Cores were assembled so that each fracture was perpendicular to the

next fracture. The composite core was sealed in the Teflon, aluminum foil, and heat shrink tubing in the same way as JA1-Frank1. Figure C.54 shows images of the fracture surface, core sections, and the composite core wrapped.

Experiment conditions

Ambient temperature (22.5 °C) and distilled water were used to maximize dissolved CO_2 concentration. Pore pressure was initially at 1,515 psi, which gives a theoretical saturation of 1.4596 mol-CO_2/kg-H_2O (6.42 wt.%). The sample was not strain hardened due to the elevated confining pressure and complex geometry of the composite cores. Confining pressure was kept at an average of 1,896 psi. The sample was flushed with distilled water prior to the experiment to get the system pressure up to experiment conditions and to remove any air in the fracture.

During the experiment the digital back pressure regulator (D-BPR) was set to maintain minimum downstream pressure and the Quizix pump used in constant pressure mode to maintain constant upstream pressure. To prevent Joule-Thompson cooling of CO_2 affecting the D-BPR the heated back pressure regulator (BPR-2) was set to 500 psi and 50° C. The dead volume between pump and core was calculated to be 6.87 mL based on length of tubing and inner diameter of tubing.

CO_2 and water mixing procedure

CO_2 and water was mixed by first filling the accumulator with distilled water (1.5 L) and chilling the accumulator to 5 °C. Next 151.2 mL of liquid CO_2 was injected into the accumulator from the bottom by driving from bottle pressure and receiving fluid from the accumulator in constant rate receive mode. The accumulator was allowed to equilibrate for 27 hours while holding constant pressure of 1,514 psi. As CO_2 dissolved into the water the pump's cumulative volume injected increased to maintain pressure.

Because the temperature was not increased to experiment conditions, an additional 43 hours was needed to increase turn off the chiller and allow the accumulator to reach equilibrium. After 70 total hours the system was assumed to be in equilibrium with 6.42 wt.% CO_2 dissolved in the water.

Results

Flow rate and pressure differential history

Pre acid flow rate was 0.1 mL/min with a corresponding pressure differential of 6.0 psi. During the experiment the average confining pressure was 1,896 psi with a standard deviation of 30 psi (Figure C.55). Figure C.56 shows the pressure transducer signals during the experiment.

The acid injection portion experiment is broken into 10 distinct time intervals that describe normal and abnormal operating behavior. Interval 1 runs from experiment start to 0.13 hours. During this time pressure differential quickly equilibrates to 6.62 psi (Figure C.57). Flow rate is constant at 0.126 mL/min (Figure C.58) and 1 mL of fluid is injected (Figure C.59). The beginning of interval 2 is defined by a flow rate decrease and the interval ends at the time it takes to inject 6.85 mL (the dead volume). By the end of this interval (0.98 hours) flow rate had decreased to 0.076 mL/min. Pressure differential was slightly higher (7.48 psi) during this interval. Interval 3 ran from 0.98 hours to 1.36 hours and is characterized by constant pressure differential and a flow rate decrease that matches slope of interval 2. By the end of interval 3 the volume injected was 8 mL. Interval 4 is characterized by abnormal flow rate behavior and runs from 1.36 hours to 2 hours. During this time, flow rate decreases from 0.02 mL/min to 0.008 mL/min at a slower rate than during interval 3. Flow rate then jumps to 0.037 mL/min for less than 10 minutes then falls to 0.012 mL/min before quickly stabilizing at 0.03 mL/min. The source

of the flow rate fluctuation is unknown, especially since flow rate begins to decrease well before the dead volume has been flown through and well past many fracture volumes of fluid have moved through the core. It is possible that the pump or accumulator might have malfunctioned (e.g. sticking of belt or piston). There is also evidence for the CO_2 saturated fluid moving faster than expected or influence of multiphase flow effects. By 0.25 hours (interval 2) there was some evidence for gas bubbles coming out of the effluent and by 0.55 hours there was distinct formation of bubbles on the outlet tubing. Interval 5 lasts until 25.03 hours was characterized by constant flow rate at 0.031 mL/min. Pressure differential was also constant at 7.61 psi. The total volume of fluid injected by the end of this interval was 52.0 mL. At the start of interval 6 there was a jump in flow rate to 0.043 mL/min with no significant change in pressure different (7.81 psi). This time period lasts until 32.07 hours and 70.3 mL of fluid injected.

The final series of time intervals are characterized by abnormal system behavior caused by plugging of the pressure transducers. For all functional purposes the experiment ended at interval 6 but the following information is useful to understand issues related to operation of the core flow system. Interval 7 ran from 32.07 hours to 41.18 hours. The abnormal behavior was characterized by a rise in the D-BPR's measured pressure from 1,507.6 psi to 1,510.5 psi. This rise was not caused by the operator increasing the back pressure set point and it was noticed that the D-BPR was showing a 'stop' warning which indicates the valve controlling flow was full open and unable to open further to release pressure and decrease back to the set point pressure. Since upstream pressure was not altered the pressure differential began to fall until it reached 3.0 psi. Correspondingly, flow rate dropped from 0.043 mL/min to 0.014 mL/min. Interval 8 captures efforts to fix the D-BPR. The interval lasted until 48.02 hours and 87.75 mL injected. During this interval, the D-BPR set point was manually raised from

1,510.5 psi to 1,512 psi to attempt to dislodge any material and flex the diaphragm. This had no effect on the D-BPR. During this time pressure differential decreased to 1.7 psi, with a flow rate of 0.012 mL/min. During interval 9 a second approach was tried to understand what was occurring in the equipment and return to normal operations. Both upstream and downstream pressures were increased to try to dislodge any material and unstick the D-BPR. This interval lasted until 54.97 hours and 91.7 mL were injected. Upstream pressure was raised to 1,524 psi, while the D-BPR pressure was set at 1,523 psi. The flow rate was low (0.008 mL/min) and pressure differential was 1.45 psi. Attempts to fix the D-BPR were deemed unsuccessful and a rebuild of the D-BPR was attempted next.

The final interval lasts until 72.3 hours and 99.8 mL of fluid was injected by the end of the experiment. After rebuilding the D-BPR and reattaching the plumbing system flow establishment was attempted. Figure C.56 shows the abrupt pressure decreases and attempts to reestablish flow in the system. However, the D-BPR had the same full open or "stop" indicator which showed flow was not coming out of the system and the experiment was terminated.

Fracture surface analysis

Figure C.54 shows pre experiment photos of JA5-Frank2. Total core length was 24.03 cm and width was 2.54 cm. Figure C.52 shows post experiment photo of the reacted fracture surfaces. A distinct reacted channel is evident running down the length of the core and narrows toward the outlet. Red arrows indicate were significant restriction in reacted channel was observed. Figure C.52 shows post experiment photos of the core ends. Not the red arrows show where outlet fluid from one fracture reacted with the face

of the subsequent core. There was also no indication of plugging or precipitation where fractures intersected.

Discussion

This experiment exhibited unexpected an abnormal behavior, even before the system began to plug. Gas arrived at the effluent possibly by 15 minutes but defiantly by 33 minutes, which is much faster than estimates of how long it would take fluid to even travel through the calculated dead volume (which should have taken an hour), let alone through the fracture and out the tubing and BPRs at the outlet. The time of bubbles in the effluent do correspond to the initial decrease in flow rate but it was not known if the bubbles were causing multiphase flow (and restricting flow) or the flow rate decrease was due to precipitation. It is possible, (though unlikely) that parts of the fracture still had air and the bubbles observed in the effluent are those and not CO_2. This is unlikely as many fracture volumes of distilled water are injected before the acid experiment and this phenomena has not been observed in other experiments at high pressure. It is also possible, though high unlikely, that the tubing upstream of the core had precipitation which reduced the effective tubing inner diameter (and thus dead volume).

In terms of self-sealing behavior, there is no evidence that it occured in this experiment. Based on the results of this experiment (and corroborated with the short core experiments) residence time plays a crucial role in determining self-sealing. It is unknown if break through occurred before significant dissolution/precipitation could begin to seal the fracture. Given the core length of 24.03 cm and initial velocity of 0.5 cm/sec, break through would occur at 48 seconds. Break through would occur well before the drop in flow rate, which begins at 0.9 hour (54 minutes). Evidence for unspent acid (as evidenced by gas bubbles) occurs as early as 15 minutes into the experiment.

However, self-limiting might have occurred in this core. The decrease in flow rate to 0.03 mL/min indicates the development of restriction to flow. When plotted against fracture volumes injected (Figure C.62) the flow rate decrease is more gradual. This of course ignores the issue of dead volume. However the jump in flow rate that occurs at 500 fracture volumes injected is still very sharp and should not occur based on our current understanding of the system. It is possible that loose precipitate is plugging the system (or unsticking and opening up flow), especially at tight juncture between cores. However, plugging must occur upstream of the D-BPR, otherwise back pressure would build (as seen in interval 7 and onward).

Failure of the experiment was due to plugging of tubing downstream from the D-BPR in addition to possible D-BPR failure. Figure C.63 shows images of the heated back pressure regulator post experiment. Significant precipitation has clogged the small metal diaphragm and sealed the outlet (or at least severely restricted flow).

This experiment provides an upper bound for residence time to show self-sealing behavior. It also highlights a potential issue with plugging of the downstream tubing.

Additional information

2 DI water samples, 1 baseline effluent sample, and 9 acid test effluent samples were collected during the experiment. The samples were unfortunately not analyzed.

Have data on dissolution of CO_2 if necessary.

Tables and figures

Table C.9 – **JA5-Frank2** experiment summary.

Core dimension (width × length), cm	2.54 × 24.03
Temperature, °C	22.5
Average confining pressure (std. dev.), psi	1,896 (30)
CO_2-saturation, wt. %	6.42
Flow rate, mL/min	0.13
Pressure differential, psi	7.4
Hydraulic aperture, μm	17
Sample permeability, mD	21
Total time, hr	72.3
Residence time, sec	48

Table C.10 – Important intervals during experiment.

Interval	Time, hr	Flow rate, mL/min	Pressure differential, psi	Volume, mL
1	0 to 0.13	0.126	6.62	1.0
2	0.13 to 0.98	0.126 to 0.076	7.48	6.85
3	0.98 to 1.36	0.076 to 0.02	7.51	8
4	1.36 to 2.0	0.02 to 0.03	7.58	8.9
5	2.0 to 25.03	0.031	7.61	52.0
6	25.3 to 32.07	0.043	7.81	71.6
7	32.07 to 41.18	0.043 to 0.014	7.81 to 3.0	83.9
8	41.18 to 48.02	0.014 to 0.012	3.0 to 1.7	87.75
9	48.02 to 54.97	0.012 to 0.008	1.7 to 1.45	91.7
10	54.97 to 72.3	-	-	99.8

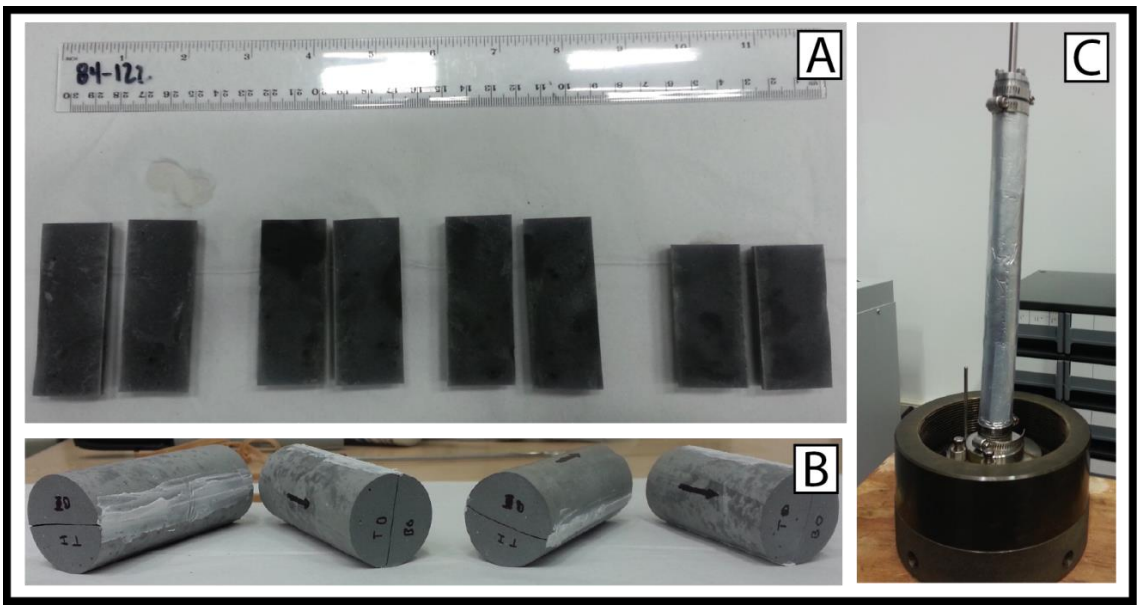

Figure C.54 – Pre experiment photos of JA5-Frank2. A) Image of fracture surfaces. B) Image of fractured cores showing orientation of fractures before being assembled. C) Core wrapped in the Teflon heat shrink tubing and foil before placing in core holder.

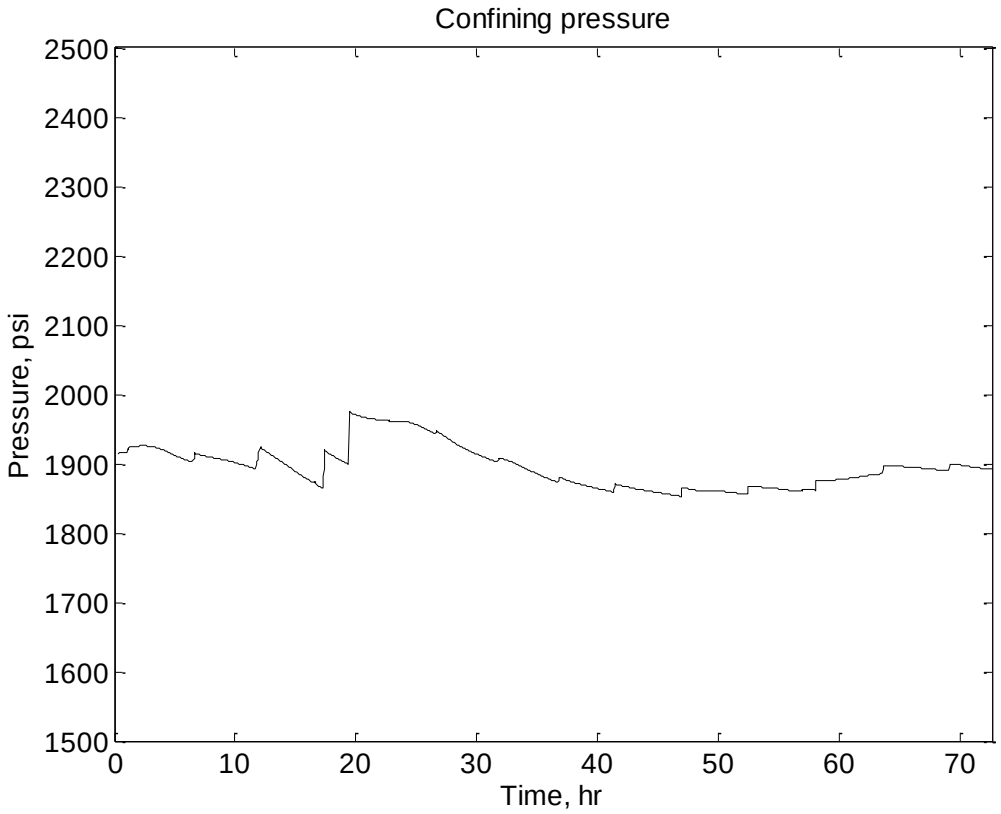

Figure C.55– Confining pressure during experiment. Average confining pressure for the experiment was 1,896 psi with a standard deviation of 30 psi.

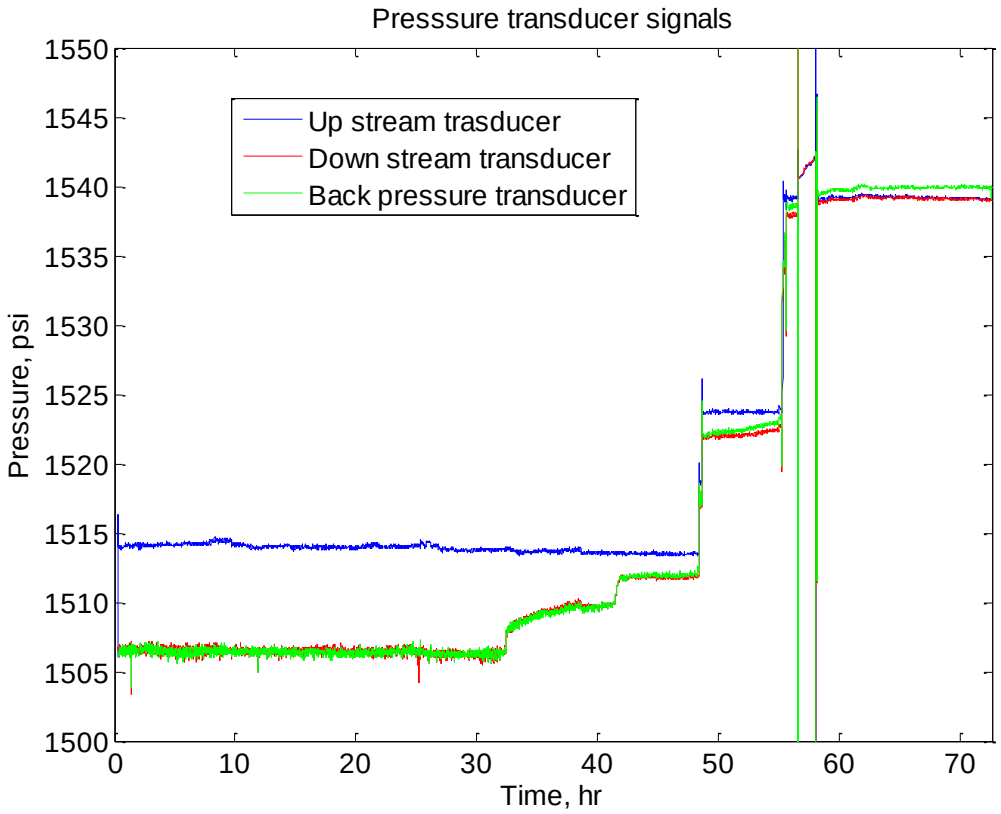

Figure C.56 – Pressure transducer signals during experiment. Driving force for flow is the difference between upstream (blue) and downstream (red) pressure.

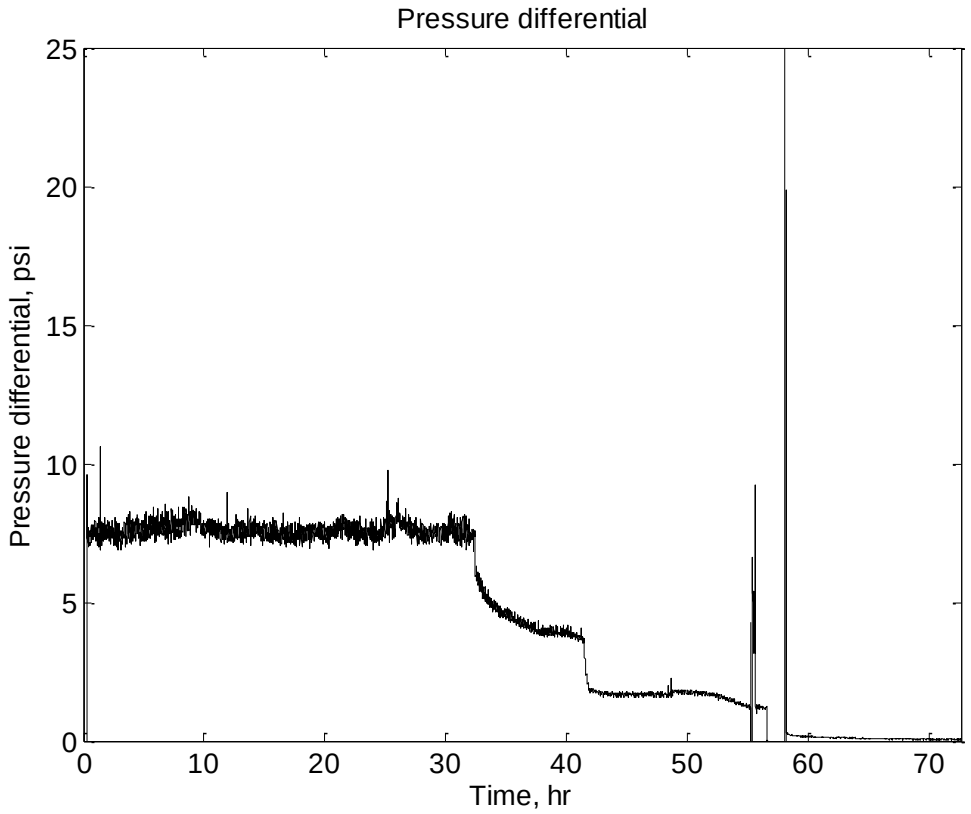

Figure C.57 – Pressure differential as a function of time. For much of the experiment the pressure differential remains constant. Drops in differential occur as a result of the D-BPR failure or due to operator manually increasing the back pressure.

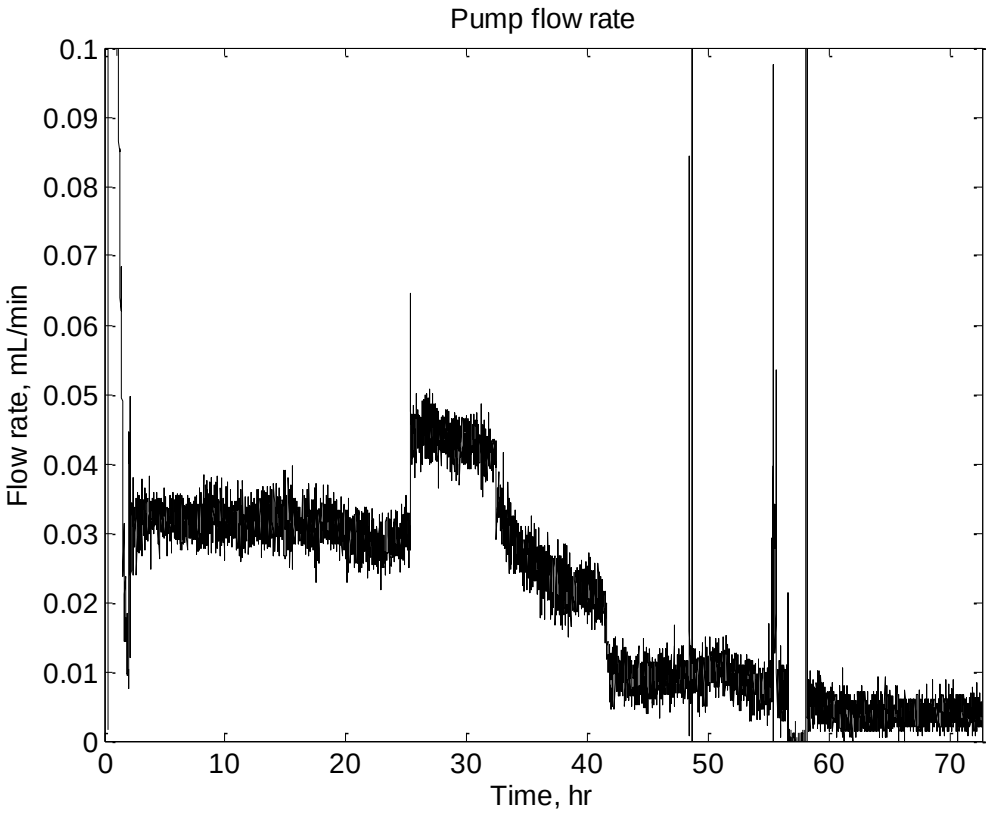

Figure C.58 – Pump flow rate as a function of time. Flow rate is initially high but then drops to a fairly steady value until the system begins to experience equipment issues.

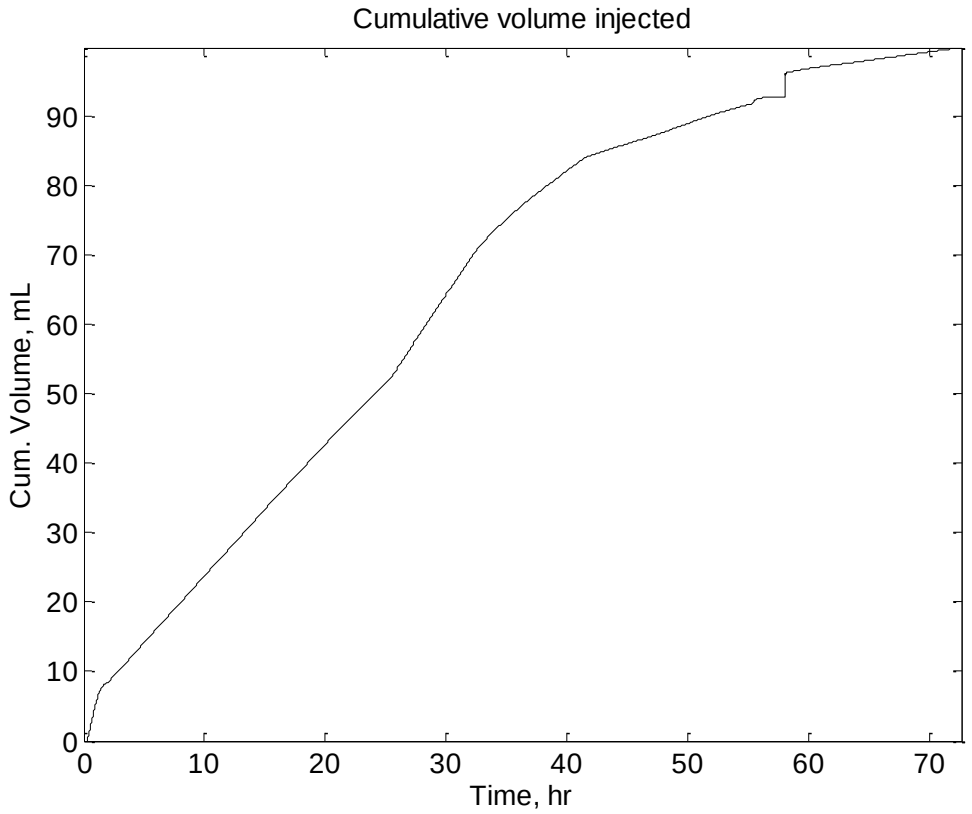

Figure C.59 – Cumulative volume injected as a function of time. In the very beginning there is a rapid injection of less than 10 mL, after which the rate of fluid injected is slower and fairly constant for the normal portion of the experiment.

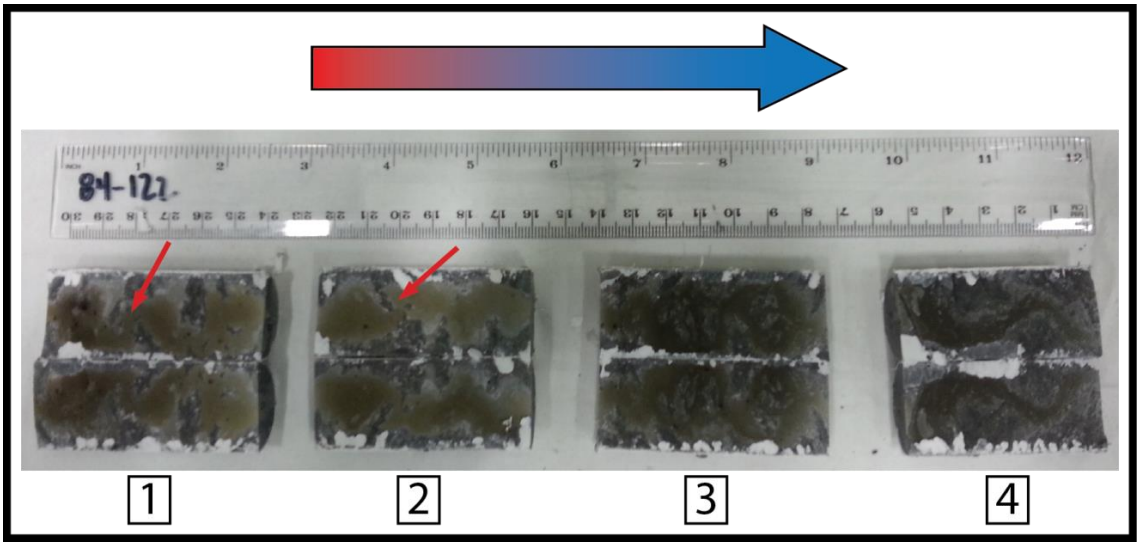

Figure C.60 – Post experiment photos of JA5-Frank2. Flow direction is from left to right. Significant reaction can be seen on the surface that narrows toward the outlet. Significant restrictions in channel width are observed on the fracture surface (red arrows).

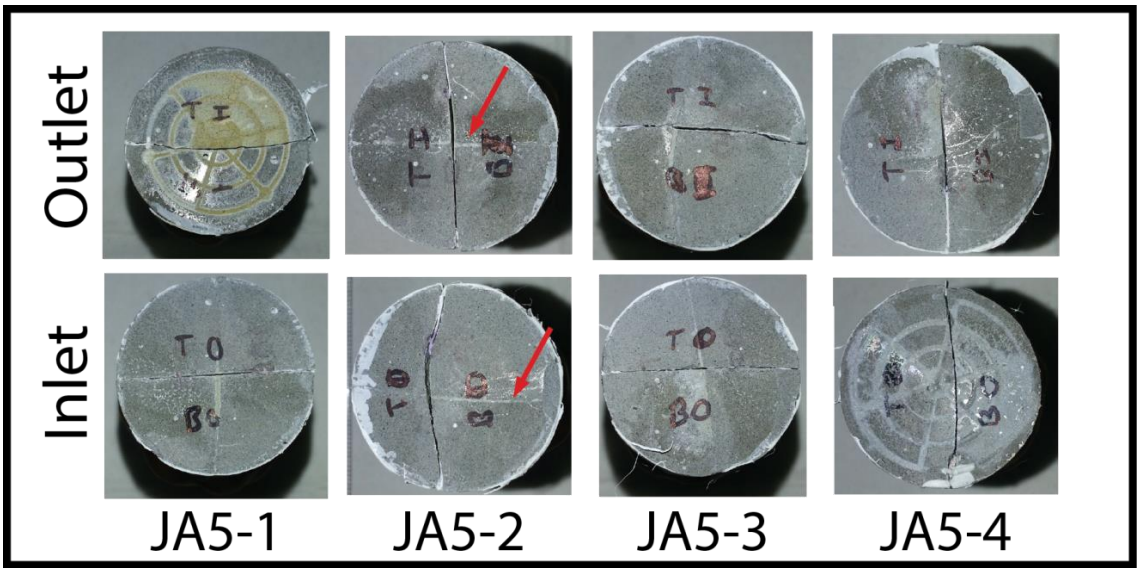

Figure C.61 – Post experiment core ends of JA5-Frank2. Flow would enter at the top left come out below and enter at the top of the next core to the right. Note significant reaction at inlet, evidence of reaction where cores touch (red arrows), and some reaction at outlet. No evidence for plugging at the interface was seen.

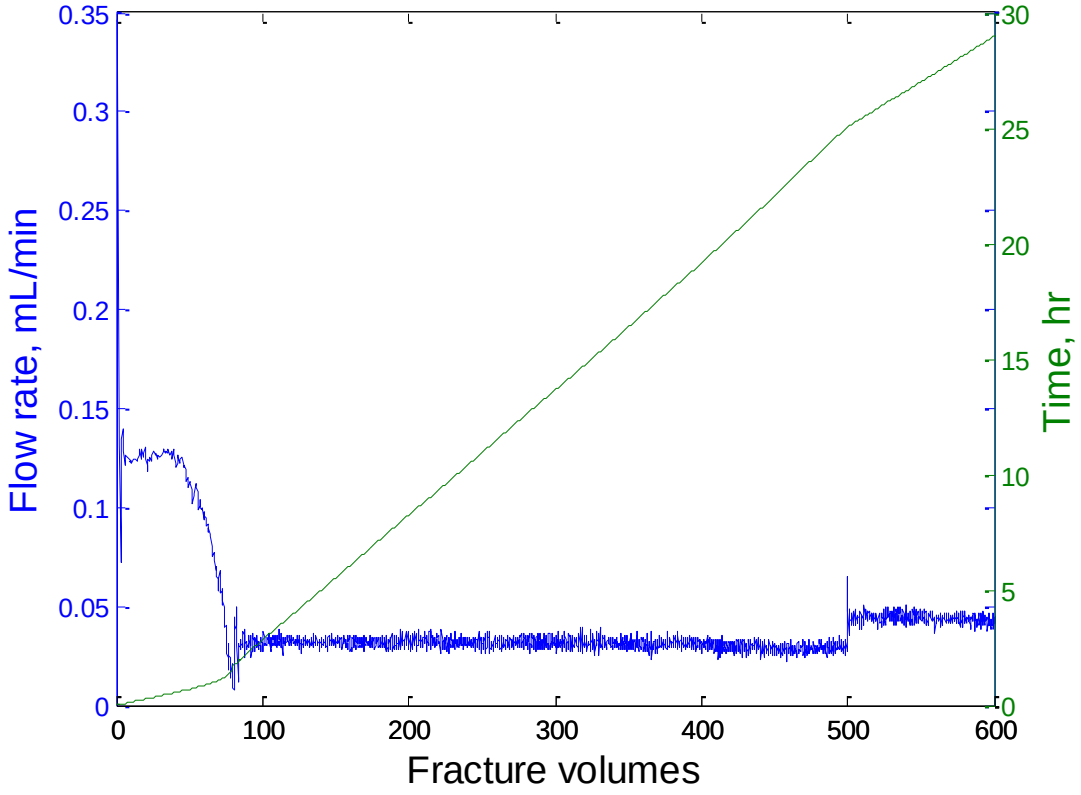

Figure C.62 – Expansion of flow rate plotted as a function of fracture volumes injected. Plot covers time period 1, 2, and part of 3.

Figure C.63 – Post experiment photo of the BPR-2 showing significant plugging due to precipitation (red arrow). This may be the source of flow throttling and subsequent increase in the back pressure building.

EXPERIMENT REPORT: JA9 – FRANK3

Summary

Experiment JA9-Frank3 was the third constant pressure differential experiment with a composite core consisting of 4 cores stacked end-to-end and with fracture planes aligned 90° to each other. The core had a very small hydraulic aperture and a small flow rate was used for the experiment. Even with a small flow rate pressure differential was very high. The experiment ran for over 70 hours but significant flow occurred for only the first 35 hours. Upstream pressure was increased at the end of the experiment to test for flow reestablishment but no significant flow occurred.

The fracture surface shows significant reaction in the first core section and a distinct band of precipitate in the second. Beyond the precipitation zone the fracture has a lighter coloration indicative of minor alteration.

This experiment showed a clear indication of self-sealing behavior.

Experiment design

The core was created using 4 fractured cement cores (Batch JA9) prepared in the same batch. Cores were poured and cured according to the standard method used for other experiments. They were also fractured and sealed according to the standard method. Cores were assembled so that each fracture was perpendicular to the next fracture. The composite core was sealed in the same manner as JA1-Frank1, using Teflon, aluminum foil, and heat shrink. Figure C.64 shows the 4 individual cores pre experiment and gives an indication of fracture alignment.

Experiment conditions

Ambient temperature (22 °C) and distilled water were used to maximize dissolved CO_2 concentration. Pore pressure was initially at 1,556 psi, which gives a theoretical

saturation of 1.4805 mol-CO_2/kg-H_2O (6.52 wt.%). The sample was not strain hardened due to the elevated confining pressure and complex geometry of the composite cores. Confining pressure was kept at an average of 2,385 psi. The sample was flushed with distilled water prior to the experiment to get the system pressure up to experiment conditions and to remove any air in the fracture.

During the experiment the digital back pressure regulator (D-BPR) was set to maintain minimum downstream pressure and the Quizix pump used in constant pressure mode to maintain constant upstream pressure. To prevent Joule-Thompson cooling of CO_2 affecting the D-BPR the heated back pressure regulator (BPR-2) was set to 500 psi and 50° C.

CO_2 and water mixing procedure

CO_2 and water was mixed by first filling the accumulator with distilled water (1.5 L) and chilling the accumulator to 5 °C. Next 143.2 mL of liquid CO_2 was injected into the accumulator from the bottom by driving from bottle pressure and receiving fluid from the accumulator in constant rate receive mode. The accumulator was then isolated from the CO_2 tank and pressurized to experiment pressure (1,556 psi). The temperature was raised to room conditions slowly and pressure held constant. Dissolution of CO_2 into the water was complete after 24 hours and the experiment began.

Results

Flow rate and pressure differential history

Table C.11 shows experiment conditions and parameters. Confining pressure remained generally stable throughout the experiment expect for one point which may have affected the experiments and is discussed below (Figure C.65).

Table C.12 shows the 4 times intervals used to describe the experiment.

Interval 1 lasts from the experiment start to the time it takes to displace the dead volume (6.872 mL), which was 23.74 hours. During this interval the pressure differential is constant at 54.8 psi. The flow rate is initially 0.0048 mL/min. Then there is an anomalous flow period between 19.13 hours and 20.03 hours where flow was 0.016 mL/min. This flow does not affect results as it occurred during the time the reactive fluid was moving through dead volume and not the core. After this time flow rate decreases to 0.006 mL/min. Interval 2 covers the time from acid reaching the core to the time when the confining pressure pump raises confining pressure, which occurs at 31.97 hours and 9.82 mL injected. During this interval pressure differential is 55.1 psi and flow rate decreases from 0.006 mL/min to 0.002 mL/min. At the start of interval 3 the system increases confining pressure from 2,324 psi to 2,579 psi (255 psi increase). The increase in confining pressure had a negligible effect on the pressure differential, which was 55 psi, (Figure C.67) but did correlate with rapid decrease in flow rate (Figure C.68). However, close inspection of the flow rate shows that the flow rate was already decreasing before 31 hours and was constant at 0.002 mL/min before and after the confining pressure increase. The final time interval consists of increasing the pressure differential by 10 psi (to 63.9 psi) to verify fracture sealing. During this interval there is essentially no flow besides the small amount required to increase the pressure.

Figure C.69 shows effective sample permeability plotted versus acid injected. The no flow time period is compressed because negligible amount of CO_2 was injected.

Fracture surface analysis

Figure C.70 shows the post reaction fracture surfaces. Near the inlet the fracture surface shows a distinct reacted channel. In the second core (gold box) there is evidence

for precipitation of white material across the entire width. In front of the precipitation zone is a less reacted zone that exists through the rest of the sample.

Figure C.71 shows the core ends of the sample post experiment. Reaction is evident at the inlet of the first core and there is no evidence for precipitation plugging the fracture at the junction point.

Discussion

This experiment provides additional evidence for the self-sealing behavior of the system. A distinct band of precipitate developed across the core and is assumed to be the source of flow restriction.

Additional information

Analysis of fracture surface by SEM/EDS/μXRD was performed but at this time I do not have the raw data.

Tables and figures

Table C.11 – **JA9-Frank3** experiment summary.

Core dimension (width × length), cm	2.54 × 24.38
Temperature, °C	22
Average confining pressure (std. dev.), psi	2,385 (41)
CO_2-saturation, wt. %	6.52
Flow rate, mL/min	0.006
Pressure differential, psi	55.1
Hydraulic aperture, μm	3
Sample permeability, mD	0.12
Total time, hr	71.2
Residence time, sec	193

Table C.12 – Important intervals during experiment.

Interval	Time, hr	Flow rate, mL/min	Pressure differential, psi	Volume, mL
1	0 to 23.75	0.0048 to 0.006	54.8	6.872
2	23.75 to 31.97	0.006 to 0.002	55.1	9.82
3	31.97 to 65.94	0.002 to 0	56.7	10.38
4	65.94 to 71.17	0	63.9	11.09

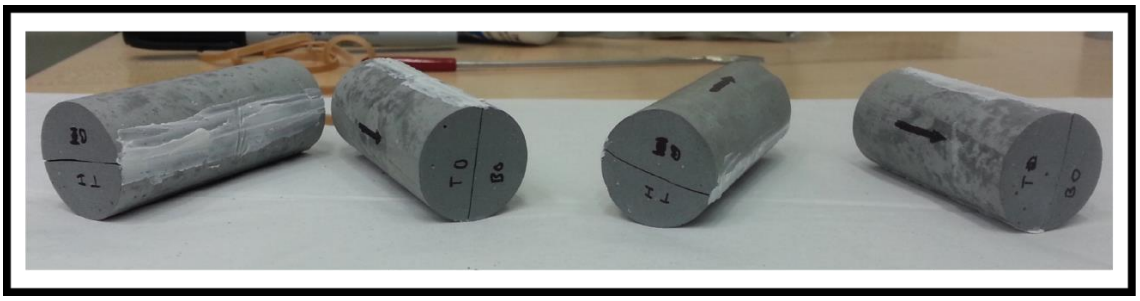

Figure C.64 – Pre experiment photos of JA9-Frank3.Shown are the individual fractured cores showing orientation of fractures before assembly of the composite core.

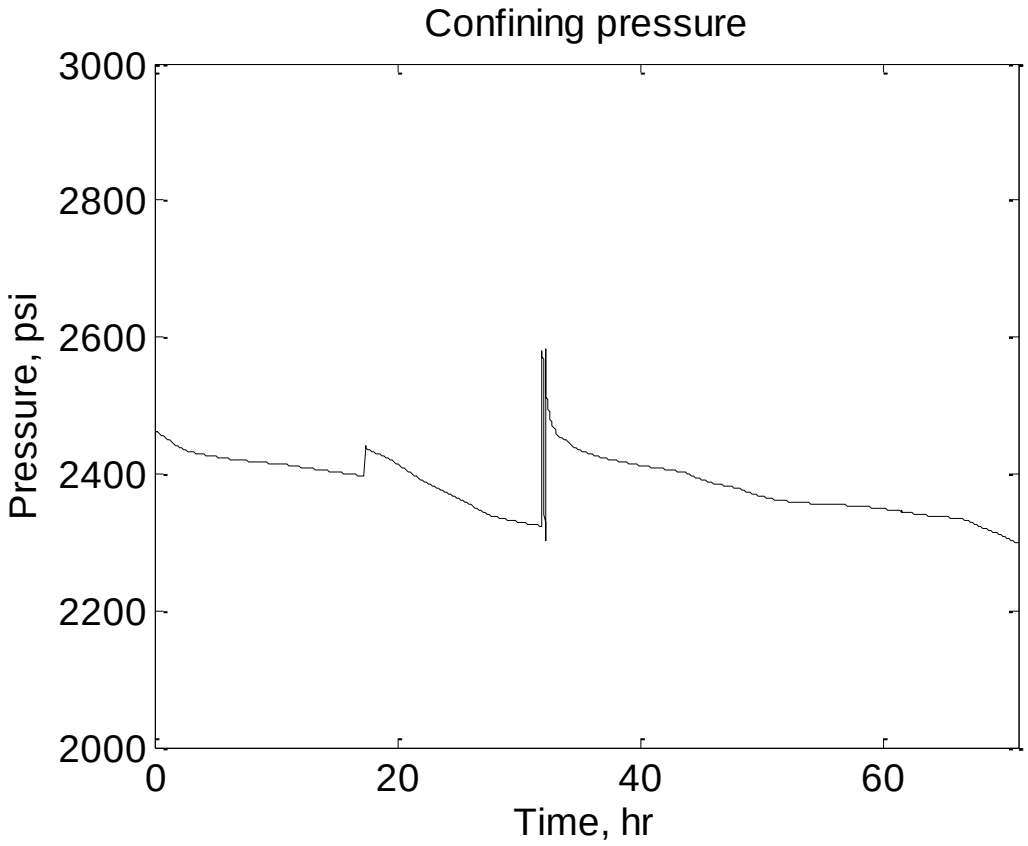

Figure C.65 – Confining pressure during experiment. Average confining pressure for the experiment was 2,385 psi with a standard deviation of 41 psi.

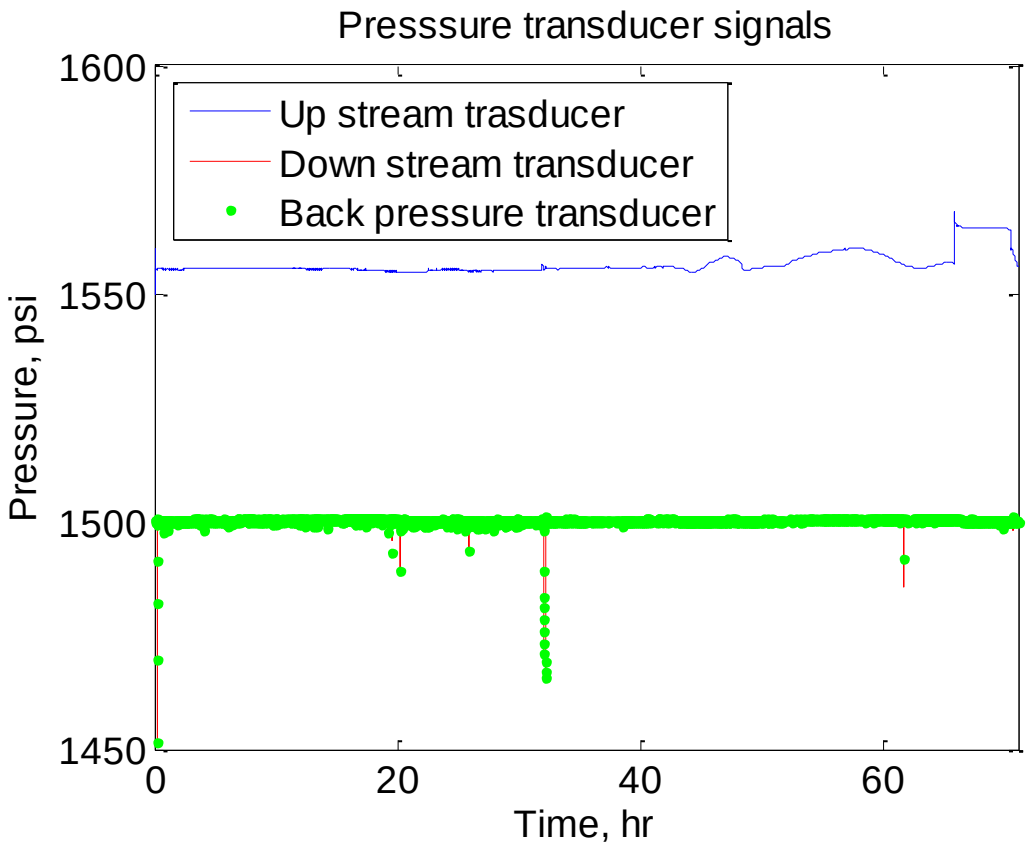

Figure C.66 – Pressure transducer signals during experiment. Driving force for flow is the difference between upstream (blue) and downstream (red) curves.

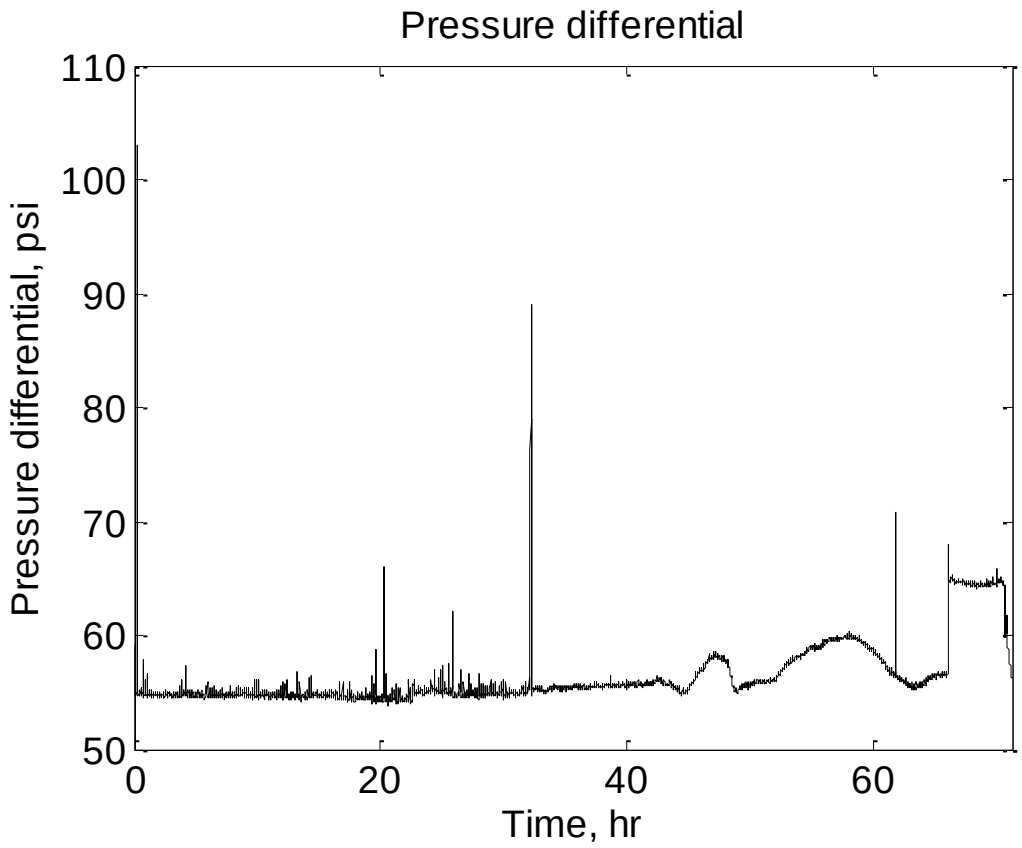

Figure C.67 – Pressure differential as a function of time. For much of the experiment the pressure differential remains constant. At the end of the experiment upstream pressure was raised by 10 psi.

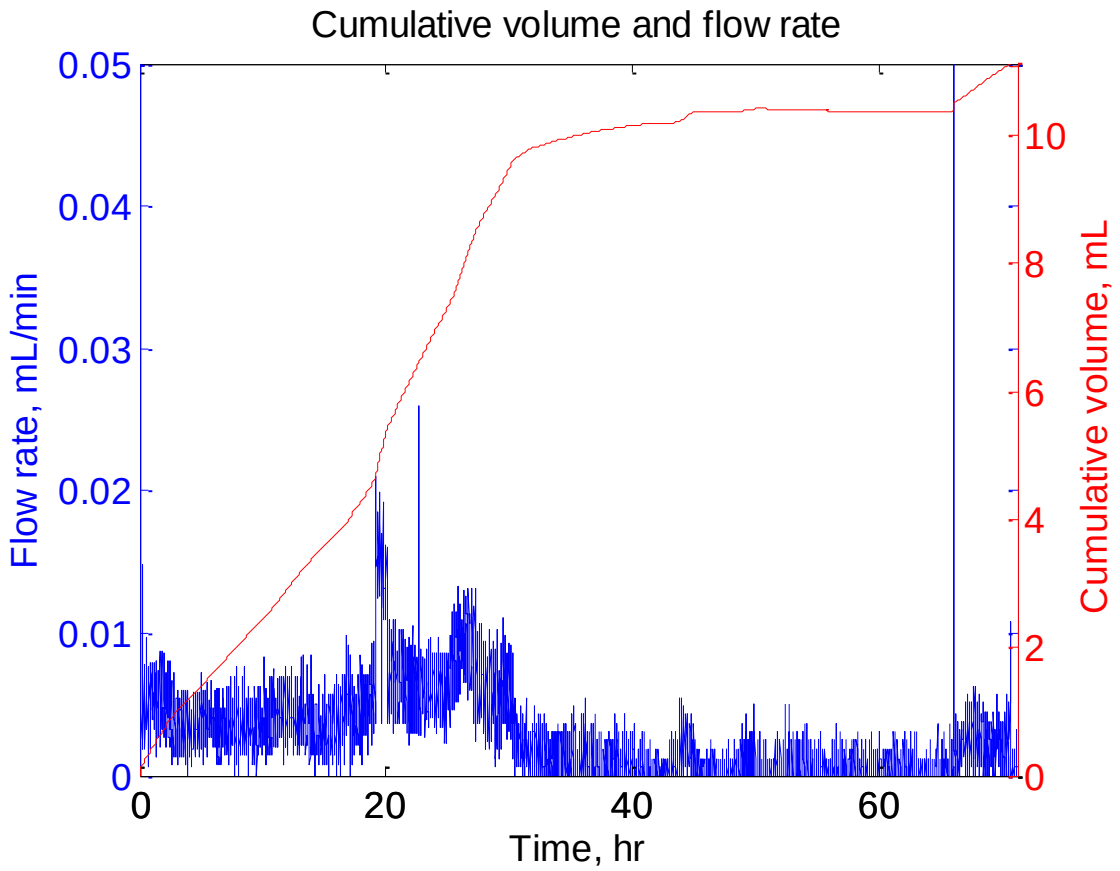

Figure C.68 – Pump flow rate (blue) and cumulative volume injected (red) as a function of time.

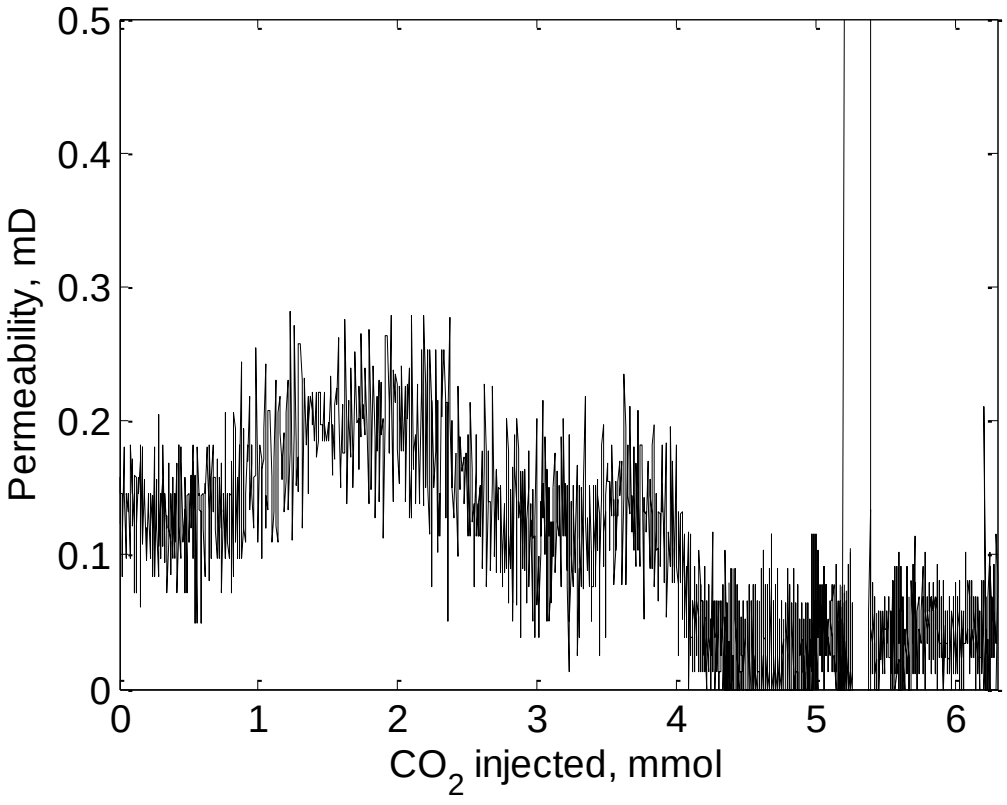

Figure C.69 – Equivalent sample permeability versus CO_2 injected. This plot has been normalized to account for dead volume.

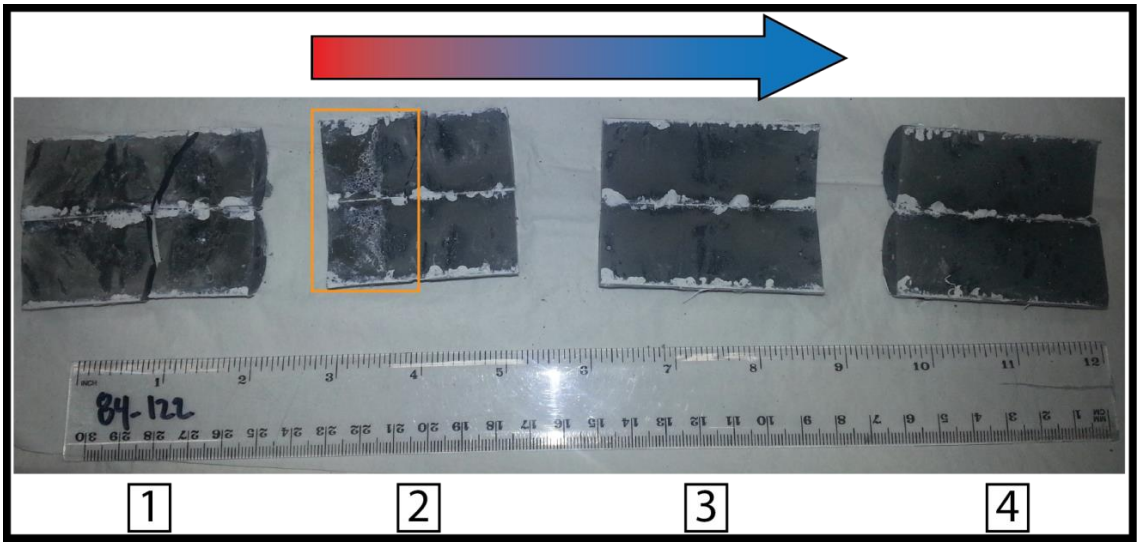

Figure C.70 – Post experiment photos of JA9-Frank3. Flow direction is from left to right.

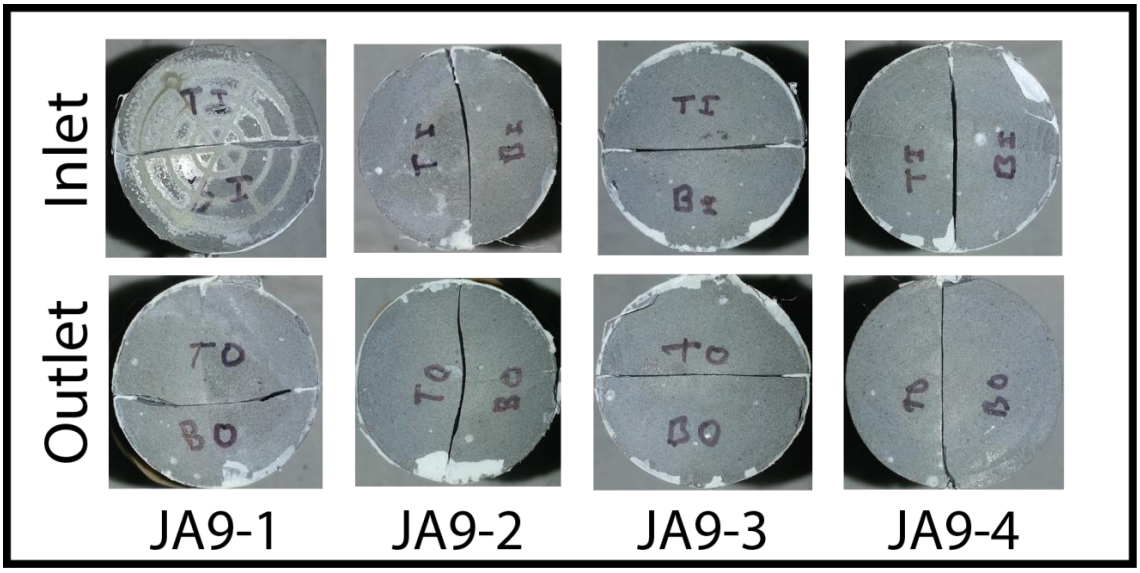

Figure C.71 – Post experiment core ends of JA9-Frank3. Flow would enter at the top left come out at the bottom right and enter at the top of the next core to the right. No evidence for plugging at the interface was seen.

EXPERIMENT REPORT: JA8 – FRANK4

Summary

Experiment JA8 was the fourth constant pressure differential experiment with a composite core consisting of 4 cores stacked end-to-end and with fracture planes aligned 90° to each other. The core had a small hydraulic aperture (6 μm) and a moderate flow rate (0.016 mL/min) was used for the experiment. Flow rate begins to decrease after 6 hours. The experiment ran for over 25 hours but began to leak at 12.4 hours.

The fracture surface shows significant reaction into the third core. There is not a distinct precipitated zone but is evidence for some precipitation in the third core. The inlet of the first core also has evidence of precipitate. This sample had evidence of self-sealing behavior before the confining pressure began to leak into the fracture fluid.

Experiment design

The core was created using 4 fractured cement cores (Batch JA8) prepared in the same batch. Cores were poured and cured according to the standard method used for other experiments. They were also fractured and sealed according to the standard method. Cores were assembled so that each fracture was perpendicular to the next fracture. The composite core was sealed in the Teflon, aluminum foil, and heat shrink tubing in the same way as JA1-Frank1.

Experiment conditions

Ambient temperature (23.5 °C) and distilled water were used to maximize dissolved CO_2 concentration. Pore pressure was initially at 1,510 psi, which gives a theoretical saturation of 1.4805 mol-CO_2/kg-H_2O (6.39 wt.%). The sample was not strain hardened due to the elevated confining pressure and complex geometry of the composite cores. Confining pressure was kept at an average of 2,457 psi. The sample was flushed

with distilled water prior to the experiment to get the system pressure up to experiment conditions and to remove any air in the fracture.

During the experiment the digital back pressure regulator (D-BPR) was set to maintain minimum downstream pressure and the Quizix pump used in constant pressure mode to maintain constant upstream pressure. To prevent Joule-Thompson cooling of CO_2 affecting the D-BPR the heated back pressure regulator (BPR-2) was set to 500 psi and 50 °C. The dead volume between pump and core was calculated to be 6.87 mL based on length of tubing and inner diameter of tubing.

CO_2 and water mixing procedure

CO_2 and water was mixed by first filling the accumulator with distilled water (1.5 L) and chilling the accumulator to 5 °C. Next 140.4 mL of liquid CO_2 was injected into the accumulator from the bottom by driving from bottle pressure and receiving fluid from the accumulator in constant rate receive mode. The accumulator was then isolated from the CO_2 tank and pressurized to experiment pressure (1,510 psi). The temperature was raised to room conditions slowly and pressure held constant. Dissolution of CO_2 into the water was complete after 24 hours and the experiment began.

Results

Flow rate and pressure differential history

Table C.11 shows experiment conditions and parameters. Confining pressure remained was stable throughout the experiment and all oscillations were caused by strokes of the pressure intensifier and subsequent decay of pressure probably through a small leak in the intensifier pump (which is normal) (Figure C.65). Figure C.66 shows pressure transducer signals for the experiment. The experiment is broken down into 3 time intervals (Table C.14). The first time period is from experiment start to the time it

takes for the acidic fluid to pass through the dead volume and reach the core (7.58 hours). The core fluid pressure had decreased between the time of distilled water flow and time for the acid experiment to begin so the early part of the acid experiment shows behavior associated with this pressure equilibration. Additionally, upstream pressure was increased during interval 1 to establish a stable upstream pressure of 1,509 psi. The corresponding pressure differential was 20.7 psi (Figure C.67). During the time of pressure equilibration the flow rate was initially fast (0.03 mL/min) but once core pressure was stable the flow rate decreased to an average of 0.015 mL/min (Figure C.68). The second time interval runs from 7.58 hours until evidence for pressure communication between core and confining fluid systems becomes apparent, which occurs at 11.73 hours. Pressure differential over this time is 21.4 psi. Flow rat starts at 0.011 mL/min and decreases to 0.003 mL/min by the end of the interval and 8.047 mL had been injected. Since the confining and core fluid system was in communication at the end of time interval 2 that is defined as the end of the experiment.

However, interval 3 is included provide insights on how it was determined that the fluid systems were in communication. The first sign that something was wrong was that upstream pressure began to increase at 11.73 hours. Since this experiment was run with the pump in constant pressure mode the upstream pressure should always be fixed at the set point value. Upstream pressure continues to build until the pump begins to receive fluid back (part of its operation) and the cumulative volume injected begins to decrease. The pump will only receive until it fills one of its cylinders (~10 mL maximum). At this point a soft limit light turns on. At 25 hours the pump pressure was cleared and reset but immediate increasing of upstream pressure well above the pump's set point indicated an outside source of pressure. The only other pressurized component in the equipment is the

confining pressure system so a leak between these two fluid systems was inferred (probably along the Teflon heat shrink tubing).

Fracture surface analysis

Figure C.70 shows the post reaction fracture surfaces. This sample appears more reacted than other samples that sealed. The evidence for a well-developed precipitation zone is also missing. There is some more diffuse white material in the third core and some evidence at the inlet of the first core but nothing conclusive can be drawn as to where the precipitation was occurring.

Figure C.71 shows the core ends of the sample post experiment. Reaction is evident at the inlet of the first core and there is no evidence for precipitation plugging the fracture at the junction point.

Discussion

This system appeared to seal before the leak developed. However, the lack of a distinct precipitation zone makes it difficult to say much more. Not much CO_2 was injected into the fracture so it is possible that the precipitation occurred at the very inlet. It is also not possible to say the confining system was not leaking at a very small rate and affected the experiment. The amount of fluid received (7 mL) during the experiment and distinct upstream pressure increase make an earlier leak unlikely.

It is interesting to note that although the confining pressure system was applying increasingly higher pressure on the fracture, the effluent from the experiment had stopped and the precipitation in the fracture appeared to be able to withstand up to 100 psi pressure differential across the core.

Additional information

None for this sample.

Tables and figures

Table C.13 – **JA8-Frank4** experiment summary.

Core dimension (width × length), cm	2.54 × 21.9
Temperature, °C	23.5
Average confining pressure (std. dev.), psi	2,457 (42)
CO_2-saturation, wt. %	6.39
Flow rate, mL/min	0.015
Pressure differential, psi	20.7
Hydraulic aperture, μm	6
Sample permeability, mD	0.7
Total time, hr	25.5
Residence time, sec	122

Table C.14 – Important intervals during experiment.

Interval	**Time, hr**	**Flow rate, mL/min**	**Pressure differential, psi**	**Volume, mL**
1	0 to 7.58	0.015	20.7	6.87
2	7.58 to 11.73	0.011 to 0.003	21.4	8.047
3	11.73 to 25.53	-	-	-

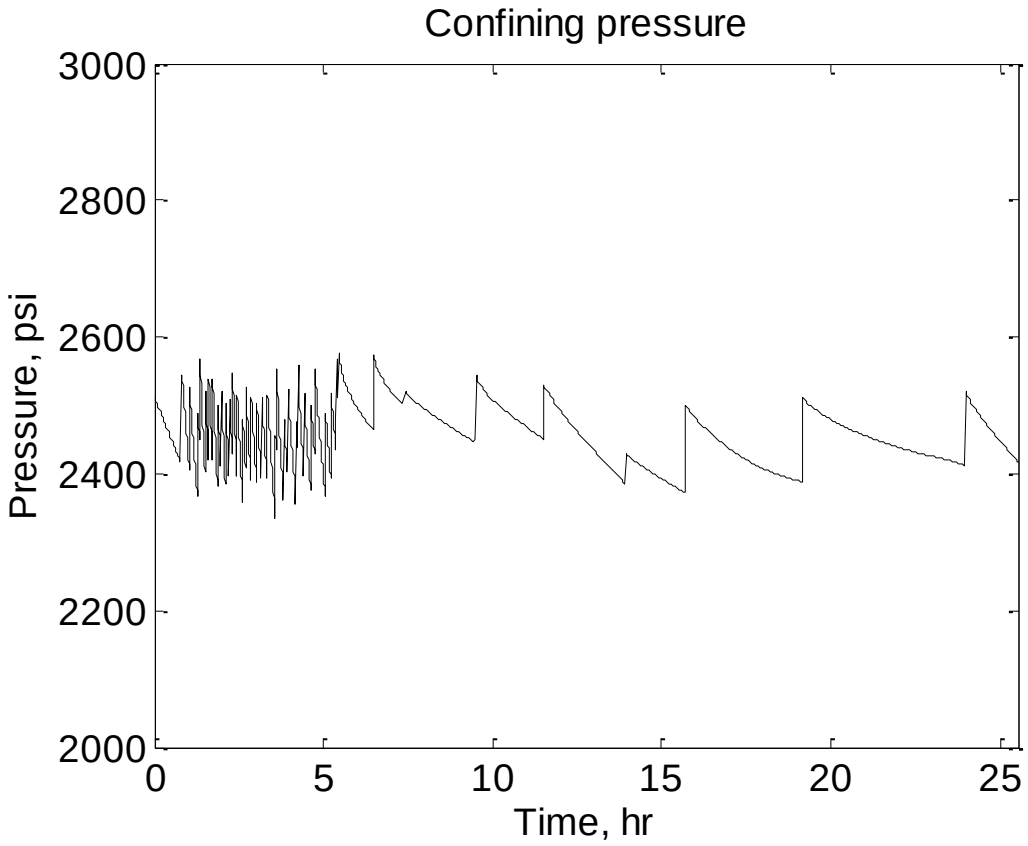

Figure C.72 – Confining pressure during experiment. Average confining pressure for the experiment was 2,457 psi with a standard deviation of 42 psi.

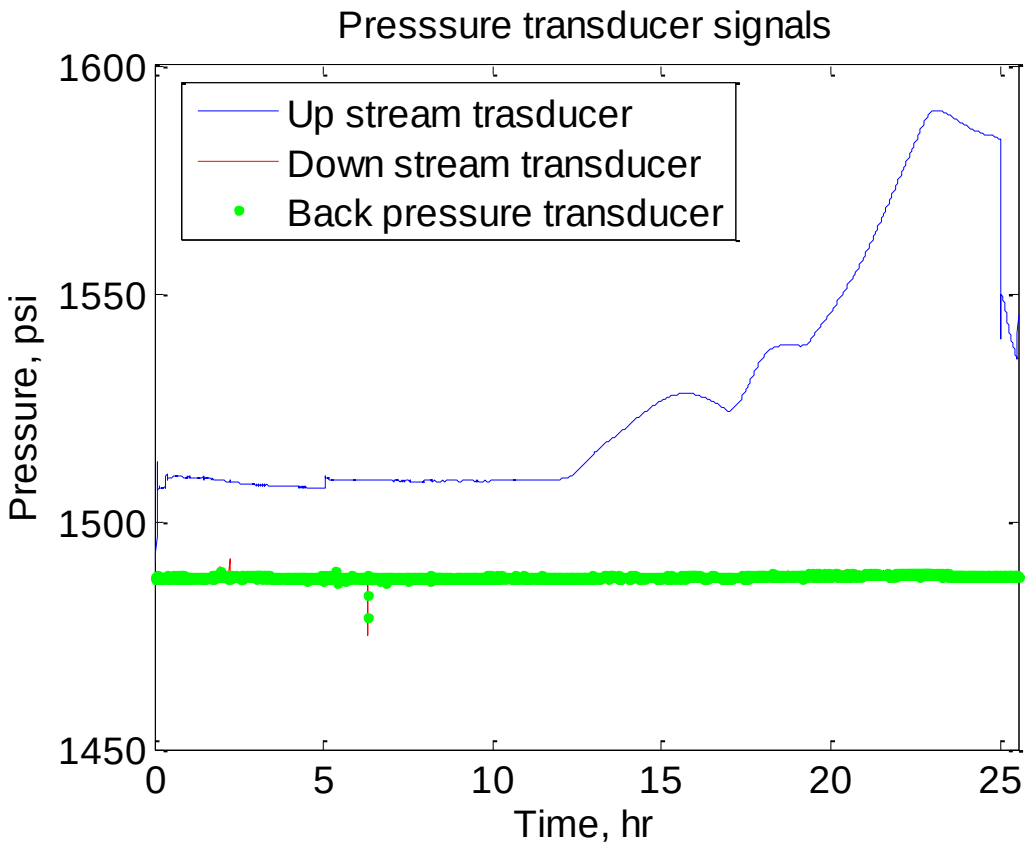

Figure C.73 – Pressure transducer signals during experiment. Driving force for flow is the difference between upstream (blue) and downstream (red) curves.

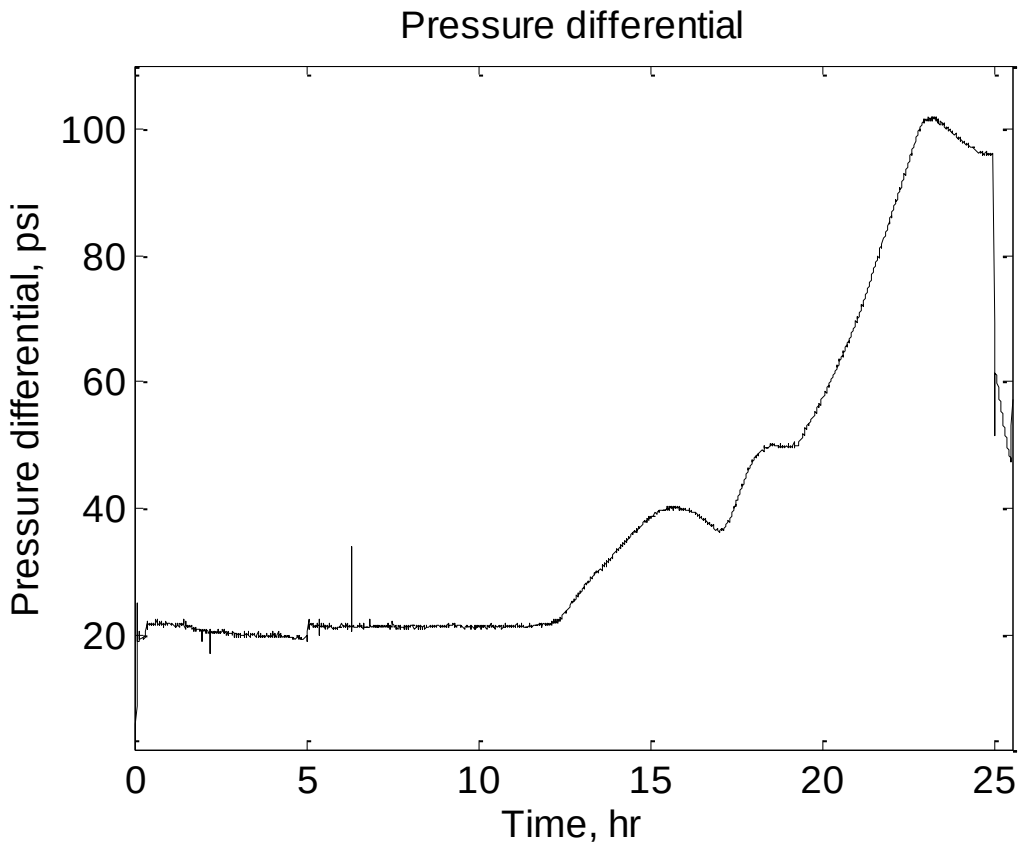

Figure C.74 – Pressure differential as a function of time. Pressure differential begin to rise due to communication between the confining pressure and fracture pressure.

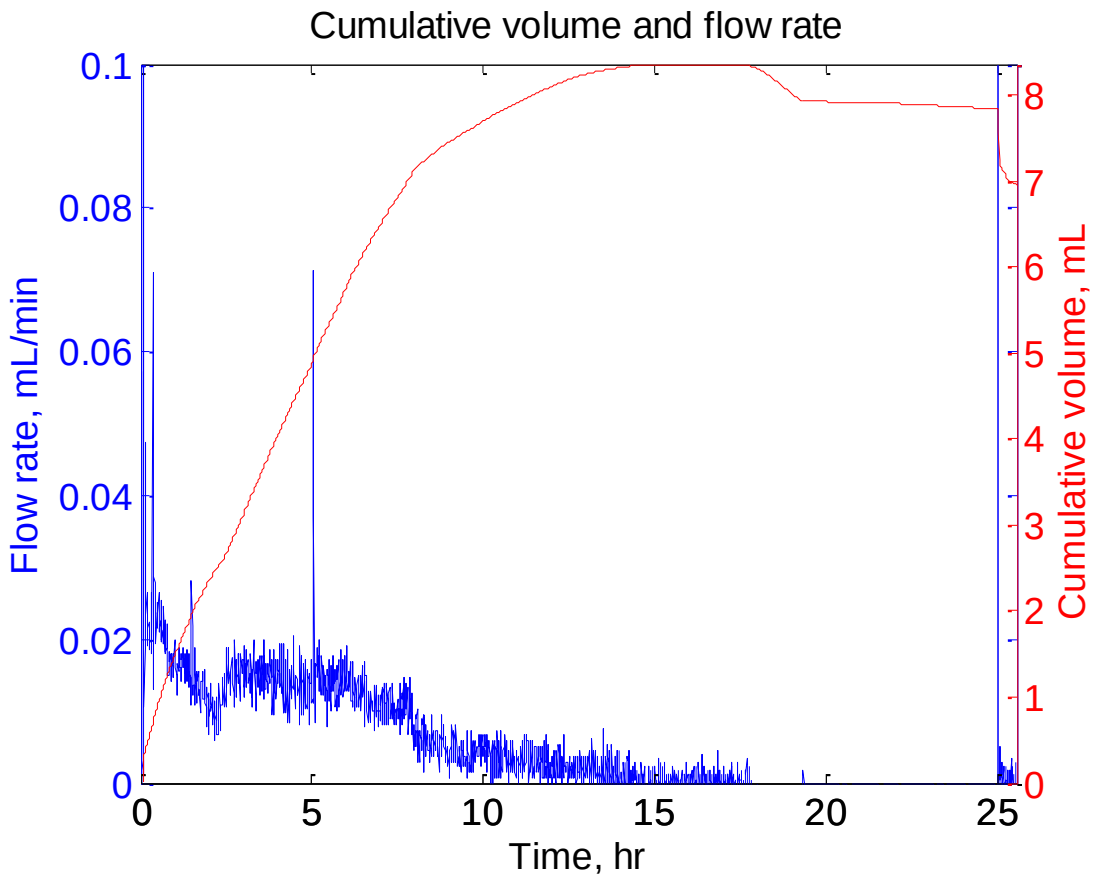

Figure C.75 – Pump flow rate (blue) and cumulative volume injected (red) as a function of time.

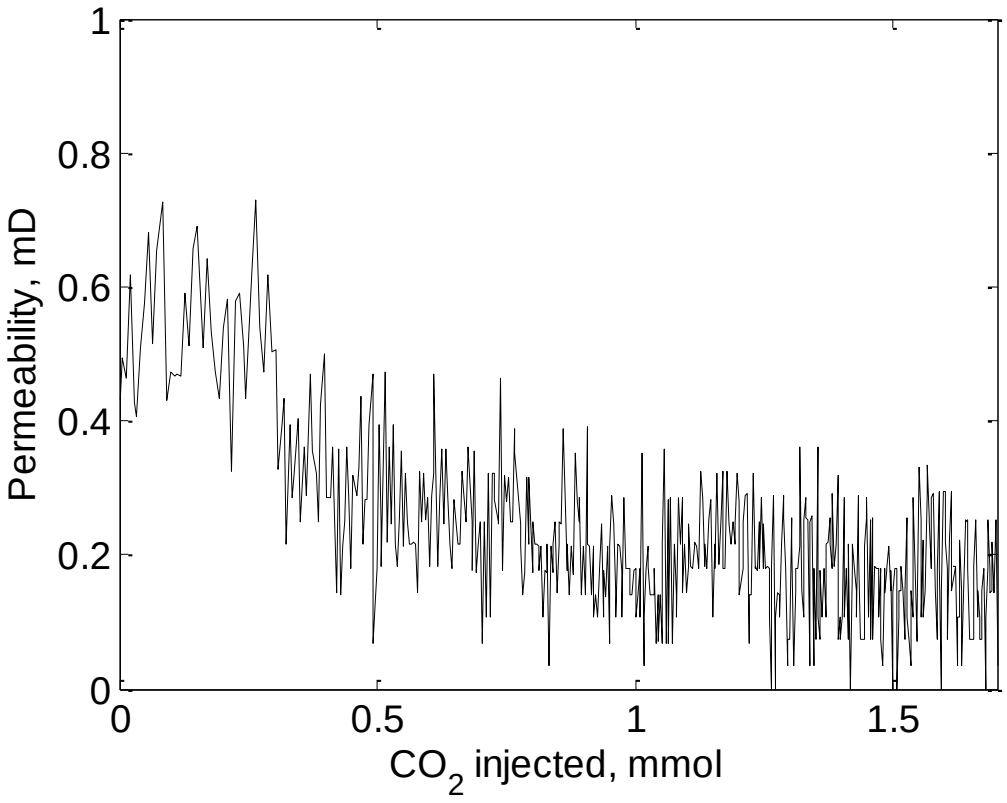

Figure C.76 – Equivalent sample permeability versus CO_2 injected. This plot has been normalized to account for dead volume.

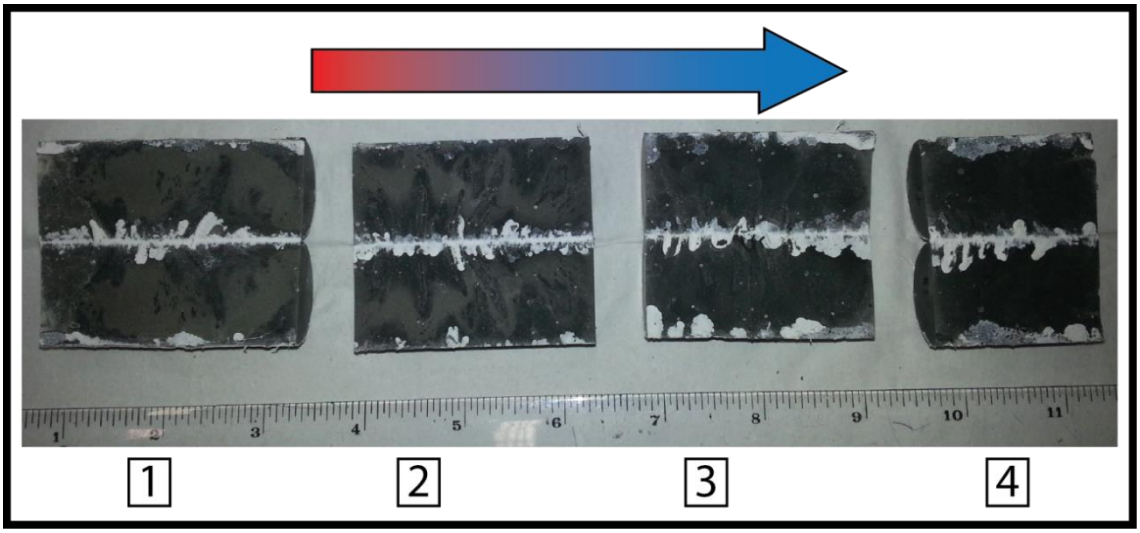

Figure C.77 – Post experiment photos of JA8-Frank4. Flow direction is from left to right.

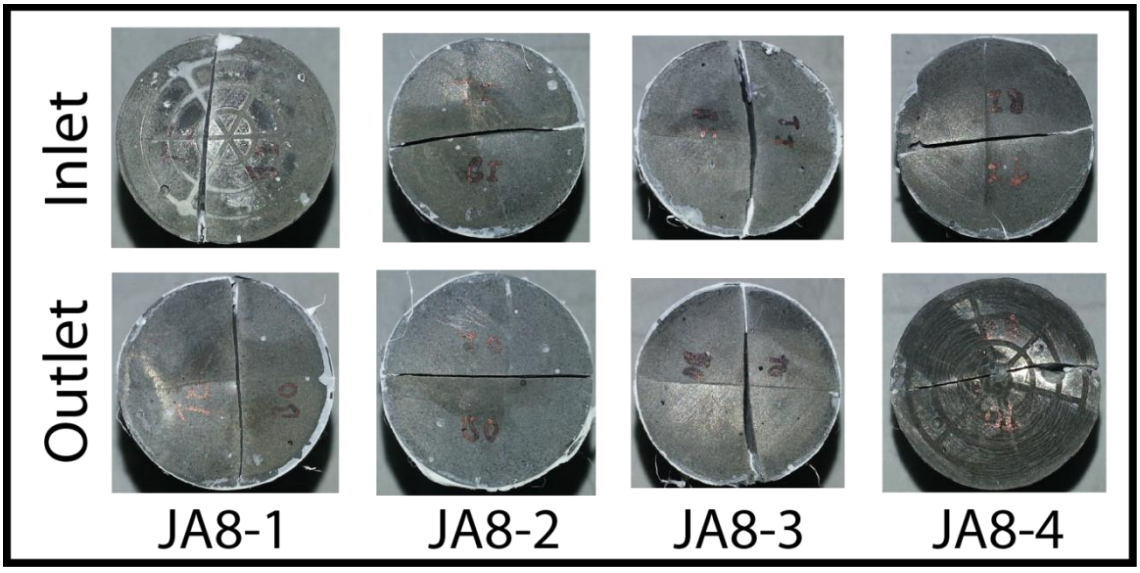

Figure C.78 – Post experiment core ends of JA8-Frank4. Flow would enter at the top left come out at the bottom right and enter at the top of the next core to the right. No evidence for plugging at the interface was seen.

EXPERIMENT REPORT: JA11 – FRANK6

Summary

Experiment JA11-Frank6 was a composite core run under constant pressure driving force like previous experiments. There was one key distinction with this core in that Teflon spacers were used between each core to remove the effect of a tight restriction in flow that occurs when the cores are placed with fracture planes 90° to each other. With the spacer it was possible for fluid to more easily move between individual cores.

The experiment ran for over 40 hours but significant flow only occurred for the first 10 hours. Some anomalous flow occurred before the acid was projected to hit the core but after this point flow rate was 0.016 mL/min and pressure differential was 22.2 psi.

Despite the presence of the Teflon spacers, the fracture surface showed very similar reaction pattern to other experiments. A distinct precipitation zone was evident in the first core.

Based on results from this sample, the effect of a tight transition point between samples seems negligible for the composite core experiments.

Experiment design

Sample preparation

The composite core (JA11-Frank6) was constructed from 4 cores of cement prepared in the same batch. Cores were poured and cured according to the standard method used for other experiments. They were also fractured and sealed according to the standard method. Cores were assembled so that each fracture was perpendicular to the next fracture with a Teflon ring place between each intersection. The purpose of inserting the spacer was to observe the effect of having a less restrictive flow path. Cores were then sealed around the joint at each interface with caulk. To seal the composite core and provide some strength the sample was wrapped in a layer of Teflon tape, sealed in heat shrink tubing, wrapped in a layer of aluminum foil, and sealed in a second sleeve of heat shrink tubing. Figure C.46 shows images of the individual cores with Teflon spacers and of the composite core.

Experiment conditions

Ambient temperature (22.8 °C) and distilled water were used to maximize dissolved CO_2 concentration. Pore pressure was initially at 1,505 psi, which gives a theoretical saturation of 1.462 mol-CO_2/kg-H_2O (6.43 wt.%). The sample was not strain hardened due to the elevated confining pressure and complex geometry of the composite cores. Confining pressure was kept at an average of 2,549 psi. The sample was flushed

with distilled water prior to the experiment to get the system pressure up to experiment conditions and to remove any air in the fracture.

CO_2 and water mixing procedure

CO_2 and water was mixed by first filling the accumulator with distilled water (1.5 L) and chilling the accumulator to 5 °C. Next 150 mL of liquid CO_2 was injected into the accumulator from the bottom by driving from bottle pressure and receiving fluid from the accumulator at a constant rate. The accumulator was then isolated from the CO_2 tank and pressurized to experiment pressure (1,505 psi). The temperature was raised to room conditions slowly and pressure held constant. Dissolution of CO_2 into the water was complete after 24 hours and the experiment began.

Results

Flow rate and pressure differential history

Table C.7 shows experiment conditions and parameters. Confining pressure remained stable throughout the experiment (Figure C.47). Upstream and downstream pressure did have a fairly complex history and is discussed below (Figure C.48). This experiment is broken down into 4 intervals (Table C.16). During interval 1 pressure differential was constant at 11.8 psi (Figure C.49). Flow rate during this time was 0.033 mL/min (Figure C.50) and by the end of the interval 6.2 mL of fluid had been injected. This interval lasts until 3.08 hours. At the start of interval 2, flow rate decreased rapidly to 0.004 mL/min however pressure differential remained constant at around 12.5 psi. This time period lasts until 5.08 hours and 6.7 mL (the dead volume) of fluid is injected. At the start of interval 3, upstream pressure is raised so that pressure differential increases to 24 psi and then to 40 psi by 7 hours. Flow rate has an initial increase at the beginning of

the interval to 0.058 mL/min but then decreases and by 7 hours the flow rate is 0.004 mL/min and unresponsive to increases in pressure differential. By the end of the interval (10 hours) 8.1 mL of fluid was injected. The final time period was from 10 hours to 40.92 hours. During this time flow is nearly shut off (0.0015 mL/min) and by the end of the experiment 10.85 mL had been injected. During this interval the back pressure decreased. A decrease in the back pressure would happen if there is a small leak in the D-BPR and the upstream pressure was not supplying sufficient fluid to maintain the D-BPR at the set point. This would occur if the cement fracture was effectively sealed and no fluid was moving out of the core. Upstream pressure was raised several times to end up at 1,657 psi. There was a response in the downstream pressure to the increases in upstream pressure but by the end of the experiment pressure differential was very high (296 psi) with negligible flow. Figure C.51 shows permeability as a function of CO_2 injected into the fracture (accounting for dead volume).

Fracture surface analysis

Figure C.52 shows a post experiment photo of the fracture surface. Flow is from left to right. Most of the fracture surface shows reaction with distilled water flow. In core 1 there is evidence for precipitation near the outlet of that core and a distinct reacted channel between the precipitation zone and the inlet. Figure C.53 shows photos of the inlet and outlet for each individual core that was stacked to create the composite core.

Discussion

The results from JA11-Frank6 have 2 important implications. The first is that the sample seemed to seal and maintain a very high pressure differential without permitting flow. This is yet more evidence for the self-sealing phenomena. The second is that the

use of Teflon spacers seems to have had no effect on experiment results. Especially when comparing to previous Frank experiments, there seems to be no difference.

One complication to this experiment is the high initial flow rate and sudden drop that occurs before acid had pass through the entire dead volume. Was the flow rate drop due to acid reaching the core faster than expected (like in JA5-Frank2) or was this some other effect (e.g. pump/accumulator related issues). Additionally, the operator imposed upstream pressure increases right at the start of when the fluid should have been reaching the core face and during key flow rate decline time make using this experiment for modeling of leakage behavior difficult.

Additional information

None for this experiment.

Tables and figures

Table C.15– **JA11-Frank6** experiment summary.

Core dimension (width × length), cm	2.54 × 21.3
Temperature, °C	22.8
Average confining pressure (std. dev.), psi	2,549 (10)
CO_2-saturation, wt. %	6.43
Flow rate, mL/min	0.016
Pressure differential, psi	22.2
Hydraulic aperture, μm	6
Sample permeability, mD	1
Total time, hr	40.85
Residence time, sec	114

Table C.16 – Important intervals during experiment.

Interval	Time, hr	Flow rate, mL/min	Pressure differential, psi	Volume, mL
1	0 to 3.08	0.033	11.8	6.2
2	3.08 to 5.08	0.004	12.5	6.7
3	5.08 to 10.0	0.058 to 0.004	24 to 40	8.1
4	10.0 to 40.92	0.0015	40 to 296	10.85

Figure C. 79 – Images of JA11-Frank6 cores before reaction. A) Image of fracture surface of each individual core before assembly with Telfon washers. B) Image of the composite core put together. Note that the joint between each individual core has been sealed with caulk.

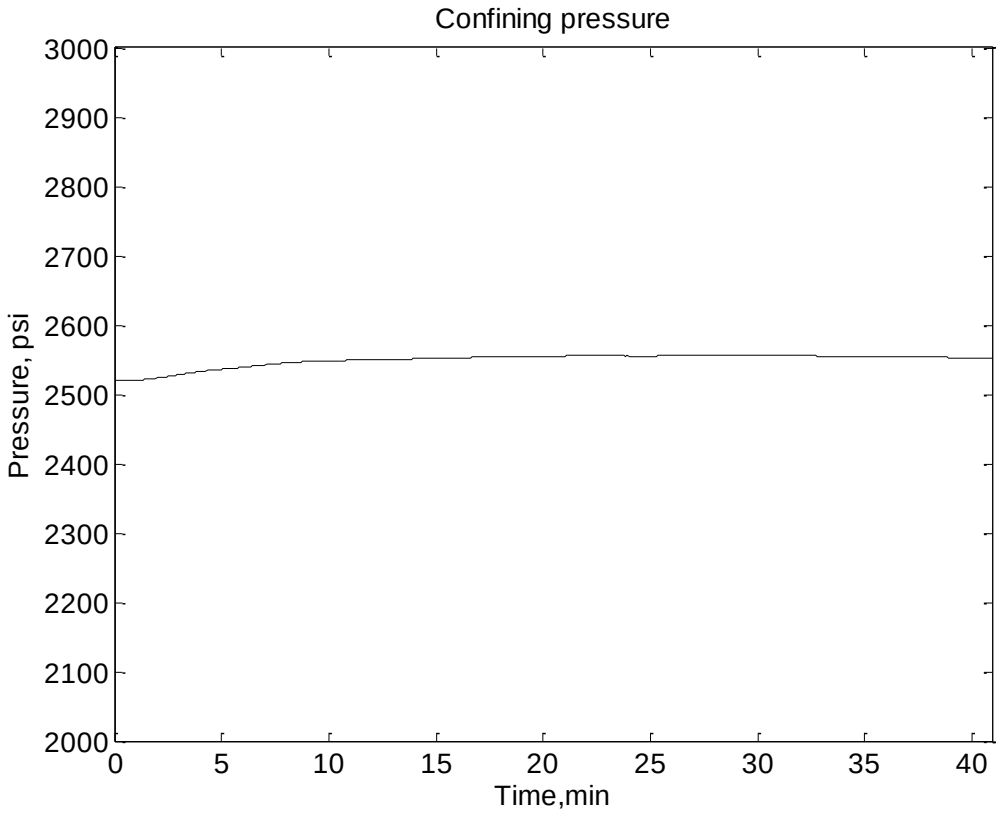

Figure C.80 – Confining pressure during experiment. Average confining pressure for the experiment was 2,549 psi with a standard deviation of 10 psi.

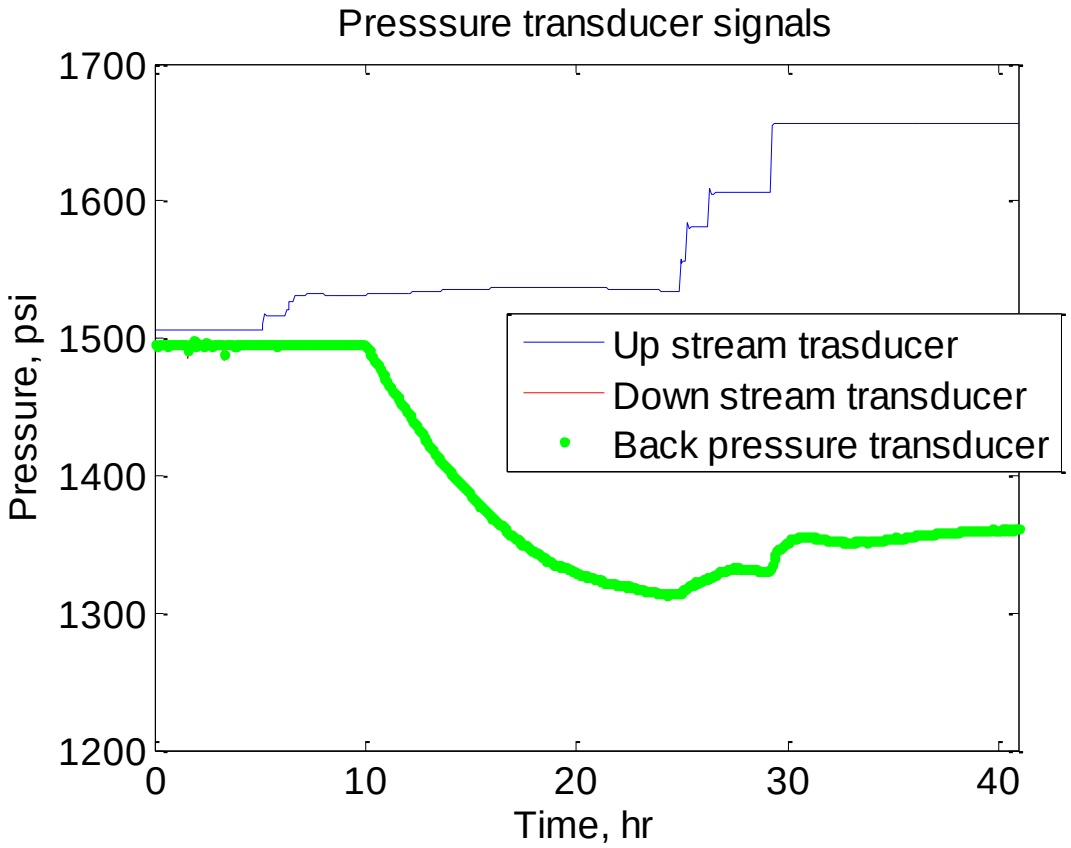

Figure C.81 – Pressure transducer signals during experiment. Driving force for flow is the difference between upstream (blue) and downstream (red) curves.

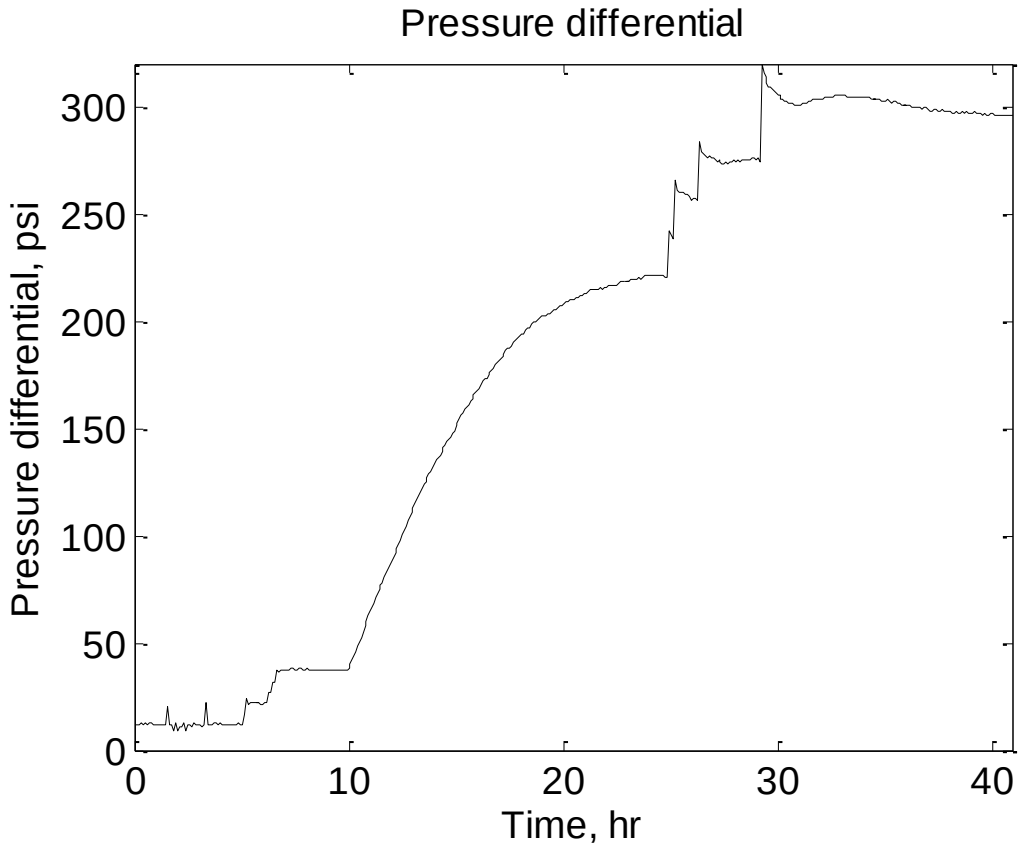

Figure C.82 – Pressure differential as a function of time.

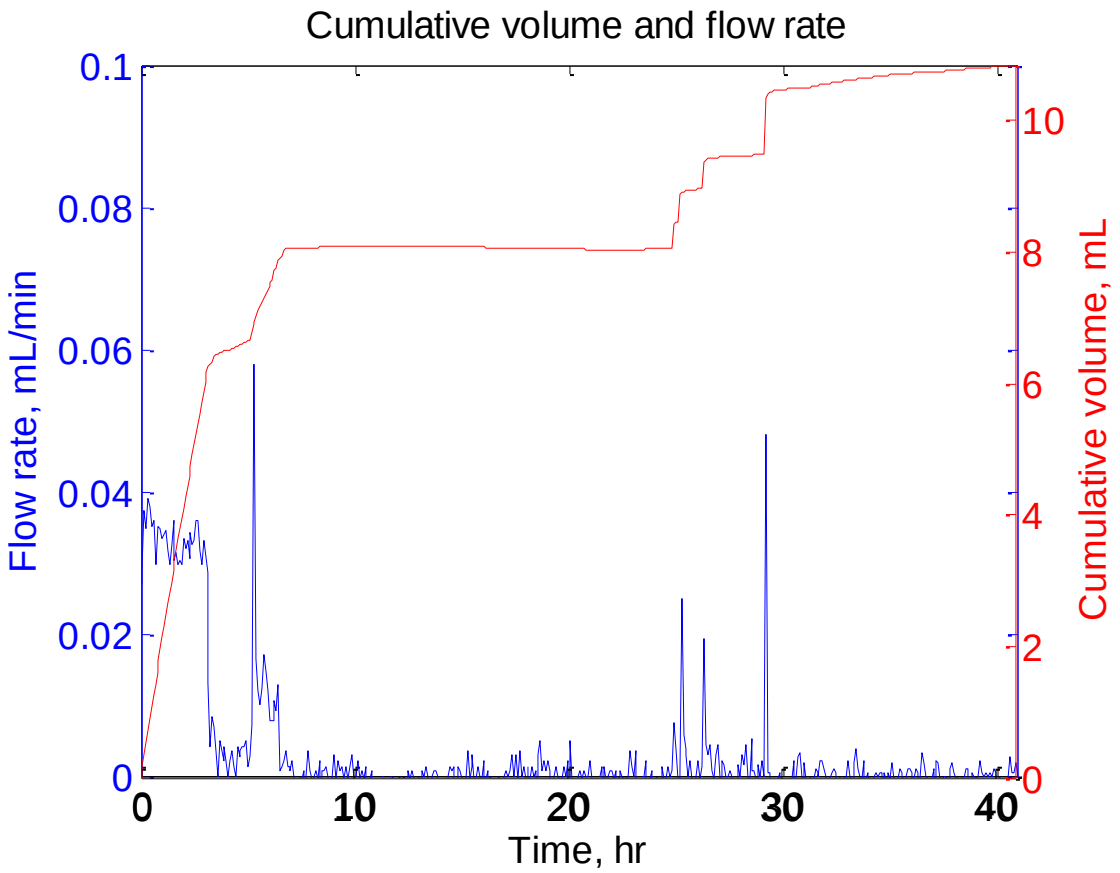

Figure C.83 – Pump flow rate (blue) and cumulative volume injected (red) as a function of time.

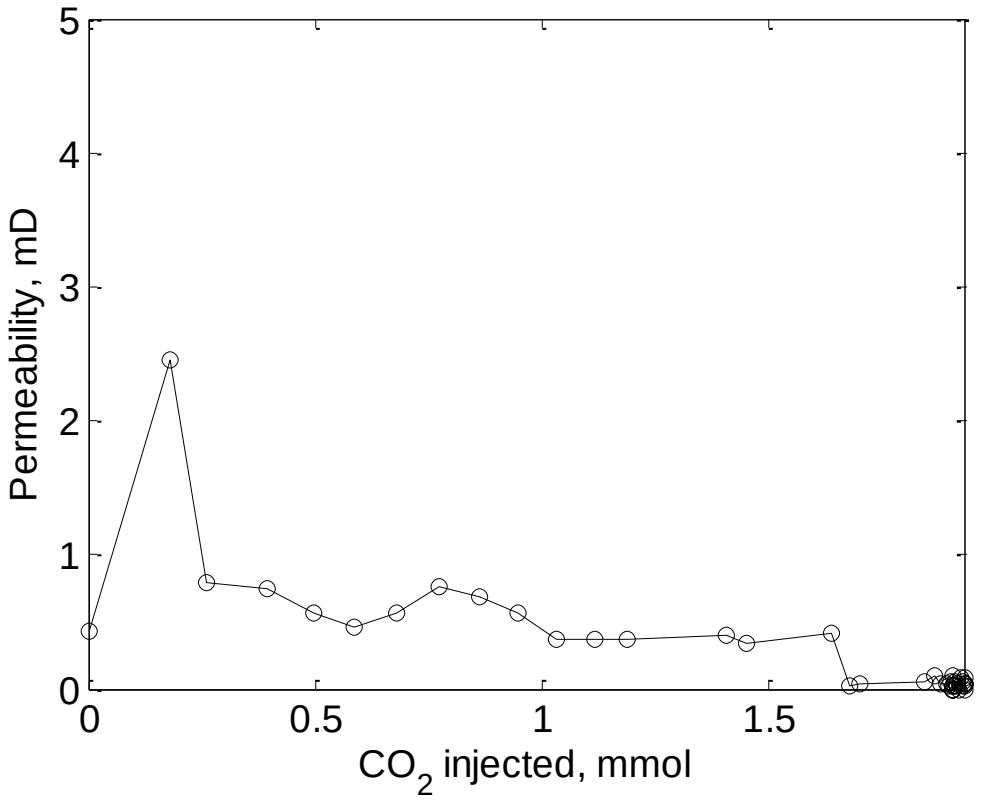

Figure C.84 – Equivalent sample permeability versus CO_2 injected.

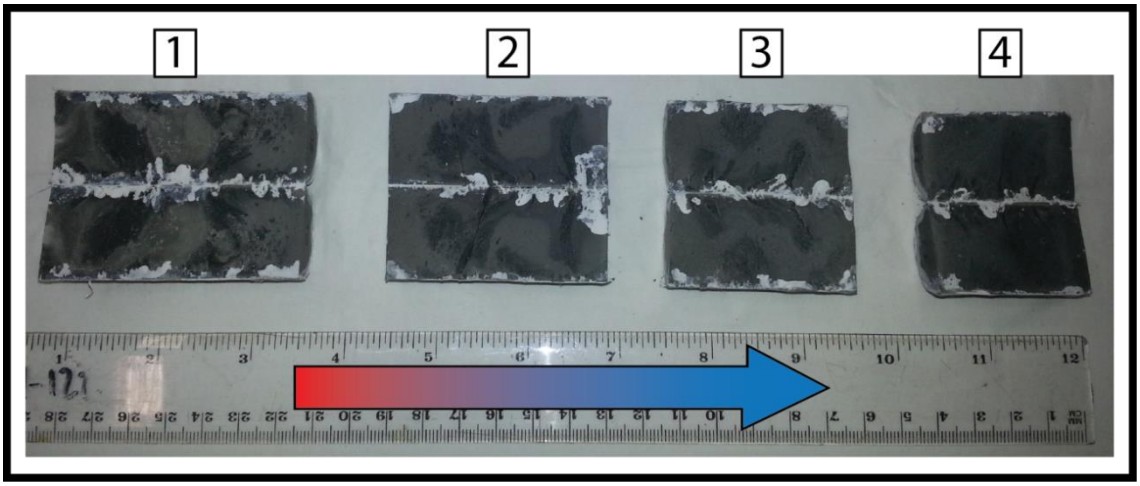

Figure C.85 – Post experiment photos of JA11-Frank6. Flow direction is from left to right.

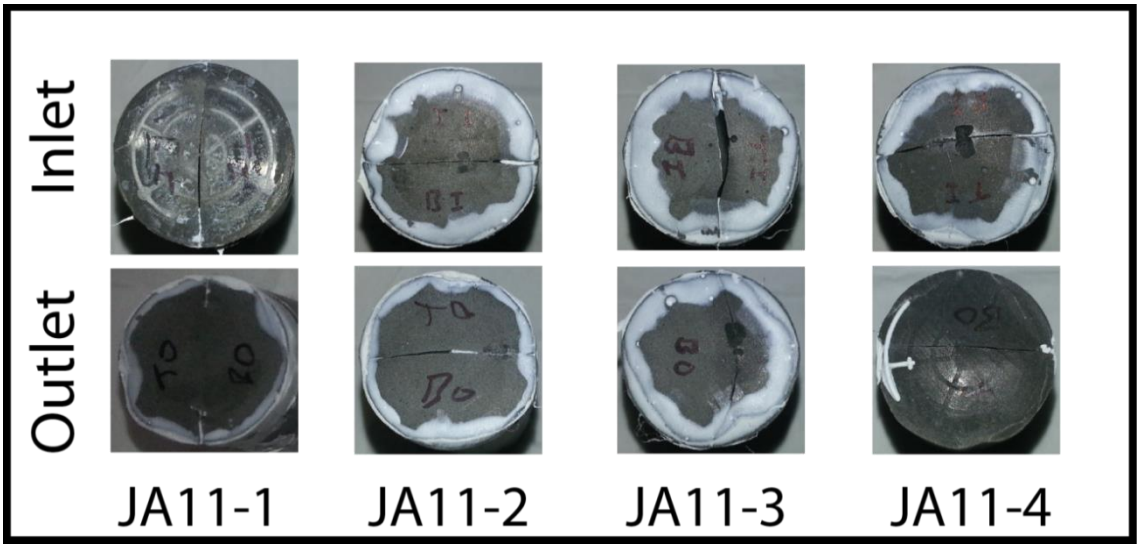

Figure C.86 – Post experiment core ends of JA11-Frank6. Flow would enter at the top left come out at the bottom right and enter at the top of the next core to the right. No evidence for plugging at the interface was seen.

Appendix D

PERMEABILITY EVOLUTION MODEL

Model derivation

This appendix presents the derivation and analysis of a simple empirical model that both matches experiment results and can be used to forecast well scale leakage. To describe fluid leakage this model follows the convention of other studies on wellbore leakage (Nordbotten et al., 2005; Tao et al., 2011) and assumes Darcy flow along the pathway (fractured core or wellbore). This model also assumes one dimensional single phase incompressible flow under isothermal conditions. Gravity is ignored and CO_2 cannot come out of solution. Fluid flux (q) is related to the pressure differential (ΔP) divided by the fluid viscosity (μ) and length (L) by the average leak path permeability ($\bar{k}$):

$$q = \bar{k}\frac{\Delta P}{\mu L} \qquad \text{(D.1)}$$

Pressure differential is assumed to be a fixed driving force in the subsurface and in this model fluid flux changes as permeability varies. This formulation is quite different from most analyses, which prescribe constant flux rate, and a key strength of this novel approach. The flux term is rewritten as a change in the position of the salinity fluid front (x_f) with a change in time (t) to get:

$$\frac{dx_f}{dt} = \bar{k}\frac{\Delta P}{\mu L} \qquad \text{(D.2)}$$

Average permeability is assumed to behave according to flow in series (Bear, 1972) between 3 zones of distinct permeability (k_i) and lengths (L_i), where i is the

specific zone. The three zones are the minimally altered zone (0), precipitation zone (1), and reacted zone (2). This model is valid until x_p reaches the end of the sample or well (depending on definition of the length L). Figure D.1 shows a schematic of the zones at two different time steps.

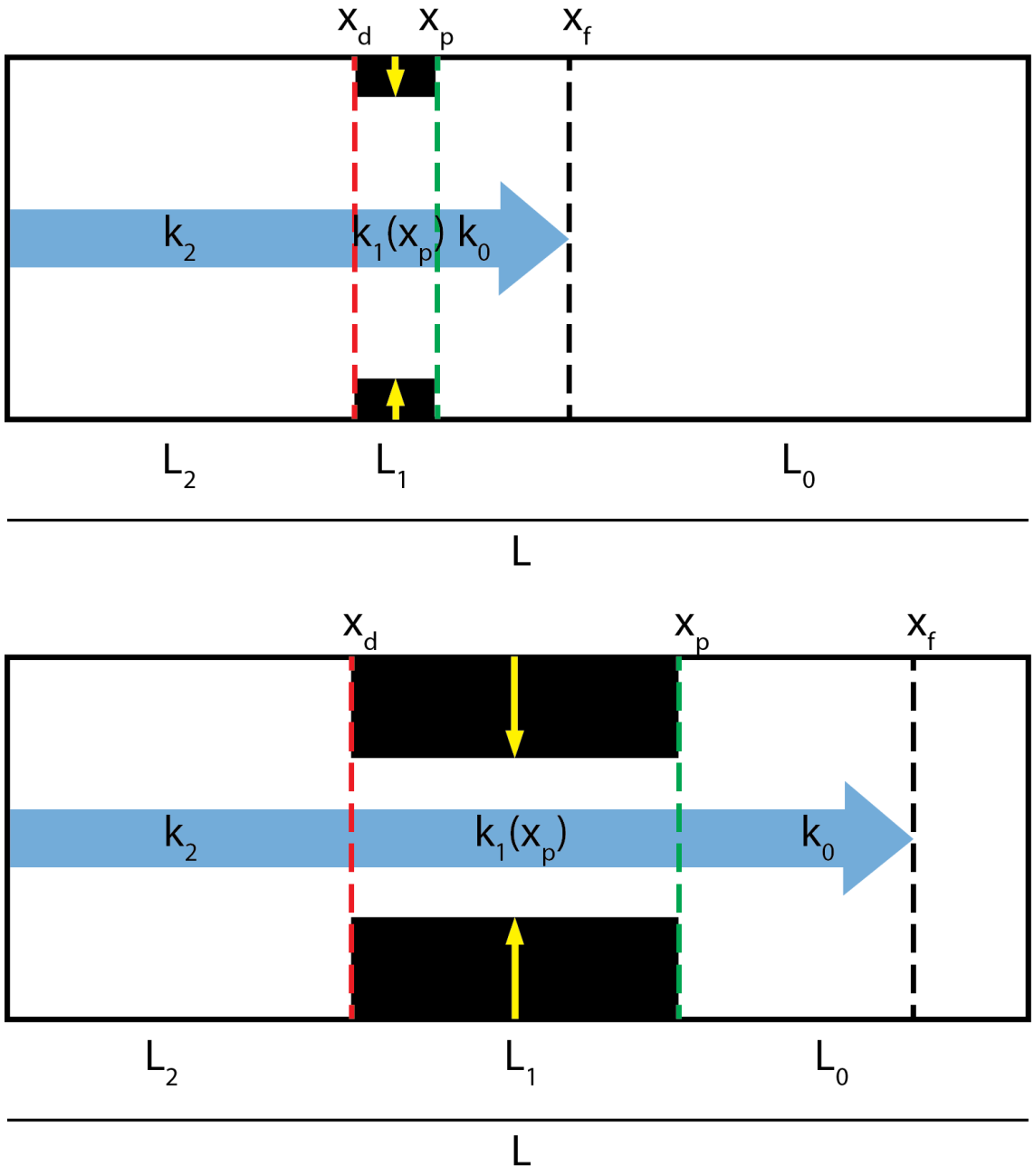

Figure D.1 – Illustration showing relation between front positions, zones, and lengths in the model. Zone 0 is between the fluid front and the precipitation front and has the same permeability of the pathway before acidic fluid was injected. Zone 1 is between the precipitation front and the dissolution front and has a permeability that evolves as the precipitation front moves along the length. Zone 2 is between the dissolution front and the inlet of the pathway. Evolution of this pathway for 2 time steps is shown.

Evolution of fluid flux is controlled by the average permeability for flow in series:

$$\bar{k} = \frac{L}{\frac{L_0}{k_0} + \frac{L_1}{k_1} + \frac{L_2}{k_2}} \qquad (D.3)$$

The model assumes the location of the precipitation front (x_p) and subsequent dissolution front (x_d) lag behind x_f by a constant parameter. For x_p the parameter is α and for x_d the parameter is β. Permeability of the precipitation zone (k_1) is assumed to decrease by some function as x_p propagates. The above relations are written in mathematical notation as:

$$x_p(x_f) = \alpha x_f \quad (D.4)$$

$$x_d(x_f) = \beta x_f \quad (D.5)$$

$$k_1(x_p) = f(x_p) = f(\alpha x_f) \qquad (D.6)$$

The length of each zone is determined by the relative position of the fronts as:

$$L_0 = L - x_p \qquad (D.7)$$

$$L_1 = x_p - x_d \qquad (D.8)$$

$$L_2 = x_d \qquad (D.9)$$

Plugging in Eqn. D.4 to Eqn. D.9 into Eqn. D.2 gives the following equation:

$$\frac{dx_f}{dt} = \frac{L}{\frac{L-\alpha x_f}{k_0} + \frac{\alpha x_f - \beta x_f}{k_1(\alpha x_f)} + \frac{\beta x_f}{k_2}} \frac{\Delta P}{\mu L} \qquad (D.10)$$

The differential equation is now solely a function the front position (x_f) and time and after grouping terms to simplify, the equation becomes:

$$\frac{dx_f}{dt} = \left[I + Mx_f + \frac{(\alpha-\beta)}{k_1(\alpha x_f)} x_f \right]^{-1} F \qquad (D.11)$$

The simplification terms F, I, and M are:

$$F = \frac{\Delta P}{\mu} \qquad (D.12)$$

$$I = \frac{L}{k_0} \qquad (D.13)$$

$$M = \frac{(\beta k_0 - \alpha k_2)}{k_0 k_2} \qquad (D.14)$$

The differential equation is then solved by separation of variables for all but the term with the precipitation zone permeability to get:

$$t = \frac{1}{F}\left[Ix_f + \frac{M}{2} x_f^2 + (\alpha-\beta)\int \frac{x_f}{k_1(\alpha x_f)} dx_f \right] \qquad (D.15)$$

The form of the permeability function for the precipitation zone is unknown. The most obvious choice would be a single constant permeability (k_1 = constant) that is less than the initial permeability. As the precipitation zone increases in width the precipitated zone would be weighted more heavily and average permeability would decrease. Solving Eqn. D.15 with the boundary condition $t = 0, x_f = 0$ gives the following equation:

$$t = \frac{1}{F}\left[Ix_f + \frac{M}{2} x_f^2 + (\alpha-\beta)\frac{x_f^2}{2k_1} \right] \qquad (D.16)$$

However, observations from the experiments imply that a more complex function may also be appropriate. The observations are that that there must be some time for which the average permeability is constant and once permeability decreases it must do so as an asymptotic decay (Figure 3.12). A logistic function allows both features observed in the experiments to be captured by the model (Figure D.2). By varying parameter *a* and *b* the shape of the logistic function can be varied. The logistic equation for k_1 is:

$$k_1 = \frac{k_0}{1+ae^{b\alpha x_f}} \qquad (D.17)$$

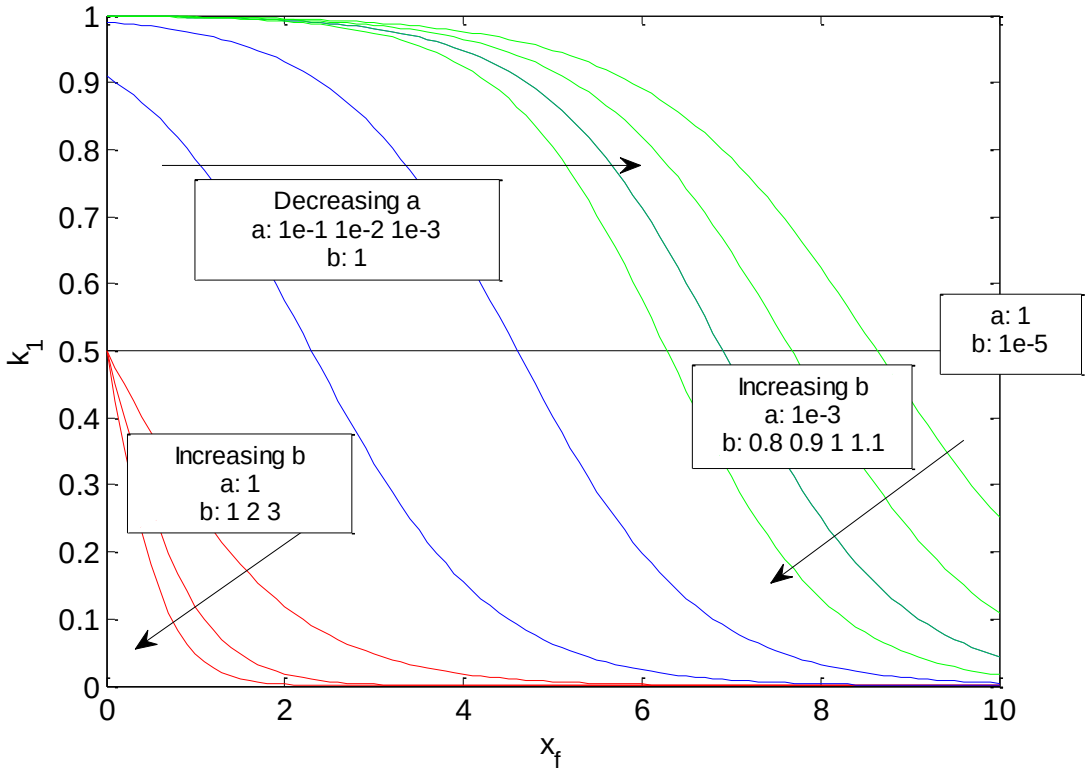

Figure D.2 – Form of the logistic function for several different sets of a and b values. Decreasing the value of a expands the distance in x_f before k_1 begins to decrease (blue lines). Increasing the value of b sharpens the front of decreasing k_1 (red lines). However, note that increasing b also has an effect of reducing the contribution of a, so the two parameters are not entirely independent (green lines).

Plugging Eqn. D.17 into Eq. D.15 and solving for boundary condition $t = 0, x_f = 0$ the solution becomes:

$$t = \frac{1}{F}\left[Ix_f + \frac{M}{2}x_f^2 + \frac{(\alpha-\beta)}{k_o}\left[\frac{x_f^2}{2} + \left(\frac{a}{b^2\alpha^2}\right)e^{b\alpha x_f}\left(b\alpha x_f - 1\right) + \left(\frac{a}{b^2\alpha^2}\right)\right]\right] \qquad \text{(D.18)}$$

Model features

The model gives the time required (dependent variable) for fluid to move a specified distance (independent variable), which is based on how the weighted average permeability evolves in the system. The other parameters (e.g. permeability and location of fronts) are then calculated for using the equations above. The model consists of six parameters which can be defined using experiment data or subsurface estimations (ΔP, μ, L, k_0, k_2 and x_f). Retardation of the fronts (α and β parameters) are unknown but observations of precipitation and dissolution on the fracture surface provide insight for estimating values for each experiment. The parameter(s) in the k_1 function are k_1 itself (constant permeability case) or a and b in the case of the logistic function. The parameters in the logistic function are unknown except that to satisfy dimensional analysis of the full leakage model, the units of parameter a must be dimensionless and the units of the parameter b must be inverse length. Additional insights can be gained from the behavior of the logistic function with different a and b values (Figure D.2). The a parameter relates to the volume injected before initiation of permeability reduction. The smaller the value of a, the longer it will take to initiate permeability reduction. The b parameter controls how sharp the reduction in flow occurs once initiated, i.e. the slope of the asymptotic curve. With a larger b value the permeability reduces faster. Thus the goal of matching the model to experiment data is to determine not only the specific α, β, k_1 or a, and b parameters for the experiments but to also determine if they can be related to other experiment parameters.

An idealized example is presented to highlight some features of the model. The model parameters are: Fluid volume injected (here equal to x_f) is 1, L is 1, k_0 and k_2 are 1, $\Delta P = 1$, μ=1, $\alpha = 0.7$, $\beta = 0.2$. To verify that the logistic function is an appropriate model

2 different cases for k_1 are presented. The first case is for when k_1 is constant and the second case is for k_1 evolving with fluid front position according to the logistic function.

According to reactive transport theory (Helfferich, 1989; Lake et al., 2002) the precipitation zone should reach an equilibrium state and advance at constant speed if reaction rates are fast. The concentration of minerals in the precipitation zone will remain unchanged but the width of the zone will grow. To test the case for constant precipitation zone permeability k_1 is set to half the initial permeability. Figure D.3 shows the evolution of the system as the precipitation zone grows. Average permeability immediately begins to asymptotically decrease towards the precipitation zone value. Figure D.4 shows results for when a = 0.01 and b = 10. This set of parameters generates an average permeability that is equal to k_0 for a period of time before decreasing asymptotically. The period of constant average permeability occurs despite an immediate decrease in the precipitation zone permeability (blue line). The precipitation zone permeability has negligible influence initially because the zone is small and cannot contribute significant flow resistance. The fluid fronts advance with constant velocities until time 0.75 after which the fronts begin to flatten out. The flattening behavior is caused by fluid front velocities beginning to slow due to the influence of k_1.

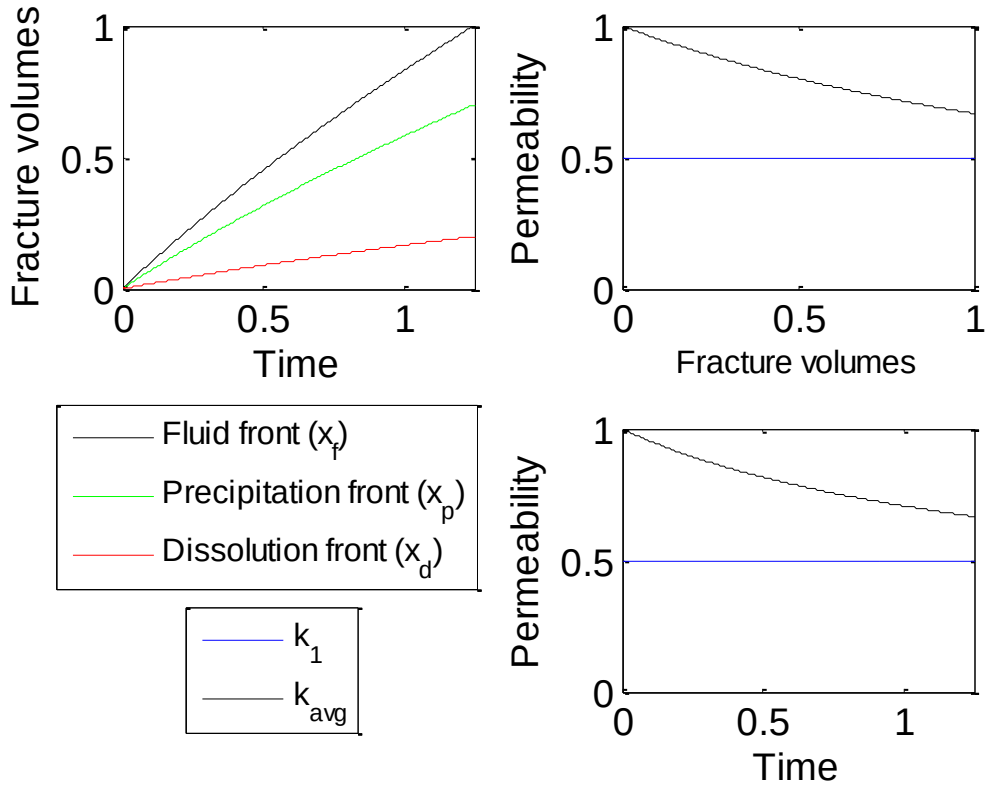

Figure D.3 – Evolution of system with a constant k_1 that is half of k_0. (Top left) Time and distance plot for each front. (Top right) Permeability evolution as a function of fracture volumes injected. (Bottom right) Average permeability plotted as a function of time.

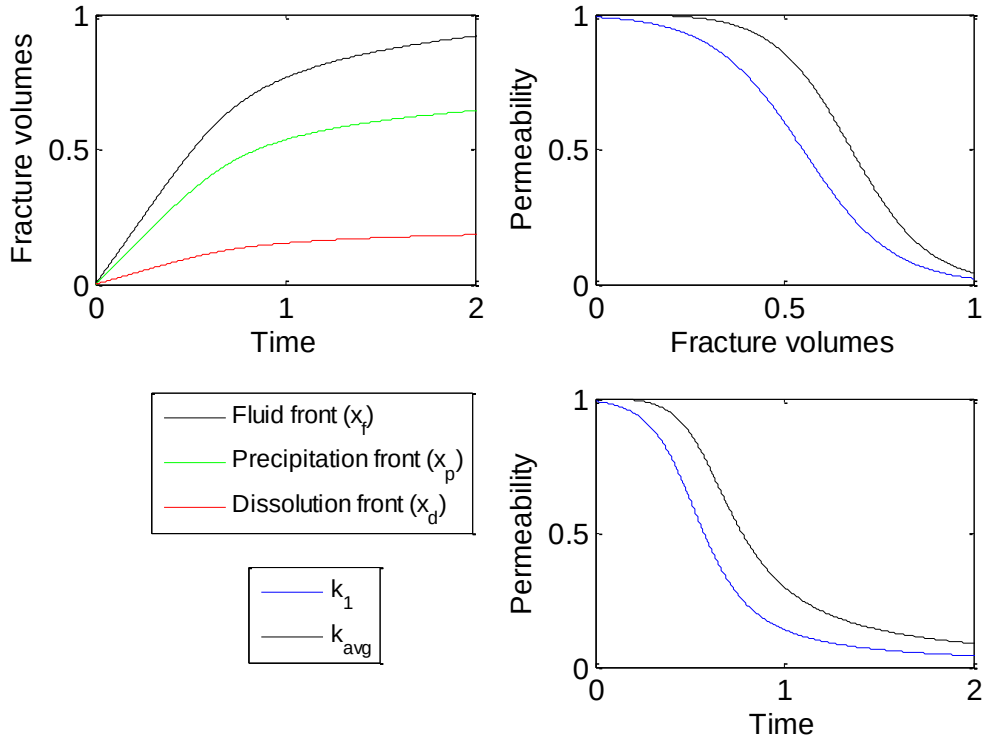

Figure D.4 – Evolution of system with logistic parameters $a = 1\times10^{-2}$ and $b = 10$, which results in an evolving k_1. (Top left) Time and distance plot for each front. (Top right) Permeability evolution as a function of fracture volumes injected. (Bottom right) Permeability evolution as a function of time.

This model is similar to classic reactive transport behavior (Lake et al., 2002) in 1D that treats reaction zones with specific velocities relative to the fluid front however some distinctions must be drawn. First is that most models assume constant fluid flux and not constant pressure differential. In constant flux, precipitation induced sealing would increase local flux and pressure differential. In the fractured cement system precipitation induces a decrease in fluid flux and increases local residence time. If reaction rates are slow this increased residence time allows for further precipitation and self-reinforcing behavior. Secondly, simple 1D reactive transport models cannot account for 2D heterogeneity that must be occurring on the fracture surface. Thus, the process of mixing

induced reaction from slow and fast flow regions is missed in 1D models derived from first principles. According to classic 1D behavior the most favorable scenario for precipitation occurs at the salinity front but experiments show the precipitation front is retarded far behind. The current hypothesis is that local heterogeneity induced fluid front retardation in zones and local mixing that induced precipitation well after the injected fluid has broken through. How the zones develop and what model parameters control the evolution is still being studied. Hence one advantage of this simple model is that new equations for permeability evolution (or modifications to the constant permeability or logistic function) or indeed new relations between front speeds or other parameters can be easily inserted and the equation solved to get a simple model for flow.

Definitions

α – Precipitation front retardation factor [-]

β – Dissolution front retardation factor [-]

a – Parameter in logistic permeability function [-]

b – Parameter in logistic permeability function [L^{-1}]

q – Fluid flux [Lt^{-1}]

$\bar{k}$ – Average permeability [L^2]

k_0 – Initial permeability [L^2]

k_1 – Precipitation zone permeability [L^2]

k_2 – Reacted zone permeability [L^2]

ΔP – Pressure differential [FL^{-2}]

μ – Fluid dynamic viscosity [$mL^{-1}t^{-2}$]

L – Total length of domain [L]

L_0 – Length of minimally altered zone [L]

L_1 – Length of precipitation zone [L]

L_2 – Length of reaction zone [L]

x_f – Fluid front position [L]

x_p – Precipitation front position [L]

x_d – Dissolution front position [L]

t – Time [t]

References

API, 1997. Recommended Practice for Testing Well Cements 10B.

API, 2011. Specification for Cements and Materials for Well Cementing.

Bear, J., 1972. Dynamics of Fluids in Porous Media. American Elsevier Publishing Company, Inc., New York.

Beddoe, R.E., Dorner, H.W., 2005. Modelling acid attack on concrete: Part I. The essential mechanisms. Cem. Concr. Res. 35, 2333–2339.

Berkowitz, B., 2002. Characterizing flow and transport in fractured geological media: A review. Adv. Water Resour. 25, 861–884.

Bird, R.B., Stewart, W.E., Lightfoot, E.N., 2002. Transport phenomena, 2nd ed. ed. J. Wiley, New York.

Boukhelifa, L., Moroni, N., James, S., Le Roy-Delage, S., Thiercelin, M., Lemaire, G., 2005. Evaluation of Cement Systems for Oil- and Gas-Well Zonal Isolation in a Full-Scale Annular Geometry. SPE Drill. Complet. 20.

Bourgoyne, A., T. , Jr., Chenevert, M.E., Millheim, K.K., Young, F.S., Jr., 1986. Applied Drilling Engineering, SPE Textbook Series. Society of Petroleum Engineers.

Brown, S.R., 1987. Fluid flow through rock joints: The effect of surface roughness. J. Geophys. Res. Solid Earth 92, 1337–1347.

Bruant, R.G., Jr., J., Celia, M.A., Guswa, A.J., Peters, C.A., 2002. Peer Reviewed: Safe Storage of CO_2 in Deep Saline Aquifers. Environ. Sci. Technol. 36, 240A–245A.

Burton, M., Bryant, S., 2009. Eliminating Buoyant Migration of Sequestered CO_2. SPE Reserv. Eval. Eng. 12.

Carey, J.W., Wigand, M., Chipera, S.J., WoldeGabriel, G., Pawar, R., Lichtner, P.C., Wehner, S.C., Raines, M.A., Guthrie Jr., G.D., 2007. Analysis and performance of oil well cement with 30 years of CO_2 exposure from the SACROC Unit, West Texas, USA. Int. J. Greenh. Gas Control 1, 75–85.

Chandra, S., 1988. Hydrochloric acid attack on cement mortar — An analytical study. Cem. Concr. Res. 18, 193–203.

Crow, W., Carey, J.W., Gasda, S., Brian Williams, D., Celia, M., 2010. Wellbore integrity analysis of a natural CO_2 producer. Int. J. Greenh. Gas Control 4, 186–197.

De Ceukelaire, L., 1992. The effects of hydrochloric acid on mortar. Cem. Concr. Res. 22, 903–914.

Detwiler, R.L., Rajaram, H., Glass, R.J., 2000. Solute transport in variable-aperture fractures: An investigation of the relative importance of Taylor dispersion and macrodispersion. Water Resour. Res. 36, 1611–1625.

Duan, Z., Møller, N., Weare, J.H., 1992. An equation of state for the CH_4-CO_2-H_2O system: I. Pure systems from 0 to 1000°C and 0 to 8000 bar. Geochim. Cosmochim. Acta 56, 2605–2617.

Duan, Z., Sun, R., 2003. An improved model calculating CO_2 solubility in pure water and aqueous NaCl solutions from 273 to 533 K and from 0 to 2000 bar. Chem. Geol. 193, 257–271.

Duan, Z., Sun, R., Zhu, C., Chou, I.-M., 2006. An improved model for the calculation of CO_2 solubility in aqueous solutions containing Na+, K+, Ca2+, Mg2+, Cl−, and $SO_4$2−. Mar. Chem. 98, 131–139.

Duguid, A., Scherer, G.W., 2010. Degradation of oilwell cement due to exposure to carbonated brine. Int. J. Greenh. Gas Control 4, 546–560.

EPA, 2010. Federal Requirements Under the Underground Injection Control (UIC) Program for Carbon Dioxide (CO_2) Geologic Sequestration (GS) Wells; Final Rule.

Falkowski, P., Scholes, R.J., Boyle, E., Canadell, J., Canfield, D., Elser, J., Gruber, N., Hibbard, K., Högberg, P., Linder, S., Mackenzie, F.T., Iii, B.M., Pedersen, T., Rosenthal, Y., Seitzinger, S., Smetacek, V., Steffen, W., 2000. The Global Carbon Cycle: A Test of Our Knowledge of Earth as a System. Science 290, 291–296.

Gaus, I., 2010. Role and impact of CO_2–rock interactions during CO_2 storage in sedimentary rocks. Int. J. Greenh. Gas Control 4, 73–89.

Gentier, S.S., Hopkins, D.L., 1997. Mapping fracture aperture as a function of normal stress using a combination of casting, image analysis and modeling techniques. Int. J. Rock Mech. Min. Sci. 34, 132.e1–132.e14.

Goodman, A., Hakala, A., Bromhal, G., Deel, D., Rodosta, T., Frailey, S., Small, M., Allen, D., Romanov, V., Fazio, J., Huerta, N., McIntyre, D., Kutchko, B., Guthrie, G., 2011. U.S. DOE methodology for the development of geologic storage potential for carbon dioxide at the national and regional scale. Int. J. Greenh. Gas Control 5, 952–965.

Gunter, W.., Perkins, E.., Hutcheon, I., 2000. Aquifer disposal of acid gases: modelling of water–rock reactions for trapping of acid wastes. Appl. Geochem. 15, 1085–1095.

Guo, H., Aziz, N.I., Schmidt, L.C., 1993. Rock fracture-toughness determination by the Brazilian test. Eng. Geol. 33, 177–188.

Hanisch, C., 1999. Exploring Options for CO_2 Capture and Management. Environ. Sci. Technol. 33, 66A–70A.

Helfferich, F.G., 1989. The theory of precipitation/dissolution waves. AIChE J. 35, 75–87.

Huerta, N.J., Bryant, S.L., Strazisar, B.R., Kutchko, B.G., Conrad, L.C., 2009. The influence of confining stress and chemical alteration on conductive pathways within wellbore cement. Energy Procedia 1, 3571–3578.

Huerta, N.J., Hesse, M.A., Bryant, S.L., Strazisar, B.R., Lopano, C.L., 2013. Experimental Evidence for Self-Limiting Reactive Flow through a Fractured Cement Core: Implications for Time-Dependent Wellbore Leakage. Environ. Sci. Technol. 47, 269–275.

Huet, B.M., Prevost, J.H., Scherer, G.W., 2010. Quantitative reactive transport modeling of Portland cement in CO_2-saturated water. Int. J. Greenh. Gas Control 4, 561–574.

IPCC, 2013. WORKING GROUP I CONTRIBUTION TO THE IPCC FIFTH ASSESSMENT REPORT CLIMATE CHANGE 2013: THE PHYSICAL SCIENCE BASIS.

Jevrejeva, S., Moore, J.C., Grinsted, A., 2010. How will sea level respond to changes in natural and anthropogenic forcings by 2100? Geophys. Res. Lett. 37, 1–5.

Ketcham, R.A., Slottke, D.T., Sharp, J.M., 2010. Three-dimensional measurement of fractures in heterogeneous materials using high-resolution X-ray computed tomography. Geosphere 6, 499–514.

Kutchko, B.G., Strazisar, B.R., Dzombak, D.A., Lowry, G.V., Thaulow, N., 2007. Degradation of Well Cement by CO_2 under Geologic Sequestration Conditions. Environ. Sci. Technol. 41, 4787–4792.

Kutchko, B.G., Strazisar, B.R., Huerta, N., Lowry, G.V., Dzombak, D.A., Thaulow, N., 2009. CO_2 Reaction with Hydrated Class H Well Cement under Geologic Sequestration Conditions: Effects of Flyash Admixtures. Environ. Sci. Technol. 43, 3947–3952.

Kutchko, B.G., Strazisar, B.R., Lowry, G.V., Dzombak, D.A., Thaulow, N., 2008. Rate of CO_2 Attack on Hydrated Class H Well Cement under Geologic Sequestration Conditions. Environ. Sci. Technol. 42, 6237–6242.

Lake, L.W., Bryant, S.L., Araque-Martinez, A.N., 2002. Geochemistry and fluid flow, Developments in geochemistry. Elsevier.

Li, D., Duan, Z., 2007. The speciation equilibrium coupling with phase equilibrium in the H_2O–CO_2–NaCl system from 0 to 250 °C, from 0 to 1000 bar, and from 0 to 5 molality of NaCl. Chem. Geol. 244, 730–751.

Lichtner, P.C., Steefel, C.I., Oelkers, E.H., 1996. Reactive transport in porous media, Reviews in mineralogy. Mineralogical Society of America, Washington, DC.

Mainguy, M., Tognazzi, C., Torrenti, J.-M., Adenot, F., 2000. Modelling of leaching in pure cement paste and mortar. Cem. Concr. Res. 30, 83–90.

Mason, H.E., Du Frane, W.L., Walsh, S.D.C., Dai, Z., Charnvanichborikarn, S., Carroll, S.A., 2013. Chemical and Mechanical Properties of Wellbore Cement Altered by CO_2-Rich Brine Using a Multianalytical Approach. Environ. Sci. Technol. 47, 1745–1752.

Matschei, T., Lothenbach, B., Glasser, F.P., 2007. The AFm phase in Portland cement. Cem. Concr. Res. 37, 118–130.

Matteo, E.N., Scherer, G.W., 2012. Experimental study of the diffusion-controlled acid degradation of Class H Portland cement. Int. J. Greenh. Gas Control 7, 181–191.

Metz, B., Davidson, O., de Coninck, H., Loos, M., Meyer, L. (Eds.), 2005. IPCC Special Report on Carbon Dioxide Capture and Storage.

Milanovic, D., Smith, L., 2005. A Case History of Sustainable Annulus Pressure in Sour Wells – Prevention, Evaluation and Remediation. Society of Petroleum Engineers.

Monlouis-Bonnaire, J.P., Verdier, J., Perrin, B., 2004. Prediction of the relative permeability to gas flow of cement-based materials. Cem. Concr. Res. 34, 737–744.

Moroni, N., Repetto, C., Ravi, K., 2008. Zonal Isolation in Reservoir Containing CO_2 and H_2S. Society of Petroleum Engineers.
Mueller, D., Virgilio, G., Dillenbeck, R., Thomas, H., 2004. Characterizing Casing-Cement-Formation Interactions Under Stress Conditions: Impact on Long-Term Zonal Isolation. Society of Petroleum Engineers.
Nelson, E.B., Guillot, D. (Eds.), 2006. Well Cementing, 2nd ed, Developments in petroleum science. Schlumberger.
Nicot, J.-P., 2009. A survey of oil and gas wells in the Texas Gulf Coast, USA, and implications for geological sequestration of CO_2. Environ. Geol. 57, 1625–1638.
Nordbotten, J.M., Celia, M.A., Bachu, S., Dahle, H.K., 2005. Semianalytical Solution for CO_2 Leakage through an Abandoned Well. Environ. Sci. Technol. 39, 602–611.
Oldenburg, C.M., Bryant, S.L., Nicot, J.-P., 2009. Certification framework based on effective trapping for geologic carbon sequestration. Int. J. Greenh. Gas Control 3, 444–457.
Park, C.-K., Keum, D.-K., Hahn, P.-S., 1995. A stochastic analysis of contaminant transport through a rough-surfaced fracture. Korean J. Chem. Eng. 12, 428–435.
Ravi, K., Bosma, M., Gastebled, O., 2002. Safe and Economic Gas Wells through Cement Design for Life of the Well. Society of Petroleum Engineers.
Regnault, O., Lagneau, V., Schneider, H., 2009. Experimental measurement of portlandite carbonation kinetics with supercritical CO_2. Chem. Geol. 265, 113–121.
Rosenzweig, C., Parry, M.L., 1994. Potential impact of climate change on world food supply. Nature 367, 133–138.
Sabins, F., Wiggins, M.L., 1997. Parametric Study of Gas Entry Into Cemented Wellbores. SPE Drill. Complet. 12.
Shen, J., Dangla, P., Thiery, M., 2013. Reactive transport modeling of CO_2 through cementitious materials under CO_2 geological storage conditions. Int. J. Greenh. Gas Control 18, 75–87.
Shen, J.C., Pye, D.S., 1989. Effects Of CO_2 Attack on Cement in High-Temperature Applications. Society of Petroleum Engineers.
Singurindy, O., Berkowitz, B., 2005. The role of fractures on coupled dissolution and precipitation patterns in carbonate rocks. Adv. Water Resour. 28, 507–521.
Soter, K., 2003. REMOVAL OF SUSTAINED CASING PRESSURE UTILIZING A WORKOVER RIG. Louisiana State University.
Stott, P.A., Tett, S.F.B., Jones, G.S., Allen, M.R., Mitchell, J.F.B., Jenkins, G.J., 2000. External Control of 20th Century Temperature by Natural and Anthropogenic Forcings. Science 290, 2133–2137.
Szymczak, P., Ladd, A.J.C., 2009. Wormhole formation in dissolving fractures. J. Geophys. Res. Solid Earth 114, 1–22.
Tao, Q., Checkai, D., Huerta, N., Bryant, S.L., 2011. An improved model to forecast CO_2 leakage rates along a wellbore. Energy Procedia 4, 5385–5391.

Tartakovsky, A.M., Meakin, P., Scheibe, T.D., Wood, B.D., 2007. A smoothed particle hydrodynamics model for reactive transport and mineral precipitation in porous and fractured porous media. Water Resour. Res. 43, 1–18.
Tartakovsky, A.M., Redden, G., Lichtner, P.C., Scheibe, T.D., Meakin, P., 2008. Mixing-induced precipitation: Experimental study and multiscale numerical analysis. Water Resour. Res. 44, 1–19.
Thompson, M.E., Brown, S.R., 1991. The effect of anisotropic surface roughness on flow and transport in fractures. J. Geophys. Res. Solid Earth 96, 21923–21932.
TRRC, 2013. Rule 13: "Casing, Cementing, Drilling, Well Control, and Completion Requirements."
Viswanathan, H.S., Pawar, R.J., Stauffer, P.H., Kaszuba, J.P., Carey, J.W., Olsen, S.C., Keating, G.N., Kavetski, D., Guthrie, G.D., 2008. Development of a Hybrid Process and System Model for the Assessment of Wellbore Leakage at a Geologic CO_2 Sequestration Site. Environ. Sci. Technol. 42, 7280–7286.
Walsh, M.P., Bryant, S.L., Schechter, R.S., Lake, L.W., 1984. Precipitation and dissolution of solids attending flow through porous media. AIChE J. 30, 317–328.
Watanabe, N., Hirano, N., Tsuchiya, N., 2008. Determination of aperture structure and fluid flow in a rock fracture by high-resolution numerical modeling on the basis of a flow-through experiment under confining pressure. Water Resour. Res. 44, 1–11.
Watson, T., Bachu, S., 2007. Evaluation of the Potential for Gas and CO_2 Leakage Along Wellbores. Society of Petroleum Engineers.
Watson, T., Bachu, S., 2008. Identification of Wells With High CO_2-Leakage Potential in Mature Oil Fields Developed for CO_2-Enhanced Oil Recovery. Society of Petroleum Engineers.
Watson, T., Bachu, S., 2009. Evaluation of the Potential for Gas and CO_2 Leakage Along Wellbores. SPE Drill. Complet. 24.
Wenning, Q.C., Huerta, N.J., Hesse, M.A., Bryant, S.L., 2013. Reactive Flow Channelization in Fractured Cement-implications for Wellbore Integrity. Energy Procedia 37, 5773–5780.
Zheng, Q., Dickson, S.E., Guo, Y., 2008. On the appropriate "equivalent aperture" for the description of solute transport in single fractures: Laboratory-scale experiments. WATER Resour. Res. 44, 9.
Zivica, V., Bajza, A., 2001. Acidic attack of cement based materials — a review.: Part 1. Principle of acidic attack. Constr. Build. Mater. 15, 331–340.